AIRCRAFT LANDING USING A MODERNIZED GLOBAL POSITIONING SYSTEM AND THE WIDE AREA AUGMENTATION SYSTEM

A DISSERTATION SUBMITTED TO THE DEPARTMENT OF AERONAUTICS AND
ASTRONAUTICS AND THE COMMITTEE ON GRADUATE STUDIES OF
STANFORD UNIVERSITY IN PARTIAL FULFILLMENT OF THE REQUIREMENTS
FOR THE DEGREE OF DOCTOR OF PHILOSOPHY

SHAU-SHIUN JAN

MAY 2003

I certify that I have read this thesis and that in my opinion it is fully adequate, in scope and in quality as a dissertation for the degree of Doctor of Philosophy.

Per Enge
(Principle Advisor)

I certify that I have read this thesis and that in my opinion it is fully adequate, in scope and in quality as a dissertation for the degree of Doctor of Philosophy.

J. David Powell

I certify that I have read this thesis and that in my opinion it is fully adequate, in scope and in quality as a dissertation for the degree of Doctor of Philosophy.

Todd Walter

Approved for the University Committee on Graduate Studies:

Abstract

This research investigates the performance of an airborne GPS receiver using differential corrections and associated error bounds from the Wide Area Augmentation System (WAAS) when three civil GPS signals (L1, L2, and L5) become available. There are three ways to take advantage of the multiple frequencies. First, one can measure ionospheric delay directly in the airplane. This would replace the grid of ionosphere delay corrections currently broadcast by the WAAS. This direct use of multiple frequencies would be more accurate, and offer higher availability. Second, one can use the additional GPS frequencies to mitigate unintentional radio frequency interference (RFI). Even if two of these frequencies are lost, the user could revert to the WAAS grid. Third, one can take advantage of stronger civil signal power of the modernized GPS to acquire a low elevation satellite before using it for the position solution. Earlier acquisition would allow for longer carrier-aided smoothing of multipath.

This research evaluates the performance of a multiple-frequency GPS landing system that depends on the number of available GPS frequencies and includes the following scenarios:

Case 1: All three GPS frequencies are available,

Case 2: Two of three GPS frequencies are available,

Case 3: One of three GPS frequencies is available.

This research also presents a solution to sustain multiple frequency performance when an aircraft descends into an RFI field and loses all but one of the frequencies. There are three available techniques. First, one can use the code-carrier divergence to continue ionospheric delay estimation; this technique would require a robust cycle slip detector. Second, one can use the WAAS ionospheric threat model to bound the error. This technique would require an ionosphere storm detector to listen to the new WAAS message which indicates the presence of ionosphere storms. Third, one can use the maximum ionospheric delay gradient model to bound the ionospheric delay during the ionosphere storm period. These three techniques all provide the ability to continue operation for more than 10 minutes after the onset of RFI.

The coverage and availability are compared for the three RFI cases from the prior page. This involved developing the MATLAB Algorithm Availability Simulation Tool (MAAST) which completes trade-off studies to assess the performance of various architectures for the WAAS. The MAAST implements the real WAAS Master Station (WMS) algorithms. The majority of MAAST is open source and can be downloaded from the Stanford WAAS web site (http://waas.stanford.edu). Therefore, it provides a common ground for different working groups to compare their results.

A barometric altimeter is also investigated in this research to enhance the vertical guidance performance, which involved developing a barometric altimeter confidence model. This confidence model is evaluated by the worst-case historical meteorological observation data and flight test data. The barometric altimeter aiding provides coverage at 99.9% LPV (VAL = 50m, HAL = 40m) availability for a single-frequency GPS/WAAS user in the Conterminous United States (CONUS). This represents a 1.61% coverage improvement for an L1-only GPS/WAAS user, a 34.29% coverage improvement for an L2-only GPS/WAAS user, and a 40.04% coverage improvement for an L5-only GPS/WAAS user.

This research provides the first three-frequency GPS/WAAS LPV coverage predictions for CONUS. The current L1-only WAAS user has LPV precision approach services available 99.9% of the time over 97.46% of CONUS, although this may be reduced during ionosphere storms. After the GPS and WAAS modernizations, an L1-L2-L5 three-

frequency user, an L1-L2 dual-frequency user, and an L1-L5 dual-frequency user all have LPV precision approach services available 99.9% of time over 100% of CONUS even during ionosphere storms. Additionally, when combining modernized GPS, WAAS, and barometric altimeter aiding, an L1-only user has 99.19%, an L2-only user has 92.63%, and an L5-only user has 89.29% coverage of CONUS.

Acknowledgments

I would like to thank my advisor, Professor Per Enge, for giving me the opportunity to pursue this research. From the very beginning of my work under his guidance until now, I have continued to benefit from his comprehensive knowledge and skill as a mentor, a researcher, and a professor. I will always be grateful for the wonderful experience.

I would also like to express my gratitude to the other member in my defense and reading committee, Professor J. David Powell, Professor Stephen Rock, Professor Bernard Widrow, and Dr. Todd Walter, for their constructive evaluation and criticism of this thesis. I gratefully acknowledge Dr. Todd Walter for his comprehensive knowledge of WAAS, and he is always willing to help me out whenever I have a WAAS question. In addition, I would like to thank Fiona Walter for her thoughtful comments and suggestions to make this manuscript clearer for future reader.

I would like to thank Federal Aviation Administration Satellite Program Office for their support of research in WAAS which made this work possible. I would also like to thank the Charles Stark Draper Laboratory in Massachusetts Institute of Technology for funding my first research project at Stanford. I gratefully acknowledge the Department of Aeronautics and Astronautics, in particular the office staff, Sherann Ellsworth, Dana Parga, Sally Gressens, and Dianne Le, for their endless help.

I would like to thank all the former and current members in our laboratory and group. It is truly my pleasure to work with the best persons in the world. In no particular order, I thank

Dr. Demoz Gebre-Egziahber, Dr. Sherman Lo, Dr. Donghai Dai, Dr. Sam Pullen, Dr. Dennis Akos, Dr. Eric Phelts, Dr. Rich Fuller, Dr. YC Chao, Dr. YJ Tsai, Dr. Jaewoo Jung, Dr. Takeyasu Sakai, Dr. Keith Alter, Dr. Sharon Houck, Doug Archdeacon, Wyant Chan, Juan Blanch, Frank Bauregger, Aubrey Chen, Chad Jennings, Richard Yang, Alexander Mitelman, Seebany Datta-Barua, Lee Boyce, Ming Luo, Guttorm Opshaug. I would also like to thank Lin Xiao and Xiaohau Chen for being my friends for the past 6 years.

Last but not least, I would like to thank my family. First my parents, Gwo-Rong Jan and Chen-Mei Liao, for the support and love they have given me during my study at Stanford and throughout my academic life. I would like to thank my brothers, Yu-Shiun and Wilson for their encouragements. Most importantly I would like to thank my wife, Yu-Lin Chao. Her love, support and time are immeasurable. No one could ask for anything more. I dedicate this thesis to her and our sons, Allen and Andrew.

Table of Contents

AIRCRAFT LANDING USING A MODERNIZED GLOBAL POSITIONING SYSTEM AND THE WIDE AREA AUGMENTATION SYSTEM............ I

ABSTRACT............ IV

ACKNOWLEDGMENTS............ VII

TABLE OF CONTENTS............ IX

LIST OF FIGURES............ XIII

LIST OF TABLES............ XX

CHAPTER 1............ 1

INTRODUCTION............ 1
1.1 BACKGROUND............ 1
1.1.1 THE GLOBAL POSITIONING SYSTEM (GPS)............ 2
1.1.2 AVIATION NAVIGATION REQUIREMENTS............ 7
1.1.3 AUGMENTATION SYSTEMS............ 10
1.1.3.1 LOCAL AREA AUGMENTATION SYSTEM (LAAS)............ 10
1.1.3.2 WIDE AREA AUGMENTATION SYSTEM (WAAS)............ 11
1.2 GPS MODERNIZATION............ 12
1.3 MOTIVATION............ 14
1.4 PREVIOUS WORK............ 16
1.4.1 THE USE OF MULTI-FREQUENCY GPS............ 16
1.4.2 WAAS AVAILABILITY ANALYSIS............ 17
1.4.3 BAROMETRIC ALTIMETER ERROR MODEL............ 17
1.5 THESIS CONTRIBUTIONS............ 18
1.5.1 DERIVED NEW PROTECTION LEVEL (PL) CALCULATION [CHAPTERS 3, 4, & 5]............ 18
1.5.2 SUSTAINED MULTI-FREQUENCY PERFORMANCE WHEN AIRCRAFT DESCENDED INTO AN RFI FIELD [CHAPTER 4]............ 18
1.5.3 PREDICTED FIRST THREE-FREQUENCY GPS/WAAS LPV COVERAGE IN CONUS UNDER VARIOUS SCENARIOS [CHAPTERS 2, 3, 4, 5, & 6]............ 19
1.5.4 DEVELOPED BAROMETRIC ALTIMETER CONFIDENCE MODEL [CHAPTER 6]............ 19
1.5.5 ANTENNA BEAM FORMING BASED ON MOBILE ANTENNA ELEMENTS AND GPS [APPENDICES A & B]............ 20
1.6 CONCLUDING REMARKS............ 21

CHAPTER 2............ 22

WIDE AREA AUGMENTATION SYSTEM............ 22
2.1 INTRODUCTION............ 22

2.2 WAAS Overview 25
2.2.1 WAAS Master Station Processing Algorithm 25
2.2.1.1 Ionosphere Errors 26
2.2.1.2 Satellite Errors 31
2.2.2 Local Errors 34
2.2.3 User Avionics 36
2.3 WAAS Availability Analysis 37
2.4 MATLAB Algorithm Availablity Simulation Tool (MAAST) 41
2.4.1 MAAST Simulation Configuration 42
2.4.2 MAAST Simulation Process 45
2.4.2.1 WMS Processing 48
2.4.2.2 User Processing 49
2.4.3 MAAST Graphic User Interface (GUI) 49
UDRE-GPS Menu 50
UDRE-GEO Menu 50
GIVE Menu 50
TROP-WRS / TROP-USR Menus 51
CNMP-WRS / CNMP-USR Menus 51
2.4.4 MAAST Outputs 51
2.5 WRS Failure 57
2.6 Conclusions 59

CHAPTER 3 60

Nominal Performance of WAAS Using L1 and L5 Frequencies 60
3.1 Introduction 60
3.2 L1-L5 Dual-Frequency User 61
3.2.1 Dual-Frequency Hardware Group Delays 64
3.2.2 New UIRE Calculation 70
3.2.2 New UDRE Calculation 74
3.3 MAAST Simulation Results 74
3.4 Conclusions 77

CHAPTER 4 79

Robust Reversion from Dual to Single Frequency WAAS in the Presence of Radio Frequency Interference 79
4.1 Introduction 79
4.2 Single-Frequency User 80
4.2.1 L1-Only Single-Frequency GPS/WAAS User 80
4.2.2 L5-Only Single-Frequency GPS/WAAS User 81
4.2.3 MAAST Coverage Simulation Results 84
4.3 Techniques For Graceful Reversion From Dual To Single Frequency WAAS 89
4.3.1 Problem Statement And Scenarios 90
4.3.2 Code And Carrier Divergence Technique 93
4.3.3 WAAS Ionosphere Threat Model Technique 103
4.3.4 Maximum Ionospheric Delay Gradient Model Technique 111
4.4 Conclusions 124

CHAPTER 5 126

WAAS Utilization of the New Civil Signal at L2 126
5.1 Introduction 126
5.2 L2-Only Single-Frequency GPS/WAAS User 127
5.2.1 Changes In The WAAS Protection Level Calculation 127
5.2.2 MAAST Simulation Results 129
5.3 L1-L2 And L2-L5 Dual-Frequency Users 133
5.3.1 L1-L2 Dual-Frequency User 133
5.3.1.1 UDRE Calculation For An L1-L2 Dual-Frequency User 135

5.3.1.2 New UIRE Calculation For An L1-L2 Dual-Frequency User ... 135
5.3.1.3 MAAST Simulation Results ... 136
5.3.2 L2-L5 Dual-Frequency User ... 139
5.3.2.1 New UDRE Calculation For The L2-L5 Dual-Frequency User ... 140
5.3.2.2 New UIRE Calculation For The L2-L5 Dual-Frequency User ... 140
5.3.2.3 MAAST Simulation Results ... 141
5.3.2.4 Combined Use Of Ionospheric Correction For An L2-L5 Dual-Frequency User ... 143
5.4 Conclusions ... 149

CHAPTER 6 ... 151

Barometric Altimeter ... 151
6.1 Introduction ... 151
6.2 Barometric Altimeter Basics ... 152
6.3 Barometric Altimeter Error Sources ... 154
6.4 Barometric Altimeter Confidence Model ... 155
6.5 Barometric Altimeter Confidence Model Verification ... 164
6.6 Barometric Altimeter Benefits ... 169
6.7 Conclusions ... 179

CHAPTER 7 ... 180

Conclusions ... 180
7.1 Summary Of Thesis Contributions ... 180
7.1.1 Developed New Protection Level (PL) Calculations ... 180
7.1.2 Sustained Multi-Frequency Performance For An Aircraft Descending Into An RFI Field ... 183
7.1.3 Predicted The First Three-Frequency GPS/WAAS LPV Coverage In Conus ... 185
7.1.4 Developed Barometric Altimeter Confidence Model ... 186
7.2 Recommendations For Future Work ... 189
7.3 Closing Remarks ... 189

APPENDIX A ... 190

Using GPS to Synthesize a Large Antenna Aperture Comprised of Mobile Antenna Elements ... 190
A.1 Introduction ... 190
A.2 Assumptions And Configuration ... 191
A.3 Basics Of Antenna Arrays ... 194
A.4 Signal Strength Measurement Feedback Only - No GPS ... 196
A.5 GPS Positioning Without Signal Strength Measurement Feedback ... 200
A.6 Combined GPS Positioning And Signal Strength Measurement Feedback ... 205
A.7 Partial GPS ... 211
A.8 Conclusions ... 215

APPENDIX B ... 218

Finding Electromagnetic Interference (EMI) Sources to GPS Using a Network of Sensors ... 218
B.1 introduction ... 218
B.2 Prior Art ... 219
B.3 Bascis Of Position Estimation ... 221
B.3.1 Single Bearing Measurement Example ... 226
B.3.2 Single Frequency Measurement Example ... 228
B.4 Network Of Sensors ... 232
B.4.1 Multiplicity Of Sensors And Sensor Span ... 232
B.4.2 Distance From Sensors To EMI Source ... 233
B.4.3 Sensor Separation ... 234
B.4.4 Sensor Failure ... 235
B.5 Concluding Comparison ... 237

BIBLIOGRAPHY 238

List of Figures

Figure 1.1: The GPS includes three segments: space segment, control segment, and user segment. 2
Figure 1.2: The Global Positioning System (GPS) space segment (Courtesy: FAA). 3
Figure 1.3: The spectrum of present GPS signals. There are two GPS frequencies, L1 at 1575.42 MHz and L2 at 1227.6 MHZ. L1 has C/A and P(Y) codes on it; L2 has only P(Y) code on it. Therefore, a civilian can only access the L1 C/A and carrier of L2. 4
Figure 1.4: The GPS error sources. 5
Figure 1.5: The definition of Availability. 8
Figure 1.6: The landing categories [ICAO] [FAA2002]. 10
Figure 1.7: The Local Area Augmentation System (LAAS) (Courtesy: FAA). 11
Figure 1.8: The Wide Area Augmentation System (WAAS) (Courtesy: FAA). 12
Figure 1.9: Comparison of the present GPS signals and the post-modernization GPS signals [ICD-GPS-200C] [PPIRN-200C-007] [ICD-GPS-705]. 13
Figure 1.10: An aircraft is equipped with a three-frequency GPS/WAAS receiver and a barometric altimeter. This aircraft approaches an airport which is under IFR conditions and suffers RFI. This thesis demonstrates what modernized GPS can do under these threats. 15
Figure 1.11: Scenarios. 16
Figure 2.1: The Wide Area Augmentation System (WAAS) (Courtesy: FAA). 23
Figure 2.2: Phase I Wide Area Augmentation System (WAAS) reference stations (WRSs). 24
Figure 2.3: A block diagram of the WAAS data processing algorithm. 25
Figure 2.4: WAAS ionospheric grid points (IGPs) [RTCA1]. 27
Figure 2.5: Ionospheric pierce point (IPP) [RTCA1]. 29
Figure 2.6: Three- and four-point interpolation algorithm definitions [RTCA1]. 30
Figure 2.7: The confidence model of the residual troposphere error in the WAAS MOPS. 35
Figure 2.8: The LAAS AAD model of the residual airborne receiver noise and multipath errors in the LAAS MASPS. 36
Figure 2.9: The triangle chart example. 38
Figure 2.10: The Protection level calculation. 41
Figure 2.11: Block diagram of MAAST. 42
Figure 2.12: User grid of CONUS. User in red are inside the CONUS boundary and users in blue are outside the CONUS boundary. 44
Figure 2.13: INMARSAT coverage (Courtesy: INMARSAT http://www.inmarsat.com). 45
Figure 2.14: Functional flowchart of WMS processing. 47
Figure 2.15: Functional flowchart of user processing. 47
Figure 2.16: Graphic user interface (GUI) of MAAST. 49
Figure 2.17: Coverage of an L1 single-frequency user in CONUS is 98.73% with VAL=50m, HAL=40m. .. 53
Figure 2.18: Vertical protection level (VPL) contour of an L1 single-frequency user in CONUS. 54
Figure 2.19: Horizontal protection level (HPL) contour of an L1 single-frequency user in CONUS. 54
Figure 2.20: UDRE histogram of CONUS. 55

Figure 2.21: GIVE histogram of CONUS. 55
Figure 2.22: GIVE contour of CONUS and Alaska, the block circles correspond to the IGPs. 56
Figure 2.23: UDRE contour as a function of GPS satellite position. 56
Figure 2.24: WRS locations. 58
Figure 3.1: Summary of changes in the protection level calculation for an L1-L5 dual-frequency user. Only the yellow highlighted portion is changed, the other terms are unchanged as defined in the WAAS MOPS. 62
Figure 3.2: Satellite hardware group delay [ICD-GPS-705]. 65
Figure 3.3: The confidence of the satellite hardware group delay (τ_{gd}). 68
Figure 3.4: The confidence of the dual-frequency ionospheric delay estimation depends on the separation between two GPS frequencies. The *C1* and *C2* for the L2-L5 dual-frequency user are much larger than the C1 and C2 for the L1-L2 and L1-L5 dual-frequency users, because of the narrow separation between the L2 and L5 frequencies. 73
Figure 3.5: Coverage of an L1-L5 dual-frequency user in CONUS is 100% with VAL = 50m, HAL = 40m. 76
Figure 3.6: Vertical Protection Level (VPL) contour of an L1-L5 dual-frequency user in CONUS. 76
Figure 3.7: Horizontal Protection Level (HPL) contour of an L1-L5 dual-frequency user in CONUS. 77
Figure 4.1: Summary of changes in User Ionosphere Range Error (UIRE) confidence calculation. 83
Figure 4.2: Summary of changes in the protection level calculation for the L1-only and L5-only single-frequency GPS/WAAS users, only the yellow highlighted portion is changed, the other terms are unchanged as defined in the WAAS MOPS. 84
Figure 4.3: Coverage of an L1-only single-frequency GPS/WAAS user in CONUS is 97.58% with VAL = 50m, HAL = 40m. 85
Figure 4.4: Vertical Protection Level (VPL) contour of an L1-only single-frequency GPS/WAAS user in CONUS. 86
Figure 4.5: Horizontal Protection Level (HPL) contour of an L1-only single-frequency GPS/WAAS user in CONUS. 86
Figure 4.6: Coverage of an L5-only single-frequency GPS/WAAS user in CONUS is 49.25% with VAL = 50m, HAL = 40m. 87
Figure 4.7: Vertical Protection Level (VPL) contour of an L5-only single-frequency GPS/WAAS user in CONUS. 88
Figure 4.8: Horizontal Protection Level (HPL) contour of an L5-only single-frequency GPS/WAAS user in CONUS. 88
Figure 4.9: The VPL maps illustrate the situation when an L1-L5 dual-frequency user is descending into an L1 RFI field. The VPL map on the left is for an L1-L5 dual-frequency airborne user right before entering an L1 RFI field. The VPL map on the right is for an L5 single-frequency WAAS user. The loss in CONUS coverage of LPV services will be about 50% for this example. 90
Figure 4.10: Typical precision approach duration example based on San Francisco International Airport (SFO) final approach. The aircraft enters the boundary of an L1 RFI field when the aircraft reaches the final approach fix. The nominal σ_{UIRE} jumps from 0.32m to 6.0m, which results in the loss of CONUS coverage of LPV services. 91
Figure 4.11: Techniques sustain the performance of the L1-L5 dual-frequency ionospheric delay estimation and the required conditions for using these techniques. 92
Figure 4.12: Slant ionospheric delay to Satellite Number 20 at Stanford University on July 13, 2001. 96
Figure 4.13: The nominal σ_{UIRE} variation along with the final approach into SFO. When user lost L1 while descending into the RFI field, user applied the L5 code and carrier divergence technique to continue estimating the ionospheric delay instead of using the WAAS grid. This technique provides good ionospheric delay estimation for full duration of approach. 97
Figure 4.14: Theoretical probability of cycle slips. This is the probability of one cycle slip in *t* seconds as a function of signal-to-noise ratio (C/N_o). 99
Figure 4.15: Real probability of cycle slips. The plot on the left is the PLL status (reported by the receiver), C/N_0 , and the elevation angle of Satellite Number 03. The plot on the right is the PLL status (reported by the receiver), C/N_0 , and the elevation angle of Satellite Number 24. 100

Figure 4.16: The 99.9% VPL contour for an L5 single-frequency user applying the code and carrier divergence technique to estimate the ionospheric delay after losing the L1 frequency while descending into the RFI field. 101
Figure 4.17: The comparison of the VPL contours. The VPL contour on the left is for an L1-L5 dual-frequency user using the code and carrier divergence technique to estimate the ionospheric delay after losing the L1 frequency to RFI. The VPL contour on the right is for an L1-L5 user using the WAAS grid to estimate the ionospheric delay after losing the L1 frequency to RFI. The color bar shows the VPL indexes in meters. The use of the code and carrier divergence technique provided better ionospheric delay estimation than using the WAAS grid for an L1-L5 dual-frequency airborne user descending into an L1 RFI field. 102
Figure 4.18: The temporal threat model. The maximum gradient occurs around 300 seconds which is 1.62m. (Courtesy: Lawrence Sparks) 104
Figure 4.19: The WAAS ionosphere threat model (ROT overbound model). The blue line is ROT overbound model, and the red line represents the confidence of it. 105
Figure 4.20: The nominal σ_{UIRE} variation along with the final approach into SFO. When user lost L1 while descending into the RFI field, user applied the WAAS ionosphere threat model technique to bound the ionospheric delay error instead of using the WAAS grid. This technique provides good ionospheric delay estimation for at least 10 minutes. 106
Figure 4.21: The 99.9% VPL contour for an L5 single-frequency user applying the WAAS ionosphere threat model technique to estimate the ionospheric delay 4.5 minutes after descending into the RFI field (or at the middle of the final approach). 108
Figure 4.22: The 99.9% VPL contour for an L5 single-frequency user applying the WAAS ionosphere threat model technique to bound the ionosphere error 9 minutes after descending into the RFI field (or at the touchdown point). 109
Figure 4.23: The comparison of the VPL contours. The VPL contour on the left is for an L1-L5 dual-frequency user using the WAAS ionosphere threat model technique to bound the ionosphere error 9 minutes after losing the L1 frequency to RFI. The VPL contour on the right is for an L1-L5 user using the WAAS grid to estimate the ionospheric delay after losing the L1 frequency to RFI. The color bar shows the VPL indexes in meters. The use of the WAAS ionosphere threat model technique provided better ionospheric delay estimation than using the WAAS grid for an L1-L5 dual-frequency airborne user descending into an L1 RFI field. 110
Figure 4.24: The maximum vertical ionospheric delay gradient model. The maximum difference in the ionospheric vertical delay for places 19 km apart ("A" and "B") is 6m. 113
Figure 4.25: The nominal σ_{UIRE} variation along with the final approach into SFO. When the user lost L1 while descending into the RFI field, that user applied the maximum ionospheric delay gradient model technique to bound the ionospheric delay error instead of using the WAAS grid. This technique provides good ionospheric delay estimation for at least 10 minutes. The σ_{UIRE} at the touchdown point is 2.3m which is higher than the user with the WAAS ionosphere threat model in Figure 4.20. 114
Figure 4.26: The 99.9% VPL contour for an L5 single-frequency user applying the maximum ionospheric delay gradient technique to estimate the ionospheric delay 4.5 minutes after descending into the RFI field. 115
Figure 4.27: The 99.9% VPL contour for an L5 single-frequency user applying the maximum ionospheric delay gradient technique to estimate the ionospheric delay 9 minutes after descending into the RFI field (or at the touchdown point). 116
Figure 4.28: The comparison of the VPL contours. The VPL contour on the left is for an L1-L5 dual-frequency user using the maximum ionospheric delay gradient model technique to bound the ionosphere error 9 minutes after losing the L1 frequency to RFI. The VPL contour on the right is for an L1-L5 user using the WAAS grid to estimate the ionospheric delay after losing the L1 frequency to RFI. The color bar shows the VPL indexes in meters. The use of the maximum ionospheric delay gradient model technique provided better ionospheric delay estimation than using the WAAS grid for an L1-L5 dual-frequency airborne user descending into an L1 RFI field. 117

Figure 4.29: The 99.9% VPL contour for an L5 single-frequency user applying the maximum ionospheric delay gradient model developed by the FAA Technical Center to estimate the ionospheric delay 9 minutes after descending into the RFI field (or at the touchdown point). 120
Figure 4.30: The maximum velocity of IPP. The maximum velocity of IPP can reach 618m/s at the latitude of 70^{o} N. 121
Figure 4.31: A summary comparison of the uses of these three techniques at the touchdown point. The VPL contour plots are shown in the order of the VPL performance from top to bottom. All of these techniques outperform the use of WAAS grid. 123
Figure 5.1: Summary of changes in User Ionosphere Range Error (UIRE) confidence calculation. 128
Figure 5.2: Summary of changes in the protection level calculation for the L1-only, the L2-only, and L5-only single-frequency GPS/WAAS users. Only the yellow highlighted portion is changed, the other terms are unchanged as defined in the WAAS MOPS. 129
Figure 5.3: Coverage of an L2-only single-frequency GPS/WAAS user in CONUS is 58.34% with VAL = 50m, HAL = 40m. 130
Figure 5.4: Vertical Protection Level (VPL) contour of an L2-only single-frequency GPS/WAAS user in CONUS. 131
Figure 5.5: Horizontal Protection Level (HPL) contour of an L2-only single-frequency GPS/WAAS user in CONUS. 131
Figure 5.6: Summary of changes in the protection level calculation for an L1-L2 dual-frequency user. Only the highlighted yellow portion is changed, the other terms are unchanged as defined in the WAAS MOPS. 134
Figure 5.7: Coverage of an L1-L2 dual-frequency GPS/WAAS user in CONUS is 100% with VAL = 50m, HAL = 40m. 137
Figure 5.8: Vertical Protection Level (VPL) contour of an L1-L2 dual-frequency user in CONUS. 137
Figure 5.9: Horizontal Protection Level (HPL) contour of an L1-L2 dual-frequency user in CONUS. 138
Figure 5.10: Coverage of an L2-L5 dual-frequency GPS/WAAS user in CONUS is only 10.81% with VAL = 50m, HAL = 40m. 142
Figure 5.11: Vertical Protection Level (VPL) contour of an L2-L5 dual-frequency user in CONUS. 142
Figure 5.12: Horizontal Protection Level (HPL) contour of an L2-L5 dual-frequency user in CONUS. 143
Figure 5.13: The comparison of the MAAST coverage simulation results for both the L2 single-frequency user and the L2-L5 dual-frequency user. 144
Figure 5.14: The modified protection level calculation for an L2-L5 dual-frequency user, only the yellow highlighted portion is changed, the other terms are unchanged as defined in the WAAS MOPS. ... 145
Figure 5.15: Coverage of an L2-L5 dual-frequency GPS/WAAS user in CONUS is 79.97% with VAL = 50m, HAL = 40m. 146
Figure 5.16: Vertical Protection Level (VPL) contour of an L2-L5 dual-frequency user in CONUS. 147
Figure 5.17: Horizontal Protection Level (HPL) contour of an L2-L5 dual-frequency user in CONUS. 147
Figure 5.18: The MAAST coverage simulation results comparison for an L2-L5 dual-frequency user. The plot on the left side is for an L2-L5 dual-frequency user who directly applied the L2-L5 dual-frequency ionospheric delay estimation. The LPV CONUS coverage is 10.58% for this case. The plot on the right side is for an L2-L5 dual-frequency user who applied the combined ionospheric correction algorithm. The LPV CONUS coverage is 79.97% for this case. 148
Figure 6.1: A barometric altimeter. 152
Figure 6.2: A barometric altimeter setting example: An aircraft receives temperature and pressure data from air traffic control. 153
Figure 6.3: The configuration of the simulation: User at place B gets the temperature (T_0) and pressure (P_0) data from air traffic control at place A to estimate his altitude $\left(\hat{h}_c\right)$. The estimated altitude, $\hat{h}_c$, was compared to the true altitude at the location B $\left(H_B\right)$ to generate an altitude error. 156
Figure 6.4: The sample data in [NOAA]. 157
Figure 6.5: A selected region in U.S.. The red lettering indicates that the airplane is at that location, Atlanta, GA in this example. 158
Figure 6.6: A selected region in U.S.. The red lettering indicates that the airplane is at that location, Toledo, OH in this example. 159
Figure 6.7: This is an example of altitude error data generated from Toledo, OH region. 160

Figure 6.9: The worst-case model for the barometric altimeter, the blue portion is for Atlanta, GA, and the red portion is for Toledo, OH. 163
Figure 6.10: Our confidence model successfully bounds these worst-case errors; this figure also shows that the worst-case error is bounded even without the 10% safety factor. 164
Figure 6.11: The distribution of altitude error. The maximum error is 47.1136 m and is well bounded by our confidence model (52.7728m). 166
Figure 6.12: The flight test data. The top plot shows the barometric altimeter altitude with respect to mean sea level (blue), and the GPS altitude (green). The bottom plot shows the distance from the aircraft to Moffett Field. 167
Figure 6.13: The barometric altimeter altitude error of the flight test. The barometric altimeter altitude error is shown in red, and our barometric altimeter confidence bound is shown in blue. The barometric altimeter altitude error is well bounded by our barometric altimeter confidence. 169
Figure 6.14: Coverage of an L1-only single-frequency WAAS user in CONUS is 97.58% with VAL=50m, HAL=40m. 172
Figure 6.15: Horizontal protection level (HPL) contour of an L1-only single-frequency WAAS user in CONUS. 172
Figure 6.16: Vertical protection level (VPL) contour of an L1-only single-frequency WAAS user in CONUS. 172
Figure 6.17: Coverage of an L1-only single-frequency WAAS user with baro-aiding in CONUS is 99.19% with VAL=50m, HAL=40m. 172
Figure 6.18: Horizontal protection level (HPL) contour of an L1-only single-frequency WAAS user with baro-aiding in CONUS. 172
Figure 6.19: Vertical protection level (VPL) contour of an L1-only single-frequency WAAS user with baro-aiding in CONUS. 172
Figure 6.20: Coverage of an L2-only single-frequency WAAS user in CONUS is 58.34% with VAL=50m, HAL=40m. 174
Figure 6.21: Horizontal protection level (HPL) contour of an L2-only single-frequency WAAS user in CONUS. 174
Figure 6.22: Vertical protection level (VPL) contour of an L2-only single-frequency WAAS user in CONUS. 174
Figure 6.23: Coverage of an L2-only single-frequency WAAS user with baro-aiding in CONUS is 92.63% with VAL=50m, HAL=40m. 174
Figure 6.24: Horizontal protection level (HPL) contour of an L2-only single-frequency WAAS user with baro-aiding in CONUS. 174
Figure 6.25: Vertical protection level (VPL) contour of an L2-only single-frequency WAAS user with baro-aiding in CONUS. 174
Figure 6.26: Coverage of an L5-only single-frequency WAAS user in CONUS is 49.25% with VAL=50m, HAL=40m. 176
Figure 6.27: Horizontal protection level (HPL) contour of an L5-only single-frequency WAAS user in CONUS. 176
Figure 6.28: Vertical protection level (VPL) contour of an L5-only single-frequency WAAS user in CONUS. 176
Figure 6.29: Coverage of an L5-only single-frequency WAAS user with baro-aiding in CONUS is 89.29% with VAL=50m, HAL=40m. 176
Figure 6.30: Horizontal protection level (HPL) contour of an L5-only single-frequency WAAS user with baro-aiding in CONUS. 176
Figure 6.31: Vertical protection level (VPL) contour of an L5-only single-frequency WAAS user with baro-aiding in CONUS. 176
Figure 6.32: Coverage of an L2-L5 dual-frequency WAAS user in CONUS is 79.97% with VAL=50m, HAL=40m. 178
Figure 6.33: Horizontal protection level (HPL) contour of an L2-L5 dual-frequency WAAS user in CONUS. 178
Figure 6.34: Vertical protection level (VPL) contour of an L2-L5 dual-frequency WAAS user in CONUS. 178
Figure 6.35: Coverage of an L2-L5 dual-frequency WAAS user with baro-aiding in CONUS is 99.42% with VAL=50m, HAL=40m. 178

Figure 6.36: Horizontal protection level (HPL) contour of an L2-L5 dual-frequency WAAS user with baro-aiding in CONUS. 178
Figure 6.37: Vertical protection level (VPL) contour of an L2-L5 dual-frequency WAAS user with baro-aiding in CONUS. 178
Figure 7.1: Summary of the new WAAS protection level calculations for the single frequency users. The yellow highlighted portion shows the differences in comparison with the current WAAS protection level calculation. 181
Figure 7.2: Summary of the new WAAS protection level calculations for the dual-frequency users. The yellow highlighted portion shows the differences in comparison with the current WAAS protection level calculation. 182
Figure 7.3: A summary comparison of the uses of all techniques 9 minutes after entering an RFI field. These VPL contour plots are shown in the order of VPL performance from top to bottom. All of the first three techniques outperform the WAAS grids. 184
Figure 7.4: The summary of MAAST simulation results. 187
Figure 7.5: Coverage of an L1-L2 dual-frequency GPS/WAAS user in North and South America is 34.27% with VAL = 50m, HAL = 40m. 188
Figure 7.6: Coverage of an L1-L5 dual-frequency GPS/WAAS user in North and South America is 34.94% with VAL = 50m, HAL = 40m. 188
Figure A.1: Configuration. 191
Figure A.2: Two cases: Feedback from the desired direction only and feedback from the desired and undesired directions. 192
Figure A.3: Using GPS positioning only (open loop), no feedback from the desired or undesired directions. 193
Figure A.4: GPS and feedback from the desired direction, GPS and feedback from the desired and undesired directions, partial GPS and feedback from the desired direction. 193
Figure A.5: Block diagram for the least mean square (LMS) adaptive algorithm [Widrow85]. 196
Figure A.6: An example of mobile antenna elements used for evaluation and comparison. 198
Figure A.7: Result for the signal strength measurement feedback from the desired receiving direction only. 198
Figure A.8: Position solution for using signal strength feedback only without using GPS positioning. 199
Figure A.9: Result for the feedback from the desired and undesired receiving directions. 199
Figure A.10: Result for using GPS positioning only, no signal strength feedback from the desired or undesired direction. 202
Figure A.11: Result for using GPS positioning only, sending the spoofing signal in an arbitrary direction. 203
Figure A.12: Result for using GPS positioning and the cost function (A.10). 204
Figure A.13: Result for using GPS positioning and signal strength feedback from the desired receiving direction only. 206
Figure A.14: Result for using GPS positioning and signal strength feedback from the desired and undesired directions. 207
Figure A.15: Sensitivity analysis, directivity, using GPS positioning only; the desired receiving site is the only destination. 208
Figure A.16: Sensitivity analysis, *SIR*, using GPS positioning only. 208
Figure A.17: Sensitivity analysis, *SIR*, combined GPS positioning and signal strength feedback. 209
Figure A.18: System requirement for using GPS positioning only; the desired receiving site is the only destination. 209
Figure A.19: System requirement for using GPS positioning only. 210
Figure A.20: System requirement for using GPS positioning and signal strength feedback. 210
Figure A.21: Comparison of system requirements: using GPS positioning only and using GPS positioning and signal strength feedback. 211
Figure A.22a: Beam solution when one of the mobile antenna elements is not reporting GPS. 213
Figure A.22b: Position solution when one of the mobile antenna elements is not reporting GPS. 213
Figure A.23a: Beam solution when two of the mobile antenna elements are not reporting GPS. 214
Figure A.23b: Position solution when two of the mobile antenna elements are not reporting GPS. 214
Figure A.24: Performance result for when some of the mobile antenna elements are not reporting GPS. 215
Figure B.1: The work of the Volpe National Transportation Systems Center. When the aircraft is banked, the antenna illuminates some areas on the ground and obscures others [Winer]. 220

Figure B.2: An example two-dimensional geometry of the sensor and the EMI source. 221
Figure B.3: A two-dimensional geometry example of the sensor and the EMI source. 226
Figure B.4: The result of the single bearing measurement example. 228
Figure B.5: The result of the single frequency measurement example. 230
Figure B.6: Three sufficient measurements are required to locate the EMI source. 231
Figure B.7: The optimal observer maneuver is required for better tracking performance. 231
Figure B.8: An example of a network of sensors. 232
Figure B.9: Comparison of system with different numbers of sensors. The bearing tracking performance of the network system with seven sensors (right) is better than that of the network system with three sensors (left). 233
Figure B.10: Comparison of systems varying distances from an EMI source. The system which is near the EMI source gives the better bearing tracking performance because of the larger geometric diversity. 234
Figure B.11: Comparison of different separations of the sensors. The larger the geometric diversity of the network of sensors the better bearing tracking performance. 235
Figure B.12: Comparison of different geometries of the sensors. The smaller area of the intersection of the ellipses gives the better bearing tracking performance. 235
Figure B.13: An example of the network system in the presence of sensor failures. We can maintain the bearing tracking performance when some of the sensors fail by moving existing sensors to form the better geometry. 236
Figure B.14: Comparison of the prior art and our approach. 237

List of Tables

Table 1.1: The NAS RNP [FAA2002] [ICAO]. 9
Table 2.1 Evaluation of GIVEI_i [RTCA1] 28
Table 2.2 Evaluation of UDREI_i [RTCA1] 33
Table 2.3: The loss of the CONUS coverage of LPV due to the WRS failure. 58
Table 3.1: The MAAST simulation configuration used in Chapter 3-6. 75
Table 3.2: The MAAST simulation results. 78
Table 4.1: The MAAST simulation results. 89
Table 4.2: The MAAST simulation results. 103
Table 4.3: The MAAST simulation results. 111
Table 4.4: The MAAST simulation results. 118
Table 5.1: The MAAST simulation results. 132
Table 5.2: The MAAST simulation results. 139
Table 5.3: Summary table of MAAST simulation results. 149
Table 6.1: Comparison of a single-frequency user with and without barometric altimeter aiding. 171
Table 6.2: Comparison of a single-frequency user with and without barometric altimeter aiding. 173
Table 6.3: Comparison of a single-frequency user with and without barometric altimeter aiding. 175
Table 6.4: Comparison of an L2-L5 dual-frequency user with and without a barometric altimeter aiding. 177
Table A.1: Summary for using signal strength feedback only 200
Table A.2: Summary for using GPS positioning only 204
Table A.3: Summary for using GPS positioning and signal strength feedback 207
Table A.4: Summary 216

Chapter 1

Introduction

1.1 BACKGROUND

The Global Positioning System (GPS) provides navigation service to around 10 million users in sea, air, terrestrial, and space applications. Many of these applications are safety-of-life operations. For example, GPS is used to guide ships while approaching harbor and navigating within narrow waterways. GPS also provides guidance in terrestrial emergency applications, such as ambulances and police cars, while they conduct their critical missions. In addition, GPS serves many aviation applications including the most demanding phase of flight – aircraft approach and landing.

This chapter is organized as follows. Section 1.1 first briefly describes the architecture of GPS and then discusses the error sources of GPS. The aircraft landing categories (requirements) will also be included in this section. Section 1.2 describes GPS modernization. The motivation of this thesis will be explained in Section 1.3. In Section 1.4, the previous work in related fields will be discussed. The thesis contributions will be given in Section 1.5. Section 1.6 presents a summary and concluding remarks.

1.1.1 THE GLOBAL POSITIONING SYSTEM (GPS)

The Global Positioning System (GPS) was developed, implemented, and is operated by the United States Department of Defense (DOD). As shown in Figure 1.1, it contains a space segment, a control segment, and a user segment.

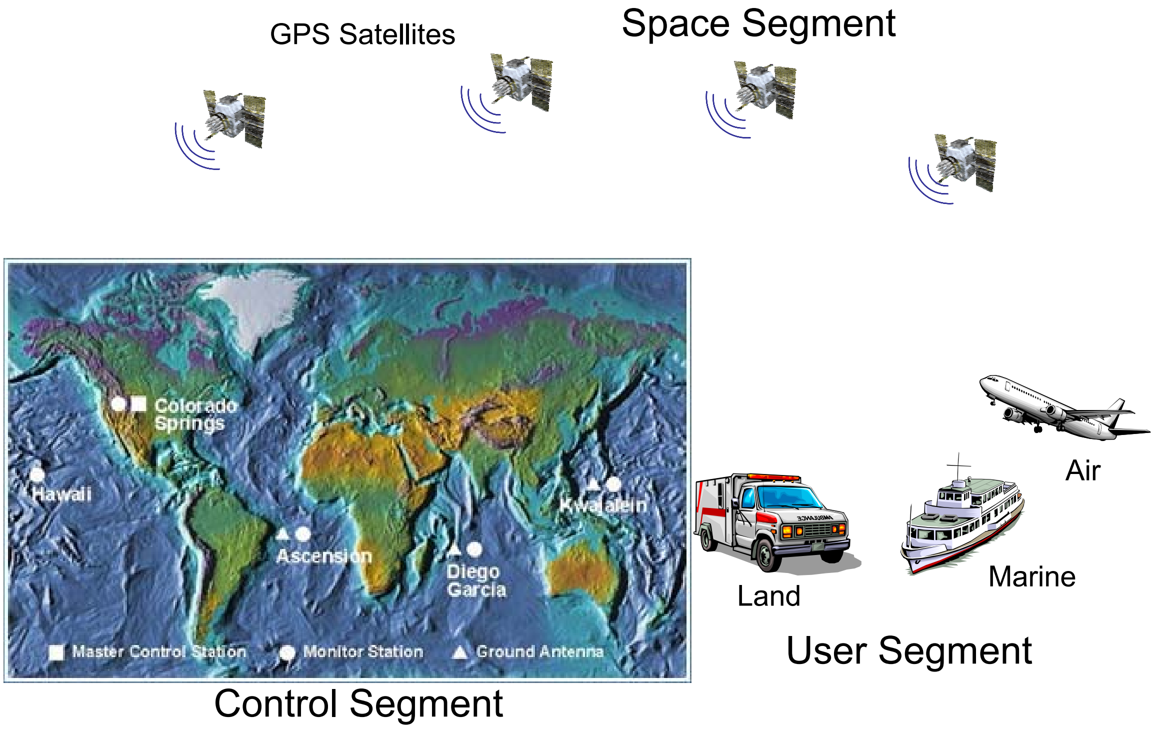

Figure 1.1: The GPS includes three segments: space segment, control segment, and user segment.

- Space segment: The GPS consists of at least 24 nominal satellites which are distributed on six orbital planes which are equally spaced 60° apart in longitude and inclined to the equator at 55°, as shown in Figure 1.2. Each satellite is at an altitude of approximately 10,898 nmi (20,183 km) and has a period of 12 hours. Currently, there are 28 operational satellites in orbit to enhance the system availability.

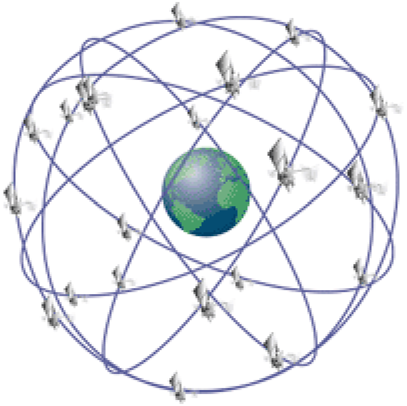

Figure 1.2: The Global Positioning System (GPS) space segment (Courtesy: FAA).

- Control segment: As shown in Figure 1.1, there are five global ground monitoring stations which are used to determine the satellite ephemeris and clock offsets, upload navigation messages, and monitor the health of the satellites.

- User segment: The user segment includes a wide variety of applications, such as surveying, land vehicle, and aircraft navigation. One of the hottest applications is wireless Enhanced 911 (E911), which is used to provide the precise location of 911 calls from wireless phones.

GPS currently has two signals, L1 at a center frequency of 1575.42 MHz and L2 at a center frequency of 1227.6 MHz. As shown in Figure 1.3, the L1 signal is modulated by both a 10.23 MHz clock rate precision P(Y) code and by a 1.023 MHz clock rate C/A code. The L2 signal is modulated by only the P(Y) code. The P(Y) code is for authorized users and the C/A code is for civil users [Parkinson96].

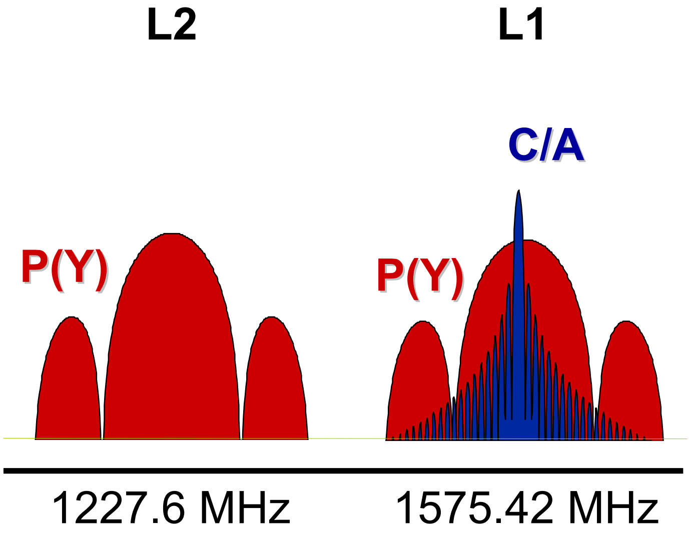

Figure 1.3: The spectrum of present GPS signals. There are two GPS frequencies, L1 at 1575.42 MHz and L2 at 1227.6 MHZ. L1 has C/A and P(Y) codes on it; L2 has only P(Y) code on it. Therefore, a civilian can only access the L1 C/A and carrier of L2.

Therefore, the current civil users can only access the L1 C/A. Each C/A code chip is approximately 293 m long and each cycle of the L1 carrier frequency is about 19 cm long. These are the features of the GPS signals that GPS receivers measure. In general, a good receiver can measure either feature with a precision of one percent.

The GPS observation equations are:

$$\rho_{L1} = R_j^i + b_j - B^i + I_j^i + T_j^i + M_j^i + \nu_j^i \tag{1.1}$$

$$\phi_{L1} = R_j^i + b_j - B^i - I_j^i + T_j^i + N_j^i \lambda + m_j^i + \varepsilon_j^i \tag{1.2}$$

where,

ρ_{L1} is the pseudorange measurement at L1 frequency

ϕ_{L1} is the carrier phase measurement at L1 frequency

R_j^i is the true range from satellite i to user j

b_j is the receiver offset from UTC

B^i is the satellite clock offset from UTC

I is the ionospheric delay

T is the tropospheric delay

M, m are the multipath delays

ν, ε are the receiver thermal noises

$N_j^i\lambda$ is the integer ambiguity

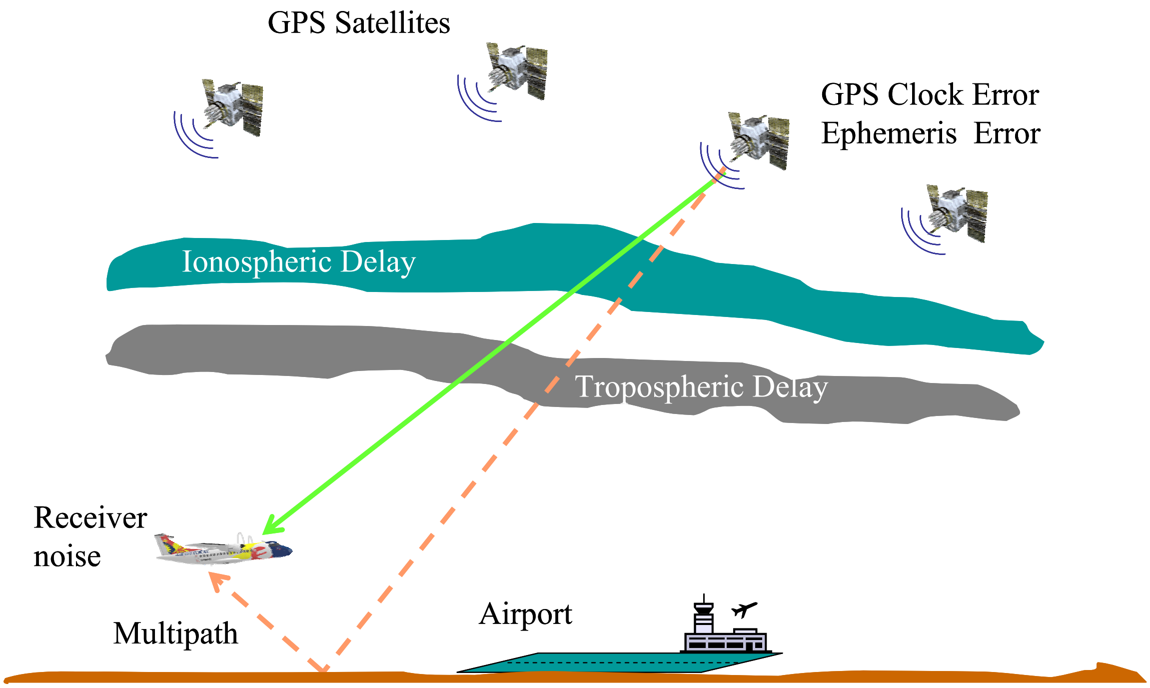

Figure 1.4: The GPS error sources.

The GPS error sources are illustrated in Figure 1.4 and summarized as follows [Misra&Enge]:

- Satellite Clock Error: This is the difference between the time of the actual clock and that of the clock model broadcast by the GPS Control Segment. There are two error sources: the real residual clock and Selective Availability (SA). SA was deactivated on May 2, 2000 in accordance with a Presidential Decision. This error was about 22 meters in the rms range domain [Parkinson96]. After deactivation, this error became about 2 meters in the rms range domain [Kovach] [McDonald].

- Satellite Ephemeris Error: This is the difference between the actual satellite position and the position predicted by the broadcast ephemeris model. The satellite clock and ephemeris errors introduce about 3 m into the rms ranging error.

- Ionospheric Delay: The ionosphere refracts the GPS signals. The code phase is delayed and the carrier phase is advanced, and this is the reason that the signs of I are different in Equations (1.1) and (1.2). The time delay is proportional to the total electron content in the ionosphere. The electron density is a function of time and location. This delay is inversely proportional to the signal frequency. The ionospheric zenith delay typically varies at mid-latitudes from about 1-3 m at night to 5-15 m in the mid-afternoon. The maximum observed ionospheric zenith delay is about 36 m near the equator at the peak of a solar cycle [Misra&Enge]. This delay can be reduced by about 50% by using the Klobuchar ionosphere model in the broadcast navigation message [Klobuchar].

- Tropospheric Delay: This delay is caused by the signal traveling through the atmosphere, and this delay is a function of local temperature, pressure, and humidity. This error is on the order of 2-25 m [Spilker]. The standard deviation of this delay can be reduced to approximately 6% of the absolute delay by using the Hopfield model [Black] [Cosentino] [RTCA1].

- Multipath Effect: Multipath refers to the phenomenon of a signal reaching an antenna via two or more paths due to reflection and diffraction, as shown in Figure 1.4.

Multipath errors can be reduced by using careful siting, a narrow correlator receiver, antenna gain pattern shaping, or a software calibration algorithm [Bishop]. The software calibration algorithm in [Bishop] takes advantage of the daily repetition of GPS observation geometry from a fixed ground station to create a template of the multipath error signature specific to each satellite pass. This template can then be applied to successive days of data to reduce the pseudorange multipath error.

- Receiver Clock Error: This is caused by the oscillator used in the receiver. This is a system state by design and it can be eliminated in the navigation solutions [Parkinson96].

- Receiver noise: This noise comes from the thermal noise in the receiver front end. This error can be approximated as white gaussian noise. In general, the receiver noise is on the order of a few meters for code-phase measurements and a few millimeters for carrier-phase measurements.

Additionally, the carrier-phase observations also suffer from integer ambiguity, because the distance between a satellite and the receiver is an unknown number of whole cycles plus the measured fractional cycle. The measurement, however, contains no information regarding the number of whole cycles. This problem is thus referred to as the integer ambiguity [Misra&Enge].

1.1.2 AVIATION NAVIGATION REQUIREMENTS

The Federal Aviation Administration's (FAA) objective in using GPS is to provide enhanced services and reduce infrastructure cost for aircraft navigation. To do so, the Required Navigation Performance (RNP) for accuracy, integrity, availability, and continuity must be met [Kelly]. These four parameters are defined as follows:

- *Accuracy*: A measure of the difference between the estimated and true position under nominal fault-free conditions. Typically, it is a 95% bound on position error.

- *Integrity*: The ability of a navigation system to provide timely warnings to users when the system should not be used for navigation. The navigation system must be able to provide error bounds in real time under all conditions. Values stated are the probability that a system has integrity, as shown in Table 1.1.

- *Availability*: The probability that the navigation and fault detection functions are operational and that the signal accuracy, integrity, and continuity of function requirements are met. This is illustrated in Figure 1.5. The System is available when the Vertical Protection Level (VPL) (an estimated vertical error bound) is less then the Vertical Alert Limit (VAL) and the Horizontal Protection Level (HPL) (an estimated horizontal error bound) is less than the Horizontal Alert Limit (HAL) for a given operation.

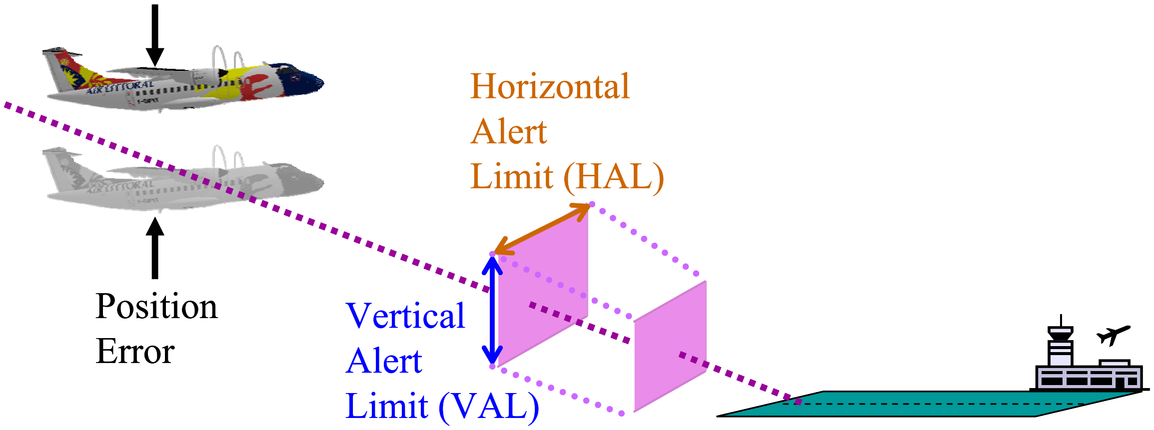

Figure 1.5: The definition of Availability.

- *Continuity*: The ability to provide the navigation function over the entire course of a flight operation. Continuity risk is the probability that a procedure will be interrupted by a loss of services. Values stated are the probability that a system have continuity, as shown in Table 1.1.

The VALs, HALs, and integrity requirements for the National Airspace System (NAS) Required Navigation Performance (RNP) are listed in Table 1.1 and shown in Figure 1.6 [FAA2002] [ICAO].

Typical Operation	Horizontal Accuracy (95%)	Vertical Accuracy (95%)	Integrity	Continuity	Horizontal Alert Limit (HAL)	Vertical Alert Limit (VAL)	Availability	Time to Alert
En Route	3700 m	NA	$1-10^{-7}$ /hr	$1-10^{-4}$ /hr to $1-10^{-8}$ /hr	7408 m	NA	.99 to .99999	60 s
Terminal	740 m	NA	$1-10^{-7}$ /hr	$1-10^{-4}$ /hr to $1-10^{-8}$ /hr	3704 m	NA	.99 to .99999	15 s
LNAV (NPA)	220 m	NA	$1-10^{-7}$ /hr	$1-10^{-4}$ /hr to $1-10^{-8}$ /hr	1852 m	NA	.99 to .99999	10 s
LNAV/ VNAV	220 m	20 m	$1-2\text{x}10^{-7}$ /approach	$1-8\text{x}10^{-6}$ /15 s	556 m	50 m	.99 to .999	10 s
LPV	16 m	20 m	$1-2\text{x}10^{-7}$ /approach	$1-8\text{x}10^{-6}$ /15 s	40 m	50 m	.99 to .999	10 s
APV II	16 m	8 m	$1-2\text{x}10^{-7}$ /approach	$1-8\text{x}10^{-6}$ /15 s	40 m	20 m	.99 to .999	6 s
CAT I (GLS)	16 m	6 m to 4 m	$1-2\text{x}10^{-7}$ /approach	$1-8\text{x}10^{-6}$ /15 s	40 m	12 m to 10 m	.99 to .99999	6 s
CAT II and CAT IIIa	6.9 m	2.0 m	$1-10^{-9}$ /15 s	$1-4\text{x}10^{-6}$ /15 s	17.3 m	5.3 m	.99 to .99999	1 s
CAT IIIb	6.2 m	2.0 m	$1-10^{-9}$ /30 s (lateral) $1-10^{-9}$ /15 s (vertical)	$1-2\text{x}10^{-6}$ /30 s (lateral) $1-2\text{x}10^{-6}$ /15 s (vertical)	15.5 m	5.3 m	.99 to .99999	1 s

Table 1.1: The NAS RNP [FAA2002] [ICAO].

LNAV (Lateral Navigation) is an approach with only lateral guidance and is also known as Non-Precision Approach (NPA). LNAV/VNAV (Vertical Navigation) is an approach with both lateral guidance and vertical guidance. LNAV/VNAV includes a prescribed descent path known as the glide slope which the aircraft follows. This path descends to a minimum altitude known as the Decision Height (DH) after which the aircraft can proceed only if the runway is visible, as shown in Figure 1.6. LPV is a new category which is a lateral precision approach with vertical guidance (highlighted yellow in Table 1.1) [Cabler]. APV II is another category with more stringent VAL (20 m) than LPV VAL (50 m). CAT I is Category I Precision Approach (PA) and GLS PA (Global Navigation Satellite System (GNSS) Landing System Precision Approach) is similar to the CAT I PA. CAT II and CAT III are the precision approaches with more stringent requirements that allow users to operate at lower DH, as shown in Figure 1.6. CAT I, II, and III are defined in [ICAO].

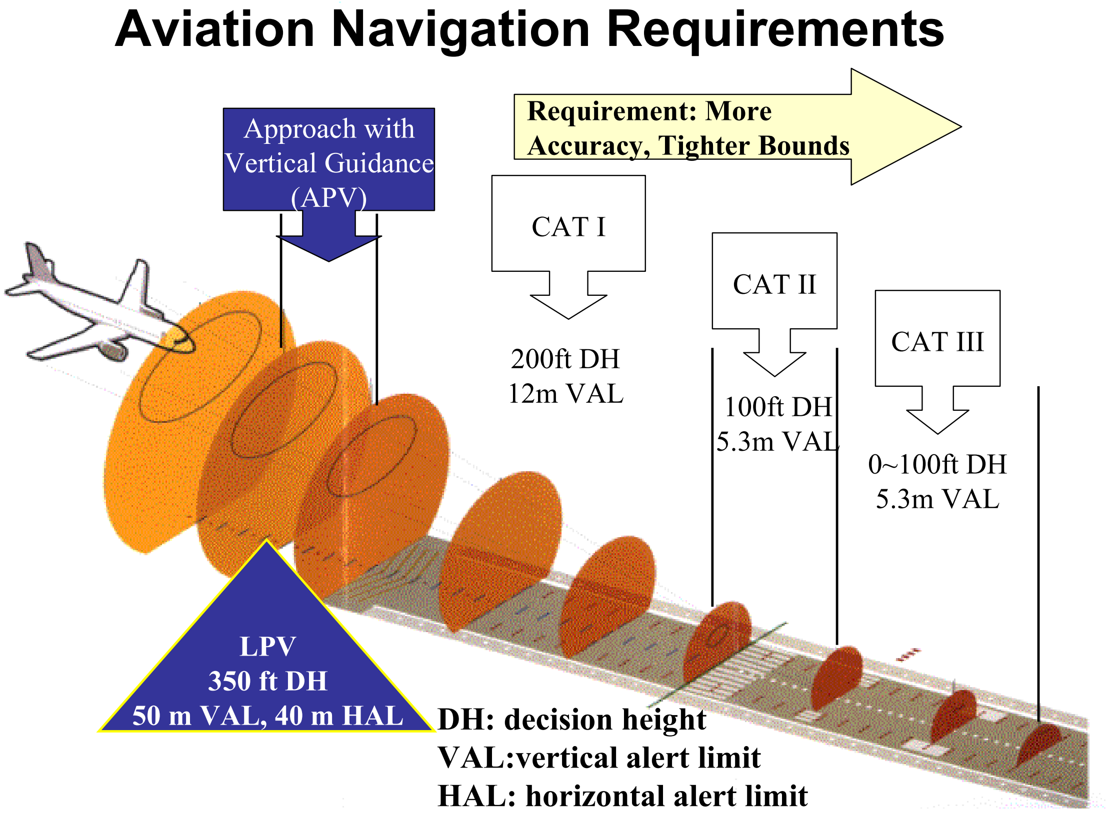

Figure 1.6: The landing categories [ICAO] [FAA2002].

1.1.3 AUGMENTATION SYSTEMS

GPS alone, however, doesn't meet the accuracy, integrity, availability, and continuity requirements for today's aviation needs. Therefore, the FAA embarked upon two programs to augment GPS and enable the combined systems to act as the primary navigation aid for aircraft. These programs are the Local Area Augmentation System (LAAS) and the Wide Area Augmentation System (WAAS).

1.1.3.1 LOCAL AREA AUGMENTATION SYSTEM (LAAS)

The Local Area Augmentation System (LAAS) uses a ground reference station located near the runway broadcasting either scalar corrections to GPS error sources or raw observation measurements to the nearby user via any suitable data link, such as UHF or VHF. The ground reference station is at a precisely surveyed location. Because the users are close to the reference station, the common mode errors can be mostly canceled, and high accuracy is achieved. However, the LAAS performance degrades as the user moves away from the reference station. LAAS is capable of providing guidance for CAT I, II, and III PA [Lawrence] [Pervan] [Swider]. An example of the LAAS architecture is shown in Figure 1.7.

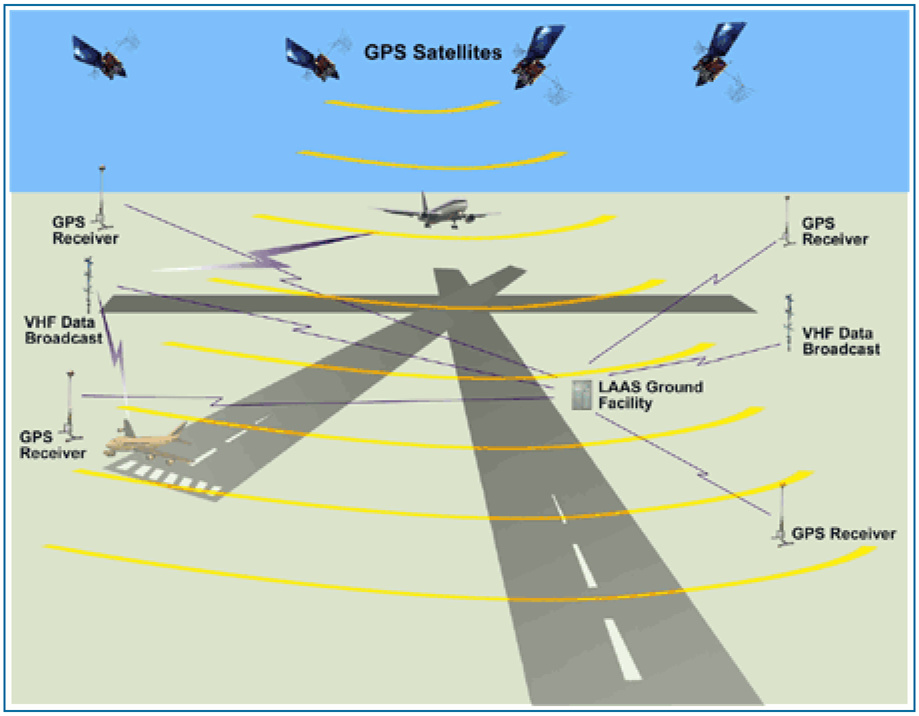

Figure 1.7: The Local Area Augmentation System (LAAS) (Courtesy: FAA).

1.1.3.2 WIDE AREA AUGMENTATION SYSTEM (WAAS)

The Wide Area Augmentation System (WAAS) contains three segments: control segment, space segment, and user segment [Enge96], as shown in Figure 1.8. The WAAS control segment includes a geographically distributed set of GPS L1 (1575.42 MHz) and L2 (1227.6 MHz) dual-frequency receivers at precisely known reference locations. These receivers continuously monitor all of the GPS satellites, and are called wide area reference stations (WRSs). These WRSs send raw GPS measurements back to the wide area master stations (WMSs) where vector corrections are generated. These vector corrections consist of the satellite ephemeris and clock errors, and a grid of ionospheric delays. The data stream also includes confidence bounds for the corrections and "Use/Do Not Use" messages to provide integrity. These messages are then passed to the WAAS space segment through a Ground Uplink System (GUS). The WAAS space segment contains two geo-stationary satellites (GEOs). These are the Pacific Ocean Region (POR, 180° east) and Atlantic Ocean Region West (AOR-W, 55° west). The GEOs broadcast the integrity messages and vector corrections on the same frequency as GPS L1 to user equipment (WAAS avionics). These GEOs also act as additional ranging sources to enhance service availability. WAAS will be the primary navigation system for all phases of flight from oceanic to precision landing over the conterminous US (CONUS).

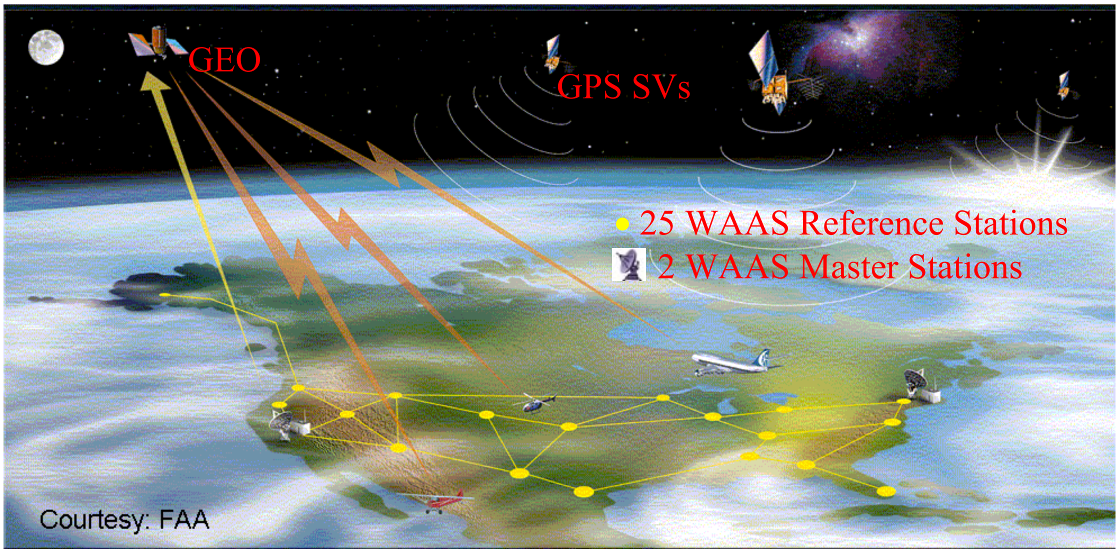

Figure 1.8: The Wide Area Augmentation System (WAAS) (Courtesy: FAA).

1.2 GPS MODERNIZATION

The GPS signal is being modernized to better meet the needs of both military and civil GPS users. GPS modernization follows the directives issued by the President and the Vice President of the United States. It will add two new civil signals to the GPS positioning and timing service. A second civil signal will be added at the second GPS frequency, L2, at

1227.6 MHz. A third civil signal, L5, will be added at a lower frequency 1176.45 MHz in the Aeronautical Radio Navigation Services (ARNS) band [ICD-GPS-200C] [PPIRN-200C-007] [ICD-GPS-705]. GPS modernization will also increase the GPS signal power (+6 dBw over current signal power) in the GPS-IIF phase of the GPS modernization program [Fontana1]. The present GPS signals and the post-modernization GPS signals are compared in Figure 1.9.

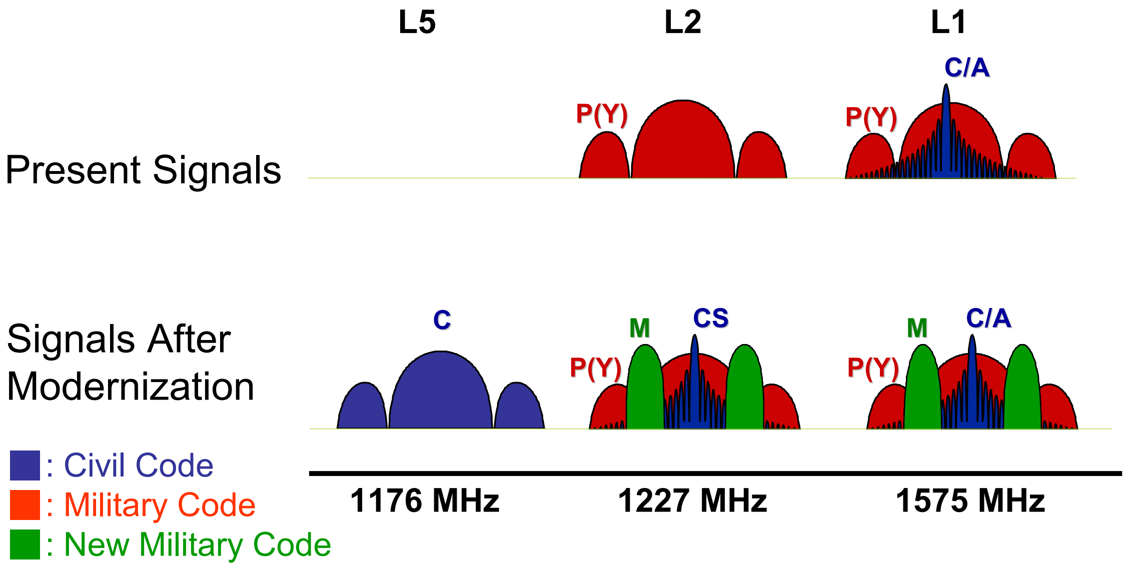

Figure 1.9: Comparison of the present GPS signals and the post-modernization GPS signals [ICD-GPS-200C] [PPIRN-200C-007] [ICD-GPS-705].

Modernized GPS is expected to enhance the performance (accuracy, integrity, continuity, availability) of GPS. Benefits of the GPS modernization include:

- Frequency Diversity: Users will have three civil signals rather than one. The GPS modernization provides the redundancies and robustness in the civil signal services to meet today's increasing dependency on GPS and its safety-of-life applications. Users have the ability to continue to operate after the onset of Radio Frequency Interference (RFI).

- Robust Ionospheric Delay Measurement: A multi-frequency GPS user can take advantage of the frequency dependence of the ionospheric delay to estimate this term. Therefore, the multi-frequency GPS user can directly estimate the ionospheric delay in the airplane, and then subtract this estimate from the pseudorange measurement. This direct use of multi-frequency will be more accurate and offer higher availability.

- More Civil Signal Power: The higher civil signal power will enable users to acquire GPS satellites earlier for smoothing before using them for position estimation. Thus, the floor of the residual user receiver noise and multipath error might be lower than the current model.

1.3 MOTIVATION

The thesis investigates an aircraft equipped with a three-frequency GPS receiver and other assets, such as WAAS real time protection and potentially a barometric altimeter to enhance the vertical performance. This aircraft approaches an airport which is under IFR (Instrument Flight Rules) control. This low visibility condition means that the aircraft is required to use WAAS for guidance. We assume the airport also suffers from RFI (Radio Frequency Interference). The RFI knocks out all but one GPS frequency near the airport, but has no effect on the WAAS reference stations. In other words, this thesis demonstrates what modernized GPS can do when an aircraft is experiencing RFI after initiating an aircraft approach. Figure 1.10 depicts the setting.

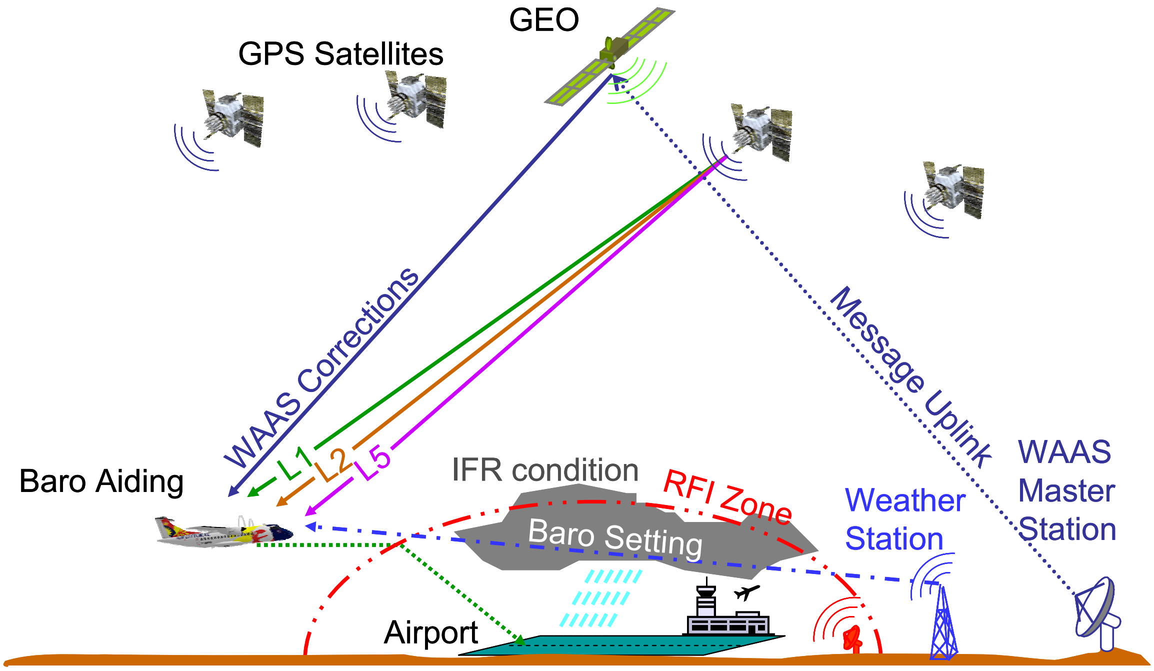

Figure 1.10: An aircraft is equipped with a three-frequency GPS/WAAS receiver and a barometric altimeter. This aircraft approaches an airport which is under IFR conditions and suffers RFI. This thesis demonstrates what modernized GPS can do under these threats.

The scenarios are shown in Figure 1.11. The aircraft has a WAAS capable three-frequency GPS receiver which is WAAS capable, and potentially a barometric altimeter. When this aircraft experiences moderate RFI, it may lose one GPS frequency, thus introducing the dual-frequency GPS user cases. Furthermore, when this aircraft experiences severe RFI, it may lose two GPS frequencies, thus introducing the single-frequency GPS user cases. For the worst case, the aircraft loses all GPS frequencies to RFI and will need to use backup navigation. This topic will not be discussed in this thesis, and the reader is referred to such systems as LORAN-C (LOng RAnge Navigation) [Lo], DME (Distance Measuring Equipment) [Gebre], and INS (Inertial Navigation System) [Diesel].

This thesis also treats the transition state from the L1-L5 dual-frequency user case to the L1-only or the L5-only single-frequency user case. These transitions are highlighted yellow in Figure 1.11.

This thesis evaluates performance by computing the CONUS coverage of LPV precision approach services under different scenarios. The LPV requirement is highlighted yellow in Table 1.1 (page 9).

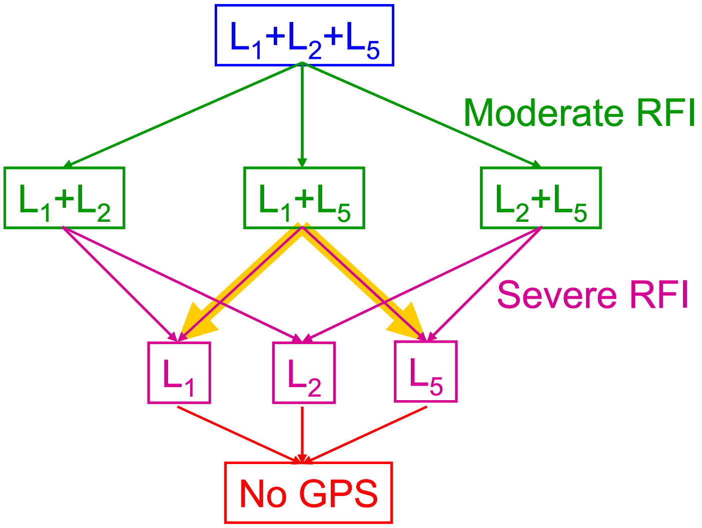

Figure 1.11: Scenarios.

1.4 PREVIOUS WORK

1.4.1 THE USE OF MULTI-FREQUENCY GPS

Many researchers have studied of the use of multi-frequency GPS. For example, Jaewoo Jung studied high integrity carrier phase navigation using multiple civil GPS signals [Jung]. Other studies focus on the new civil signal architectures. For example, Van Dierendonck is developing the signal specifications of the L5 civil signal [Van Dierendonck] and Fontana, et al., developed the signal specification of the L2 civil signal [Fontana2]. More recently, McDonald and Hegarty provide a prediction of the post-modernization GPS performance for the Standard Positioning Service (SPS) [McDonald]. None of the previous studies addressed the benefits of the use of multi-frequency GPS for civil aviation applications in the presence of bad weather, disturbed ionosphere, and Radio Frequency Interference (RFI).

Therefore, this thesis studies the use of multi-frequency GPS for civil aviation applications and shows the CONUS coverage of LPV precision approach services under different scenarios.

1.4.2 WAAS AVAILABILITY ANALYSIS

The availability of WAAS is determined by the confidence bounds on position errors. Several groups developed the algorithms for the WAAS confidence computations [RTCA1] and are presently working on the next generation algorithms [WIPP1-2]. WAAS availability analysis has been used by algorithm developers as a tool to assess relative performance benefits of an entire algorithm or parameter changes. For example, Poor, et al., developed a WAAS availability model which used constant confidences for various error sources and constant user errors [Poor]. Other WAAS availability models also used constant error confidences [Enge96] [IWG] [Pullen98] [Malla98] [Walter95], which are not adequate for this research.

Therefore, this thesis co-develops a MATLAB Algorithm Availability Simulation Tool (MAAST) with Dr. Todd Walter and Wyant Chan for the WAAS availability analysis. The MAAST implements the real WAAS Master Station (WMS) algorithms, and will be detailed in Section 2.4 of this thesis.

1.4.3 BAROMETRIC ALTIMETER ERROR MODEL

In addition to multi-frequency GPS and WAAS, this thesis also investigates the effect of using a barometric altimeter. There are many proprietary barometric altimeter models. Dobyne developed a barometric altimeter error model based on military atmospheric data [Dobyne]. Lee applied the standard deviation from the barometric altimeter error model to his Receiver Autonomous Integrity Monitoring (RAIM) availability work [Lee]. However, the barometric altimeter error model was based on military data, which is not available to the general public, and readers will not be able to re-produce this error model.

As part of this research, a barometric altimeter simulator is developed. The simulator is used to estimate altitude from historical meteorological observation data collected at different locations in the Conterminous United States (CONUS) [NOAA]. By comparing the estimated altitude with true altitude, altitude error data was generated. By applying statistical and linear estimation techniques to the altitude error data, a model for barometric altimeter confidence is developed. This barometric altimeter confidence model is evaluated via the historical worst-case meteorological observation data and flight test data.

1.5 THESIS CONTRIBUTIONS

1.5.1 DERIVED NEW PROTECTION LEVEL (PL) CALCULATION [CHAPTERS 3, 4, & 5]

The availability of WAAS is determined by the confidence bounds on position errors. This error bound is called the protection level (PL). The current PL calculation is defined in the WAAS MOPS [RTCA1], which is specified for L1-only single-frequency user. For other single-frequency users and all dual-frequency users, new PL calculations are required. The new PL equations for an L1-L5 dual-frequency user are derived in Chapter 3. The treatments of the satellite hardware group delay and the user receiver hardware group delay are also discussed in this chapter. As discussed in Section 1.1.1, the ionospheric delay is inversely proportional to the square of signal frequency. Therefore, new PL equations are needed for an L5-only GPS user. Chapter 4 derives the new PL equations for this specific case. The derivations of the new PL equations for the L2-only single-frequency user as well as the L1-L2 and L2-L5 dual-frequency users are shown in Chapter 5. These new PL equations are used to determine the WAAS availability under various scenarios which are shown in Figure 1.11.

1.5.2 SUSTAINED MULTI-FREQUENCY PERFORMANCE WHEN AIRCRAFT DESCENDED INTO AN RFI FIELD [CHAPTER 4]

Based on information available to the user, this thesis develops three techniques that will sustain a performance similar to the dual-frequency ionospheric delay estimation, when this dual-frequency user is descending into an RFI field and loses a GPS signal. A dual-frequency GPS airborne user can directly estimate the ionospheric delay in the aircraft and then subtract this estimation from the pseudorange measurements. This direct use of dual-frequency will be more accurate and offer higher availability. However, if this dual-frequency user loses one GPS frequency due to RFI and instead uses the WAAS grids for ionospheric delay estimation, the accuracy will be degraded and the availability lowered. The techniques for graceful reversion from dual to single frequency WAAS are detailed in Chapter 4. The simulation results for these techniques are also included in Chapter 4.

1.5.3 PREDICTED FIRST THREE-FREQUENCY GPS/WAAS LPV COVERAGE IN CONUS UNDER VARIOUS SCENARIOS [CHAPTERS 2, 3, 4, 5, & 6]

This thesis provides the first prediction of the three-frequency GPS/WAAS LPV precision approach service coverage in CONUS under various scenarios. I co-develop the MAAST (MATLAB Algorithm Availability Simulation Tool) with Dr. Todd Walter and Wyant Chan, which implements the real WMS (WAAS Master Station) algorithm. The MAAST is detailed in Chapter 2. The MAAST is then used to show benefits of the WAAS operation. Chapter 3 modifies the MAAST to adopt the changes in PL calculation for an L1-L5 dual-frequency user. The modifications in the MAAST which adopt the changes in PL calculation for an L5 single-frequency user are shown in Chapter 4. Chapter 5 modifies the MAAST to adopt the changes in PL calculations for the L2-only single-frequency user, the L1-L2 dual-frequency user and the L2-L5 dual-frequency user. In Chapter 6, the MAAST is modified to include barometric altimeter aiding for all different users. The corresponding MAAST simulation results are included in each chapter.

1.5.4 DEVELOPED BAROMETRIC ALTIMETER CONFIDENCE MODEL [CHAPTER 6]

This thesis takes meteorological observation data at locations in different regions, and estimates the altitude of those locations. This thesis then compares the estimated altitude with the true altitude to generate altitude error data. It then analyzes the altitude error data, and calculates the 68% and maximum error bounds in the probability density function (PDF) of the altitude error. A linear least-square estimation technique is then applied to the resulting error bounds in different regions and an altitude error model is built showing that the altitude error is a function of the distance between a user and his reference location. This thesis also develops a worst-case model of the barometric altimeter based on the historical meteorological observation data. This barometric altimeter confidence model is verified by flight test data. The development of the barometric altimeter confidence model is detailed in Chapter 6. The MAAST simulation results in Chapter 6 identify a barometric altimeter complementing GPS navigation. Because the barometric altimeter acts as a virtual satellite above user location, barometric altimeter information is extremely beneficial, primarily in the vertical direction. It is particularly useful when the other satellites have poor geometry.

1.5.5 ANTENNA BEAM FORMING BASED ON MOBILE ANTENNA ELEMENTS AND GPS [APPENDICES A & B]

This thesis designs a transmitting antenna array comprised of mobile antenna elements, where GPS is used to estimate the current location and velocity of those elements. GPS is also used to synchronize the clocks carried by mobile users. With this information, a central algorithm can control the phase of the radio signal radiated from each element such that the multiple signals add constructively at the desired receiving site. The algorithm can also control the elemental phases to cause destructive interference at any undesired receiving site. In this way, GPS is used to synthesize an antenna aperture larger than any single robot or human could carry. This enhanced system is able to communicate over longer distances and has the capability to avoid communication to undesired listeners. This enhanced mobile communication system is detailed in Appendix A.

In addition to these contributions, any RFI affecting GPS must invoke a fast location and removal response because of the high military and civilian reliance on GPS. In Appendix B, this thesis presents an approach for estimating the location of an RFI source utilizing the deployment of a network of sensors.

1.6 CONCLUDING REMARKS

This dissertation presents research on using a modernized GPS and the WAAS for aircraft landing. The objective of this research is to show that the performance of multiple civil GPS signals is exceeds both the current system and general users' expectations.

Chapter 2

Wide Area Augmentation System

2.1 INTRODUCTION

GPS is providing great benefits to aviation users, but in order to increase accuracy and reliability, GPS needs to be augmented. The Federal Aviation Administration (FAA) is deploying the Wide Area Augmentation System (WAAS) [Enge96] to augment GPS to provide a satellite based navigation capability for in-flight services. WAAS is a revolution in air navigation and will provide precision approach guidance to thousands of airports where there is no precision landing capability. WAAS is the core element of the future satellite based air traffic control (ATC) system. WAAS will be the primary navigation system for all phases of flight from oceanic to precision Category I landing over the CONterminous United States (CONUS).

WAAS contains three segments: control segment, space segment, and user segment, as shown in Figure 2.1. The WAAS control segment includes, first, a geographically distributed set of GPS L1 (1575.42 MHz) and L2 (1227.6 MHz) dual-frequency receivers at precisely known reference locations. These receivers continuously monitor all of the GPS satellites, and are called wide area reference stations (WRSs), as shown in Figure 2.2.

These WRSs send raw GPS measurements back to the wide area master stations (WMSs), the second control segment element, where the vector corrections are generated. These vector corrections consist of the satellite ephemeris and clock errors, a grid of ionospheric delays, and confidence bounds of these corrections. The current WAAS has two WMSs and twenty-five WRSs. These messages are then passed to the WAAS space segment through a Ground Uplink System (GUS). The WAAS space segment contains two geostationary satellites (GEOs), and they are Pacific Ocean Region (POR, 180^{o} east) and Atlantic Ocean Region West (AOR-W, 55^{o} west). GEOs broadcast integrity messages and vector corrections on the same frequency as GPS L1 to user equipment (WAAS avionics). These GEOs also act as additional ranging sources to enhance the service availability.

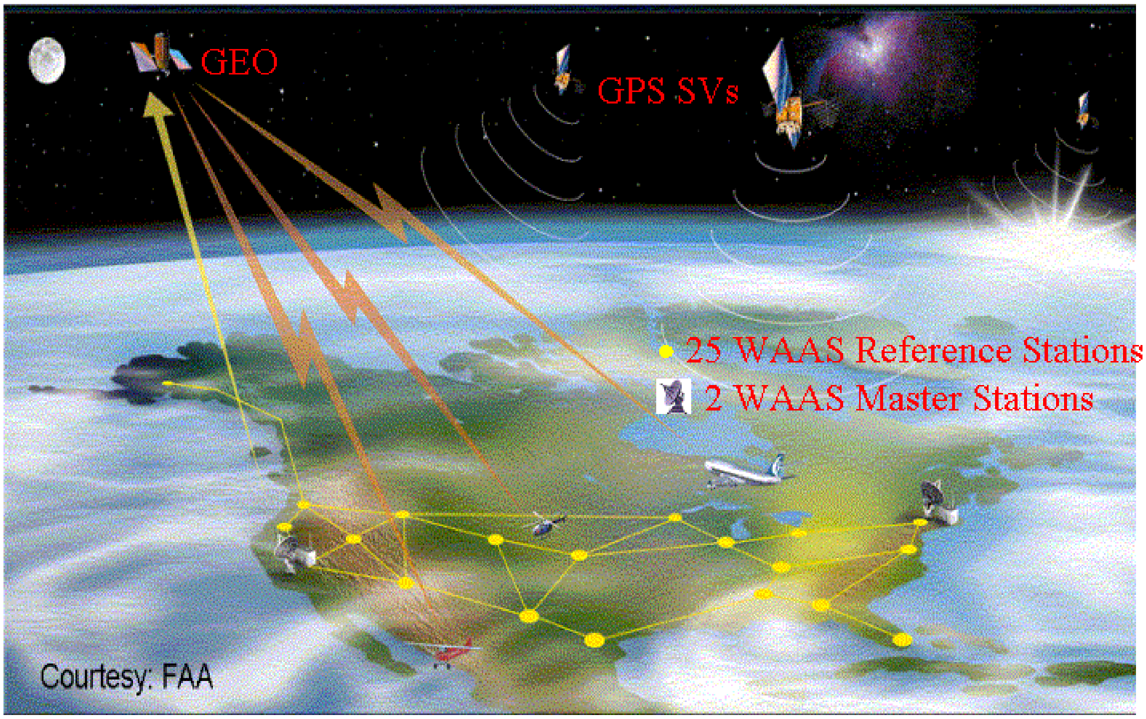

Figure 2.1: The Wide Area Augmentation System (WAAS) (Courtesy: FAA).

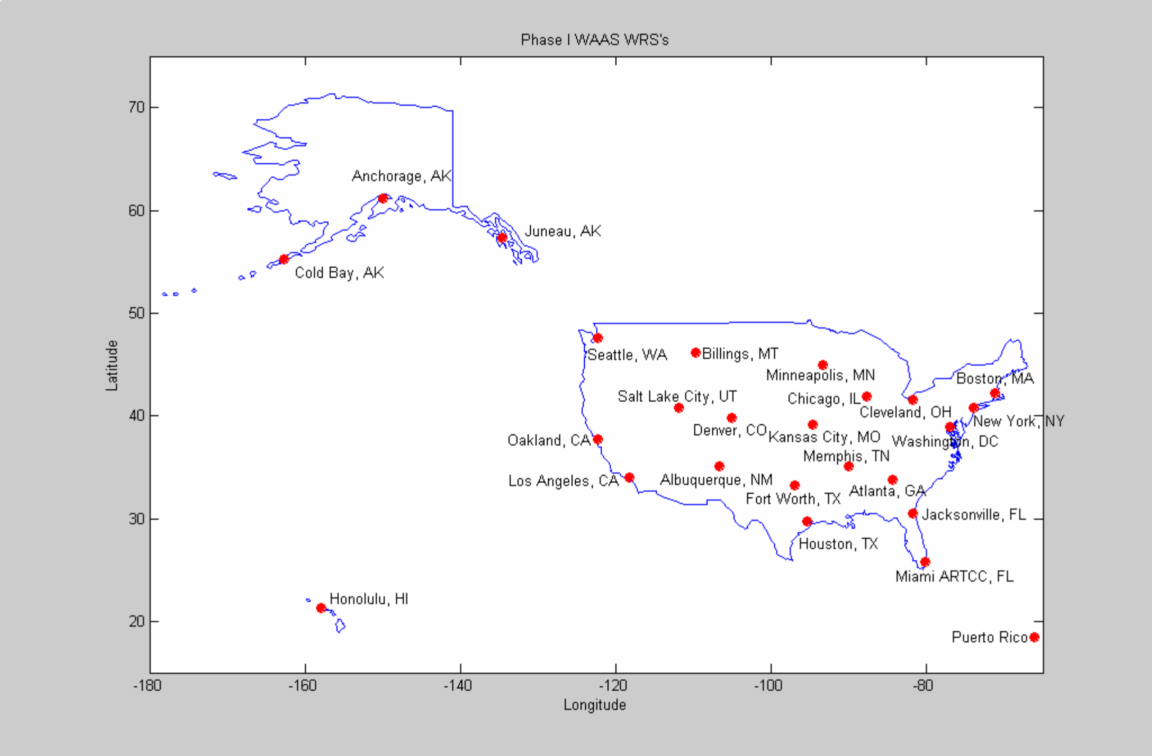

Figure 2.2: Phase I Wide Area Augmentation System (WAAS) reference stations (WRSs).

As described briefly above, WAAS services include [Enge96]:

1. Vector Corrections: WAAS will provide vector differential corrections for the orbit and clock errors of GPS and the signal delays due to the ionosphere.

2. Integrity Messages: WAAS will provide the confidence bounds associated with above vector corrections, such as Grid Ionospheric Vertical Error (GIVE) for ionospheric correction errors and User Differential Range Error (UDRE) for clock and orbit correction errors.

3. Ranging signals: WAAS will provide additional ranging signals from GEOs, which are “GPS-like” signals, and will enhance the satellite constellation.

The WAAS signals will carry 250 b/s data and this capacity will be used to carry all the messages described above. In summary, WAAS will augment GPS so that it can be used as the primary navigation sensor for an aircraft in all phases of flight. In addition, it will be approved for use on non-precision approach and precision approach. Figure 2.3 presents a diagram that summarizes the overall WAAS system architecture and data flow.

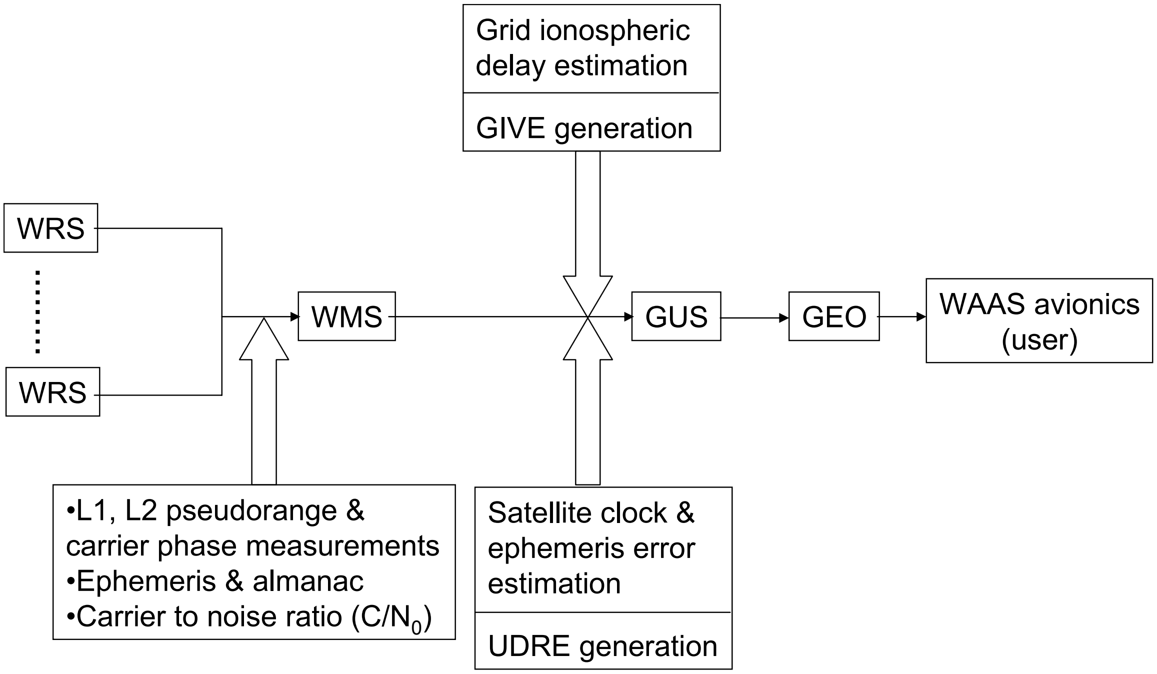

Figure 2.3: A block diagram of the WAAS data processing algorithm.

Accordingly, this chapter is organized as follows. The WAAS overview is described in Section 2.2. Section 2.3 discusses the WAAS availability analysis. Section 2.4 discusses the MAAST (MATLAB Algorithm Availability Simulation Tool). The example MAAST simulation results are also included in this section. In Section 2.5, the failure of the WRS is investigated. Section 2.6 presents a summary and concluding remarks.

2.2 WAAS OVERVIEW

2.2.1 WAAS MASTER STATION PROCESSING ALGORITHM

The WAAS master stations (WMSs) receive and process the measurements from all WAAS reference stations (WRSs). The data collected from each WRS is calibrated and used to generate the differential corrections to ionosphere and satellite errors. There are two main correction generation modules: one is for the ionosphere and the other is for satellite errors. WAAS provides the user with the differential corrections and two system accuracy metrics, namely, the UDRE and the GIVE. The estimation of ionospheric delay and the calculation of GIVE will be detailed in Section 2.2.1.1. The estimation of satellite errors and the calculation of UDRE will be described in Section 2.2.1.2.

2.2.1.1 IONOSPHERE ERRORS

Ionospheric delay is one of the major error sources of GPS, as described in Chapter 1. Thus, one of WAAS' major functions is to correct this delay. Because the ionosphere is a dispersive medium, ionospheric refraction will cause the carrier phase to advance and code phase to retard. In addition, the ionospheric delay is different for the different GPS transmission frequencies. The pseudorange measurements from a WRS L1-L2 dual-frequency receiver can be used to calculate the ionospheric delay. Equation (2.1) calculates the ionospheric slant delay from the pseudorange measurements on L1 and L2 frequencies.

$$I_{L1} = \left(\frac{f_2^2}{f_1^2 - f_2^2} \right) \left(\rho_{L1} - \rho_{L2} \right) \tag{2.1}$$

where f_1 and f_2 are the frequencies at L1 and L2, respectively.

The WRSs measure the slant ionospheric delays to all satellites in view. These measurements must be translated into a form that can be applied by the user because the user will have a different line of sight to the satellite than the WRSs. The current WAAS uses a two-dimensional grid model to represent the vertical ionospheric delay distribution [RTCA1]. The ionospheric grid points (IGPs), a preset grid of locations, are generally spaced 5 degrees apart from each other in longitude and latitude, as shown in Figure 2.4.

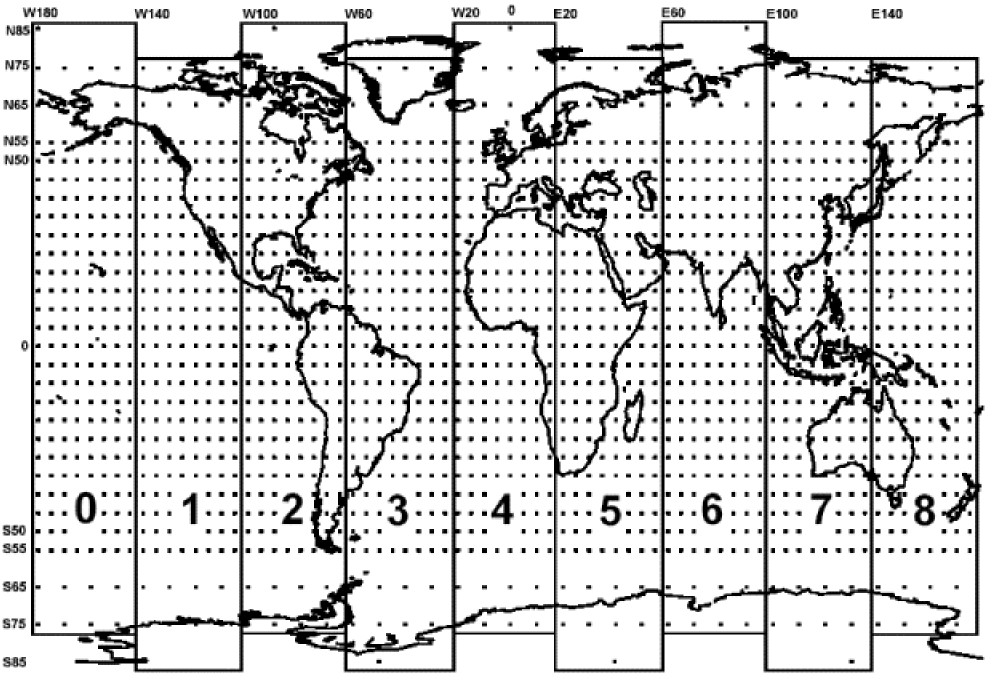

Figure 2.4: WAAS ionospheric grid points (IGPs) [RTCA1].

If enough ionosphere measurements are available, WAAS calculates the ionospheric vertical delay for a given IGP. WAAS also calculates an error bound on the post-correction ionospheric vertical error at each IGP. This error bound is called the GIVE (Grid Ionospheric Vertical Error). It is a 99.9% error bound on the error in the IGPs vertical delay estimate [RTCA1], provided that the error distribution is gaussian.

$$GIVE = 3.29\sigma_{GIVE} \tag{2.2}$$

where σ_{GIVE} is the standard deviation of the gaussian distribution that overbounds the post-correction residual ionospheric vertical error at an IGP.

The user receives both the IGP vertical delay estimate and the GIVE indicator (GIVEI). The conversion table of GIVEI and $\sigma^2_{i,GIVE}$ is shown in Table 2.1. The use of the IGP vertical delay estimates to calculate a user ionospheric vertical delay and the user ionospheric range delay is specified in the WAAS MOPS [RTCA1].

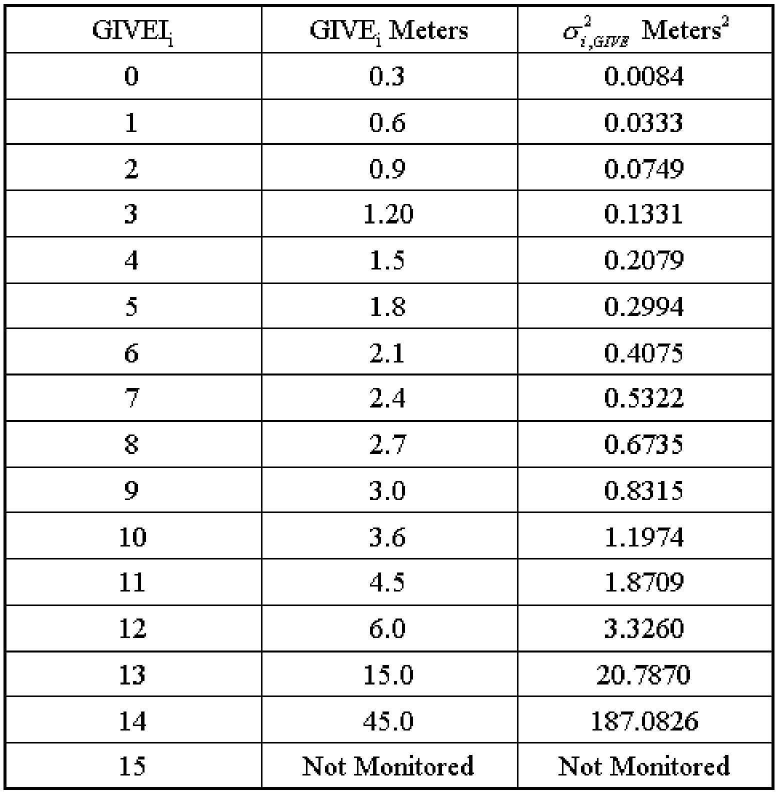

$GIVEI_i$	$GIVE_i$ Meters	$\sigma^2_{i,GIVE}$ Meters^2
0	0.3	0.0084
1	0.6	0.0333
2	0.9	0.0749
3	1.20	0.1331
4	1.5	0.2079
5	1.8	0.2994
6	2.1	0.4075
7	2.4	0.5322
8	2.7	0.6735
9	3.0	0.8315
10	3.6	1.1974
11	4.5	1.8709
12	6.0	3.3260
13	15.0	20.7870
14	45.0	187.0826
15	Not Monitored	Not Monitored

Table 2.1 Evaluation of $GIVEI_i$ [RTCA1]

The GIVE is used to calculate the UIVE (User Ionospheric Vertical Error) and the UIRE (User Ionospheric Range Error). The UIVE and UIRE are the confidence bounds on the user vertical and range errors due to the ionosphere, respectively. To determine the user's ionospheric delay for a given satellite, WAAS uses a simpler and relatively accurate thin shell ionosphere model at an altitude of 350 km. The user first calculates the location of the ionospheric pierce point (IPP) of the satellite signal. The IPP is the location at which the line of sight between user and the given satellite pierces the shell, as shown in Figure

2.5. After calculating the IPP latitude (ϕ_{pp}) and longitude (λ_{pp}), the ionospheric vertical delay at that pierce point, $\tau_{vpp}\left(\phi_{pp},\lambda_{pp}\right)$, can be calculated by the three- and four-point interpolation algorithms, as shown in Figure 2.6. The definitions of three- and four-point interpolation algorithms, and when the three- and four-point algorithms are applicable, are detailed in the WAAS MOPS Appendix A [RTCA1].

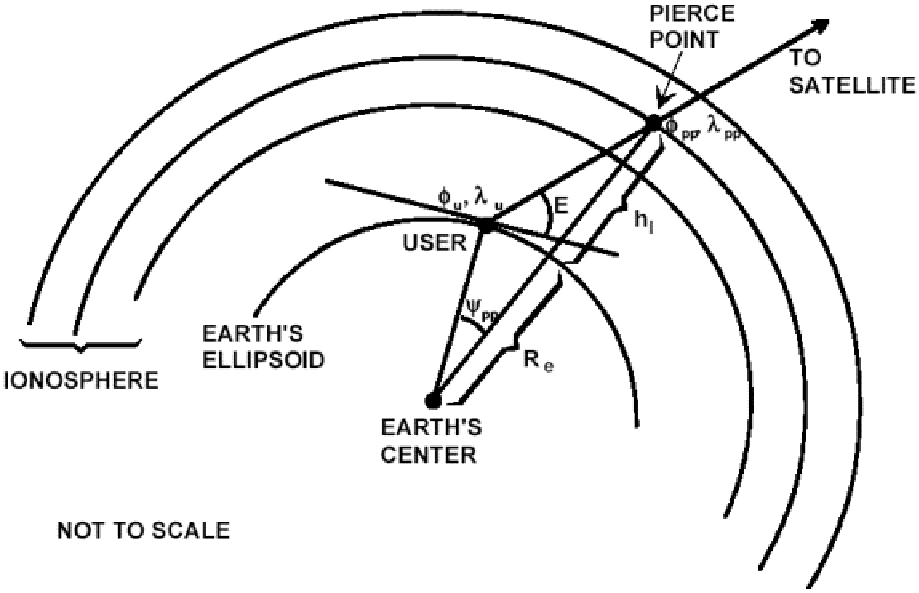

Figure 2.5: Ionospheric pierce point (IPP) [RTCA1].

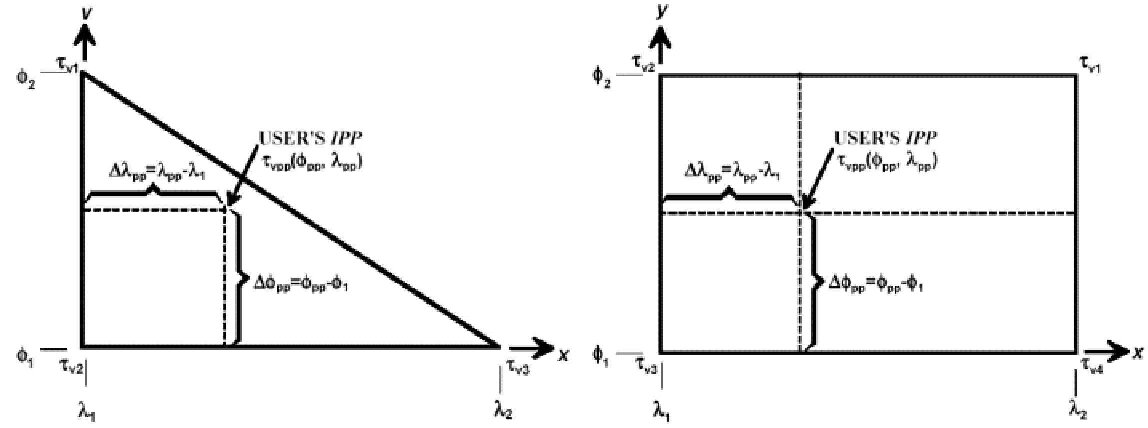

Figure 2.6: Three- and four-point interpolation algorithm definitions [RTCA1].

When the user establishes the vertical delay at the pierce point, the user can multiply the vertical delay at the IPP by the obliquity factor (*F_{pp}*) to obtain the ionospheric correction (*IC_i*) to be added to the pseudorange measurement.

$$IC_i = -\tau_{spp}\left(\lambda_{pp}, \phi_{pp}\right) = -F_{pp} \bullet \tau_{vpp}\left(\lambda_{pp}, \phi_{pp}\right) \tag{2.3}$$

where, $\tau_{spp}\left(\phi_{pp}, \lambda_{pp}\right)$ is the slant delay at the IPP, F_{pp} is the obliquity factor, and $\tau_{vpp}\left(\phi_{pp}, \lambda_{pp}\right)$ is the vertical delay at the IPP.

$$F_{pp} = \left[1 - \left(\frac{R_e \cos E}{R_e + h_I}\right)^2\right]^{-\frac{1}{2}} \tag{2.4}$$

where, E is the elevation angle to satellite, R_e is the radius of earth, and h_I is the height of the ionosphere.

The confidence bound on the user's ionospheric correction is calculated from the GIVE in a similar manner. First, calculate the variance of the residual ionospheric error at each IGP, $\sigma^2_{ionogrid}$. Then, convert the variance of the residual ionospheric error at each IGP to the variance of the residual vertical ionospheric error at the user IPP, σ^2_{UIVE}. Finally, the variance of the residual slant range ionospheric error, σ^2_{UIRE}, is calculated by multiplying σ^2_{UIVE} by the square of the obliquity factor:

$$\sigma^2_{UIRE} = F^2_{pp} \bullet \sigma^2_{UIVE} \tag{2.5}$$

A more detailed calculation is described in the WAAS MOPS Appendix A [RTCA1]. Other ionospheric delay models and algorithms are available in [Klobuchar] [Enge96] [Chao] [Howe] [Hansen].

2.2.1.2 SATELLITE ERRORS

Satellite errors are another error source for GPS, so an additional WAAS function is to correct for these errors. In general, satellite errors can be broken into two components – satellite clock errors and satellite ephemeris errors. WAAS uses two kinds of corrections for these errors – fast and long-term corrections [RTCA1].

Satellite clock errors can be calibrated using broadcast clock parameters. However, remaining errors include SA (Selected Availability) and real residual satellite clock error. SA was the largest error on GPS when WAAS was first designed, so the satellite clock error corrections were designed with this in mind. SA was deactivated by a Presidential Order on May 2nd, 2000. The broadcast GPS ephemeris is calculated by using a least squares fit over four or six hours [Spilker]. As a result of the fit, the position solution calculated from the ephemeris has small residual errors. Because the satellite clock errors have shorter time constants than the satellite ephemeris errors, the fast corrections are predominantly satellite clock errors and the long-term corrections are predominantly satellite ephemeris errors.

The satellite position error and the error velocities are estimated by the WMS as a three-dimensional vector correction for each satellite. The user projects the satellite error vector onto his line of sight to calculate a scalar pseudorange correction. The satellite clock error and error rate are estimated by the WMS. The WMS uplinks a satellite correction that is extrapolated into the future such that the correction is valid at the time of reception. The user applies this correction according to the specifications in the WAAS MOPS [RTCA1].

The system also calculates a bound on the projection of the satellite orbit determination and satellite clock estimation errors onto the line of sight of the worst-case user, namely User Differential Range Error (UDRE). The WAAS UDRE calculation is specified in [Peck] [Wu]. The UDRE is transmitted in the form of a UDRE indicator (UDREI). The conversion table of UDREI and $\sigma_{i,UDRE}^2$ is shown in Table 2.2. σ_{UDRE} is the standard deviation of a distribution that overbounds the residual satellite error after applying the fast and long-term correction.

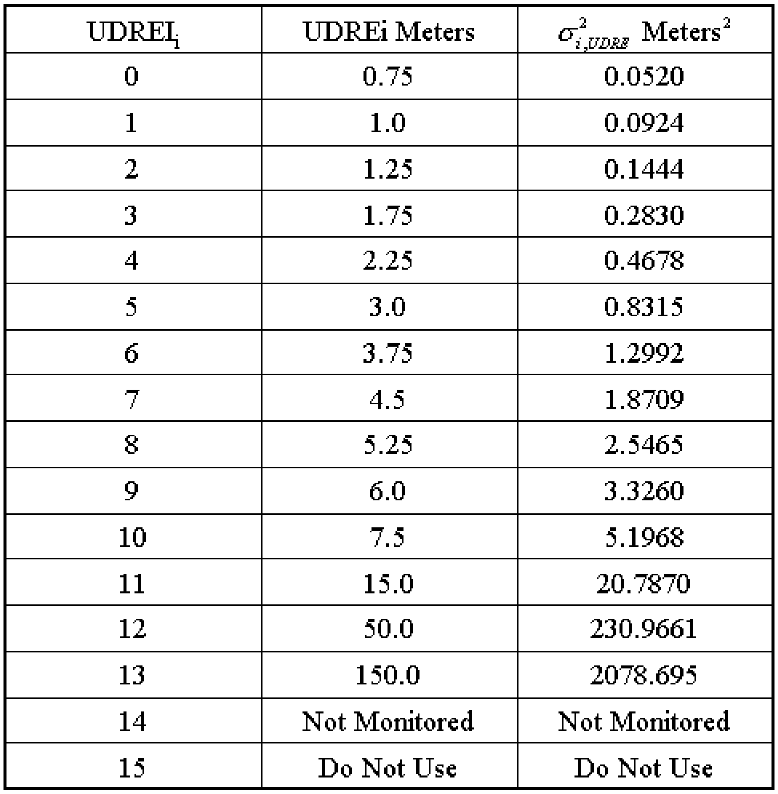

UDREI_i	UDREi Meters	$\sigma^2_{i,UDRE}$ Meters^2
0	0.75	0.0520
1	1.0	0.0924
2	1.25	0.1444
3	1.75	0.2830
4	2.25	0.4678
5	3.0	0.8315
6	3.75	1.2992
7	4.5	1.8709
8	5.25	2.5465
9	6.0	3.3260
10	7.5	5.1968
11	15.0	20.7870
12	50.0	230.9661
13	150.0	2078.695
14	Not Monitored	Not Monitored
15	Do Not Use	Do Not Use

Table 2.2 Evaluation of UDREI_i [RTCA1]

The residual error associated with the fast and long-term corrections (residual satellite error), σ_{flt}, can be calculated from the WAAS transmitted data. This calculation is detailed in the WAAS MOPS Appendix A [RTCA1].

$$\sigma^2_{flt} = \begin{cases} \left[\left(\sigma_{UDRE}\right)\cdot\left(\delta UDRE\right) + \varepsilon_{fc} + \varepsilon_{rrc} + \varepsilon_{ltc} + \varepsilon_{er}\right]^2, if\ RSS_{UDRE} = 0 \\ \left[\left(\sigma_{UDRE}\right)\cdot\left(\delta UDRE\right)\right]^2 + \varepsilon^2_{fc} + \varepsilon^2_{rrc} + \varepsilon^2_{ltc} + \varepsilon^2_{er}, if\ RSS_{UDRE} = 1 \end{cases} \tag{2.6}$$

where,

RSS_{UDRE} is the root sum square flag in WAAS Message Type 10

$\delta UDRE$ is a factor derived from Message Type 27 or 28, and is used to adjust σ_{UDRE} for user location

The old but active data (OBAD), ε terms are detailed in WAAS MOPS Appendix A

Message Type 27 modifies the UDRE for different portions of the service volume. Message Type 28 contains a relative clock and ephemeris covariance matrix for individual satellites. From this matrix, users can reconstruct their location specific error bound rather than applying the largest bound in the service volume. Users can determine a more accurate value of σ_{UDRE} by applying Message Type 28. The matrix in the Message Type 28 is projected along the user's line of sight and the resulting value is $\delta UDRE$ [Walter01].

2.2.2 LOCAL ERRORS

Local error sources include tropospheric delay, and user receiver code noise and multipath, as described in Chapter 1. These are not corrected by WAAS. However, the WAAS MOPS does provide a means of bounding these errors.

Users apply the standard troposphere model described in the WAAS MOPS to remove the tropospheric delay. The residual tropospheric error model is bounded as follows,

$$\sigma_{i,tropo}^2 = \left(0.12 \cdot m\left(E_i\right)\right)^2 \tag{2.7}$$

where,

$m\left(E_i\right)$ is the troposphere correction mapping function for satellite elevation given by:

$$m\left(E_i\right) = \frac{1.001}{\sqrt{0.002001 + \sin^2\left(E_i\right)}} \tag{2.8}$$

E_i is the satellite elevation angle

Equation (2.12) is valid for satellite elevation angles of not less than 5 degrees. This residual troposphere error confidence model is plotted in Figure 2.7.

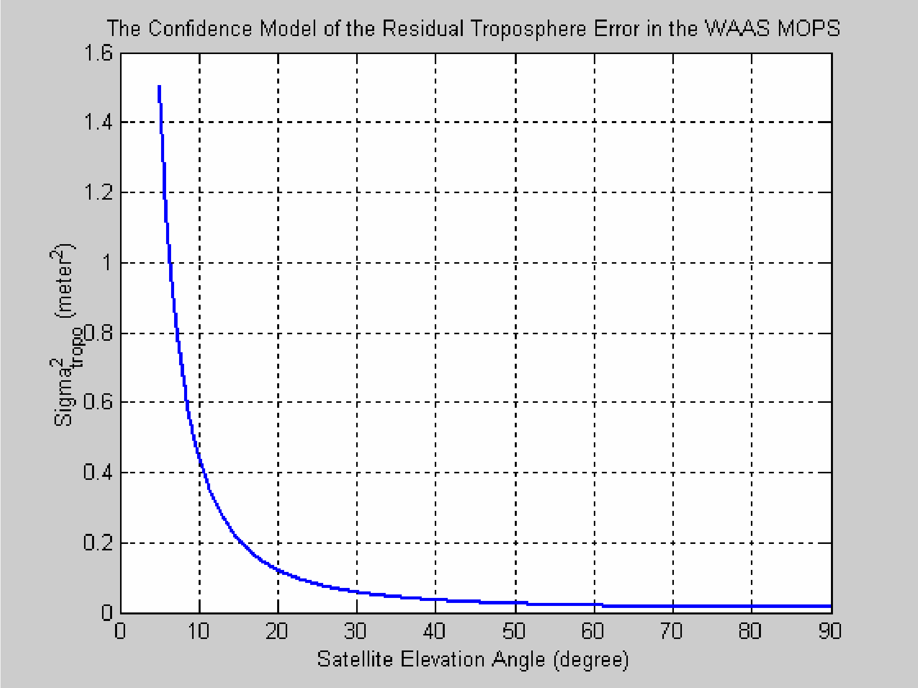

Figure 2.7: The confidence model of the residual troposphere error in the WAAS MOPS.

This thesis used a confidence model of the residual airborne receiver noise and multipath errors which is defined in the Local Area Augmentation System Airborne Accuracy Designator (LAAS AAD) of the LAAS MASPS [RTCA2], and is estimated as follow,

LAAS AAD-A,

$$\sigma_{i,air}^{2}=\left(0.16+0.23e^{-E_i/19.6^o}\right)^2 \tag{2.9}$$

LAAS AAD-B,

$$\sigma_{i,air}^{2}=\left(0.0741+0.18e^{-E_i/27.7^o}\right)^2 \tag{2.10}$$

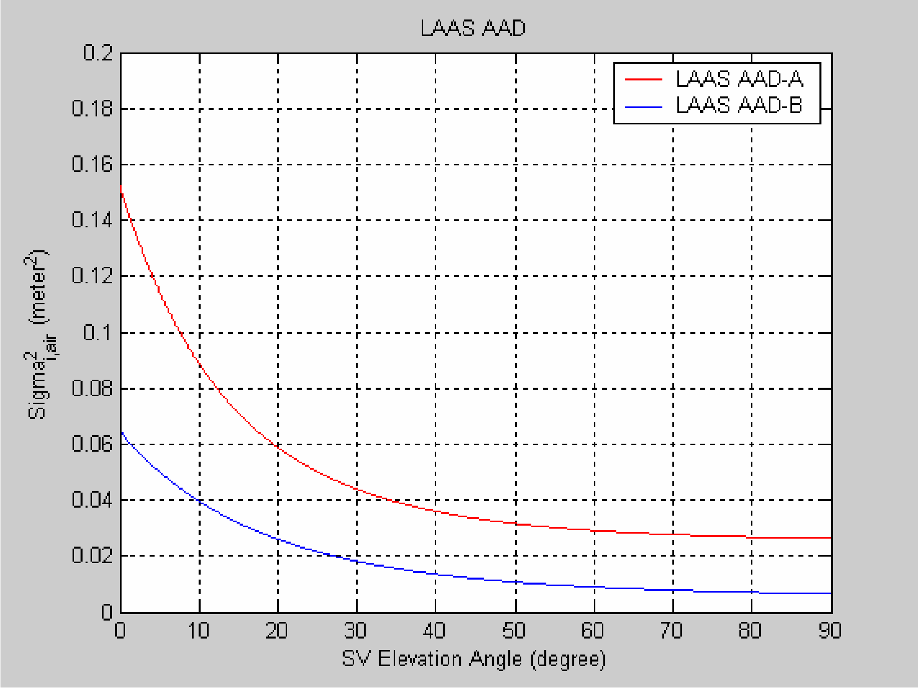

Figure 2.8: The LAAS AAD model of the residual airborne receiver noise and multipath errors in the LAAS MASPS.

The difference between the LAAS AAD-A model and LAAS AAD-B model is the early-minus-late (EML) correlator spacing for the delay-lock detector [McGraw]. For the LAAS AAD-A model, the EML correlator spacing is 1.0 chip, and for the LAAS AAD-B model, the EML correlator spacing is 0.2 chip. The LAAS AAD-A model is designed to permit the legacy receivers to be used for the LAAS early operational benefit. It is envisioned that fractional-chip EML correlator spacing receivers will be adopted by avionics manufactures to support LAAS operations. This thesis studies the modernized GPS/WAAS system. Therefore, the LAAS AAD-B model is chosen as the confidence model of the residual airborne receiver noise and multipath errors in this thesis.

2.2.3 USER AVIONICS

All FAA certified WAAS user avionics can perform the weighted navigation solutions according to the WAAS MOPS. The WAAS MOPS also specifies how users can combine the error confidences from the different sources to form a position error bound using the integrity equation in [Walter97]. This equation specifies the protection level calculation, that provides an indication of the service quality. In general, a WAAS receiver is required to perform the following functions [RTCA1].

- Receive the GPS and WAAS signals.
- Use the broadcast ephemeris and clock parameters to calculate the geometric range and satellite clock bias.
- Compute the tropospheric delay using a standard model described in [RTCA1].
- Apply the WAAS corrections and integrity information.
- Compute the navigation solution using weighted least squares (Equation (2.11)).

This section described the system overview of the WAAS. This thesis co-develops the MAAST (MATLAB Algorithm Availability Simulation Tool) to evaluate the benefits of the WAAS operation. This toolset will be detailed in the following section.

2.3 WAAS AVAILABILITY ANALYSIS

Stanford University developed the triangle chart to help visualize the performance of the corrections and error bounds of a GPS integrity messaging system. The chart helps evaluate availability, accuracy, and integrity. The performance is evaluated in the user position domain in a two-dimensional space. The horizontal axis represents the true position error magnitude, and the vertical axis represents the estimated protection level according to the WAAS MOPS integrity equation [RTCA1]. The protection level calculation is an error bound estimation and is described later in this section. One triangle chart example is shown in Figure 2.9. There are three major regions: *Service Available, Service Unavailable,* and *Hazardously Misleading Information (HMI)*. If the estimated protection level is smaller than the alert limit of a designed operation mode, the service will be *available*. If the estimated protection level is larger than the alert limit of a designed operation mode, the service will be *unavailabl*e. If the true error is larger than the estimated protection level, it is *hazardously misleading information*, because the protection level is meant to bound the true error and users have no knowledge of the excessive true error. This situation should occur with a probability of less than one in ten million operations or 10^{-7} and should be avoided. As a result, this triangle chart can intuitively present system performance in terms of accuracy, availability and integrity. The availability of the system can be determined by examining the percentage of points that lie within the service available region.

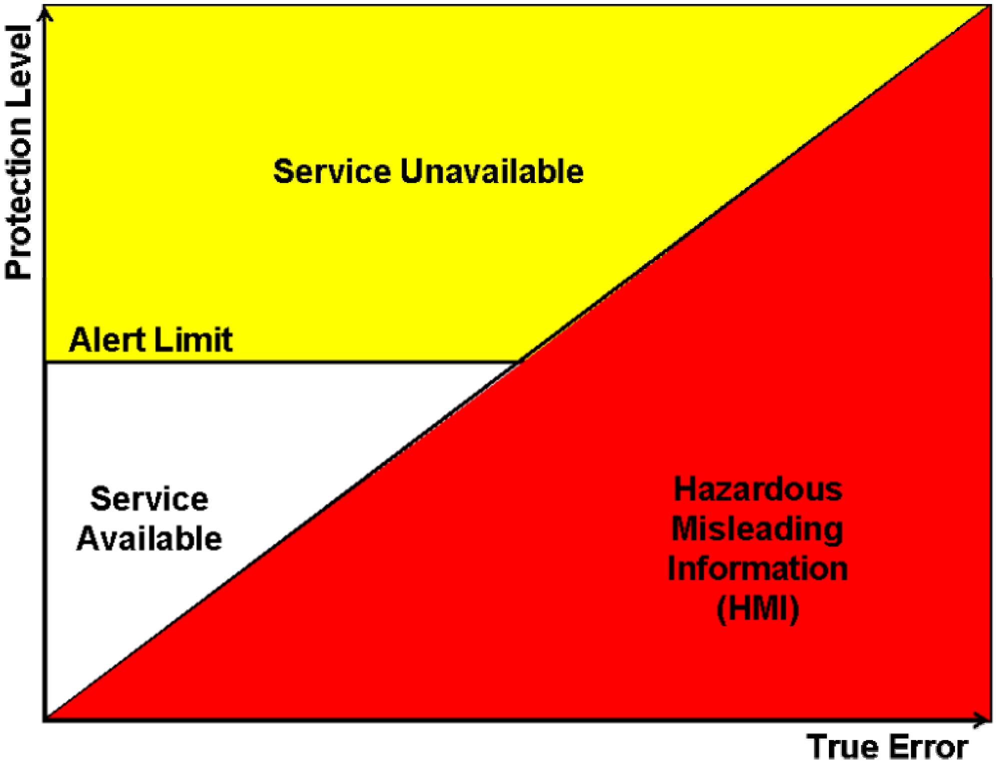

Figure 2.9: The triangle chart example.

The availability of WAAS is determined by the confidence bounds on position errors. The computation of confidence estimates for the corrections to various error sources are explained in Section 2.2. The error due to ionospheric delay and satellite errors will be corrected according to the WAAS MOPS, and then the local errors such as error due to tropospheric delay and user receiver noise and multipath errors will be removed by a standard model [RTCA1]. The corrected range measurements are used to compute the GPS solution using weighted least squares as follows,

$$\hat{x} = \left(G^T W G\right)^{-1} G^T W y \tag{2.11}$$

where,

$\hat{x}$ is position and clock errors

G is the observation matrix

W is the weighting matrix for the measurement

y is the corrected range residual vector

The weighting matrix, W, is a diagonal matrix and the inverse of the i^{th} diagonal element is given by the variance for the corresponding satellite, σ_i^2, which is calculated in Equation (2.12) [RTCA1].

$$\sigma_i^2 = \sigma_{i,flt}^2 + \sigma_{i,UIRE}^2 + \sigma_{i,air}^2 + \sigma_{i,tropo}^2 \tag{2.12}$$

where,

$\sigma_{i,flt}^2$ is the fast and long-term degradation confidence, which is the confidence bound on satellite clock and ephemeris corrections, and is described in Section 2.2.1.2.

$\sigma_{i,UIRE}^2$ is the user ionospheric range error confidence, which is the confidence bound on ionospheric delay corrections, and is described in Section 2.2.1.1

$\sigma_{i,air}^2$ is the airborne receiver error confidence, which is the confidence bound on aircraft user receiver error, and is described in Section 2.2.2

$\sigma_{i,tropo}^2$ is the tropospheric error confidence, which is the confidence bound on residual tropospheric error, and is described in Section 2.2.2

As a result, the inverse of W can be written in Equation (2.13)

$$W^{-1} = \begin{bmatrix} \sigma_1^2 & 0 & \cdots & 0 \\ 0 & \sigma_2^2 & \cdots & 0 \\ \vdots & \vdots & \ddots & \vdots \\ 0 & 0 & & \sigma_N^2 \end{bmatrix} \tag{2.13}$$

The variance of the vertical position estimate is the third diagonal element of the position estimate covariance matrix,

$$d_{3,3} = \left[\left(G^T W G \right)^{-1} \right]_{3,3} \tag{2.14}$$

where,

$d_{3,3}$ is the variance of the vertical position estimate

The VPL (Vertical Protection Level) is

$$VPL_{WAAS} = K_{V,PA} d_{3,3} \tag{2.15}$$

where, $K_{V,PA}$ equals 5.33. This is a multiplier on the standard deviation of the vertical error such that the VPL is only exceeded at most one time in ten million $\left(10^{-7}\right)$, the tolerable probability of HMI (Hazardously Misleading Information), provided that the error distribution is a zero mean Gaussian [Walter97]. The protection level calculation can be summarized in Figure 2.10, and is specified in the WAAS MOPS Appendices A and J [RTCA1]. Figure 2.10 also shows the section number where the confidence estimates for the corrections to various error sources are derived.

The VPL is very important, because no truth is available for the airborne receiver, and the result of this protection level calculation (Equation (2.15)) will be used to decide if the approach should be continued or a missed approach should be executed [RTCA1].

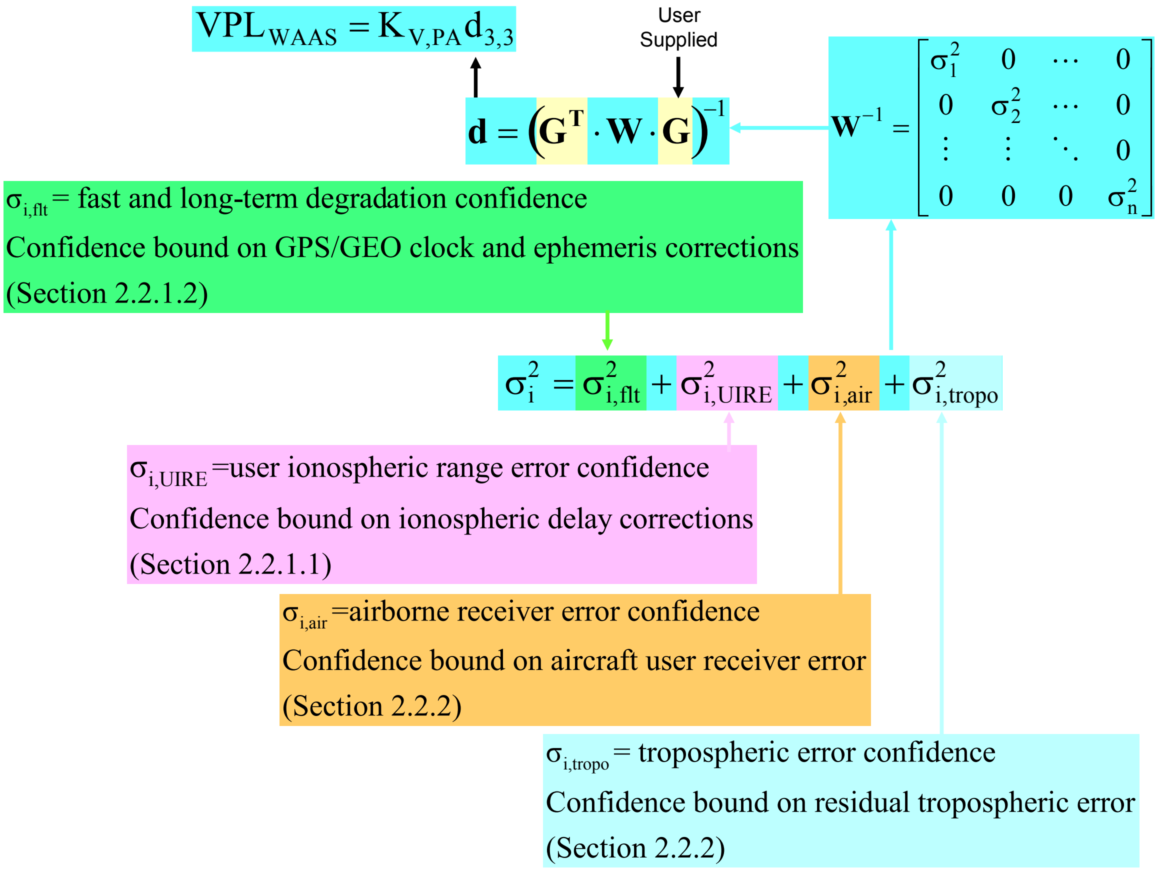

Figure 2.10: The Protection level calculation.

2.4 MATLAB ALGORITHM AVAILABLITY SIMULATION TOOL (MAAST)

This section describes a set of MATLAB [MATLAB] functions currently being developed for WAAS availability analysis. This toolset is called the MATLAB Algorithm Availability Simulation Tool (MAAST). It includes simulation algorithms that are constantly being developed and updated by various working groups. This set of functions is intended for use as a fast, accurate, and highly customizable experimental test bed for algorithm development. A user-friendly interface has also been developed for the tool. It is open source and can be downloaded from the Stanford WAAS web site (http://waas.stanford.edu). Therefore, it provides a common ground for different working groups to compare their results.

2.4.1 MAAST SIMULATION CONFIGURATION

MAAST has four parts: MAAST directory files, graphic user interface (GUI), MAAST main program, and outputs. The MAAST directory files contain WAAS simulation algorithms and configurations. The GUI provides a control panel to allow the program user to make selections from the algorithm and simulation options. Then the selected algorithms and configurations are fed into the MAAST main program *svmrun.m*. The MAAST main program performs WAAS master station processing, user processing, and output processing. The outputs provide several graphic options including a availability contour, VPL and HPL contours, and UDRE/GIVE plots. This approach is summarized in Figure 2.11.

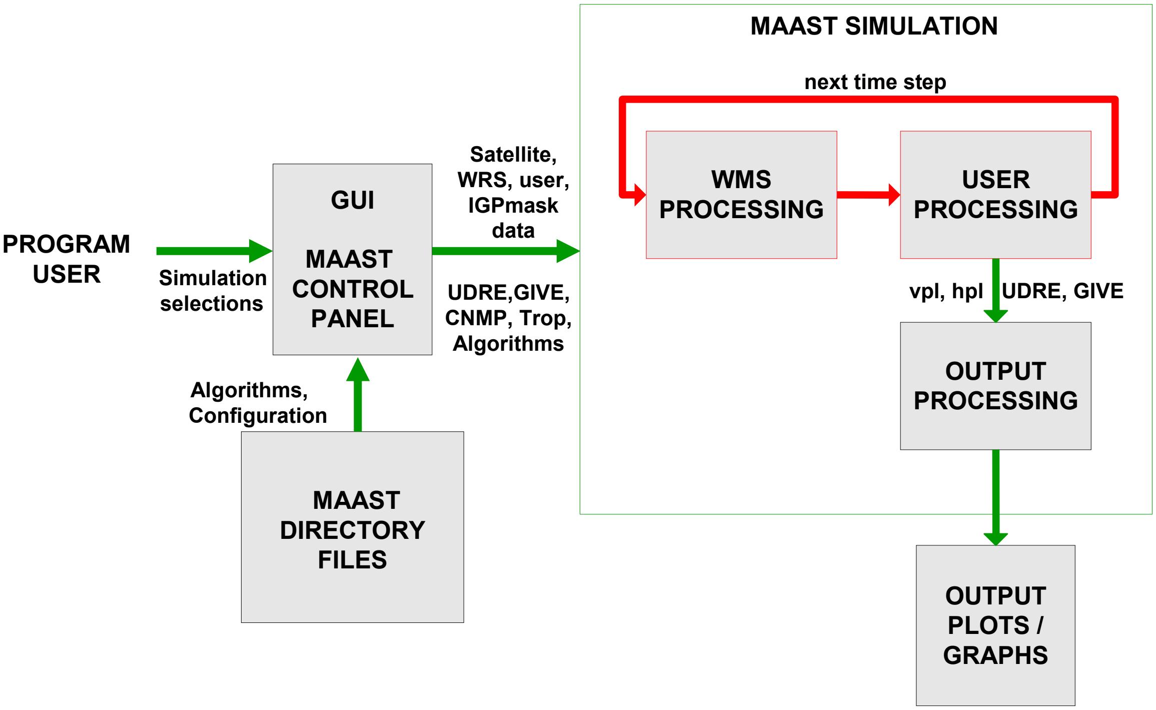

Figure 2.11: Block diagram of MAAST.

The simulation configuration of MAAST includes:

1. **WAAS Reference Stations (WRSs)**: MAAST uses the 25 U.S. WAAS reference stations as shown in Figure 2.2. The associated file name in MAAST is *wrs25.dat*, which is in the format of [WRS number, WRS latitude in degrees, WRS longitude in degrees, WRS height in meters]. It is easily configurable to accommodate different locations. A user could build their WRS list in the same format as *wrs25.dat*.

2. **User**: MAAST simulates users on a rectangular grid, but only the nodes contained inside the specified boundary (CONUS or Alaska) will be used to calculate coverage and to fill in histogram data. The associated files are *usralaska.dat* and *usrconus.dat*, which specify polygon boundaries of Alaska and CONUS, respectively, in the format of [latitude (degrees), longitude (degrees)]. Figure 2.12 shows an example for CONUS. The users colored red are inside the CONUS boundary and contribute to the output while the blue users are outside the CONUS boundary and are excluded from coverage and histogram calculations. If program users want to customize their own user boundary, then they need to build their user boundary in the same format as *usrconus.dat* or *usralaska.dat*.

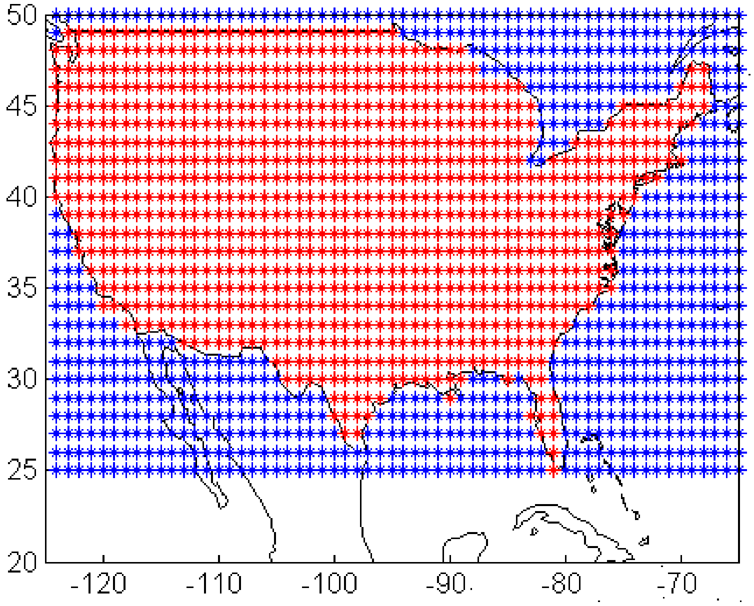

Figure 2.12: User grid of CONUS. User in red are inside the CONUS boundary and users in blue are outside the CONUS boundary.

3. **GPS Satellite Constellation**: MAAST accepts the standard YUMA almanac format. The defult constellation is the standard constellation specified in Appendix B of the MOPS [RTCA1]. In addition, other constellation in the YUMA format may be used corresponding to a specified week. YUMA formatted ephemeris files can be downloaded from the U.S. Coast Guard website (http://www.navcen.uscg.gov/ftp/GPS/almanacs/yuma/). Files must be stored in the same directory as MAAST and named *almyuma[week number].dat*, where week number can be specified in the GUI.

4. **GEOs**: There are four GEO satellites (INMARSAT) that are currently specified: AOR−E, AOR−W, IOR, and POR. The INMARSAT coverage map is shown in Figure 2.13. The associated file in MAAST is *geo.dat*, which is in the format of [GEO PRN number, GEO latitude in degree, flag if the button of the GUI should default to on, and name for the button]. If program users want to customize the GEO list, then they need to build their own GEO list in the same format as *geo.dat* and replace *geo.dat* with their

version. Note that the PRNs need to be between 120 and 138 as per the WAAS MOPS [RTCA1]. The GUI has space for up to six GEOs.

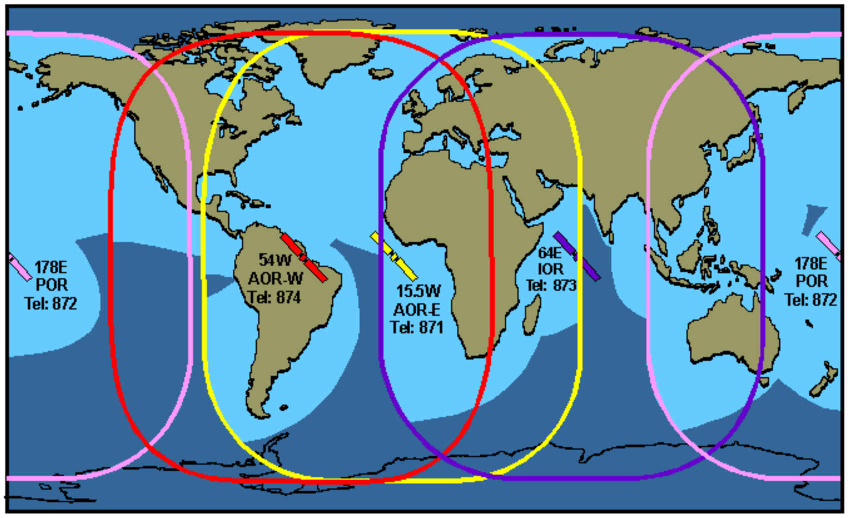

Figure 2.13: INMARSAT coverage (Courtesy: INMARSAT http://www.inmarsat.com).

2.4.2 MAAST SIMULATION PROCESS

An overview of the main simulation engine of MAAST is shown in the upper right section of Figure 2.11. It is subdivided into three major components: WAAS master station (WMS) processing, WAAS user processing, and output processing. The corresponding MATLAB functions are *wmsprocess.m*, *usrprocess.m*, and *outputprocess.m*. The WMS processing and user processing blocks constitute the main computational loop and are stepped through in sequence at every time step. Time step resolution is chosen by the program user through the GUI. WMS processing simulates the computations of UDREs, GIVEs [RTCA1], and Message Type 28 [Walter01] covariance matrices performed by the WAAS master station using data gathered from reference stations. These computations are to be broadcast to WAAS users. User processing, on the other hand, simulates the WAAS user's computation of confidence bounds on clock/ephemeris and ionospheric corrections at the user site, from which VPL/HPL can be derived. All the confidence bound models are discussed in Section

2.2. The output processing block then takes all the data and creates visual outputs of VPL/HPL and availability contours, as well as UDRE and GIVE plots.

WAAS service availability at user locations is based on vertical and horizontal protection levels, which are determined from confidence estimates on corrections to the different error sources. Algorithms for these confidence estimates are being developed by several working groups. Aside from having predefined algorithm functions, MAAST offers common templates for including custom algorithms. This is achieved by defining standardized input and output arguments for each customizable algorithm function. This provides an efficient way for developers to test their own algorithm implementations against the whole system in a modular fashion. Selectable modules for this tool include algorithms for computing troposphere errors (TROP), receiver code noise and multipath errors (CNMP) [Shallberg] [RTCA2], and confidence bounds on GPS/GEO clock and ephemeris corrections (UDRE) and ionospheric corrections (GIVE).

The simulation does not include old but active data (OBAD) [RTCA1]. Degradation of fast correction, range-rate correction, long-term correction and en route data are not modeled, and all these degradation terms are defined in Appendix A of the WAAS MOPS.

To gain some perspective on how these algorithm modules fit in the simulation, refer to Figures 2.14 and 2.15 for functional flowcharts of the simulated processing performed by the WAAS master station (WMS) and the WAAS user, respectively, to obtain confidence estimates.

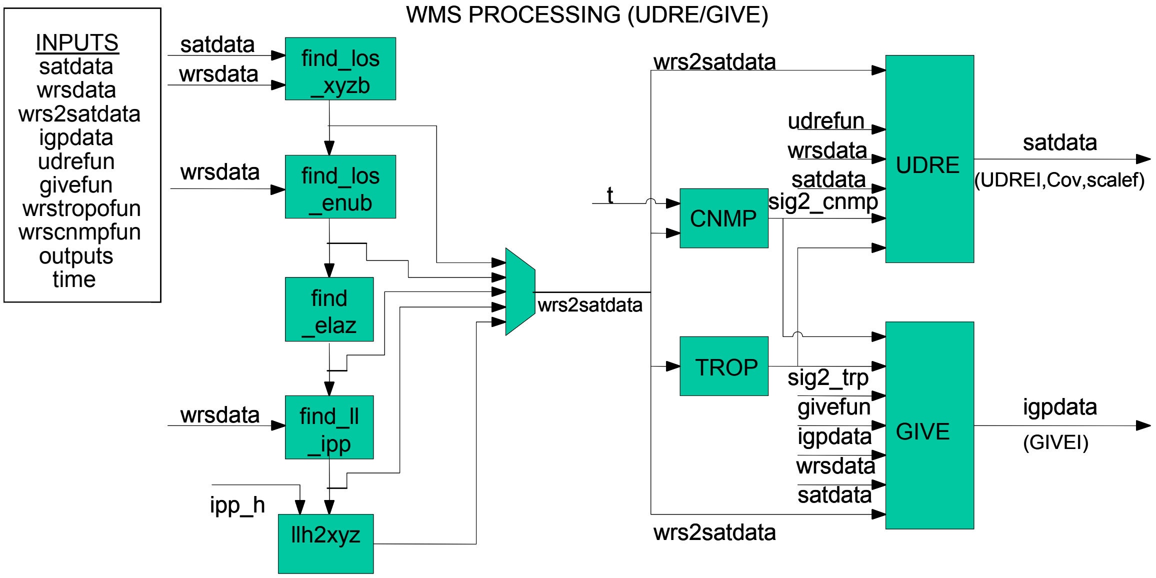

Figure 2.14: Functional flowchart of WMS processing.

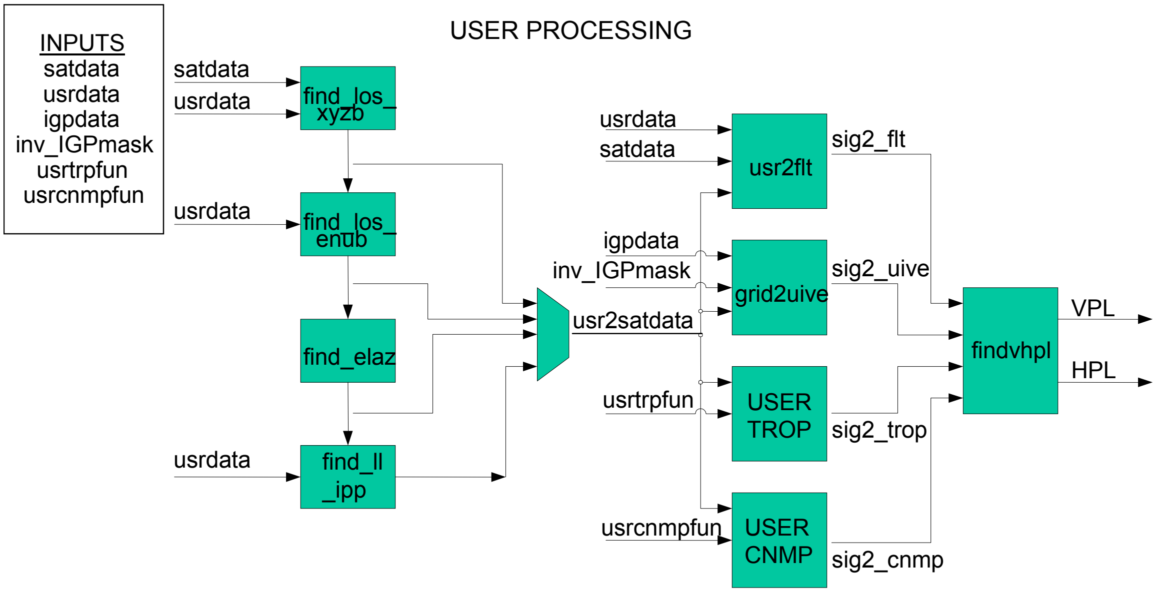

Figure 2.15: Functional flowchart of user processing.

2.4.2.1 WMS PROCESSING

In the simulation of master station processing, location data of reference stations and satellites for the current time step are passed through functional blocks (left half of Figure 2.14) to compute relevant line-of-sight and ionospheric pierce point information for each reference station-satellite pair. Satellite and WRS information is input into the function *find_los_xyzb.m* to give line-of-sight vectors in ECEF coordinates. These are translated into east-north-up coordinates by the function *find_los_enub.m*. Elevation and azimuth are calculated by *find_elaz.m*. The function *find_ll_ipp.m* then computes ionospheric pierce point (IPP) locations. All these data are packaged into a matrix, *wrs2satdata*, which is passed into succeeding functions that need line-of-sight information. Each row of this matrix corresponds to a particular line-of-sight, while the columns correspond to information fields. The details of the column definitions corresponding to the fields of the matrix, as well as other relevant matrices used in the MAAST, can be found in *init_col_labels.m*.

After line-of-sight computation is done, the TROP module takes elevation angles as inputs and generates troposphere error variances. The CNMP module takes as input the elevation angle and/or track time since last cycle slip of each pair and generates the noise and multipath error variance. Here it was assumed that the carrier phase is continuous as long as the satellite-to-reference station elevation angle exceeds the visibility limit, currently set as 5 degrees by the WAAS MOPS, and cycle slips never occur. Using this assumption, the times at which a satellite rises into view of a reference station are predetermined with up to 1-second accuracy before entering the time step loop. This results in marked improvement in execution speed of track time calculations. The troposphere and CNMP error variances, together with line-of-sight information, are then fed into the UDRE module to generate UDREIs and Message Type 28 covariance matrices for each satellite. Likewise, the GIVE module uses this information, together with ionospheric pierce point data, to generate GIVEIs for each ionospheric grid point.

2.4.2.2 USER PROCESSING

User processing includes functional blocks similar to those used in WMS processing for computing line-of-sight data between the satellite-user pairs, as shown in Figure 2.15. Using these line-of-sight data, the *udre2flt* module projects satellite UDREs with Message Type 28 covariance matrices onto fast and long-term correction variances, σ_{flt}^2, for each user line-of-sight. Similarly, the *grid2uive* module derives user ionospheric correction variances, σ_{UIVE}^2, from ionospheric grid point GIVEs. Implementation of these two modules is based on the WAAS MOPS. User processing has its own selectable TROP and CNMP algorithms independent of the selections made for WMS processing. User VPL and HPL for each time step are the final outputs of the user processing block.

2.4.3 MAAST GRAPHIC USER INTERFACE (GUI)

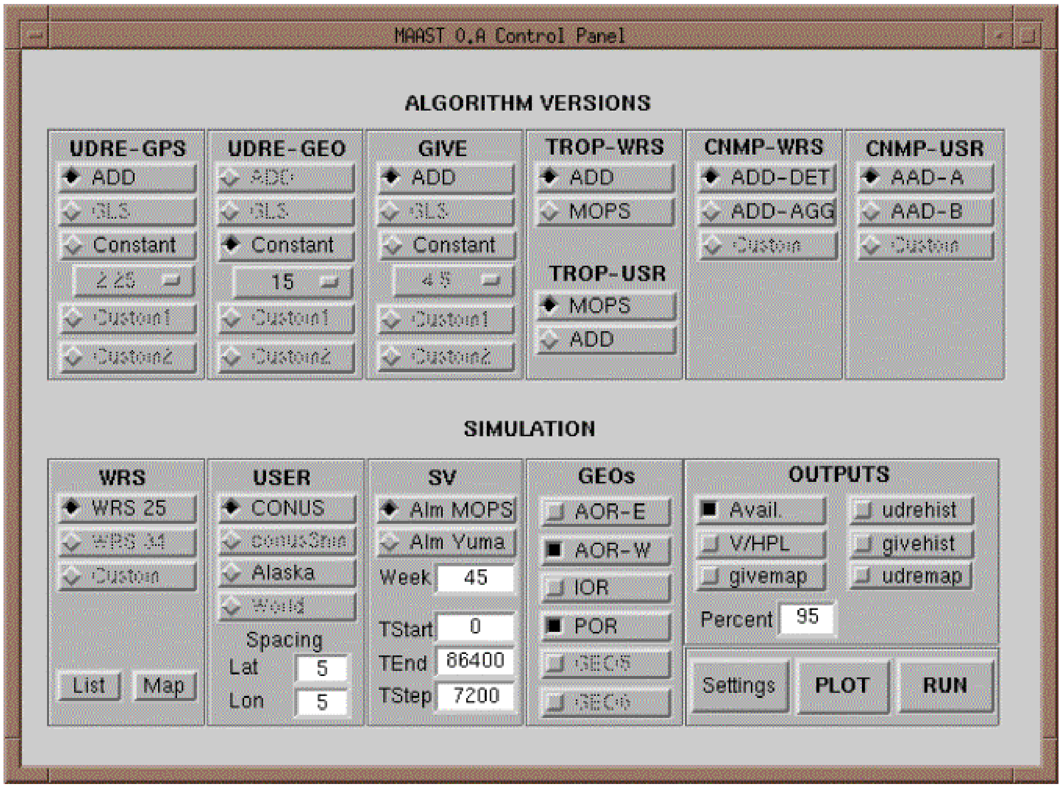

UDRE-GPS: ● ADD ○ GLS ○ Constant 2.25 ○ Custom1 ○ Custom2

UDRE-GEO: ○ ADD ○ GLS ● Constant 15 ○ Custom1 ○ Custom2

GIVE: ● ADD ○ GLS ○ Constant 4.5 ○ Custom1 ○ Custom2

TROP-WRS: ● ADD ○ MOPS

TROP-USR: ● MOPS ○ ADD

CNMP-WRS: ● ADD-DET ○ ADD-AGG ○ Custom

CNMP-USR: ● AAD-A ○ AAD-B ○ Custom

WRS: ● WRS 25 ○ WRS 34 ○ Custom

USER: ● CONUS ○ conus3nia ○ Alaska ○ World

Spacing Lat 5 Lon 5

SV: ● Alm MOPS ○ Alm Yuma

Week 45

TStart 0

TEnd 86400

TStep 7200

GEOs: ☐ AOR-E ■ AOR-W ☐ IOR ■ POR ☐ GEO5 ☐ GEO6

OUTPUTS: ■ Avail. ☐ udrehist ☐ V/HPL ☐ givehist ☐ givemap ☐ udremap

Percent 95

Figure 2.16: Graphic user interface (GUI) of MAAST.

The top half of the graphic user interface (GUI) contains menus for algorithm selection. The bottom half of the GUI contains menus for the simulation configuration and is described in Section 2.4.1. Grayed out buttons represent options that are not yet available. For example, the GLS button in the UDRE-GPS menu is not yet available. Due to the proprietary nature of some algorithms, certain options may not be available for general distribution. For instance, the Algorithm Description Documents (ADDs) of the WAAS Integrity Performance Panel (WIPP) are not available for the general public.

UDRE-GPS MENU

The UDRE-GPS menu specifies the algorithm for calculating the UDREs of GPS satellites. The ADD option activates the GPS UDRE model algorithm from the Algorithm Description Document (ADD) of the WAAS Integrity Performance Panel (WIPP) [WIPP1]. The CONSTANT option activates a list of indexed UDRE values to choose from. The list corresponds to the indexed values in the WAAS MOPS and sets all GPS satellite UDREs to the specified constant. Custom algorithms can easily be added by creating modular MATLAB files with appropriate inputs and outputs.

UDRE-GEO MENU

The UDRE-GEO menu specifies the algorithm for calculating UDRE for geostationary satellites. Options in this menu are similar to the ones in the UDRE-GPS menu.

GIVE MENU

The GIVE menu specifies the algorithm to calculate GIVE for ionosphere grid points (IGPs). The ADD option activates the model algorithm from the GIVE Algorithm Description Document (ADD) of the WIPP [WIPP2]. CONSTANT sets all IGP GIVEs to the specified constant.

TROP-WRS / TROP-USR MENUS

The TROP menus specify the equations for calculating the troposphere error confidence bound for reference stations and for the users. Option in this menu is either the equation specified by the WIPP ADD or the WAAS MOPS.

CNMP-WRS / CNMP-USR MENUS

The CNMP menus are used to select the method of generating the confidence bounds of the residual receiver noise and multipath errors at the reference stations and at the user locations. The CNMP for WRSs is specified in [Shallberg], while the confidence model of the residual airborne receiver noise and multipath errors is specified in Section 2.3.2.

2.4.4 MAAST OUTPUTS

There are seven output plots currently available in MAAST: availability contour, VPL/HPL contours, UDRE/GIVE histograms, and UDRE/GIVE contours, as shown in the bottom right of Figure 2.16. There is a “percent” option in the outputs menu and it has different definitions for the different outputs. In this chapter, we choose 95% as an example.

The availability contour plots the availability as a function of user location. We compute the percentage of time that the user vertical protection level (VPL) is less than the vertical alarm level (VAL) and the horizontal protection level (HPL) is below the horizontal alert level (HAL) to determine the availability percentage contour for the CONterminous U.S. (CONUS) or Alaska. The option of 95% here calculates the fraction of users within those regions that had a time availability of 95% or greater. This measure is referred to as coverage.

The VPL/HPL contours plot the VPL and HPL as a function of user location. The option of 95% here indicates that a user at each specific location had a VPL or an HPL equal to or below the value indicated by the color bar 95% of the time. A selection of 50%, for example, would display the median value.

The UDRE histogram plots the probability distributions of UDRE values and the confidences associated with the fast and long-term corrections ($3.29 * \sigma_{flt}$). The GIVE histogram plots the probability distributions of GIVE values and user ionosphere vertical error (UIVE) values. The percent option box is not applicable to either of these plots.

The UDRE map generates a UDRE contour as a function of the satellite position. The UDRE contour gathers UDRE data at positions in the satellite orbits and interpolates UDRE values to the points in between. The GIVE map generates a GIVE contour by gathering GIVE values at the ionosphere grid points (IGPs). As in the VPL/HPL plots, the percent chosen indicates that the GIVE value at a location is less than or equal to the displayed contour level 95% of the time.

After making algorithm, simulation, and output selections, users then click on the RUN button to begin simulation. The selected output plots are displayed after the simulation, and all relevant data are stored in a temporary binary file *outputs.mat*. Clicking the PLOT button will bypass the simulation process and instead plot the selected output options from data stored in the *outputs.mat*. This allows users to quickly plot other output options if algorithm and simulation configurations have not changed.

Figures 2.17-23 show the plots generated by a sample run to demonstrate the benefits of the WAAS operation. For this particular example, we chose WIPP ADDs for UDRE, GIVE, WRS TROP, and WRS CNMP. We used WAAS MOPS for user TROP and LAAS AAD-B for user CNMP. The simulation was configured for a CONUS user grid, using the 25 current U.S. WRSs, satellite almanac from the WAAS MOPS, two GEOs (AOR−W and POR), 1-degree user grid and 300-second time steps over a 24-hour simulation period.

Figure 2.17 shows availability contours of CONUS users. It indicates that the coverage for users with availability of at least 95% is 98.73% of the CONUS. Figures 2.18 and 2.19 show VPL and HPL contours, respectively. As described in this section, these plots are contours in which V/HPLs are less than corresponding values listed in the bottom color bars of the plots for 95% of time. For example, users in the light green color area of Figure 2.18 have a VPL less than or equal to 30 meters 95% of time.

Figure 2.20 shows histograms for the UDRE plotted in red and the residual errors associated with the fast and long-term corrections ($3.29 * \sigma_{flt}$) plotted in blue. Figure 2.21 shows histograms for the GIVE plotted in red and the UIVE plotted in blue.

Figure 2.22 is the GIVE contour for CONUS and Alaska. The black circles shown in the plot correspond to the ionosphere grid points (IGPs). Figure 2.23 plots a UDRE contour by gathering UDRE data at positions in the satellite orbits and interpolating values to the points in between.

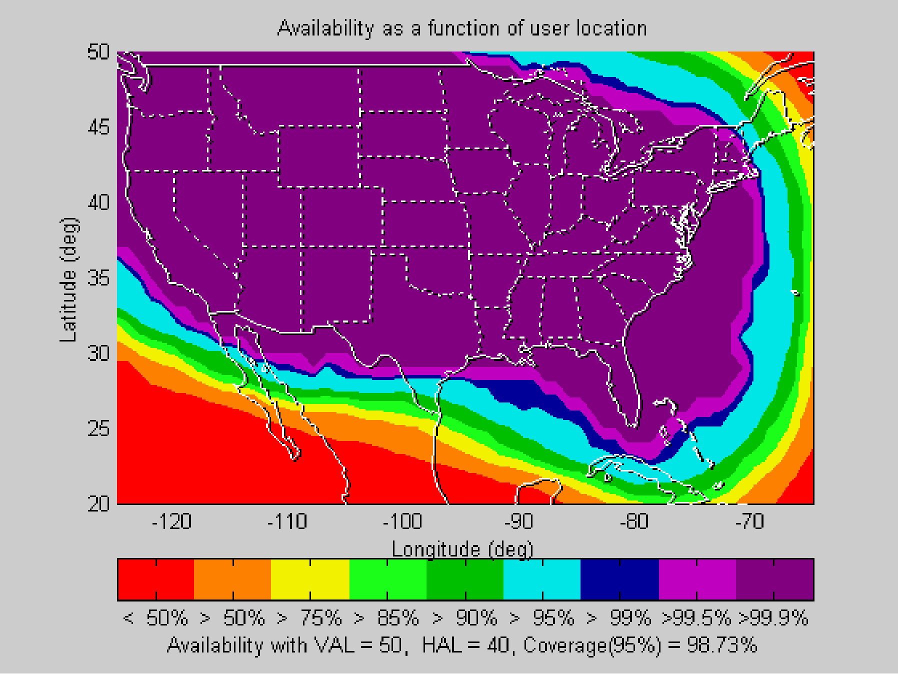

Figure 2.17: Coverage of an L1 single-frequency user in CONUS is 98.73% with VAL=50m, HAL=40m.

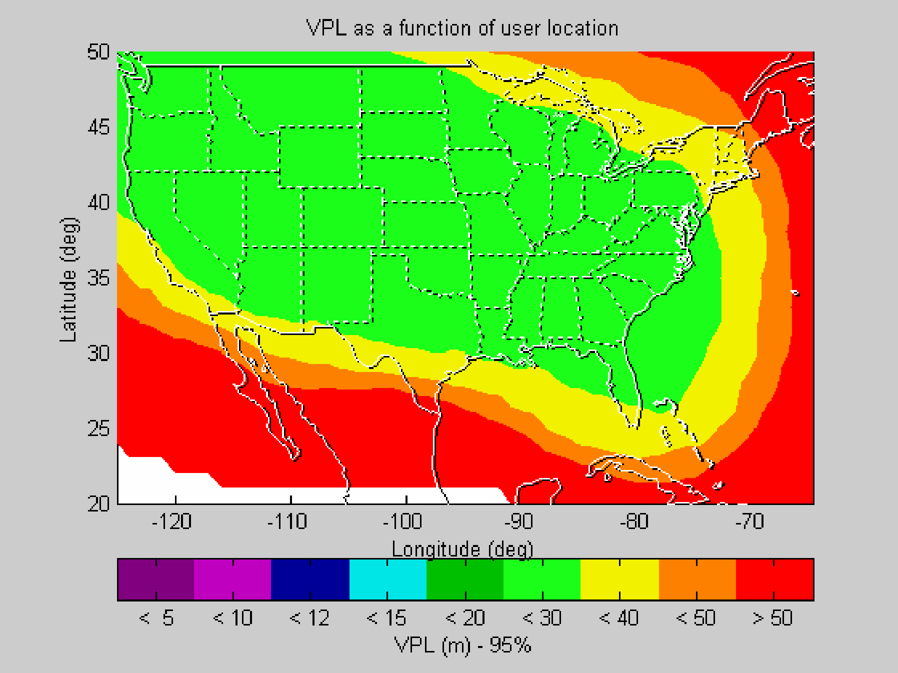

Figure 2.18: Vertical protection level (VPL) contour of an L1 single-frequency user in CONUS.

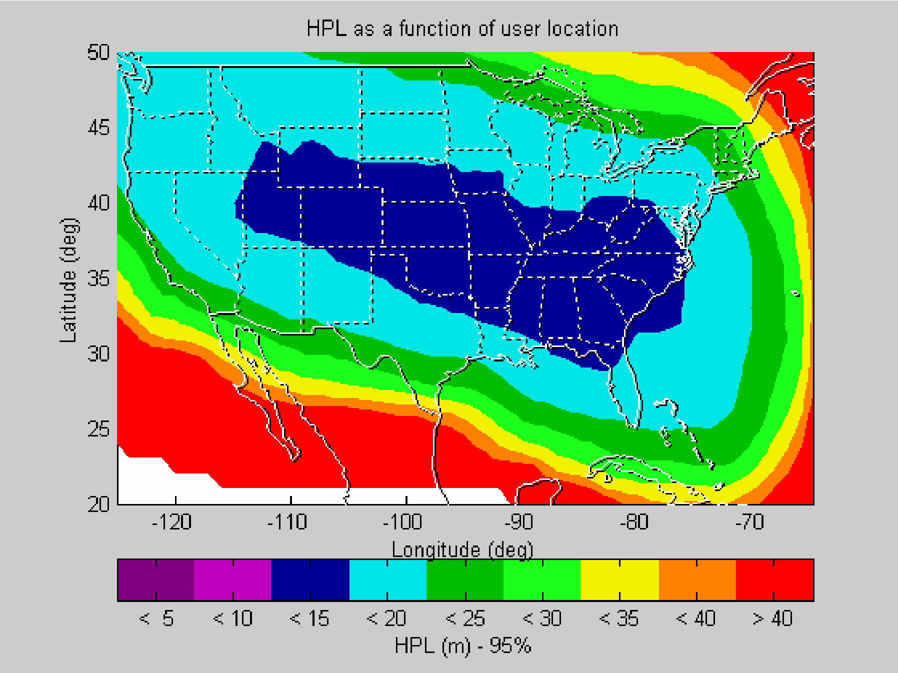

Figure 2.19: Horizontal protection level (HPL) contour of an L1 single-frequency user in CONUS.

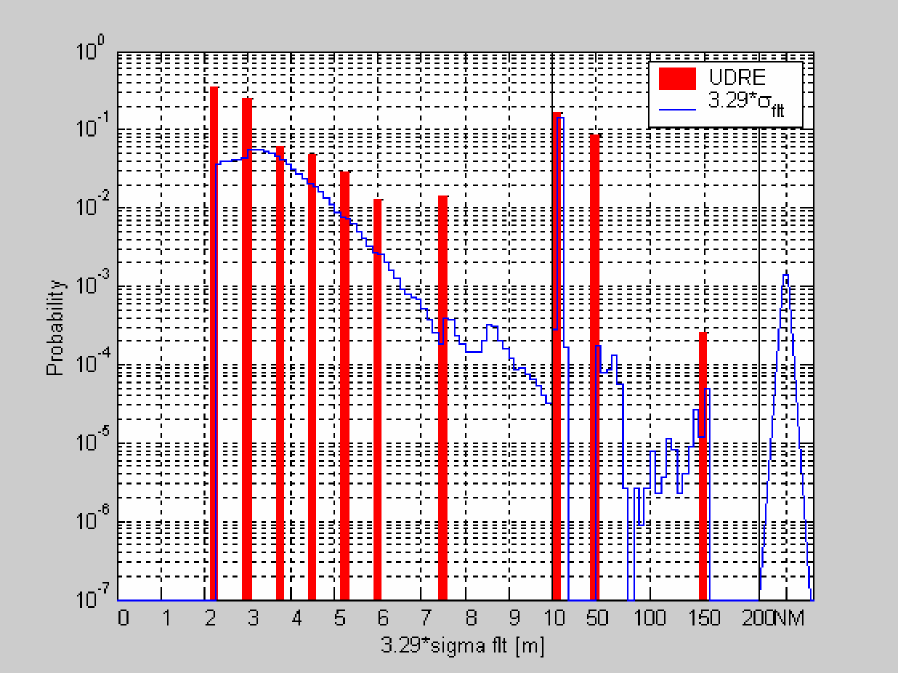

Figure 2.20: UDRE histogram of CONUS.

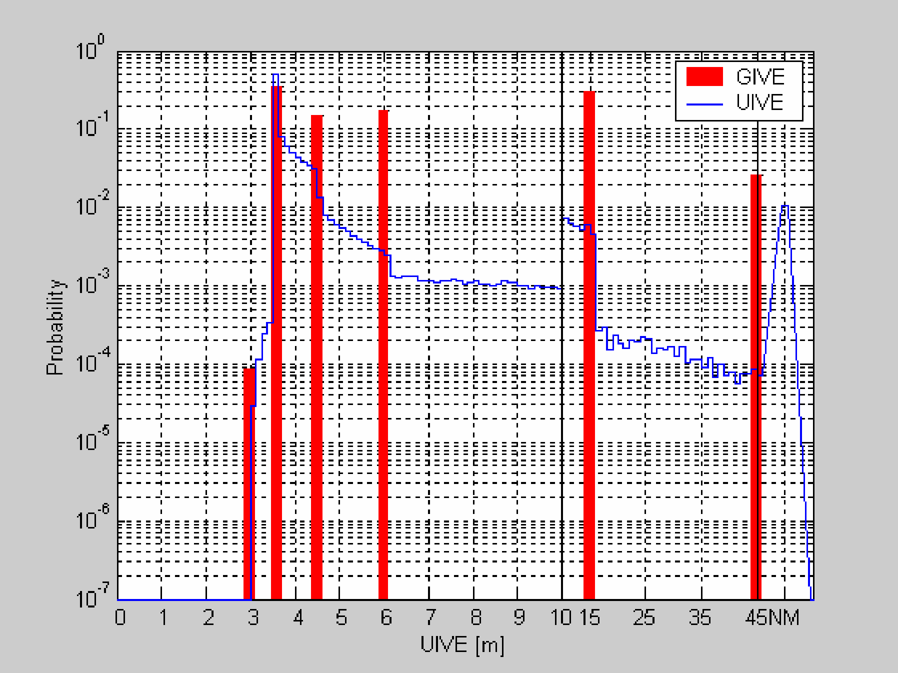

Figure 2.21: GIVE histogram of CONUS.

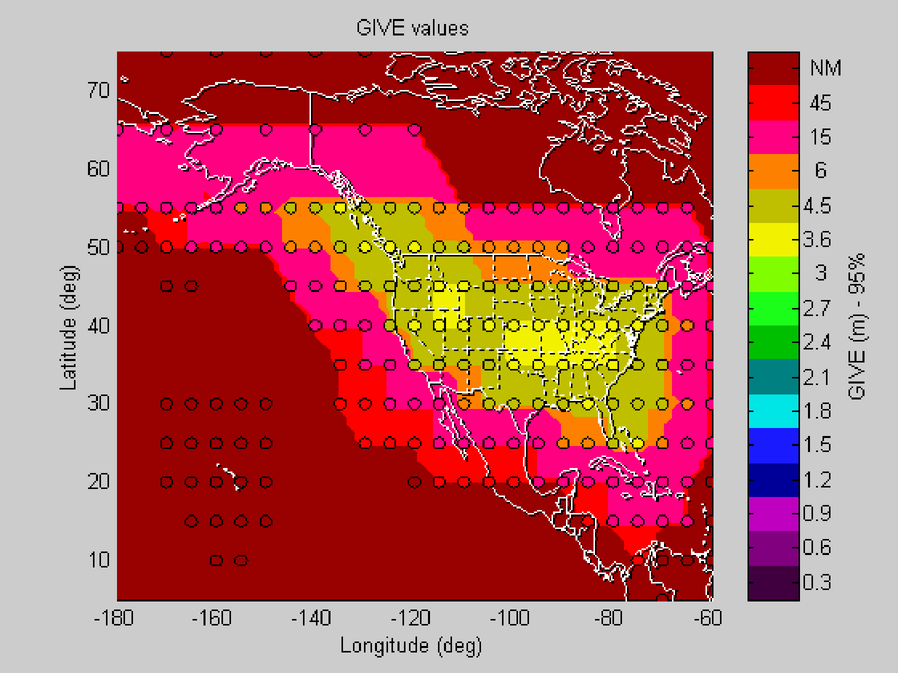

Figure 2.22: GIVE contour of CONUS and Alaska, the block circles correspond to the IGPs.

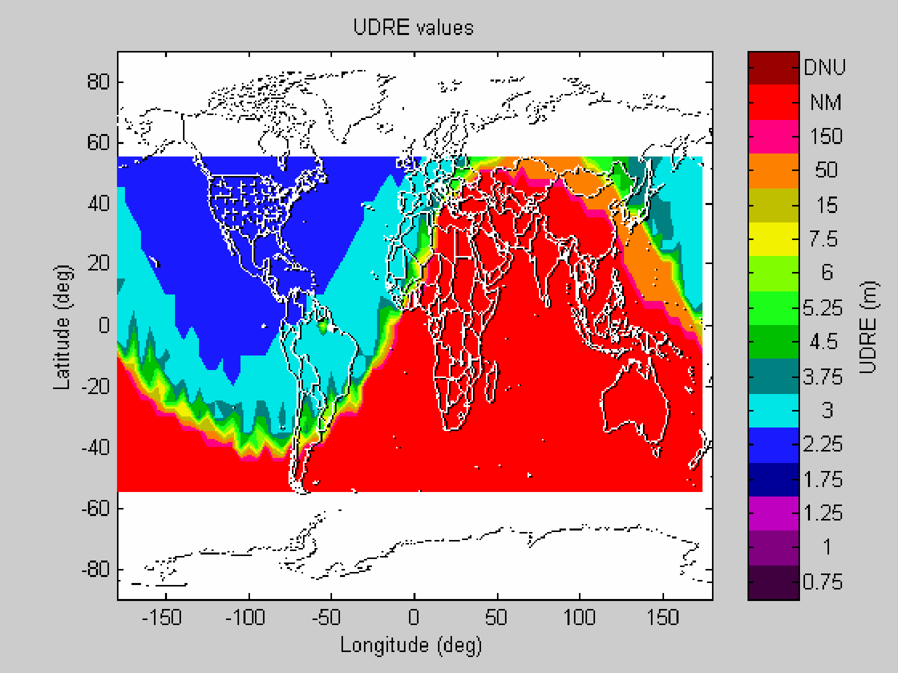

Figure 2.23: UDRE contour as a function of GPS satellite position.

MAAST is intended as an efficient and effective tool for algorithm development. It is not intended to guarantee that we will see exactly that level of availability at each location. In creating MAAST, a number of assumptions have been made. MAAST algorithms are for confidence bounding only; they do not model corrections. Furthermore, it is strictly deterministic, and does not model asset failures in a probabilistic manner. Despite these limitations, the results of this section show that a simple yet powerful framework has been developed that allows us to rapidly model availability. MAAST is a valuable tool for WAAS algorithm research.

2.5 WRS FAILURE

This section examines the coverage loss due to the failure of one of the current 25 WRSs. In MAAST, we deleted one WRS from the list of 25 WRSs for each simulation. To be consistent and in order to easily compare the results the simulation configuration is identical to the earlier configuration, that is, the WIPP ADDs for UDRE, GIVE, WRS TROP, and WRS CNMP, WAAS MOPS for user TROP, and LAAS AAD-B for user CNMP, are chosen. The simulations were configured for a CONUS user grid, satellite almanac from the WAAS MOPS, two GEOs (AOR-W and POR), 1-degree user grid, and 300-second time steps over a 24-hour simulation period. The simulation results are shown in Table 2.3 for CONUS coverage of LPV for 99.9% of time. The table shows the coverage % for a single failure of each of the reference stations and are listed in order of increasing coverage loss.

W/O WRS Failure	97.58%	Jacksonville, FL	97.35%
Cold Bay, AK	97.58%	Puerto Rico	97.23%
Atlanta, GA	97.58%	Seattle, WA	97.12%
Anchorage, AK	97.46%	New York, NY	97.12%
Juneau, AK	97.46%	Minneapolis, MN	97%
Honolulu, HI	97.46%	Oakland, CA	96.77%
Fort Worth, TX	97.46%	Los Angeles, CA	96.66%
Albuquerque, NM	97.46%	Boston, MA	96.43%
Denver, CO	97.46%	Miami ARTCC, FL	96.43%
Salt Lake City, UT	97.46%	Washington, DC	96.2%
Memphis, TN	97.46%	Chicago, IL	95.97%
Billings, MT	97.46%	Cleveland, OH	95.97%
Kansas City, MO	97.46%	Houston, TX	94.59%

Table 2.3: The loss of the CONUS coverage of LPV due to the WRS failure.

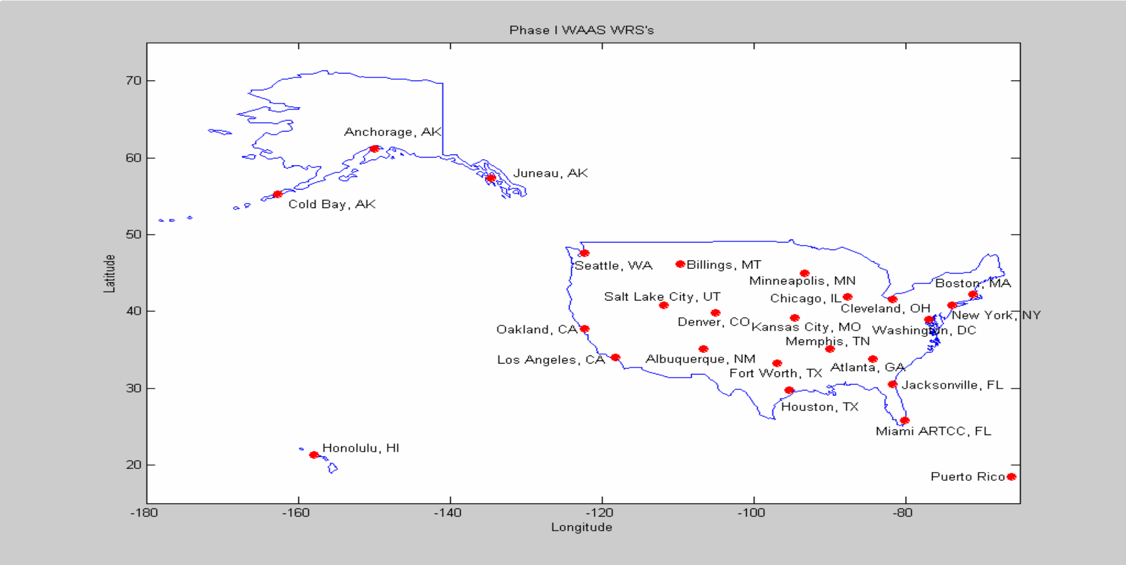

Figure 2.24: WRS locations.

The simulation results showed that a failure of the WRS at the boundary of CONUS caused more coverage loss than the failure of a WRS at the center. In reality, the failure of the

WRS is an unlikely event. The other possible source of the asset failures is the GPS satellite failure, however, this thesis does not model this failure.

2.6 CONCLUSIONS

This chapter provided WAAS background and a WAAS availability simulation tool, MAAST. The benefits of the WAAS operation for an L1 single-frequency user also are demonstrated in this chapter by using MAAST. Later chapters use the protection level calculation presented in this chapter as a background to derive the new protection level calculations for an L1-L5 dual-frequency GPS/WAAS user (Chapter 3), an L5 single-frequency GPS/WAAS user (Chapter 4), an L1-L2 dual-frequency GPS/WAAS user (Chapter 5), an L2-L5 dual-frequency GPS/WAAS user (Chapter 5), and an L2 single-frequency GPS/WAAS user (Chapter 5). The major WAAS benefit to the aircraft approach and landing is to lower the Decision Height (DH), that is, lower the landing minimum which will enable an aircraft to operate in more adverse visibility conditions.

Chapter 3

Nominal Performance of WAAS Using L1 and L5 Frequencies

3.1 INTRODUCTION

GPS currently has two frequencies L1 (1575.42 MHz) and L2 (1227.6 MHz), but only L1 has civil code (C/A) on it. Modernized GPS will have a new frequency L5 (1176.45 MHz), and all three frequencies will have civil codes on them. Figure 1.9 (page 13) shows this configuration and includes C/A on L1, C/A or CS (C) on L2, and C (I5) on L5 [ICD-GPS-705]. Both L1 and L5 are for civil aviation safety-of-life services, and only L1 and L5 are in the Aeronautical Radio Navigation Services (ARNS) protection band. L2 is for non-safety critical applications even though many would like to promote its use for civil aviation [Fontana2]. The use of modernized GPS is expected to enhance the performance (accuracy, integrity, continuity, availability) of the existing GPS.

The current WAAS Master Station (WMS) algorithms use the coded L1 signal and codeless L2 signal to generate the corrections. The current WAAS user algorithms are designed for an L1-only single-frequency user. For modernized GPS, there are three civil coded GPS signals: L1, L2, and L5. Since L1 and L5 are for civil aviation safety-of-life services, the WMS will use these signals to generate the corrections, and the WAAS airborne user will also be an L1-L5 dual-frequency user. This thesis discusses civil aviation applications. Therefore, the nominal system is the L1-L5 dual frequency GPS/WAAS.

This chapter is organized as follows. Section 3.2 discusses the issues of using the L1-L5 dual-frequency GPS. This section first discusses the dual-frequency hardware group delays and then discusses the necessary changes in the WAAS protection level calculation for an L1-L5 dual-frequency GPS/WAAS user. The modified MAAST simulation results for an L1-L5 dual-frequency user are shown in Section 3.3. Section 3.4 presents a summary and concluding remarks.

3.2 L1-L5 DUAL-FREQUENCY USER

An L1-L5 dual-frequency user can directly estimate the ionospheric delay in the airplane, and then subtract this estimate from the pseudorange measurement. This direct use of dual-frequency will be more accurate and offer higher availability. The current WAAS protection level calculation, as shown in Figure 2.10 (page 41), needs to be modified for an L1-L5 dual-frequency user. The new WAAS protection level calculation for an L1-L5 dual-frequency user is summarized in Figure 3.1. Figure 3.1 also shows the section number where the new confidence estimates for the corrections are derived.

In comparison with the current protection level calculation defined in the WAAS MOPS, the changes in this calculation for an L1-L5 dual-frequency user are yellow highlighted in Figure 3.1 and summarized as follows:

- The new calculation of the fast and long term correction degradation confidence ($\sigma_{i,flt}$) includes the confidence of the satellite L1-L5 group delay (σ_{SV_L1L5}) in the UDRE calculation. The satellite L1-L5 group delay will be discussed in Section 3.2.1, and the new UDRE calculation will be discussed in Section 3.2.3.

- The new calculation of the user ionosphere range error confidence ($\sigma_{i,UIRE\_L1L5}$) will be specified in Section 3.2.2.

- There is no separate airborne receiver confidence ($\sigma_{i,air}$) term in the protection level calculation for the L1-L5 dual-frequency GPS user because it is already included in the new $\sigma_{i,UIRE\_L1L5}$ calculation. This issue will be discussed in Section 3.2.2.

- The calculation of the tropospheric delay confidence ($\sigma_{i,tropo}$) is the same as defined in the WAAS MOPS for an L1-L5 dual-frequency GPS user.

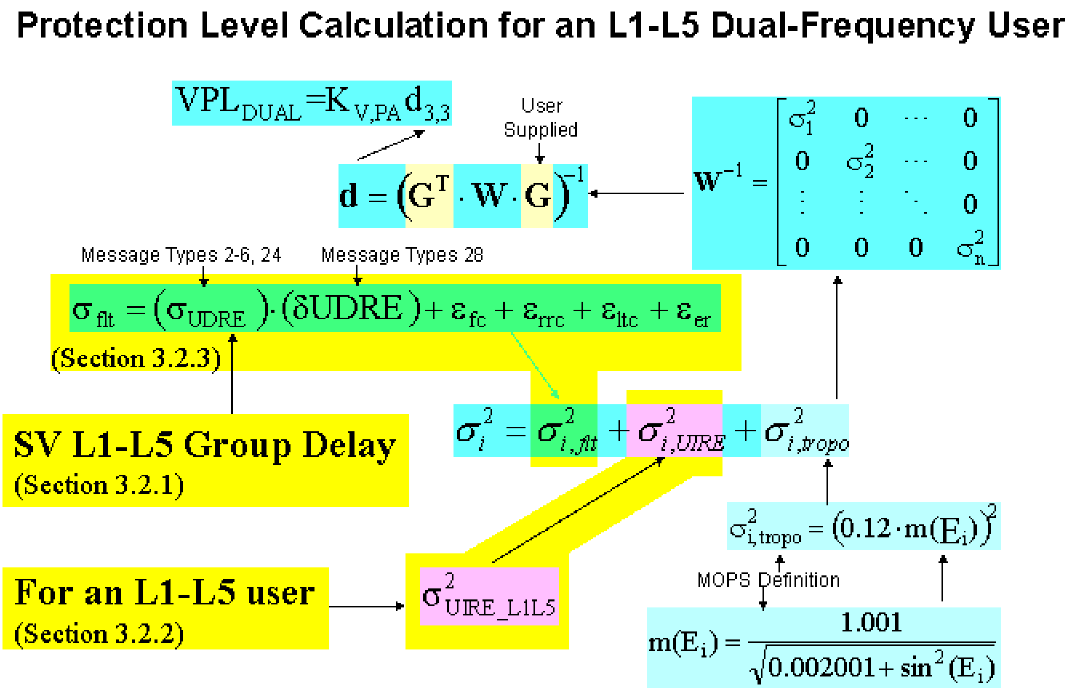

Figure 3.1: Summary of changes in the protection level calculation for an L1-L5 dual-frequency user. Only the yellow highlighted portion is changed, the other terms are unchanged as defined in the WAAS MOPS.

In order to show the improvement in availability, this thesis first examines the observation equations for three GPS frequencies. The three observation equations are shown in Equations (3.1)-(3.3).

$$\rho_{L1} = R_j^i + b_j - B^i + I_j^i + T_j^i + M_j^i + \nu_j^i \tag{3.1}$$

$$\rho_{L2} = R_j^i + b_j - B^i + \gamma_{1,2}\left(I_j^i + \tau_{gd1,2}^i\right) + IFB_{j1,2} + T_j^i + M_j^i + \nu_j^i \tag{3.2}$$

$$\rho_{L5} = R_j^i + b_j - B^i + \gamma_{1,5}\left(I_j^i + \tau_{gd1,5}^i\right) + IFB_{j1,5} + T_j^i + M_j^i + \nu_j^i \tag{3.3}$$

where,

ρ_{Li} is pseudorange measurement at *Li* frequency

R_j^i is true range from satellite *i* to user *j*

b_j is receiver offset from UTC

B^i is satellite clock offset from UTC

I is ionospheric delay

T is tropospheric delay

M is multipath delay

ν is thermal noise

$\tau_{gd1,2}$ is satellite L1-L2 hardware group delay

$\tau_{gd1,5}$ is satellite L1-L5 hardware group delay

$IFB_{1,2}$ is receiver L1-L2 hardware group delay

$IFB_{1,5}$ is receiver L1-L5 hardware group delay

$$\gamma_{1,2} = \left(\frac{f_1^2}{f_2^2} \right) = 1.65$$

$$\gamma_{1,5} = \left(\frac{f_1^2}{f_5^2} \right) = 1.80$$

The differences in these three observation equations are the ionospheric delays, the satellite hardware group delays, and the user receiver hardware group delays. To investigate the L1-L5 dual-frequency user case, this thesis first discusses these differences in the following sections.

3.2.1 DUAL-FREQUENCY HARDWARE GROUP DELAYS

The hardware group delay is defined as the time required for the signal to travel through a device or transmission medium (Federal Standard 1037C). For example, the satellite hardware group delay is the delay between the L-band radiated output of a specific satellite and the output of that satellite's on-board frequency source [ICD-GPS-200C]. There are three hardware group delays in the WAAS: satellite hardware group delay, WRSs receiver hardware group delay, user avionics hardware group delay.

A notional representation of the satellite group delay difference (τ_{gd}) between the radiated L1, L2, and L5 signals (i.e., L1 P(Y) and L2 P(Y), L1 P(Y) and L1 C/A, L1 P(Y) and L2 CS, L1 P(Y) and L5 I5, L1 P(Y) and L5 Q5) is shown in Figure 3.2. The corrections for the group delay differential are provided to the users in the Navigation message using parameters designated as τ_{gd} [ICD-GPS-200C] and Inter-Signal Correction (ISC) [ICD-GPS-705].

According to [ICD-GPS-200C], the mean group delay difference between the L1 P(Y) and L2 P(Y) signals is less than 15 nanoseconds and the effective uncertainty about the mean is less than 3 nanoseconds (two sigma, i.e. a 95% error bound). All transmitted signals for a particular satellite shall be coherently derived from the same on-board frequency standard, while all digital signals shall be clocked in coincidence with the PRN transitions for the P-signal and occur at the P-signal transition speed. On the L1 channel the data transitions of two modulating signals (P(Y) and C/A) shall be such that the average time difference between the transitions does not exceed 10 nanoseconds (two sigma).

[ICD-GPS-705 rev. March 2002]

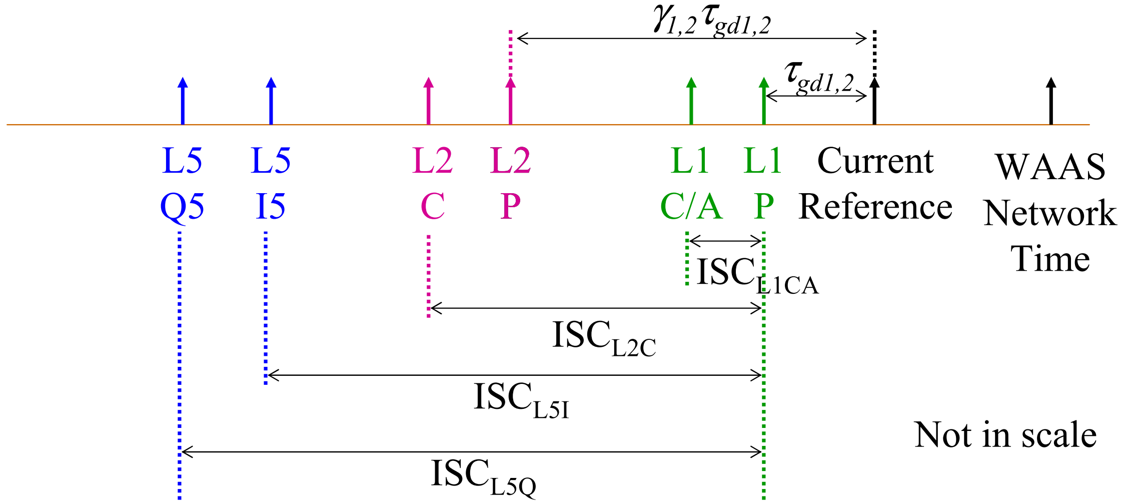

ISC: Inter-signal Correction

Figure 3.2: Satellite hardware group delay [ICD-GPS-705].

The software calibration methods of the hardware group delay are specified in [Chao] and [Hansen]. The hardware group delay is estimated as follows. First, fit a model to the true ionosphere. Second, filter the measurements through the model to separate the ionospheric delays from the hardware group delay. These steps collect large numbers of ionospheric delay measurements and leverage the redundancy of the *IFB* and τ_{gd} terms to isolate them from the ionosphere, multipath, and thermal noise terms [Hansen].

In order to calculate the confidence of τ_{gd}, we use Equation (3.4) to estimate the ionospheric delay on L1 from an L1-L5 dual-frequency receiver by taking the difference of the pseudorange measurements in Equations (3.1) and (3.3).

$$\tilde{I}^{i}_{j,L1} = \frac{\rho_{L5}-\rho_{L1}}{\gamma_{1,5}-1} = I^{i}_{j} + \frac{\gamma_{1,5}}{\gamma_{1,5}-1}\left(\tau^{i}_{gd1,5}\right) + \frac{1}{\gamma_{1,5}-1}\left(IFB_{j1,5}\right) \tag{3.4}$$

Similarly, the ionospheric delays on L2 and L5 can be estimated. Thus, we can form a state space equation as follows.

$$A\tilde{X} = \tilde{I} = \begin{bmatrix} \dfrac{\rho_{L2}-\rho_{L1}}{\gamma_{1,2}-1} \\ \dfrac{\rho_{L5}-\rho_{L1}}{\gamma_{1,5}-1} \\ \dfrac{\rho_{L5}-\rho_{L2}}{\gamma_{2,5}-1} \end{bmatrix} \tag{3.5}$$

where,

$$A = \left[\begin{array}{cccc|cccc|cccc} A_{00} & \cdots & \cdots & A_{0N} & \dfrac{1}{\gamma-1} & 0 & 0 & \cdots & \dfrac{\gamma}{\gamma-1} & 0 & \cdots & 0 \\ A_{10} & & & A_{1N} & \dfrac{1}{\gamma-1} & 0 & 0 & \cdots & 0 & \dfrac{\gamma}{\gamma-1} & & 0 \\ \vdots & & & \vdots & & & & & \vdots & & \ddots & \\ A_{M0} & & & A_{MN} & 0 & 0 & \cdots & \dfrac{1}{\gamma-1} & 0 & 0 & \cdots & \dfrac{\gamma}{\gamma-1} \end{array}\right] \tag{3.6}$$

$$\tilde{X} = \left[N_{e_0} \quad \cdots \quad N_{e_N} \quad \middle| IFB_0 \quad \cdots \quad IFB_R \middle| \quad \tau^{0}_{gd} \quad \cdots \quad \tau^{S}_{gd} \right]^{T} \tag{3.7}$$

where,

A_{ij} is an element of the observation matrix which maps the electron density model to the ionospheric delay ($\tilde{I}$)

N_{e_i} is the variable electron density along the signal path [Misra&Enge] [Hansen]

As mentioned above, the hardware group delay calibration must separate the ionosphere portion of the measurements from the satellite and receiver group delays by taking repeated measurements as the satellites orbit and Earth rotates. It then stacks measurements and the corresponding observation matrices over time. To obtaining a quality calibration, we must collect enough measurements over time for the hardware group delay states to be fully determined. That is, the calibration process determines a mean fit to the electron density model. As the line of sight rotates into the reconstructed electron density, the ionospheric component is subtracted out [Hansen]. In mathematical operations we are solving the least squares problem,

$$X = pinv(A)\tilde{I} \tag{3.8}$$

where, the *pinv(.)* is the pseudo-inverse operation of a matrix.

$$pinv(A) = (A^T A)^{-1} A^T \tag{3.9}$$

The covariance matrix of Equation (3.8) gives the residual error of the estimation,

$$\Sigma_X = pinv(A)\Sigma_{\tilde{I}}\, pinv(A)^T \tag{3.10}$$

To calculate the dependence of the confidence of satellite hardware group delay (τ_{gd}) estimation error on frequency, the third block in A of Equation (3.6) is a diagonal matrix with the element of $\left(\frac{\gamma}{\gamma-1}\right)$. As a result, the first and last terms in the right side of Equation (3.10) will generate a coefficient of $\left(\frac{\gamma-1}{\gamma}\right)^2$. Also in the right side of Equation (3.5), there is a factor of $\left(\frac{1}{\gamma-1}\right)$. Therefore, $\Sigma_{\tilde{I}}$ will have a factor of $\left(\frac{1}{\gamma-1}\right)^2$. This is detailed in Figure 3.3.

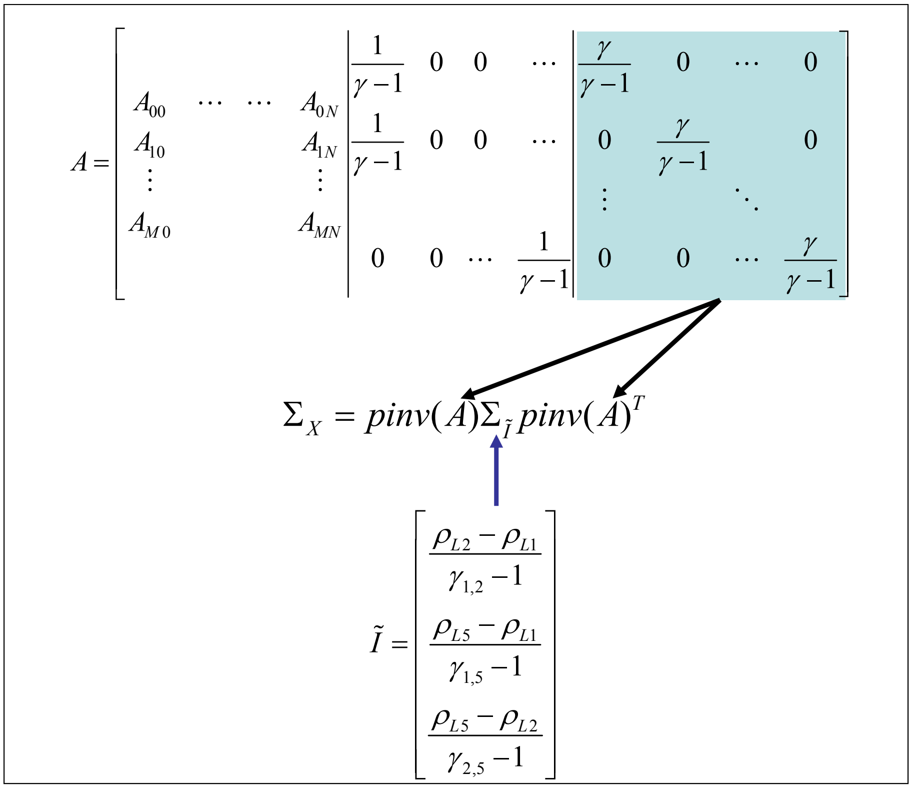

Figure 3.3: The confidence of the satellite hardware group delay (τ_{gd}).

Combine all the coefficients and factors of Equation (3.10) together to determine that confidence of the satellite hardware group delay (τ_{gd}) is proportional to

$$\left(\frac{\gamma-1}{\gamma}\right)\left(\frac{1}{\gamma-1}\right)^2\left(\frac{\gamma-1}{\gamma}\right)=\left(\frac{1}{\gamma}\right)^2 \tag{3.11}$$

That is,

$$\left(\frac{1}{\gamma_{1,2}}\right)^2=0.3687,\ \left(\frac{1}{\gamma_{1,5}}\right)^2=0.3110,\ \left(\frac{1}{\gamma_{2,5}}\right)^2=0.8435 \tag{3.12}$$

Based on the current observed performance, the confidence of the satellite L1-L2 group delay estimation error (σ_{SV_L1L2}) is 0.192m. Therefore, the confidence of the satellite L1-L5 group delay estimation error is

$$\sigma_{SV\_L1L5} = 0.192 * \sqrt{\frac{\left(\frac{1}{\gamma_{1,5}}\right)^2}{\left(\frac{1}{\gamma_{1,2}}\right)^2}} = 0.176(\mathrm{m}) \tag{3.13}$$

Similarly, the confidence of the satellite L2-L5 group delay estimation error is

$$\sigma_{SV\_L2L5} = 0.192 * \sqrt{\frac{\left(\frac{1}{\gamma_{2,5}}\right)^2}{\left(\frac{1}{\gamma_{1,2}}\right)^2}} = 0.290(\mathrm{m}) \tag{3.14}$$

As a result, the confidence bounds of the satellite hardware group delay estimation errors have the same characteristic as the dual-frequency ionospheric delay estimations.

The user receiver hardware group delay (*IFB*) can be calibrated using two methods: 1) factory calibrations, and 2) software calibrations. This thesis assumes that the user receiver receives at least one satellite with two GPS frequencies. The user receiver hardware group delay can then be calibrated out as mentioned above. However, this thesis does not model the user receiver hardware group delay (*IFB*) errors.

In the next section, we will investigate how the confidence of the satellite hardware group delay (τ_{gd}) affects the UIRE calculation for a dual-frequency user. The subsequent section discusses the effect of the confidence of the satellite hardware group delay (τ_{gd}) on the UDRE calculation for a dual-frequency user.

3.2.2 NEW UIRE CALCULATION

The User Ionosphere Range Error (UIRE) is a confidence bound on the residual error of the ionospheric delay estimation, and is described in Section 2.2.1.1 or in the WAAS MOPS. The current UIRE calculation is designed for an L1-only single-frequency user. Ionospheric delay is different for the different GPS transmission frequencies, as shown in the observation Equations (3.1)-(3.3).

As discussed in Section 2.2.1.1, the ionospheric delays can be estimated directly by taking the difference of the pseudorange measurements between two frequencies. For example, an L1-L5 dual-frequency user can estimate the ionospheric delay directly in the airplane, and then subtract this estimation from the pseudorange measurements. Equation (3.4) calculates the ionospheric slant delay on L1 from an L1-L5 dual-frequency receiver. It is repeated below.

$$\tilde{I}^i_{j,L1} = \frac{\rho_{L5} - \rho_{L1}}{\gamma_{1,5} - 1} = I^i_j + \frac{\gamma_{1,5}}{\gamma_{1,5} - 1}\left(\tau^i_{gd1,5}\right) + \frac{1}{\gamma_{1,5} - 1}\left(IFB_{j1,5}\right) \tag{3.4}$$

There are three factors which affect the quality of the L1-L5 dual-frequency ionospheric delay estimation, as shown in Equation (3.4):

- The receiver noise and multipath errors of the L1-L5 dual-frequency receiver.
- The satellite L1-L5 hardware group delay error (τ_{gd}).
- The receiver L1-L5 hardware group delay error (IFB).

As mentioned in the previous section, this thesis does not model the receiver L1-L5 error (IFB). The receiver IFB term is not needed as it falls into the clock when all satellites use the same frequency combination. However, the mixing frequencies (e.g., PRN 1 is L1-L5, but PRN 2 is L1 only) then an IFB term is required for all but one of the combinations. The confidence model of the satellite L1-L5 group delay estimation (σ_{SV_L1L5}) is also given in the previous section. The confidence model of the residual error of the receiver noise and multipath errors ($\sigma_{i,air}$) is given in Section 2.2.2. The additional assumption in this section is that the noises (errors) of the different measurements are uncorrelated. The ionosphere-free pseudorange measurement is provided in Equation (3.15) [Misra&Enge], the confidence of the residual receiver noise and multipath errors for an L1-L5 dual-frequency receiver can be calculated by Equation (3.16).

$$\rho_{iono-free} = \left[\frac{f_1^2}{f_1^2 - f_5^2}\right]\left[\rho_{L1}\right] - \left[\frac{f_5^2}{f_1^2 - f_5^2}\right]\left[\rho_{L5}\right] \tag{3.15}$$

$$\sigma_{L1L5}^2 = \left[\frac{f_1^2}{f_1^2 - f_5^2}\right]^2 \left[\sigma_{air,L1}^2\right] + \left[\frac{f_5^2}{f_1^2 - f_5^2}\right]^2 \left[\sigma_{air,L5}^2\right] \tag{3.16}$$

As mentioned above, the other factor (error source) that contributes to the measured differential delay between L1 and L5 is the satellite hardware group delay ($\tau_{gd,1,5}$). The quality of the estimation of $\tau_{gd,1,5}$ also affects the quality of the L1-L5 dual-frequency ionosphere delay estimation. As a result, this thesis derives Equation (3.17) to measure the quality (confidence) of the L1-L5 dual-frequency ionospheric delay estimation.

$$\sigma_{UIRE\_L1L5}^2 = \left[\frac{f_1^2}{f_1^2 - f_5^2}\right]^2 \left[\sigma_{air,L1}^2\right] + \left[\frac{f_5^2}{f_1^2 - f_5^2}\right]^2 \left[\sigma_{air,L5}^2\right] + \left[\sigma_{SV\_L1L5}^2\right] \tag{3.17}$$

where,

σ_{UIRE_L1L5} is the confidence of the L1-L5 dual-frequency ionospheric delay estimation

f_i is GPS frequency, $i = 1$: L1, $i = 5$: L5

$\sigma_{air,Li}$ is the confidence of the user receiver noise and multipath errors, $i = 1$: L1, $i = 5$: L5, which is a function of satellite elevation angle and described in Section 2.2.2

σ_{SV_L1L5} is the confidence of the satellite L1-L5 hardware group delay

Similarly, the qualities (confidence) of the L1-L2 and L2-L5 dual-frequency ionospheric delay estimations can be calculated by Equations (3.18) and (3.19), respectively.

$$\sigma^2_{UIRE\_L1L2} = \left[\frac{f_1^2}{f_1^2 - f_2^2}\right]^2 \left[\sigma^2_{air,L1}\right] + \left[\frac{f_2^2}{f_1^2 - f_2^2}\right]^2 \left[\sigma^2_{air,L2}\right] + \left[\sigma^2_{SV\_L1L2}\right] \tag{3.18}$$

$$\sigma^2_{UIRE\_L2L5} = \left[\frac{f_2^2}{f_2^2 - f_5^2}\right]^2 \left[\sigma^2_{air,L2}\right] + \left[\frac{f_5^2}{f_2^2 - f_5^2}\right]^2 \left[\sigma^2_{air,L5}\right] + \left[\sigma^2_{SV\_L2L5}\right] \tag{3.19}$$

where,

σ_{UIRE_L1L2} is the confidence of the L1-L2 dual-frequency ionospheric delay estimation

σ_{SV_L1L2} is the confidence of the satellite L1-L2 hardware group delay

σ_{UIRE_L2L5} is the confidence of the L2-L5 dual-frequency ionospheric delay estimation

σ_{SV_L2L5} is the confidence of the satellite L2-L5 hardware group delay

The two coefficients, $\left[\frac{f_i^2}{f_i^2 - f_j^2}\right]^2$ called *C1* and $\left[\frac{f_j^2}{f_i^2 - f_j^2}\right]^2$ called *C2*, in Equations (3.17), (3.18), and (3.19), depend on the separation between two GPS frequencies. As shown in Figure 3.4, the *C1* and *C2* for the L2-L5 dual-frequency user are much larger than the *C1* and *C2* for the L1-L2 and L1-L5 dual-frequency users, because of the much narrower separation between the L2 and L5 frequencies. Therefore, the confidence of the L2-L5 dual-frequency ionospheric delay estimation will not be as good as other dual-frequency users.

$$\sigma^2_{DUAL\_LiLj} = \underbrace{\left[\frac{f_i^2}{f_i^2 - f_j^2}\right]^2}_{C1} \left[\sigma^2_{air,Li}\right] + \underbrace{\left[\frac{f_j^2}{f_i^2 - f_j^2}\right]^2}_{C2} \left[\sigma^2_{air,Lj}\right] + \left[\sigma^2_{SV\_LiLj}\right]$$

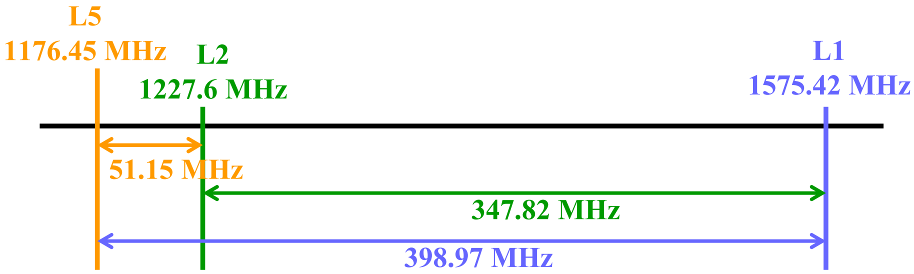

Dual-frequency user	C1	C2
L2-L5	150	127
L1-L2	6.5	2.4
L1-L5	5.1	1.6

Figure 3.4: The confidence of the dual-frequency ionospheric delay estimation depends on the separation between two GPS frequencies. The *C1* and *C2* for the L2-L5 dual-frequency user are much larger than the C1 and C2 for the L1-L2 and L1-L5 dual-frequency users, because of the narrow separation between the L2 and L5 frequencies.

For an L1-L5 dual-frequency user, the Equation (3.17) will be used as the UIRE calculation to replace the current UIRE calculation defined in the WAAS MOPS.

As shown in Equation (3.17), the confidence of the residual airborne receiver noise and multipath errors is already included in the calculation of the L1-L5 dual-frequency user ionosphere range error confidence. Thus, there is no additional term needed in the protection level calculation for the airborne receiver confidence for an L1-L5 dual-frequency user.

WAAS will broadcast the old GIVE (UIRE) message to protect legacy users, as well as new τ_{gd} parameters needed to adjust the UIRE to protect the new dual-frequency user.

3.2.2 NEW UDRE CALCULATION

The User Differential Range Error (UDRE) is a 10^{-7} error bound on the satellite ephemeris and clock correction errors, and is described in Section 2.2.1.2 and the WAAS MOPS. The current UDRE calculation is designed for an L1-only single frequency user. For an L1-L5 dual-frequency user, the estimation error of the satellite L1-L5 group delay needs to be taken into account for the UDRE calculation. The satellite L1-L5 group delay ($\tau_{gd,1,5}$) is caused by the group delay differences between the L1 and L5 transmission chains on the satellite [ICD-GPS-705] [ICD-GPS-200C]. The calculation of the confidence of the satellite hardware group delay estimation error is given in Section 3.2.1.

The current UDRE calculation used the confidence of the satellite L1-L2 group delay estimation error. The modernized UDRE calculation should include the confidence of all possible group delays estimation errors for all potential users, that is, L1-L5, L1-L2, and L2-L5 dual-frequency users.

The new UDRE calculation will include the confidence of the satellite group delay estimation errors, σ_{SV_L1L2}, σ_{SV_L1L5}, and σ_{SV_L2L5}, to protect the L1-L2, L1-L5, and L2-L5 dual-frequency users, respectively. Therefore, for an L1-L5 dual-frequency user, Equation (3.13) will be included in the new UDRE calculation.

Again, WAAS will broadcast the old UDRE message to protect the legacy users, as well as the parameters needed to adjust the UDRE to protect the new dual-frequency user.

3.3 MAAST SIMULATION RESULTS

The MAAST was modified to adopt all the changes in the protection level calculation, as shown in Figure 3.1, for an L1-L5 dual-frequency user. The important parameters used in the simulation are: the 24 standard GPS satellites constellation defined in the WAAS MOPS, two GEOs (AOR-W and POR), 1-degree user grid within CONUS and 30-second time steps over a 24-hour simulation period. The other important parameters used in the simulation are VAL = 50m, and HAL = 40m (LPV). These simulation parameters are summarized in Table 3.1.

Satellite Constellation	GEO	User	Time Step	VAL	HAL
24 standard GPS satellites (WAAS MOPS)	2 GEOs (AOR-W, POR)	1-degree user grid within CONUS	30-second over a 24-hour period	50 m	40 m

Table 3.1: The MAAST simulation configuration used in Chapter 3-6.

The simulation results for the L1-L5 dual-frequency user are shown in Figures 3.5-3.7. Figure 3.5 is the LPV CONUS coverage simulation result, which shows that an L1-L5 dual-frequency user has LPV precision approach services available 99.9% of the time over 100% of CONUS. Figure 3.6 shows the VPL contour for an L1-L5 user in CONUS, and Figure 3.7 shows the HPL contour for an L1-L5 user in CONUS. The 99.9% shown in Figures 3.5-3.7 represents the fraction of users within those regions that had an availability of 99.9% or greater.

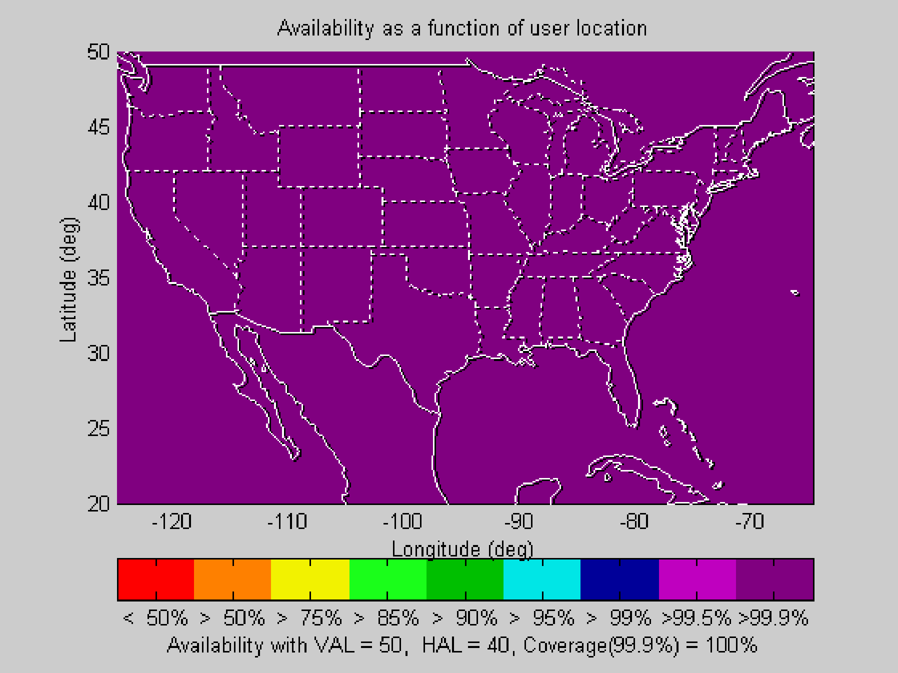

Figure 3.5: Coverage of an L1-L5 dual-frequency user in CONUS is 100% with VAL = 50m, HAL = 40m.

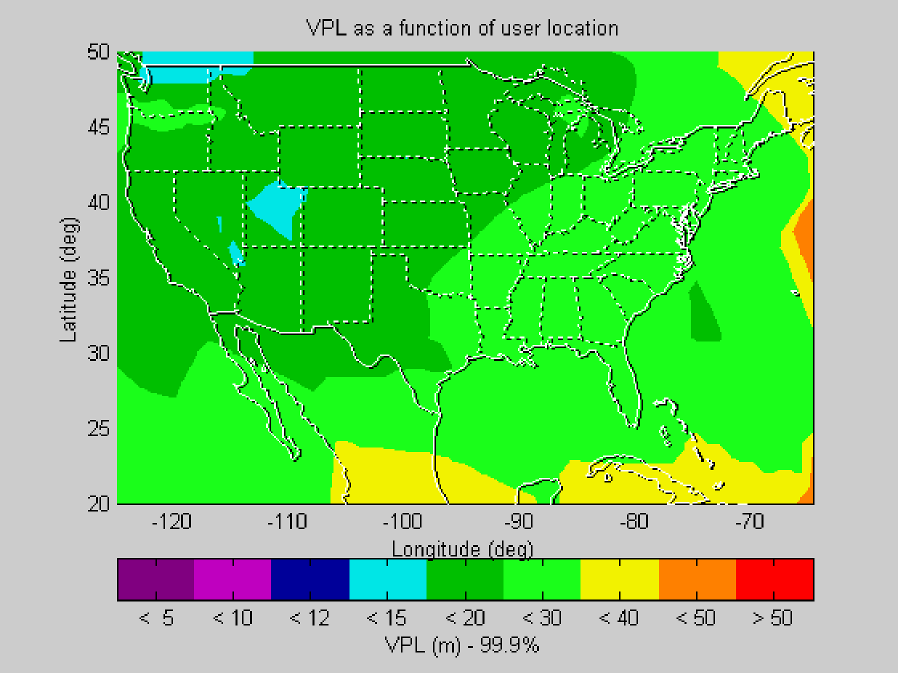

Figure 3.6: Vertical Protection Level (VPL) contour of an L1-L5 dual-frequency user in CONUS.

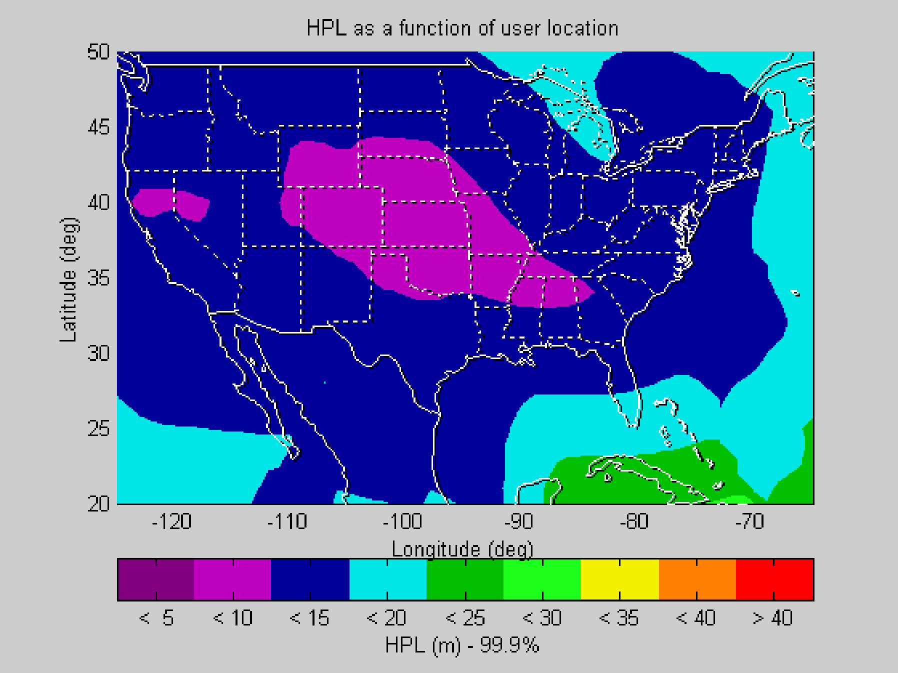

Figure 3.7: Horizontal Protection Level (HPL) contour of an L1-L5 dual-frequency user in CONUS.

3.4 CONCLUSIONS

This chapter first discussed the dual-frequency hardware group delays for the different dual-frequency users, and then computed the confidence bounds on the satellite hardware group delay estimation errors. The confidences of the different satellite dual-frequency hardware group delay estimation errors must be included in the WAAS protection level calculation to provide integrity to the different dual-frequency users.

The model of the WAAS Master Station (WMS) algorithm was changed to use L1 and L5 to generate corrections for the satellite clock and ephemeris errors and the ionospheric delays. The new WAAS protection level calculation for an L1-L5 dual-frequency user is derived in this chapter. First, because the L1-L5 dual-frequency user can estimate the ionospheric delay directly, the new confidence calculation of the User Ionosphere Range Error (UIRE) is derived, which included the new dual-frequency user ionosphere range error confidence, $\sigma_{i,UIRE}$, and the airborne receiver confidence ,$\sigma_{i,air}$. Second, the new confidence calculation of the User Differential Range Error (UDRE) was derived. For example, the new UDRE calculation included the confidence of the satellite L1-L5 group delay estimation error, σ_{SV_L1L5}, to protect the L1-L5 dual-frequency users.

The MAAST coverage simulation results in this chapter show that an L1-L5 dual-frequency user has LPV precision approach services available 99.9% of the time over 100% of CONUS, as summarized in Table 3.2.

User Type	CONUS Coverage of LPV precision approach services (Availability ≥ 99.9%)	VPL (in meter)	HPL (in meter)
L1-L5 dual-frequency	100%	12 ≤ VPL < 40	5 ≤ HPL < 20

Table 3.2: The MAAST simulation results.

Chapter 4

Robust Reversion from Dual to Single Frequency WAAS in the Presence of Radio Frequency Interference

4.1 INTRODUCTION

GPS is a space-to-earth signal and the received signal power is -160 dBW. This low power level makes GPS highly susceptible to interference. It presently serves around 10 million users in sea, air, terrestrial, and space applications. Many of these applications are safety-of-life operations. For example, GPS is used to guide ships while approaching harbor and navigating within narrow waterways. GPS also provides guidance in terrestrial emergency applications, such as ambulances and police cars, while they conduct their critical missions. In addition, GPS will serve many aviation applications including the most demanding phase of flight – aircraft approach and landing. Most aircraft approach operations allow no more than one missed approach per 100,000 landings. Today, radio frequency interference (RFI) is the single greatest threat to this continuity of service [APL] [Volpe] [RTCA3].

This chapter shows the MAAST simulation results for users with only one available GPS frequency. Furthermore, this chapter discusses the possible techniques which provide robust reversion from dual to single frequency WAAS. The goal is to provide the techniques necessary for single-frequency users to sustain a performance similar to dual-frequency users. The proposed techniques are: 1) The code and carrier divergence technique, 2) The WAAS ionosphere threat model technique, and 3) The maximum ionospheric delay gradient model technique. Additionally, any RFI to GPS must invoke a fast location and removal response. In Appendix B an approach is presented to estimate the location of an RFI source. This approach is based on deploying a network of sensors to assist with location estimation.

This chapter is organized as follows. Section 4.2 discusses the necessary changes in the WAAS protection level calculation for the L1-only and L5-only single-frequency GPS/WAAS users. The corresponding MAAST simulation results for the L1-only and L5-only single-frequency users are also included in this section. The techniques for graceful reversion from dual to single frequency WAAS and the required conditions for using these techniques are discussed in Section 4.3. This section includes a typical precision approach example based on San Francisco International Airport (SFO). The MAAST simulation results for the code and carrier divergence technique, the WAAS ionosphere threat model technique, and the maximum ionospheric delay gradient model technique are also given in Section 4.3. Section 4.4 presents a summary and concluding remarks.

4.2 SINGLE-FREQUENCY USER

While experiencing RFI, an L1-L5 dual-frequency GPS/WAAS user might lose all but one GPS frequency, which would introduce L1-only and L5-only single-frequency user cases. These cases will be discussed in this section.

4.2.1 L1-ONLY SINGLE-FREQUENCY GPS/WAAS USER

An L1-only single-frequency user will rely on WAAS to provide corrections to various GPS error sources, such as, corrections to the satellite clock and ephemeris errors, and corrections to the group delays due to the ionosphere. Furthermore, an L1-only single-frequency airborne user is required to use WAAS for precision approaches. The protection level calculation for an L1-only single-frequency GPS/WAAS user is specified in Chapter 2 and is detailed in the WAAS MOPS [RTCA1].

4.2.2 L5-ONLY SINGLE-FREQUENCY GPS/WAAS USER

An L5-only single-frequency user will also rely on WAAS to provide corrections to various GPS error sources, and an L5-only single-frequency airborne user is also required to use WAAS for precision approaches. However, the current WAAS corrections are specified for L1 only. The L5-only single frequency users will require some additional modifications before they can apply WAAS correction to their position-fix.

We first compare the pseudorange measurement on L5 in Equation (3.3) with the pseudorange measurement on L1 given in Equation (3.1) (both equations repeated below):

$$\rho_{L5} = R_j^i + b_j - B^i + \gamma_{1,5}\left(I_j^i + \tau_{gd1,5}^i\right) + IFB_{j1,5} + T_j^i + M_j^i + \nu_j^i \tag{3.3}$$

$$\rho_{L1} = R_j^i + b_j - B^i + I_j^i + T_j^i + M_j^i + \nu_j^i \tag{3.1}$$

The differences will be the ionospheric delays, the satellite L1-L5 hardware group delays, and user receiver L1-L5 hardware group delays.

We can estimate the ionospheric delays on L1 and L5 from a WRS L1-L5 dual-frequency receiver by using Equations (4.1) and (4.2), respectively [Misra&Enge]:

$$I_{L1} = \frac{f_{L5}^2}{\left(f_{L1}^2 - f_{L5}^2\right)}\left(\rho_{L5} - \rho_{L1}\right) \tag{4.1}$$

$$I_{L5} = \frac{f_{L1}^2}{\left(f_{L1}^2 - f_{L5}^2\right)}\left(\rho_{L5} - \rho_{L1}\right) \tag{4.2}$$

Comparing I_{L1} with I_{L5}, yields

$$\frac{I_{L5}}{I_{L1}} = \frac{f_{L1}^2}{f_{L5}^2} = \gamma_{1,5} = 1.80 \tag{4.3}$$

In Equation (3.3), $\gamma_{1,5}$ is the square of the frequency ratio (i.e., f_1^2 / f_5^2), which equals 1.80. Thus, the ionospheric delay on L5 is 1.80 times larger than the ionospheric delay on L1. That also means the uncertainty of the ionospheric delay estimation on L5 is 1.80 times larger than the uncertainty of the ionospheric delay estimation on L1. The same relationship could be found from the ionospheric delay estimation from a WRS L1-L5 dual-frequency receiver, as shown in Equations (4.1)-(4.3). The lower GPS frequency (L5) has larger ionospheric delay and larger ionospheric delay uncertainty. Therefore, the WAAS L1 ionospheric delay correction needs to be multiplied by 1.80 for an L5-only user, and the associated variance (confidence) needs to be multiplied by $(1.80)^2$ for an L5-only user. In the protection level calculation, the new UIRE calculation for an L5-only user is

$$\sigma_{i,UIRE\_L5}^2 = \gamma_{1,5}^2 \cdot \sigma_{i,UIRE\_L1}^2 = (1.80)^2 \cdot \sigma_{i,UIRE\_L1}^2 \tag{4.4}$$

This change of the UIRE confidence calculation is summarized in Figure 4.1.

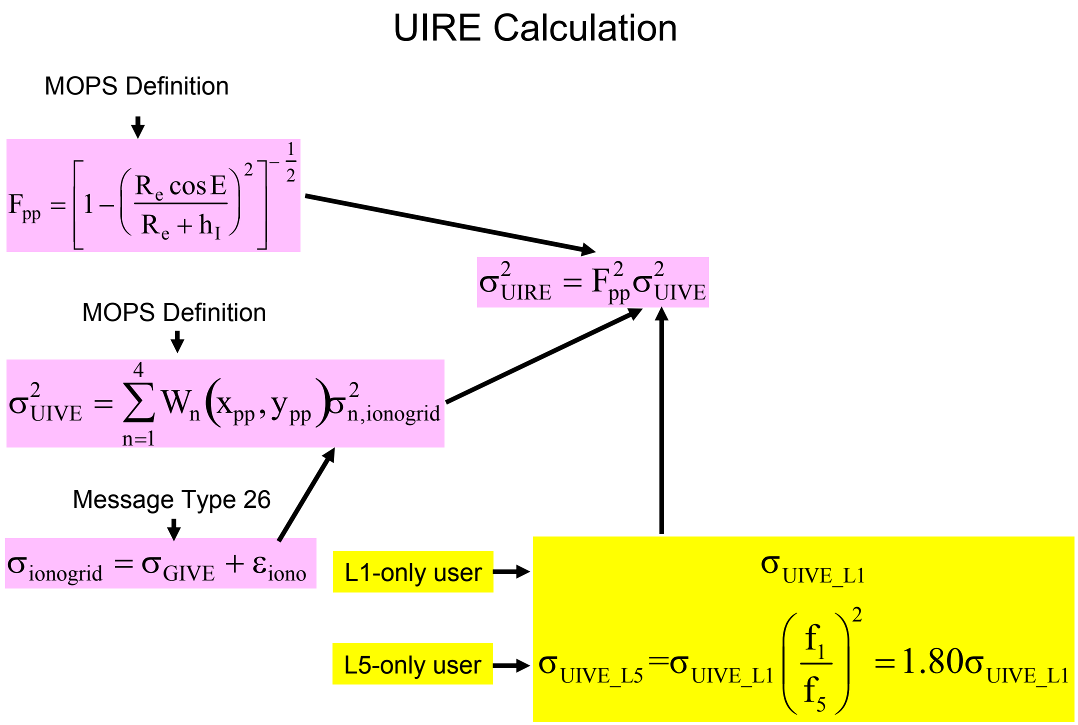

Figure 4.1: Summary of changes in User Ionosphere Range Error (UIRE) confidence calculation.

The confidence calculation of the satellite L1-L5 group delay is already included in the new UDRE calculation as described in Section 3.2.1. This thesis assumes that all three frequencies are available to the ground (WRSs), but not to the airborne user. This new UDRE model will be used for the L1-only or L5-only single frequency user.

The protection level calculation for the L1-only and the L5-only single-frequency GPS/WAAS users is summarized in Figure 4.2. The yellow highlighted portion represents the changes.

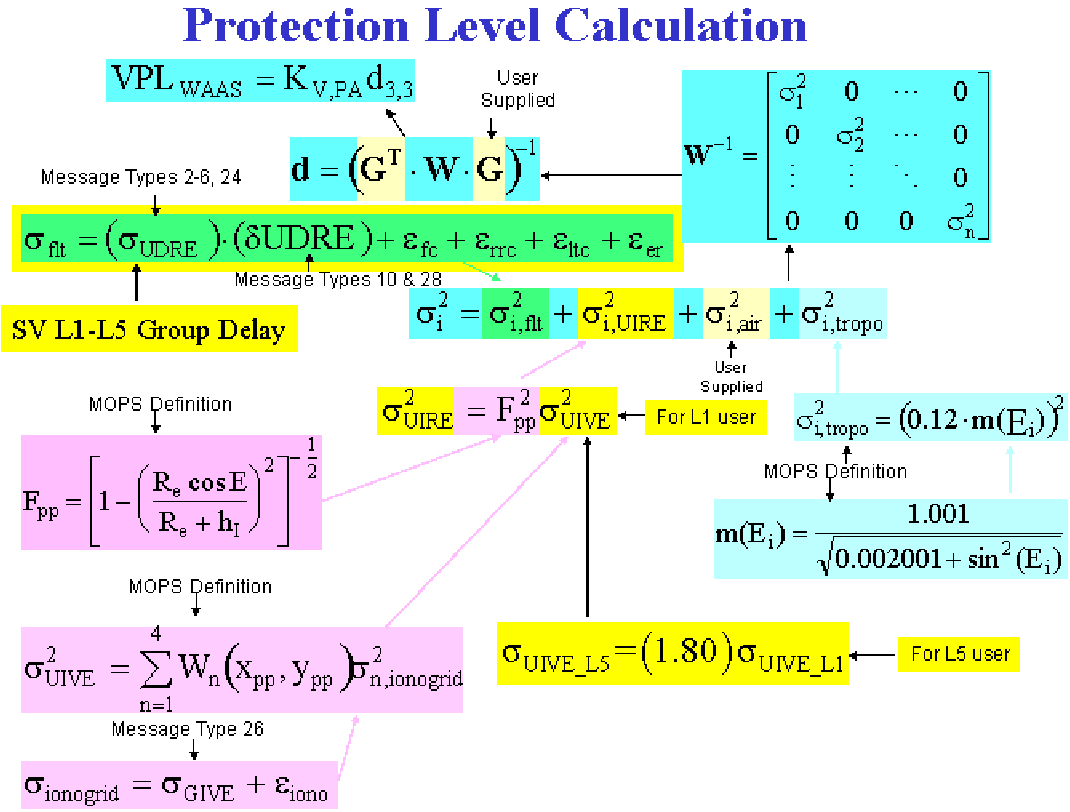

Figure 4.2: Summary of changes in the protection level calculation for the L1-only and L5-only single-frequency GPS/WAAS users, only the yellow highlighted portion is changed, the other terms are unchanged as defined in the WAAS MOPS.

4.2.3 MAAST COVERAGE SIMULATION RESULTS

This thesis modified the MAAST with the protection level calculation shown in Figure 4.2 to simulate both L1-only and L5-only single-frequency users. To be consistent and for ease of comparison in the results, the simulation configurations of MAAST will remain the same as in previous chapters (Table 3.1).

The simulation results for an L1-only single-frequency GPS/WAAS user are shown in Figures 4.3-4.5. Figure 4.3 is the LPV coverage simulation results for an L1-only single-frequency user. An L1-only single-frequency user has LPV precision approach services available 99.9% of the time over 97.58% of CONUS. Figure 4.4 shows the VPL contour for an L1-only user in CONUS, and Figure 4.5 represents the HPL contour for an L1-only user in CONUS. The 99.9% shown in Figures 4.3-4.5 represents the fraction of users within those regions that had an availability of 99.9% or greater.

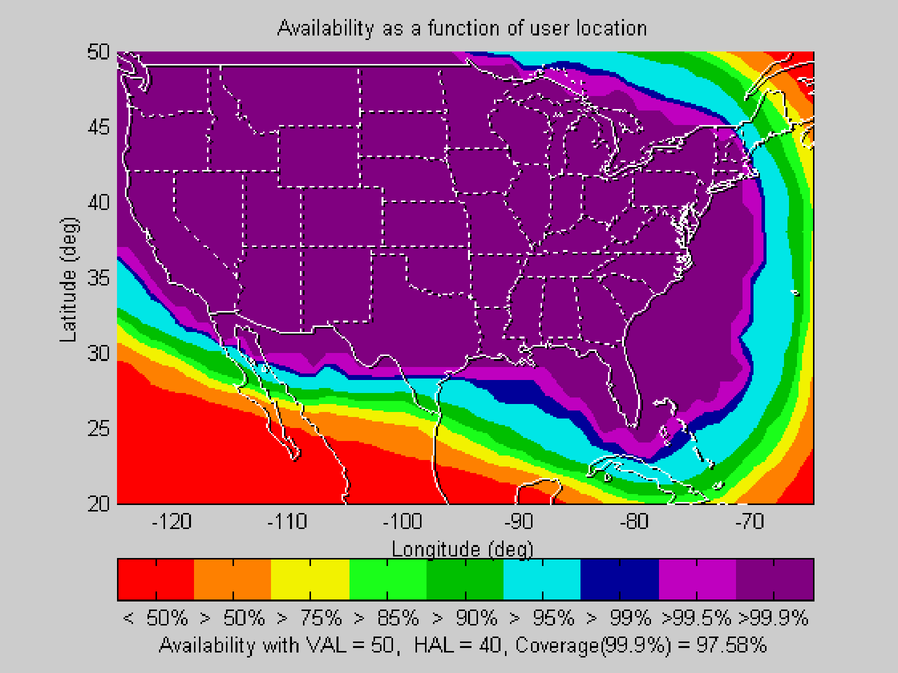

Figure 4.3: Coverage of an L1-only single-frequency GPS/WAAS user in CONUS is 97.58% with VAL = 50m, HAL = 40m.

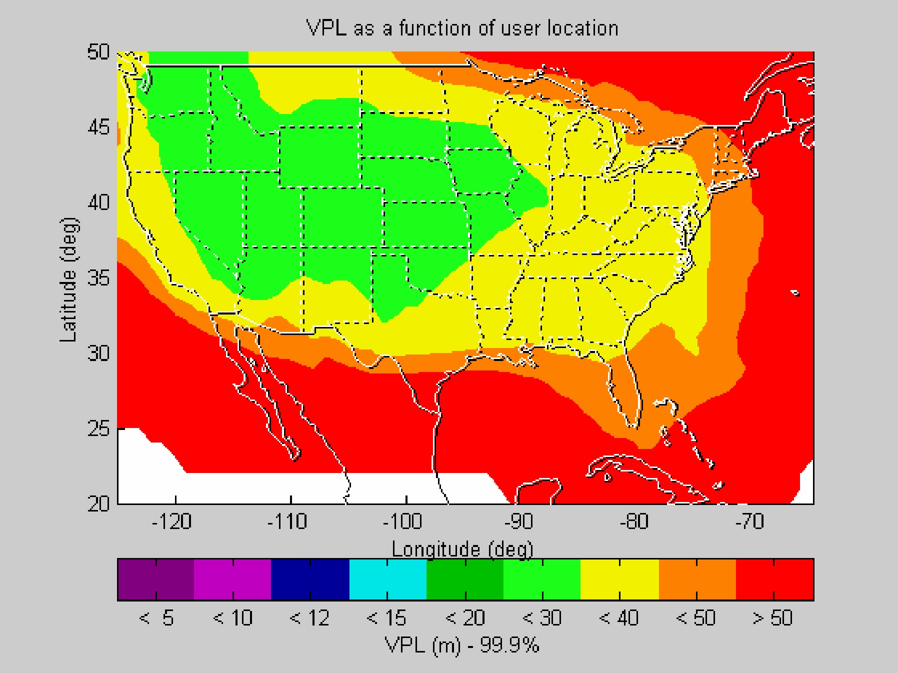

Figure 4.4: Vertical Protection Level (VPL) contour of an L1-only single-frequency GPS/WAAS user in CONUS.

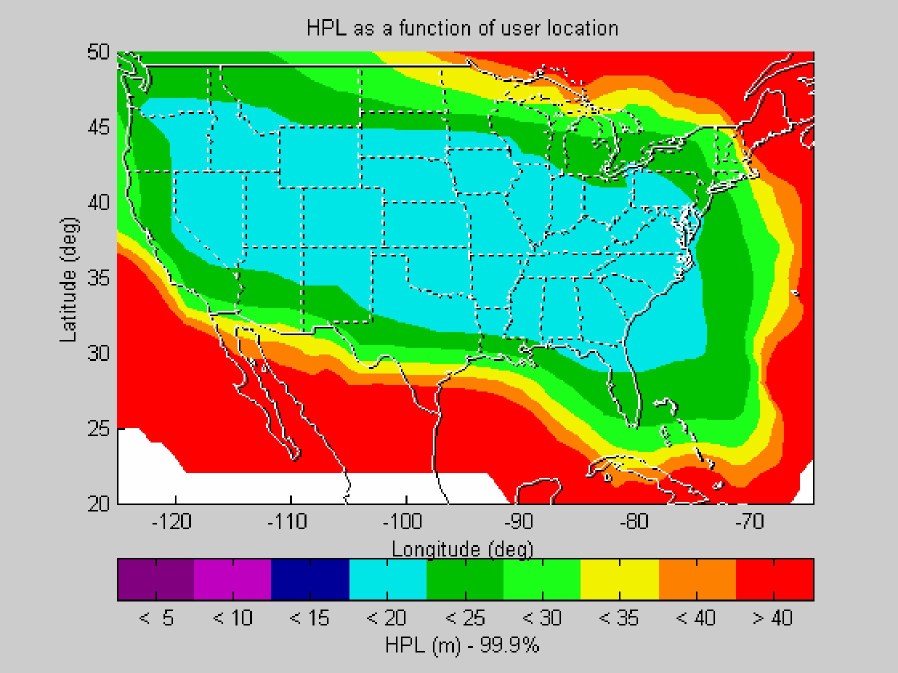

Figure 4.5: Horizontal Protection Level (HPL) contour of an L1-only single-frequency GPS/WAAS user in CONUS.

Figures 4.6-4.8 show the simulation results for an L5-only single-frequency GPS/WAAS user. Figure 4.6 is the LPV coverage simulation results for an L5-only single-frequency user. An L5-only single-frequency user has LPV precision approach services available 99.9% of the time over 49.25% of CONUS. Figures 4.7 and 4.8 show the VPL contour and HPL contour for an L5-only user in CONUS, respectively. The 99.9% shown in Figures 4.6-4.8 represents the fraction of users within those regions that had an availability of 99.9% or greater.

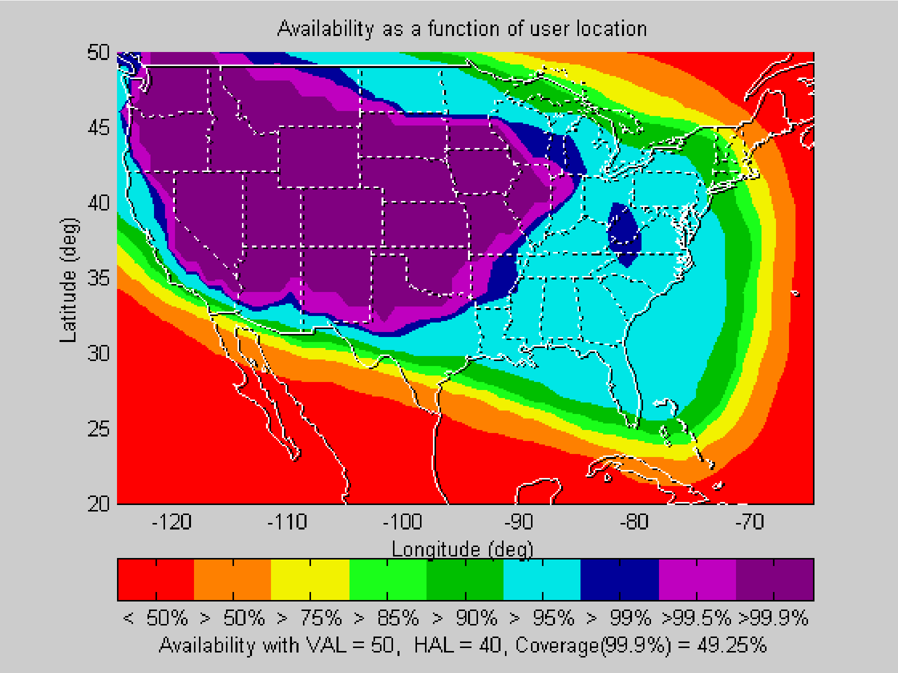

Figure 4.6: Coverage of an L5-only single-frequency GPS/WAAS user in CONUS is 49.25% with VAL = 50m, HAL = 40m.

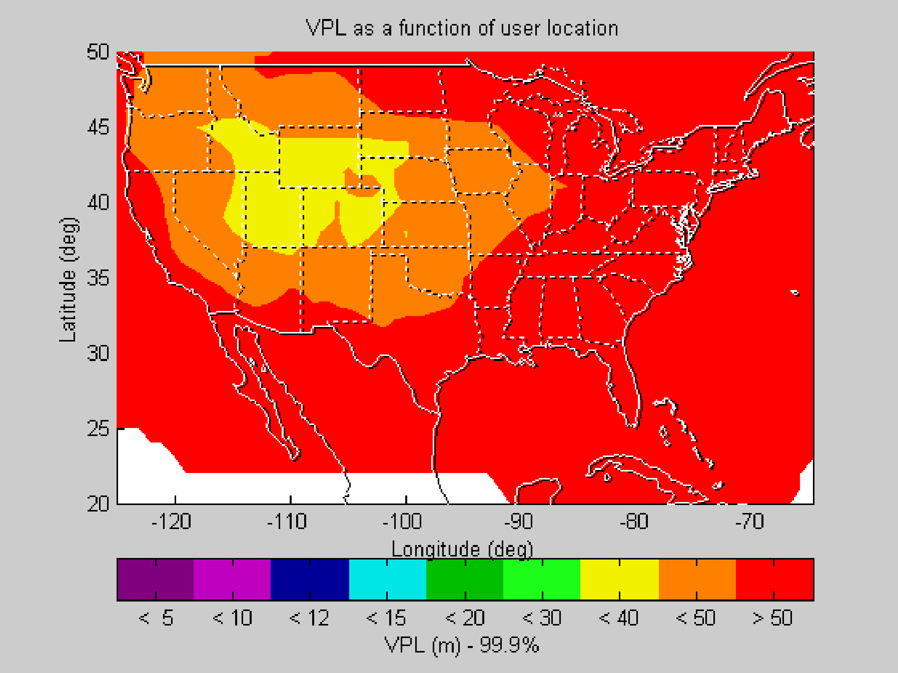

Figure 4.7: Vertical Protection Level (VPL) contour of an L5-only single-frequency GPS/WAAS user in CONUS.

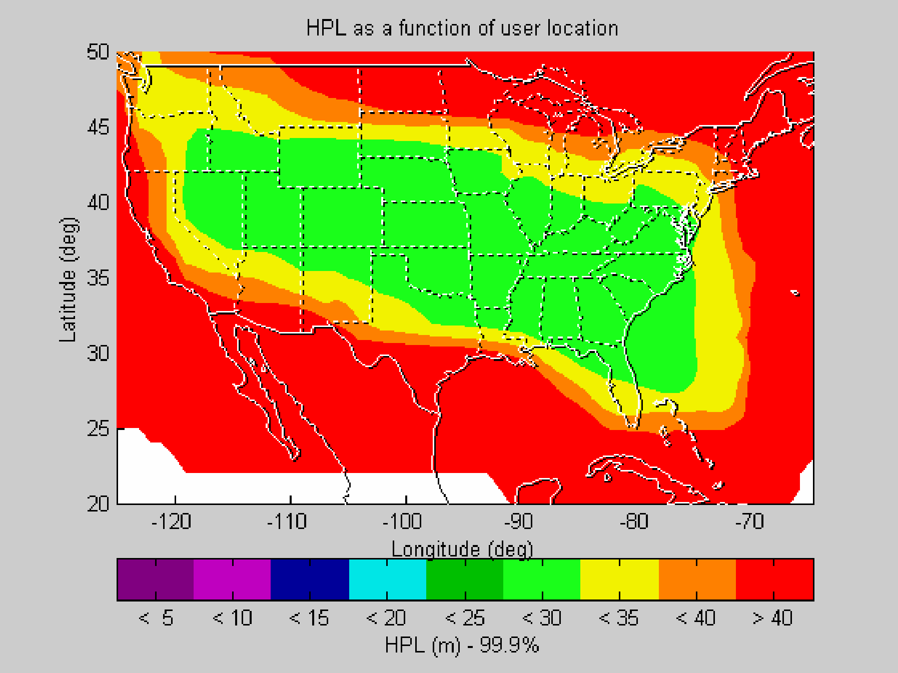

Figure 4.8: Horizontal Protection Level (HPL) contour of an L5-only single-frequency GPS/WAAS user in CONUS.

The LPV precision approach service coverage of an L1-only single-frequency GPS/WAAS user is 97.58%, which is better than the coverage of an L5-only single-frequency GPS/WAAS user (49.25%). The loss of coverage is due to the lower GPS frequency (L5) having larger ionospheric delay uncertainty. Table 4.1 provides a summary table of the MAAST simulation results.

User Type	CONUS Coverage of LPV precision approach services (Availability ≥ 99.9%)	VPL (in meter)	HPL (in meter)
L1-L5 dual-frequency	100%	12 ≤ VPL < 40	5 ≤ HPL < 20
L1-only single-frequency	97.58%	20 ≤ VPL	15 ≤ HPL
L5-only single-frequency	49.25%	30 ≤ VPL	25 ≤ HPL

Table 4.1: The MAAST simulation results.

4.3 TECHNIQUES FOR GRACEFUL REVERSION FROM DUAL TO SINGLE FREQUENCY WAAS

This thesis also investigates techniques to sustain dual-frequency performance when an L1-L5 dual-frequency airborne user is descending into an RFI field and loses all but one frequency. We are particularly interested in the case where the receiver transitions from L1-L5 to L5-only. That is because the uncertainty of the L5-only ionospheric delay estimation is larger than the L1-only ionospheric delay estimation. Therefore, the objective is to find the solutions that will sustain a performance similar to the L1-L5 dual-frequency ionospheric delay estimation.

4.3.1 PROBLEM STATEMENT AND SCENARIOS

An L1-L5 dual-frequency user has LPV (HAL = 40m, VAL = 50m) precision approach services available 99.9% of the time over 100% of CONUS, with a nominal σ_{UIRE} of 0.32m [Jan02a]. An L5 single-frequency user has LPV precision approach services available 99.9% of the time over 49.25% of CONUS. In this situation, the nominal σ_{UIRE} is 6m at the coasts, and 3.5m at the center of the country. In other words, if an L1-L5 dual-frequency user loses L1 due to RFI and instead uses the WAAS grid for ionospheric delay estimation, the loss in CONUS coverage of LPV services will be about 50%. The loss in CONUS coverage of LPV services is mainly because of the uncertainty of the ionospheric delay on L5. This situation is summarized in Figure 4.9.

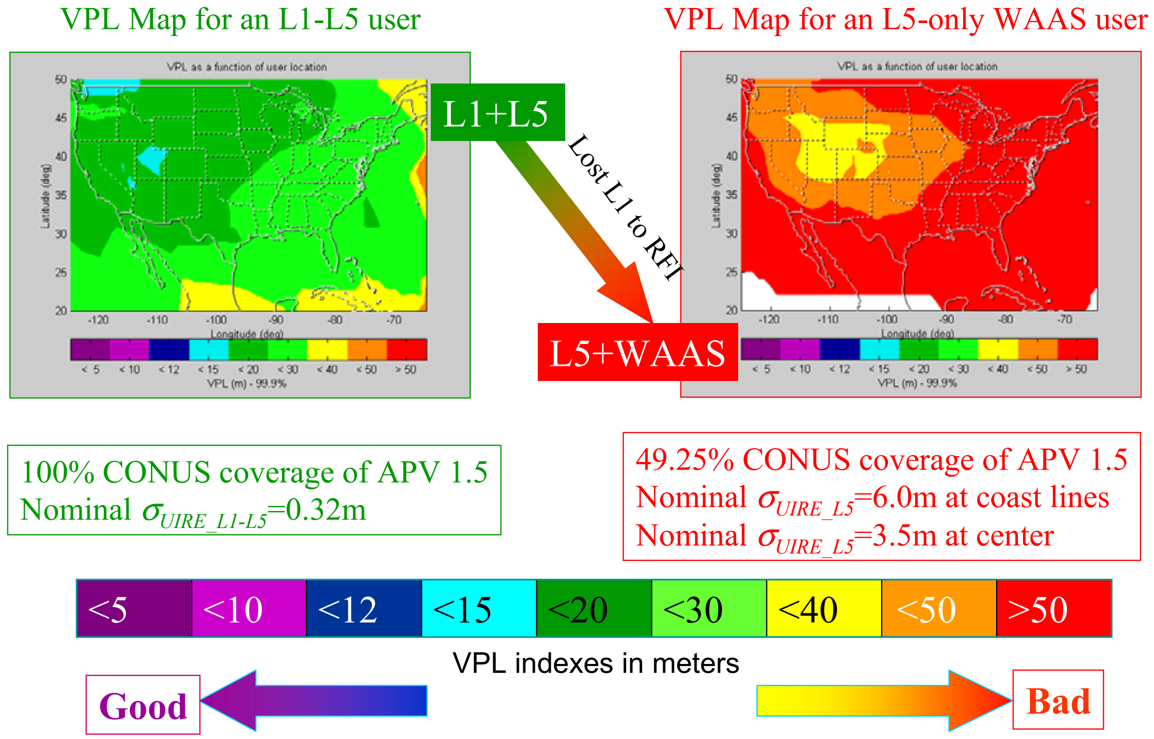

Figure 4.9: The VPL maps illustrate the situation when an L1-L5 dual-frequency user is descending into an L1 RFI field. The VPL map on the left is for an L1-L5 dual-frequency airborne user right before entering an L1 RFI field. The VPL map on the right is for an L5 single-frequency WAAS user. The loss in CONUS coverage of LPV services will be about 50% for this example.

Consider a typical precision approach example based on the San Francisco International Airport (SFO). In this example, the final approach length is about 14.1 nm (26.1 km), and the final approach velocity for a general aviation (GA) aircraft is 90-120 knots (167-222 km/hour). Thus the final approach duration is about 7-9 minutes depending on the final approach velocity. We assume that the aircraft enters the boundary of an L1 RFI field when the aircraft reaches the final approach fix. This example is shown in Figure 4.10. Therefore, for this typical precision approach example, a qualified technique must provide at least 9 minutes of useful ionospheric delay estimation which is similar in performance to the dual-frequency ionospheric delay estimation.

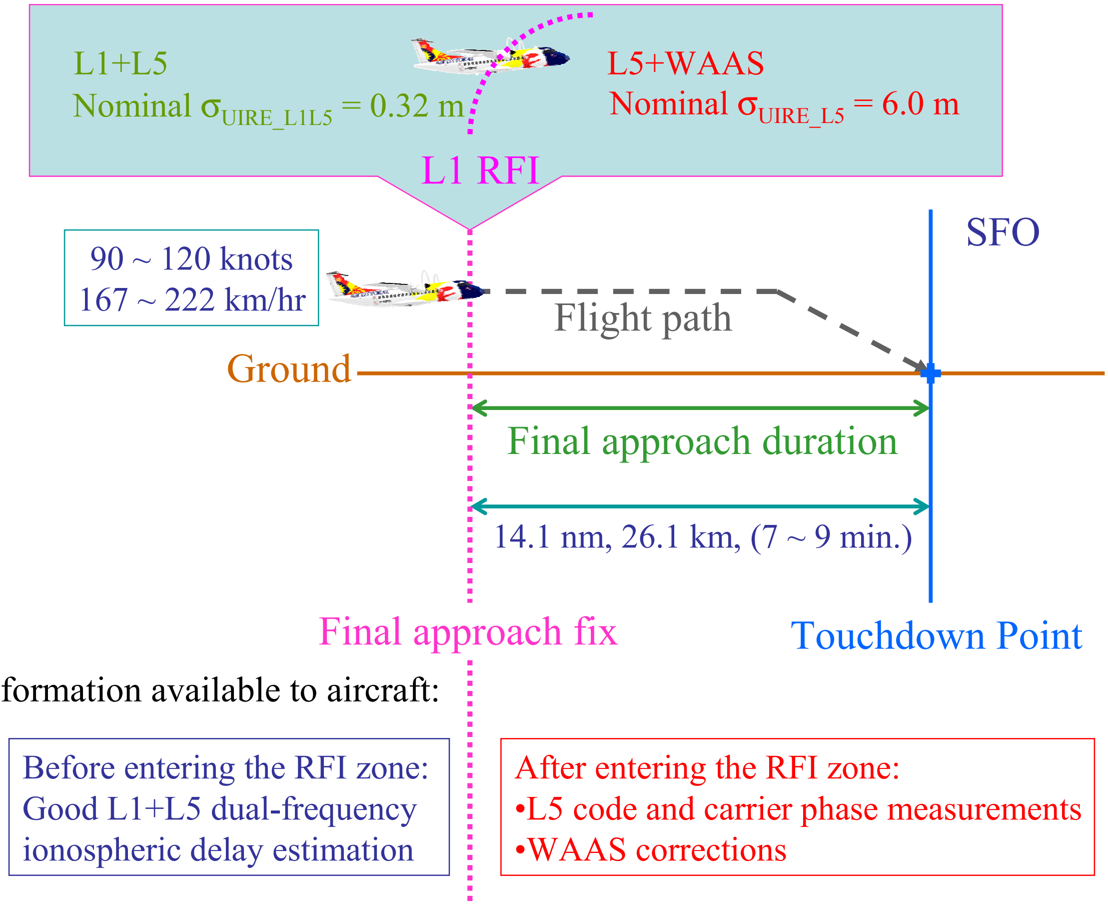

Figure 4.10: Typical precision approach duration example based on San Francisco International Airport (SFO) final approach. The aircraft enters the boundary of an L1 RFI field when the aircraft reaches the final approach fix. The nominal σ_{UIRE} jumps from 0.32m to 6.0m, which results in the loss of CONUS coverage of LPV services.

Figure 4.10 also shows the available information to an aircraft before and after entering the RFI field. Before entering an L1 RFI field, an aircraft has good L1-L5 dual-frequency ionospheric delay estimates. After entering an L1 RFI field, an aircraft has L5 code and carrier phase measurements plus WAAS corrections. We explore three techniques to sustain the dual-frequency ionospheric delay estimation.

- L5 code and carrier divergence technique.

- WAAS ionospheric threat model technique.

- Maximum ionospheric delay gradient model technique.

The requirements for these techniques are shown in Figure 4.11. The requirement for using the L5 code and carrier divergence technique is the absence of cycle slips. When cycle slips are present, one could utilize the WAAS ionospheric threat model technique as long as there is not an ionospheric storm. If both cycle slips and ionospheric storm may be present, one could use the maximum ionospheric delay gradient model technique.

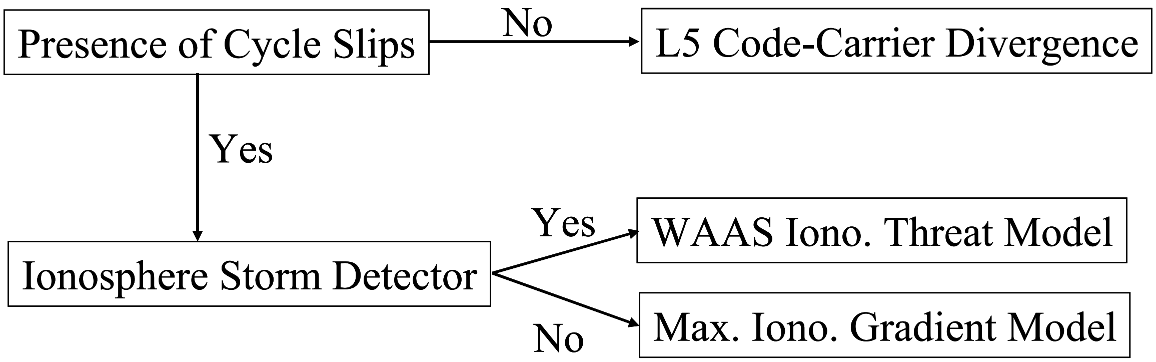

Figure 4.11: Techniques sustain the performance of the L1-L5 dual-frequency ionospheric delay estimation and the required conditions for using these techniques.

The 9 minutes final approach duration used in this chapter is derived from the final approach velocity of general aviation (GA) aircraft, but these techniques are not limited to these aircraft. The final approach velocities of commercial airliners are faster than the GA aircraft, so the final approach duration is simply shorter in time.

4.3.2 CODE AND CARRIER DIVERGENCE TECHNIQUE

As described in Section 1.1.1, the basic observables of a single-frequency receiver include:

$$\rho = R_j^i + b_j - B^i + I_j^i + T_j^i + M_j^i + v_j^i \tag{4.5}$$

$$\phi = R_j^i + b_j - B^i - I_j^i + T_j^i + N_j^i\lambda + m_j^i + \varepsilon_j^i \tag{4.6}$$

$$\rho - \phi = 2I_j^i + N_j^i\lambda + M_j^i + v_j^i - m_j^i - \varepsilon_j^i \tag{4.7}$$

One distinction between the code and carrier observables is the magnitude of the multipath and noise terms which are fractions of a wavelength ($\lambda_{L1} \approx 19$ cm, $\lambda_{L2} \approx 24$ cm, $\lambda_{L5} \approx 25$ cm, and $\lambda_\rho \approx 300$ m), where, λ_ρ is the C/A code wavelength (the duration of each C/A code chip is about 1 μs, thus, the chip wavelength is about 300 m) [Misra&Enge]. For the carrier signal, the m_j^i and ε_j^i terms are over two orders of magnitude smaller than the corresponding M_j^i and v_j^i on the pseudorange observations. At that level they are negligible, and Equation (4.7) can be rewritten as:

$$\rho - \phi = 2I_j^i + N_j^i\lambda + M_j^i + v_j^i \tag{4.8}$$

In Equation (4.8) the v_j^i term can be averaged out easily and the M_j^i term can be mitigated by the aircraft narrow-correlator receivers with the simplest carrier smoothing technique. The time constant used for the carrier smoothing technique is an important factor. As the time constant increases, M_j^i goes down, but the time to alarm increases. However, in an airplane, the time constant can be kept short, because the M_j^i is varying quickly. Although the multipath and noise errors could be limited to a reasonably low level, Equation (4.8) still suffers from integer ambiguity ($N_j^i\lambda$). Fortunately, the integer ambiguity is a constant offset unless there are cycle slips. As a result, there are two methods to solve the integer ambiguity in Equation (4.8). First, one can take advantage of the integer ambiguity solution before losing all but one GPS frequencies, and then subtract this estimate from

Equation (4.8). Thus, the ionospheric delay can be calculated as in Equations (4.9) and (4.10).

$$\rho - \phi = 2\hat{I}_j^i \tag{4.9}$$

$$\hat{I}_j^i = \frac{\rho - \phi}{2} - \frac{\hat{N}\lambda}{2} \tag{4.10}$$

Second, one can take advantage of the WAAS ionosphere corrections to estimate the integer ambiguity from an information fusion viewpoint [Dai]. Specifically, user integer ambiguity can be estimated by combining the user local observables and WAAS messages, as shown in Equation (4.11).

$$\frac{\hat{N}_j^i\lambda}{2} + \xi = \frac{\rho - \phi}{2} - I_{WAAS} \tag{4.11}$$

where, ξ is the residual error of the estimation, and I_{WAAS} is the WAAS ionosphere corrections.

Therefore, the ionospheric delay can be estimated by the code and carrier divergence technique, as in Equation (4.12).

$$\hat{I}_{\rho\phi} = \frac{\rho - \phi}{2} - \frac{\hat{N}\lambda}{2} \tag{4.12}$$

This thesis uses the observables of Satellite Number 20 at Stanford University on July 13, 2001 as an example. Figure 4.12 shows the slant ionospheric delay in meters measured in three methods. The blue line shows the ionospheric delay $I_{L1\rho}$ at the L1 frequency as measured by the L1 and L2 code difference. The equation with which pseudorange measurements, ρ_{L1} and ρ_{L2}, at the L1 and L2 frequencies, respectively, can be used to measure the ionospheric delay $I_{L1\rho}$ at L1 is

$$I_{L1\rho} = \frac{f_{L2}^2}{\left(f_{L1}^2 - f_{L2}^2\right)}\left(\rho_{L2} - \rho_{L1}\right) \tag{4.13}$$

This measurement of the slant ionospheric delay is noisy but unambiguous. This measurement is also affected by the satellite L1-L2 hardware group delay (τ_{gd}) which will be explained in Section 5.3.1.2.

The red line plots the delay $I_{L1\phi}$ at L1 as obtained from the L1 and L2 carrier phase measurements, ϕ_{L1} and ϕ_{L2} . The equation with which carrier phase measurements, ϕ_{L1} and ϕ_{L2} , at the L1 and L2 frequencies, respectively, can be used to measure the ionospheric delay $I_{L1\phi}$ at L1 is

$$I_{L1\phi} = \frac{f_{L2}^2}{\left(f_{L1}^2 - f_{L2}^2\right)}\left[\lambda_{L1}\left(\phi_{L1} - N_{L1}\right) - \lambda_{L2}\left(\phi_{L2} - N_{L2}\right)\right] \tag{4.14}$$

The carrier measurement of the ionospheric delay is significantly less noisy than the code measurement, but this measurement $I_{L1\phi}$ of the delay was offset from the correct absolute value because of the integer ambiguity. In Figure 4.12, the $I_{L1\phi}$ was re-centered using the time-averaged code measurement $I_{L1\rho}$. The green line is the $I_{L1\rho\phi}$ given in Equation (4.12).

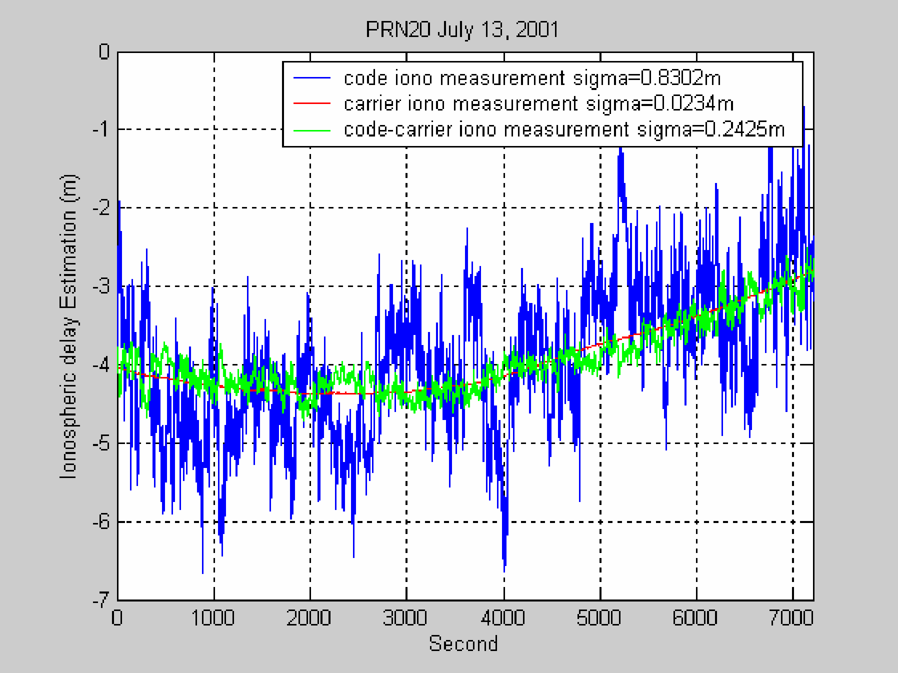

Figure 4.12: Slant ionospheric delay to Satellite Number 20 at Stanford University on July 13, 2001.

As shown in Figure 4.12, the code and carrier divergence technique provides good ionospheric delay estimation (the standard deviation $\sigma_{Code\_Carrier}$ is 0.2425m in this example), but cycle slips cannot be tolerated. If cycle slips are present, the Phase Lock Loop (PLL) of the GPS receiver will lose carrier tracking. Momentary loss of phase lock can result in a discontinuity in the integer cycle count. As a result, the integer ambiguity has to be resolved.

For our precision approach example, when one aircraft loses L1 while descending into the RFI field, this aircraft can use the L5 code and carrier divergence technique to continue the ionospheric delay estimation. The resulting nominal σ_{UIRE} will change as follows:

$$\sigma_{UIRE} = \sigma_{UIRE\_L1L5} + \sigma_{Code\_Carrier} = 0.32 + 0.2425 \approx 0.56 \text{ (m)} \tag{4.15}$$

where,

σ_{UIRE_L1L5} is the nominal σ_{UIRE} for an L1-L5 dual-frequency user, which is 0.32m [Jan02a]

$\sigma_{Code\_Carrier}$ is the standard deviation of the code and carrier divergence technique in the example shown in Figure 4.12

The σ_{UIRE} in Equation (4.15) is much less than the nominal σ_{UIRE_L5} using the WAAS grid which is 6.0m. Based on this model, users at SFO will be able to maintain good ionospheric delay estimation without using the WAAS grid for the full duration of approach, provided cycle slips can be avoided. The SFO example is summarized in Figure 4.13.

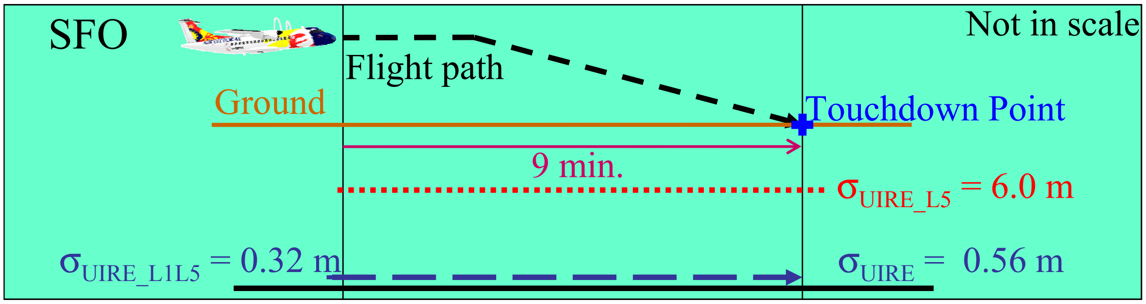

Figure 4.13: The nominal σ_{UIRE} variation along with the final approach into SFO. When user lost L1 while descending into the RFI field, user applied the L5 code and carrier divergence technique to continue estimating the ionospheric delay instead of using the WAAS grid. This technique provides good ionospheric delay estimation for full duration of approach.

The risk of cycle slips is now examined in three ways. First, we examine the probability of having one cycle slip in *t* seconds against the signal-to-noise ratio (C/N_o). Second, we examine the probability of having K cycle slips in 600 seconds against the C/N_o. The above two methods show the theoretical probability of cycle slips, which is a theoretical lower bound if noise were the dominate factor. Therefore, for the third method, we present some empirical data to show what the real probability is. The detailed description and equations used in the prediction of the theoretical probability of cycle slips can be found in [Hegarty] [Holmes]. We use a third order Phase Lock Loop (PPL) model. The PLL is used to adjust the frequency of a local oscillator to match the frequency of an input signal. The conventional PLL in an airborne GPS receiver is usually of third order. Equation (4.18) is the probability of not slipping in *t* seconds.

$$\bar{T}W_L = \frac{\pi^2}{\sigma_\phi^2} I_0^2\left(\frac{1}{\sigma_\phi^2}\right) \tag{4.16}$$

$$\bar{s} = \frac{1}{\bar{T}} \tag{4.17}$$

$$P_{\overline{SL}} = e^{-\bar{s}t} \tag{4.18}$$

where,

$\bar{T}$ is the mean slip time for the first order loop [Holmes]

W_L is the loop noise bandwidth [Holmes]

σ_ϕ is the PLL noise [Holmes]

$I_0(x)$ is the modified Bessel function of zeroth order

$\bar{s}$ is the cycle slipping rate [Holmes]

The probability of *K* slips in *t* seconds is given in Equation (4.19).

$$P_{SL}(K,t) = \frac{(\bar{s}t)^K e^{-\bar{s}t}}{K!} \tag{4.19}$$

Figure 4.14 shows the theoretical probability of having cycle slips. This is an approximation of the first order PLL. Although closed-form expressions for the slip rate of higher order PLLs have not been obtained, simulation results have indicated that higher order loops require slightly higher values of C/N$_o$ to achieve the performance of first order loops. About 1 dB of additional C/N$_0$ is required for a second order loop and roughly 2 dB more for a third order loop [Hegarty].

Figure 4.14 shows the theoretical lower bound on the probability of having one cycle slip in t seconds. As shown in the plot, the higher C/N$_0$ will have lower probability of cycle slips than the lower C/N$_0$, and the probability will grow with time.

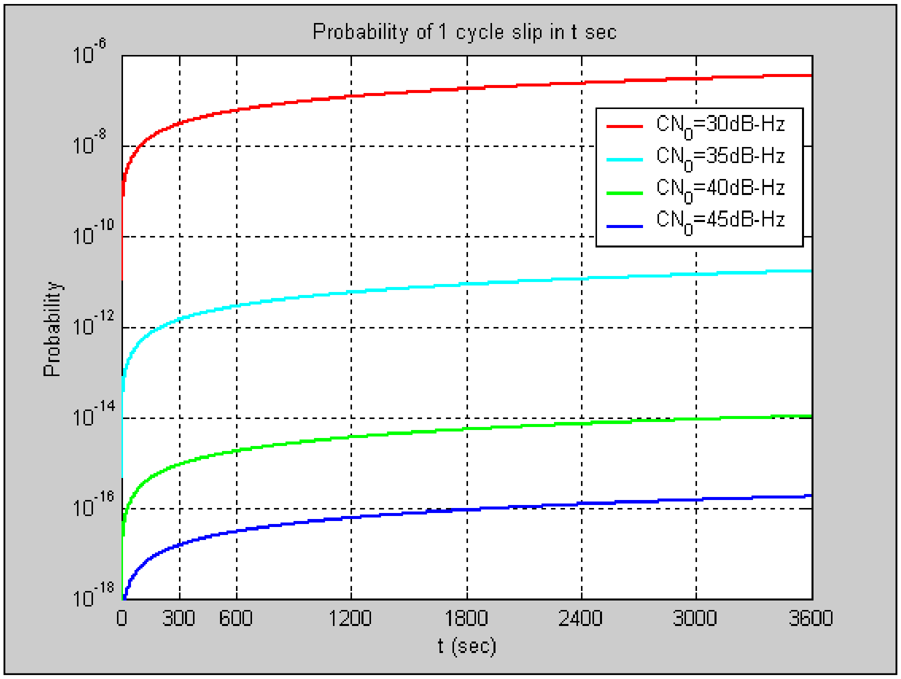

Figure 4.14: Theoretical probability of cycle slips. This is the probability of one cycle slip in *t* seconds as a function of signal-to-noise ratio (C/N$_0$).

Figure 4.15 shows the real probability of cycle slips. This thesis uses the observables of Satellite Number 03 and Satellite Number 24 at Stanford University on July 13,2001 as examples. The top left plot of Figure 15 shows the PLL status of Satellite Number 03 reported by the receiver, and “1” means “Lock”, “0” means “Not Lock” (i.e., having cycle slips). The middle left plot of Figure 4.15 shows the signal to noise density ratio $\left(C/N_0\right)$ in dB-Hz of Satellite Number 03. The bottom left plot of Figure 4.15 shows the elevation angle of Satellite Number 03. Similarly, the top right plot of Figure 15 shows the PLL status of Satellite Number 24 reported by the receiver, the middle right plot of Figure 4.15

shows the $\left(C/N_0\right)$ of Satellite Number 24, and the bottom right plot of Figure 4.15 shows the elevation angle of Satellite Number 24. The real probability of cycle slips for Satellite Number 03 is 0.0014 and the real probability of cycle slips for Satellite Number 24 is 0.0085, which is calculated as follows:

$$\mathrm{P}\left(\text{Cycle Slips}\right)=\frac{\left(\text{Total Number of "0s" Reported by Receiver}\right)}{\left(\text{Total Number of Data Points }\right)}$$

The real probabilities of cycle slips for both cases in Figure 4.15 are higher than the theoretical lower bound shown in Figure 4.14.

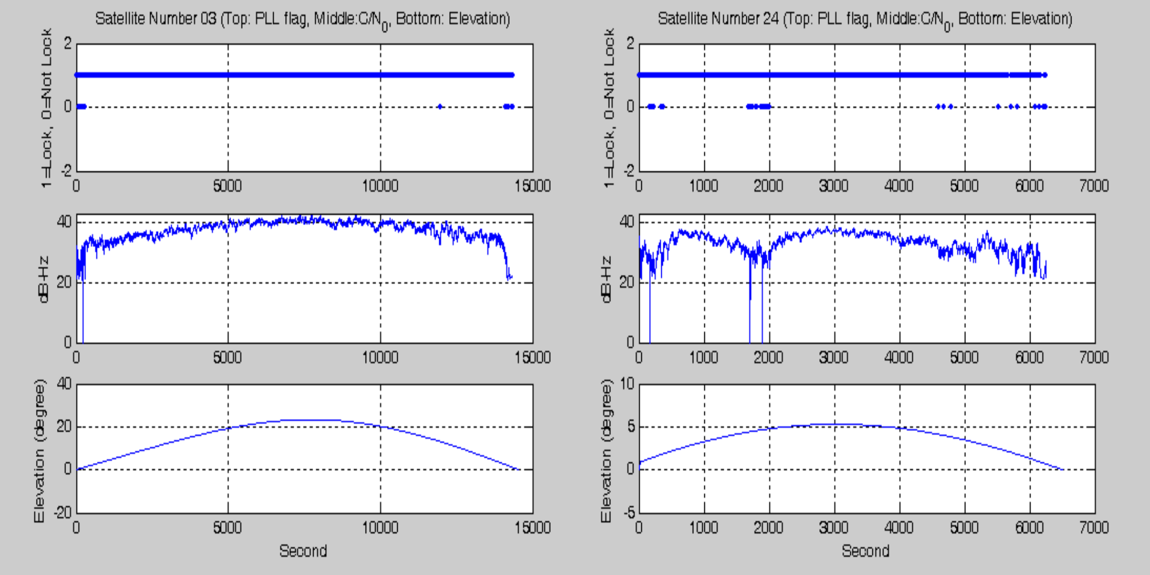

Figure 4.15: Real probability of cycle slips. The plot on the left is the PLL status (reported by the receiver), C/N_0 , and the elevation angle of Satellite Number 03. The plot on the right is the PLL status (reported by the receiver), C/N_0 , and the elevation angle of Satellite Number 24.

Figure 4.13 showed the simulation result for the typical precision approach example based on SFO. Next, we will use MAAST to measure aircraft applying this code and carrier divergence technique at all other airports within CONUS. The MAAST simulation configuration is specified in Table 3.1.

The MAAST is modified to adopt the changes in the UIRE calculation for an L1-L5 dual-frequency user losing the L1 frequency while descending into the RFI field and then applying the L5 code and carrier divergence technique to continue the ionospheric delay estimation. The new UDRE calculation used in the MAAST simulation is given in Equation (4.20).

$$\sigma_{UIRE} = \sigma_{UIRE\_L1L5} + \sigma_{Code\_Carrier} = \sigma_{UIRE\_L1L5} + 0.2425 \text{ (m)} \tag{4.20}$$

Figure 4.16 shows the simulation result, which is the 99.9% VPL contour for an L1-L5 dual-frequency user applying the code and carrier divergence technique to continue the ionospheric delay estimation while losing the L1-frequency to RFI. Figure 4.16 shows that the VPL values are less than 40m for 99.9% of the time over 100% of CONUS (Note: LPV VAL = 50m). Based on this simulation result, the L1-L5 dual-frequency aircraft losing the L1-frequency to RFI within CONUS will be able to use this technique to maintain good ionospheric delay estimation without using the WAAS grid for the full duration of approach.

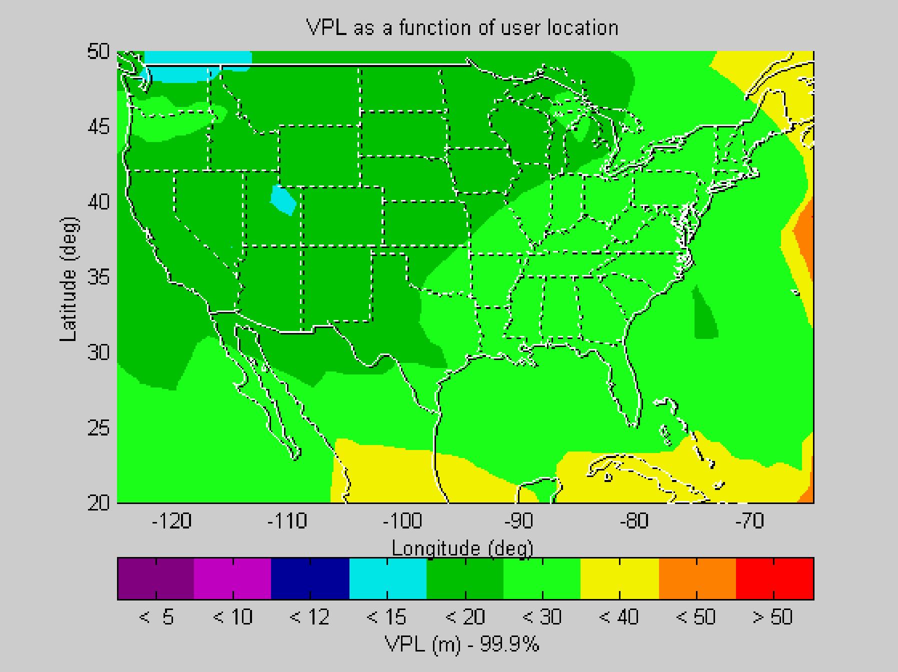

Figure 4.16: The 99.9% VPL contour for an L5 single-frequency user applying the code and carrier divergence technique to estimate the ionospheric delay after losing the L1 frequency while descending into the RFI field.

In order to show the benefit for using the code and carrier divergence technique, the comparison of two VPL contours is shown in Figure 4.17. The VPL contour on the left is for an L1-L5 dual-frequency user using the code and carrier divergence technique to estimate the ionospheric delay after losing the L1 frequency to RFI. The VPL values in CONUS in this plot are greater than 12m but less than 40m. The VPL contour on the right is for an L1-L5 user using the WAAS grid to estimate the ionospheric delay after losing the L1 frequency to RFI. The VPL values in CONUS in this plot are greater than 30m, and some places are higher than 50m (LPV VAL). Therefore, the VPL contour for using the code and carrier divergence technique is better than the VPL contour for using the WAAS grid. However, the cycle slip risk accumulated. Table 4.2 provides a summary table of the MAAST simulation results. As shown in Table 4.2, an L1-L5 dual-frequency user using the code and carrier divergence technique to estimate the ionospheric delay after losing the L1 frequency to RFI can have performance similar to the L1-L5 dual-frequency user.

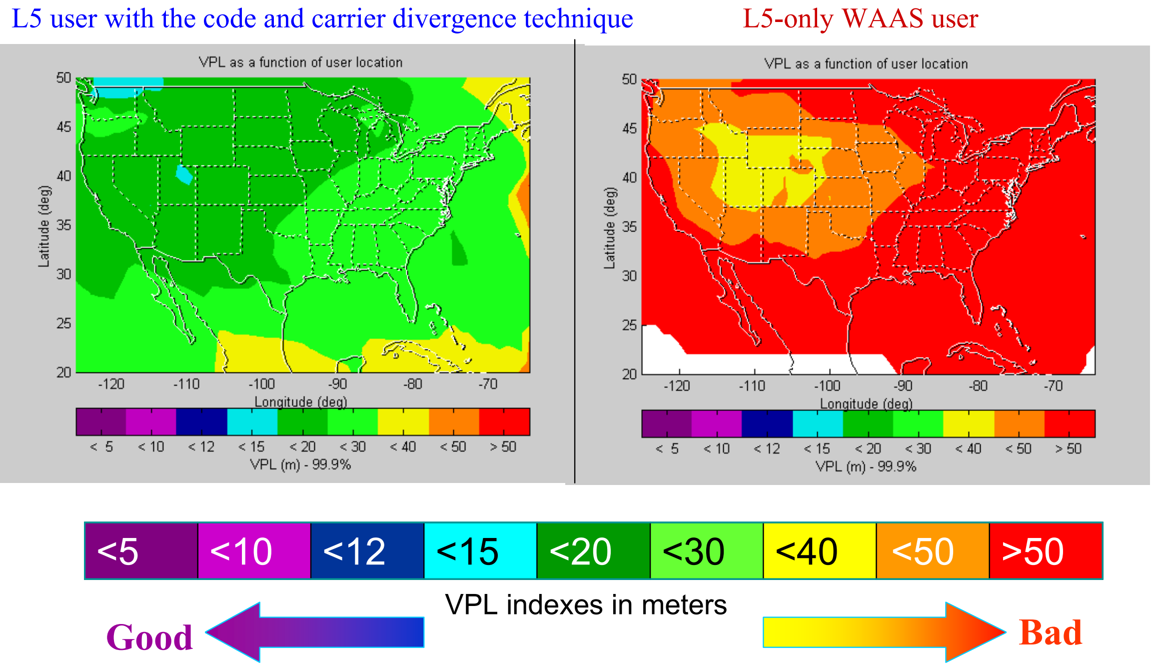
L5 user with the code and carrier divergence technique

L5-only WAAS user

Figure 4.17: The comparison of the VPL contours. The VPL contour on the left is for an L1-L5 dual-frequency user using the code and carrier divergence technique to estimate the ionospheric delay after losing the L1 frequency to RFI. The VPL contour on the right is for an L1-L5 user using the WAAS grid to estimate the ionospheric delay after losing the L1 frequency to RFI. The color bar shows the VPL indexes in meters. The use of the code and carrier divergence technique provided better ionospheric delay estimation than using the WAAS grid for an L1-L5 dual-frequency airborne user descending into an L1 RFI field.

User Type	CONUS Coverage of LPV precision approach services (Availability ≥ 99.9%)	VPL (in meter)	HPL (in meter)
L1-L5 dual-frequency	100%	12 ≤ VPL < 40	5 ≤ HPL < 20
L1-only single-frequency	97.58%	20 ≤ VPL	15 ≤ HPL
L5-only single-frequency	49.25%	30 ≤ VPL	25 ≤ HPL
L5-only with the code and carrier divergence technique	100%	12 ≤ VPL < 40	5 ≤ HPL < 20

Table 4.2: The MAAST simulation results.

The GPS receiver manufactures have their own algorithms to detect cycle slips. If there are cycle slips, the airborne user will no longer be able to use this technique and will have to use one of the other two techniques: the WAAS ionosphere threat model technique or the maximum ionospheric delay gradient model technique.

4.3.3 WAAS IONOSPHERE THREAT MODEL TECHNIQUE

A future WAAS message could include the new message bits to indicate the presence of ionosphere storm in addition to the GIVE message. An aircraft can listen to this particular WAAS message. If there are cycle slips and the aircraft has such ionosphere storm detector information available, that aircraft can use the WAAS ionosphere threat model technique to bound the ionosphere error while descending into the RFI field.

This WAAS ionosphere threat model is detailed in [Sparks]. It is a temporal threat model which tracks the deviations in time since the last planar fit. A plot of the temporal threat model is shown in Figure 4.18, which includes the histogram of Equation (4.21).

$$\Delta I_{t=t_{iono}} = \hat{I}_{t=t_{iono}} - \hat{I}_{t=t_0} \tag{4.21}$$

where, $\hat{I}$ is the estimated ionospheric delay at a specific time.

In [Sparks], only the points that pass the chi-square test are used in determining the threat model. The chi-square test is a reliable indicator of the "goodness of fit," and is used to detect the ionosphere irregularity. Readers can refer to [Walter00] for more information about the chi-square test and ionosphere irregularity detection.

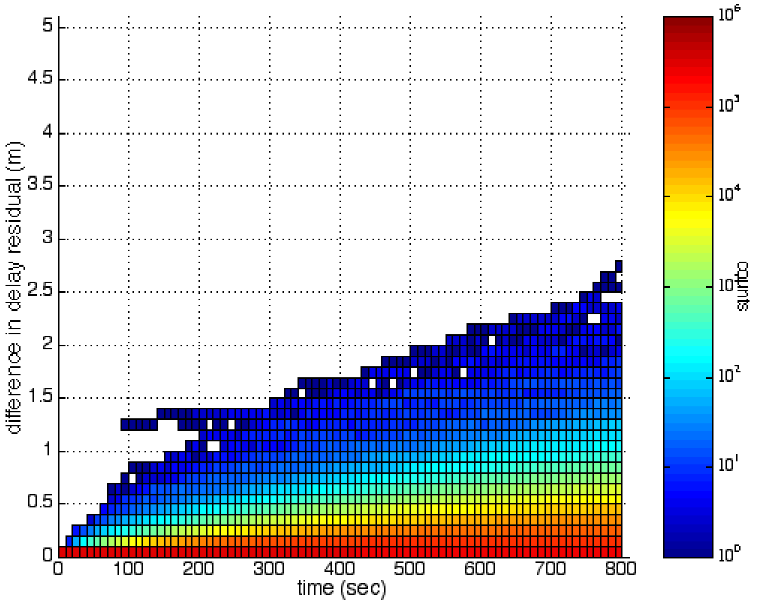

Figure 4.18: The temporal threat model. The maximum gradient occurs around 300 seconds which is 1.62m. (Courtesy: Lawrence Sparks)

Figure 4.18 shows the differences between fit residuals at the time of a fit and fit residuals at subsequent times. The gradient shows the *ROT* (Rate of TEC (i.e., ionospheric delay)). In Figure 4.18 the maximum gradient occurs around 300 seconds which is 1.62m. The equation to overbound the *ROT* in Figure 4.18 is as follows:

$$ROT_{bound} = \begin{cases} 1.62\,\text{m, if t<120}\,\text{sec} \\ \sqrt{1.62^2 + (5.33 * 0.00075 * (t-120))^2}\ \text{m, if t>120}\,\text{sec} \end{cases} \tag{4.22}$$

The blue line in Figure 4.19 plots the ROT_{bound} and the red line in Figure 4.19 plots the confidence, σ_{ROT}, which is calculated in Equation (4.23).

$$\sigma_{ROT} = \begin{cases} \dfrac{1.62}{5.33} \text{ (m), if t<120sec} \\ \dfrac{\sqrt{1.62^2 + (5.33 * 0.00075 * (t-120))^2}}{5.33} \text{ (m), if t>120sec} \end{cases} \tag{4.23}$$

where, 5.33 is the K_{HMI} value defined in Section 2.3, and 5.33 is used to convert a 10^{-7} error bound to one sigma level.

The overbound model is originally designed to protect the WAAS users from using GIVE messages. As a result, this model is valid before the time receiving the next GIVE message, which is 600 seconds [Sparks]. However, the blue line in Figure 4.19 still bounds the data shown in Figure 4.18 at 800 seconds.

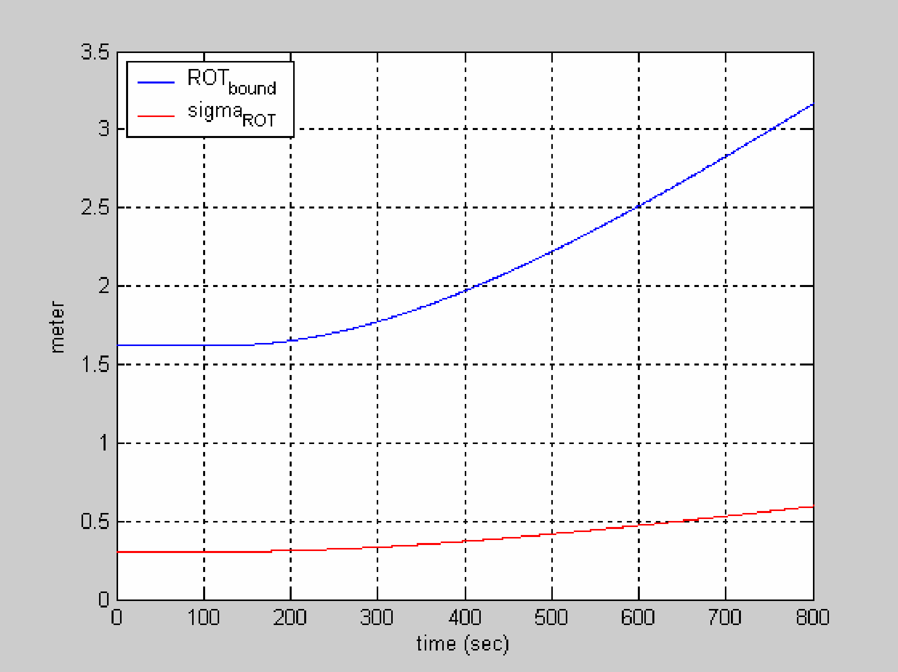

Figure 4.19: The WAAS ionosphere threat model (ROT overbound model). The blue line is ROT overbound model, and the red line represents the confidence of it.

For our precision approach example, when an aircraft lost L1 while descending into the RFI field, the aircraft can use the WAAS ionosphere threat model technique to bound the ionospheric error. The nominal σ_{UIRE} at the touchdown point can be calculated by substituting $t = 540$ sec into Equation (4.23).

$$\sigma_{ROT_{bound}SFO} = \frac{\sqrt{1.62^2 + (5.33*0.00075*(540-120))^2}}{5.33} = 0.4377\ (\mathrm{m}) \tag{4.24}$$

$$\sigma_{UIRE} = \sigma_{UIRE\_L1L5} + \sigma_{ROT_{bound}SFO} = 0.32 + 0.4377 \approx 0.76\ (\mathrm{m}) \tag{4.25}$$

The σ_{UIRE} in Equation (4.25) is much less than the nominal σ_{UIRE_L5} = 6.0m for L5-only users. Based on this model, users at SFO will be able to maintain useful ionospheric delay estimation without using the WAAS grid for at least 10 minutes. The SFO example is summarized in Figure 4.20.

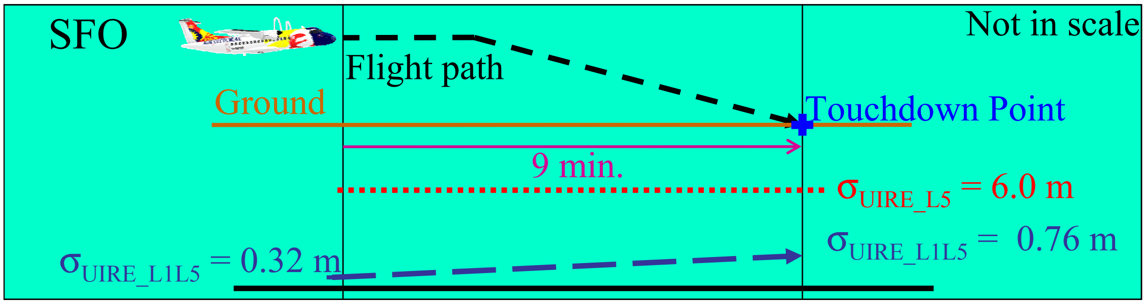

Figure 4.20: The nominal σ_{UIRE} variation along with the final approach into SFO. When user lost L1 while descending into the RFI field, user applied the WAAS ionosphere threat model technique to bound the ionospheric delay error instead of using the WAAS grid. This technique provides good ionospheric delay estimation for at least 10 minutes.

Figure 4.20 shows the simulation result for the typical precision approach example based on SFO. Next, we will use MAAST to measure aircraft applying this WAAS ionosphere threat model technique at all other airports within CONUS. The MAAST simulation configuration is specified in Table 3.1.

The MAAST is modified to adopt the changes in the UIRE calculation for an L1-L5 dual-frequency user losing the L1 frequency while descending into an RFI field and then applying the WAAS ionosphere threat model technique to continue bounding the ionosphere error.

This new UIRE calculation is a time dependent function. Therefore, MAAST simulated the aircraft using the WAAS ionosphere threat model technique to bound the ionosphere error for 4.5 minutes (at the middle of final approach) and 9 minutes (at the touchdown point) after descending into the RFI field. The corresponding new UDRE calculations used in the MAAST simulation are given in Equation (4.26) and Equation (4.27), respectively.

$$\sigma_{UIRE} = \sigma_{UIRE\_L1L5} + \sigma_{ROT_{bound}\_4.5\min} = \sigma_{UIRE\_L1L5} + 0.3241 \text{ (m)} \tag{4.26}$$

$$\sigma_{UIRE} = \sigma_{UIRE\_L1L5} + \sigma_{ROT_{bound}\_9\min} = \sigma_{UIRE\_L1L5} + 0.4377 \text{ (m)} \tag{4.27}$$

Figure 4.21 shows the first simulation result, which is the 99.9% VPL contour for an L1-L5 dual-frequency user applying the WAAS ionosphere threat model technique to bound the ionosphere error 4.5 minutes after losing L1. Figure 4.21 shows the VPL values are less than 40m for 99.9% of the time over 100% of CONUS (Note: LPV VAL = 50m). Based on this simulation result, the L1-L5 dual-frequency aircraft losing L1-frequency to RFI within the CONUS will be able to use this technique to bound the ionosphere error without using the WAAS grid 4.5 minutes after entering the RFI field.

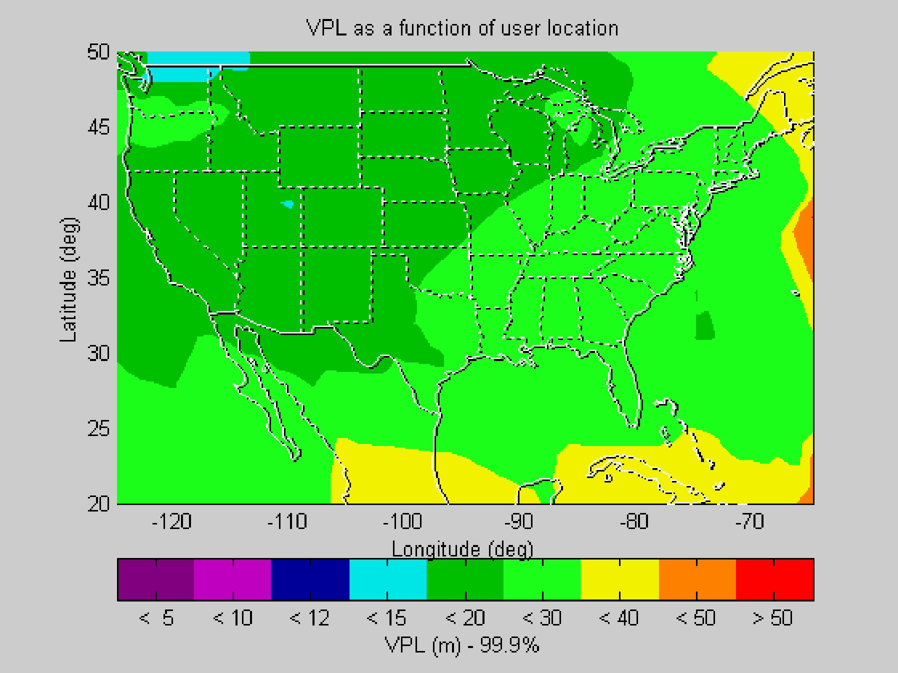

Figure 4.21: The 99.9% VPL contour for an L5 single-frequency user applying the WAAS ionosphere threat model technique to estimate the ionospheric delay 4.5 minutes after descending into the RFI field (or at the middle of the final approach).

Figure 4.22 shows the second simulation result, which is the 99.9% VPL contour for an L1-L5 dual-frequency user applying the WAAS ionosphere threat model technique to bound the ionosphere error 9 minutes after losing the L1-frequency to RFI. Figure 4.22 shows the VPL values are less than 40m for 99.9% of the time over 100% of CONUS (Note: LPV VAL = 50m). Based on this simulation result, the L1-L5 dual-frequency aircraft losing L1 within CONUS will be able to use this technique to bound the ionosphere error without using the WAAS grid 9 minutes after entering the RFI field.

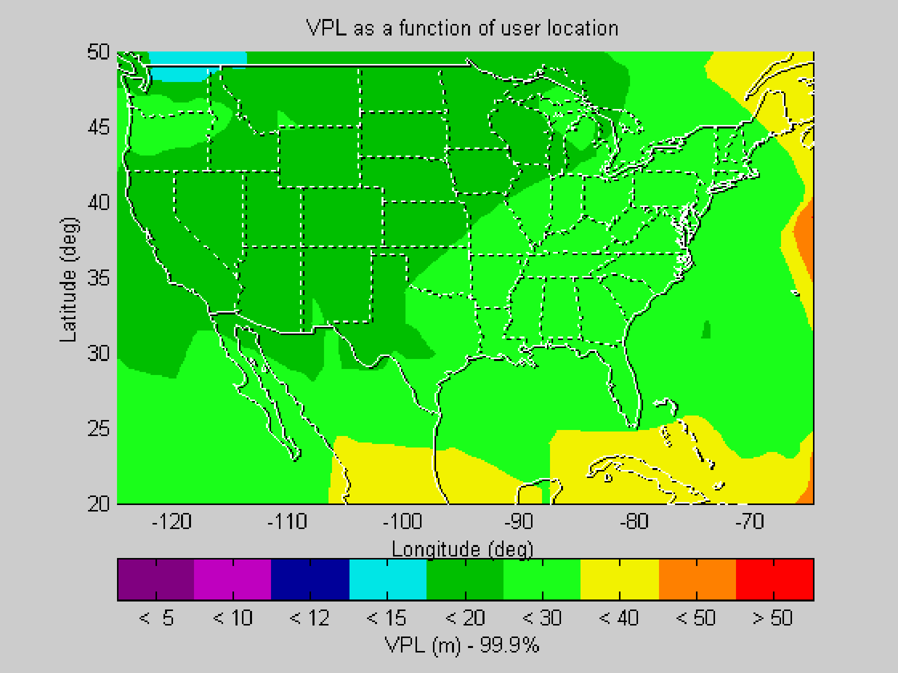

Figure 4.22: The 99.9% VPL contour for an L5 single-frequency user applying the WAAS ionosphere threat model technique to bound the ionosphere error 9 minutes after descending into the RFI field (or at the touchdown point).

To show the benefits of using the WAAS ionosphere threat model technique, comparison of two VPL contours is shown in Figure 4.23. The VPL contour on the left is for an L1-L5 dual-frequency user using the WAAS ionosphere threat model technique to bound the ionosphere error after losing the L1 frequency to RFI. The VPL values in CONUS of this plot are greater than 12m but less than 40m. The VPL contour on the right is for an L1-L5 user using the WAAS grid to estimate the ionospheric delay after losing the L1 frequency to RFI. The VPL values in CONUS of this plot are greater than 30m, and some places are even greater than 50m (LPV VAL). Therefore, the VPL contour for using the WAAS ionosphere threat model technique is better than the VPL contour for using the WAAS grid. However, this technique requires an ionosphere storm detector. Table 4.3 provides a summary table of the MAAST simulation results. As shown in Table 4.3, an L1-L5 dual-frequency user using the WAAS ionosphere threat model technique to estimate the ionospheric delay after losing the L1 frequency to RFI can have a performance similar to the L1-L5 dual-frequency user.

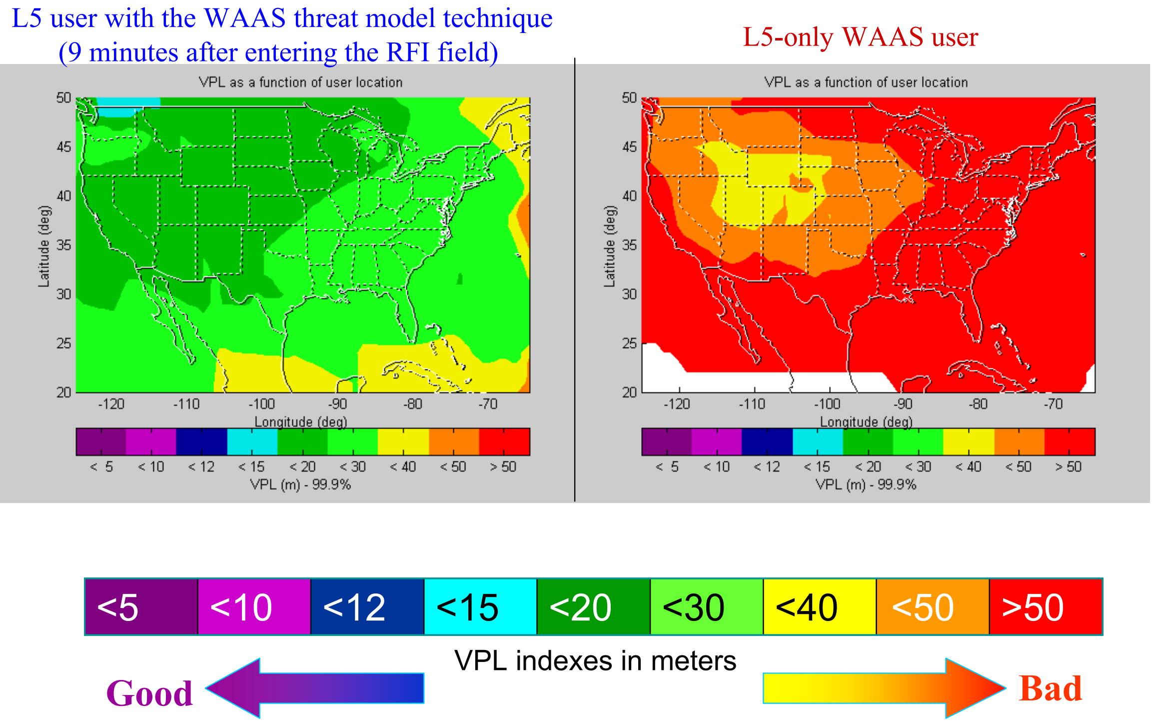

Figure 4.23: The comparison of the VPL contours. The VPL contour on the left is for an L1-L5 dual-frequency user using the WAAS ionosphere threat model technique to bound the ionosphere error 9 minutes after losing the L1 frequency to RFI. The VPL contour on the right is for an L1-L5 user using the WAAS grid to estimate the ionospheric delay after losing the L1 frequency to RFI. The color bar shows the VPL indexes in meters. The use of the WAAS ionosphere threat model technique provided better ionospheric delay estimation than using the WAAS grid for an L1-L5 dual-frequency airborne user descending into an L1 RFI field.

User Type	CONUS Coverage of LPV precision approach services (Availability ≥ 99.9%)	VPL (in meter)	HPL (in meter)
L1-L5 dual-frequency	100%	12 ≤ VPL < 40	5 ≤ HPL < 20
L1-only single-frequency	97.58%	20 ≤ VPL	15 ≤ HPL
L5-only single-frequency	49.25%	30 ≤ VPL	25 ≤ HPL
L5-only with the code and carrier divergence technique	100%	12 ≤ VPL < 40	5 ≤ HPL < 20
L5-only with the WAAS ionosphere threat model technique (9 minutes after losing L1)	100%	12 ≤ VPL < 40	5 ≤ HPL < 20

Table 4.3: The MAAST simulation results.

The use of the WAAS ionosphere threat model technique requires information from an ionosphere storm detector. This information would be broadcasted in a new WAAS message which is designed to indicate the presence of ionosphere storm. If there is an ionosphere storm or there is no available ionosphere storm detector, an aircraft will have to use the maximum ionospheric delay gradient model technique to sustain a performance similar to the dual-frequency ionospheric delay estimation while descending into the RFI field.

4.3.4 MAXIMUM IONOSPHERIC DELAY GRADIENT MODEL TECHNIQUE

If there are cycle slips and there is no available ionosphere storm detector, the aircraft can use the maximum ionospheric delay model technique to bound the ionosphere error while descending into the RFI field. This maximum ionospheric delay gradient model is detail in [Datta-Barua]. In her work, she analyzed the supertruth data, which is the ionosphere data obtained for the past few years for the CONUS region from the twenty-five WRSs. She found an ionospheric delay gradient of 6m/19km in the vertical. This is the maximum for the data sets she investigated but large values are possible, particularly in equatorial regions. For now, we will treat this gradient as thought it is the largest possible. In other words, the difference of the measured ionospheric vertical delay at location A and the measured ionospheric vertical delay at location B which is 19km apart from location A, could be 6m in the worst case, as shown in Figure 4.24. In addition, this ionospheric storm data showed that the velocity of the ionospheric wall front $\left(V_{Iono\_wall}\right)$ is 110m/s and the velocity of the IPP $\left(V_{IPP}\right)$ is 63m/s. This IPP velocity is the nominal IPP velocity observed in her data, and this IPP velocity is not the maximum IPP velocity. This maximum gradient model is developed based on a static receiver. For a moving aircraft, the velocity of the aircraft $\left(V_{aircraft}\right)$ must be taken into account, which is 46.4 m/s for the typical final approach example shown in Figure 4.10. In the worst-case condition, the ionospheric wall front is moving in the completely opposite direction of the aircraft and IPP. Therefore, the model in [Datta-Barua] is modified to include all the velocities, and the gradient in the new model will grow faster than the gradient in [Datta-Barua] by a factor of *T*. Thus, the confidence bound can be calculated as

$$\sigma_{MAX\_IONOgradient} = \left(\frac{6m}{5.33}\right)\cdot\left(\frac{d}{19}\right)\cdot T \tag{4.28}$$

where,

5.33 is the K_{HMI} value defined in Section 2.3

d is distance from the current position to the place with the last dual-frequency ionospheric delay estimation

T is a multiplier to translate the static receiver model to the dynamic receiver model, which is calculated as follows:

$$T = \frac{V_{Iono\_wall} + V_{IPP} + V_{aircraft}}{V_{Iono\_wall} + V_{IPP}} = \frac{110 + 63 + 46.4}{110 + 63} = 1.2681$$

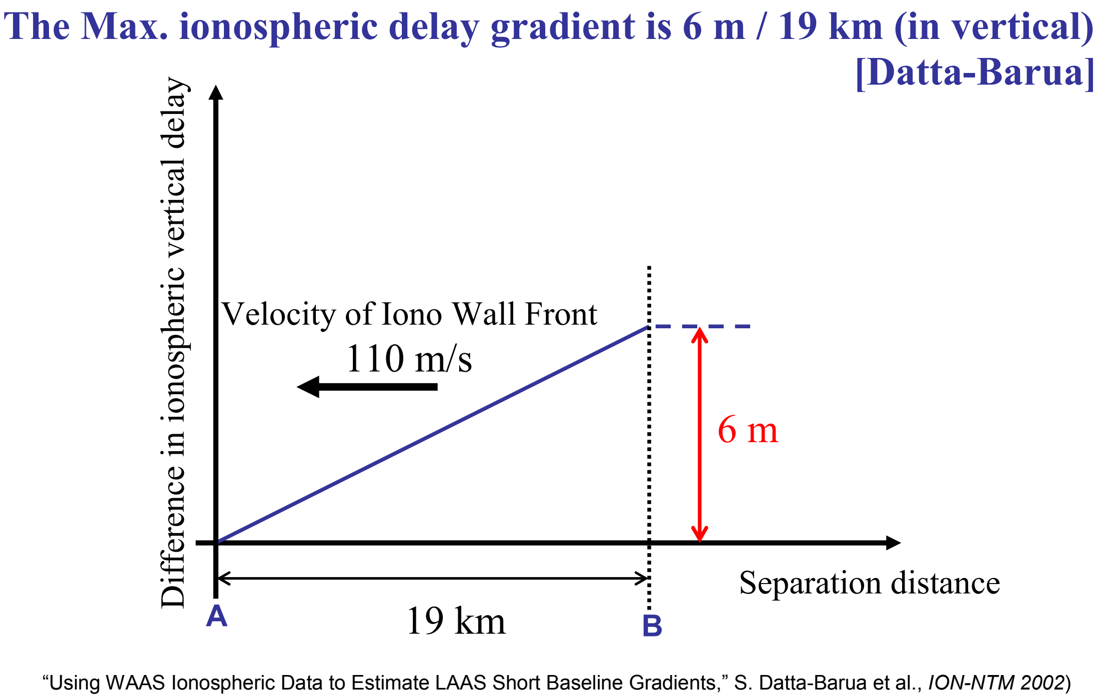

The Max. ionospheric delay gradient is 6 m / 19 km (in vertical) [Datta-Barua]

"Using WAAS Ionospheric Data to Estimate LAAS Short Baseline Gradients," S. Datta-Barua et al., *ION-NTM 2002*)

Figure 4.24: The maximum vertical ionospheric delay gradient model. The maximum difference in the ionospheric vertical delay for places 19 km apart ("A" and "B") is 6m.

If an aircraft loses L1 while descending into an RFI field, it can use the maximum ionospheric delay gradient model technique to bound the ionospheric error. The nominal σ_{UIRE} at the touchdown point can be calculated by substituting $d = 26.1\ \text{km}$ (Figure 4.10) and $V_{aircraft} = 46.4\ \text{m/s}$ (Figure4.10) into Equation (4.28).

$$\sigma_{MAX\_IONOgradientSFO} = \left(\frac{6}{5.33}\right)\cdot\left(\frac{26.1}{19}\right)\cdot(1.2681) = 1.9611\ (\text{m}) \tag{4.29}$$

$$\sigma_{UIRE} = \sigma_{UIRE\_L1L5} + \sigma_{MAX\_IONOgradientSFO} = 0.32 + 1.9611 \approx 2.3\ (\text{m}) \tag{4.30}$$

The σ_{UIRE} in Equation (4.30) is much less than the nominal σ_{UIRE_L5} = 6.0m for L5-only users. Based on this model, users at SFO will be able to maintain useful ionospheric delay estimation without using the WAAS grid for at least 10 minutes after L1 loss. Our precision approach example is summarized in Figure 4.25.

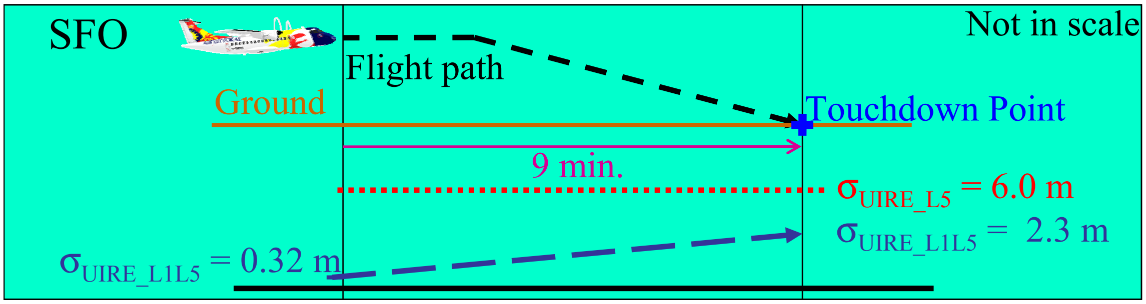

Figure 4.25: The nominal σ_{UIRE} variation along with the final approach into SFO. When the user lost L1 while descending into the RFI field, that user applied the maximum ionospheric delay gradient model technique to bound the ionospheric delay error instead of using the WAAS grid. This technique provides good ionospheric delay estimation for at least 10 minutes. The σ_{UIRE} at the touchdown point is 2.3m which is higher than the user with the WAAS ionosphere threat model in Figure 4.20.

Figure 4.25 shows the simulation result for the typical precision approach example based on SFO. Next, we will use MAAST to measure aircraft applying this maximum ionospheric delay gradient model technique at all other airports within CONUS. The MAAST simulation configuration is specified in Table 3.1.

The MAAST is modified to adopt the changes in the UIRE calculation for an L1-L5 dual-frequency user losing the L1 frequency while descending into an RFI field and then applying the maximum ionospheric delay gradient model technique to continue bounding the ionosphere error.

This new UIRE calculation is also a time dependent function. Therefore, MAAST simulated the aircraft using the maximum ionospheric delay gradient model technique to bound the ionosphere error while 4.5 minutes (at the middle of final approach) and 9 minutes (at the touchdown point) after descending into the RFI field. The corresponding new UDRE calculations used in the MAAST simulation are given in Equation (4.31) and Equation (4.32), respectively.

$$\sigma_{UIRE} = \sigma_{UIRE\_L1L5} + \sigma_{MAX\_IONOgradient\,4.5\,\text{min}} = \sigma_{UIRE\_L1L5} + 0.9805 \text{ (m)} \qquad (4.31)$$

$$\sigma_{UIRE} = \sigma_{UIRE\_L1L5} + \sigma_{MAX\_IONOgradient9\min} = \sigma_{UIRE\_L1L5} + 1.9611 \text{ (m)} \qquad (4.32)$$

Figure 4.26 shows the first simulation result, which is the 99.9% VPL contour for an L1-L5 dual-frequency user applying the maximum ionospheric delay gradient model technique to bound the ionosphere error 4.5 minutes after losing the L1-frequency to RFI. Figure 4.26 shows that the VPL values are less than 40m for 99.9% of the time over 100% of CONUS (Note: LPV VAL = 50m). Based on this simulation result, the L1-L5 dual-frequency aircraft losing the L1-frequency to RFI within CONUS will be able to use this technique to bound the ionosphere error without using the WAAS grid 4.5 minutes after entering the RFI field.

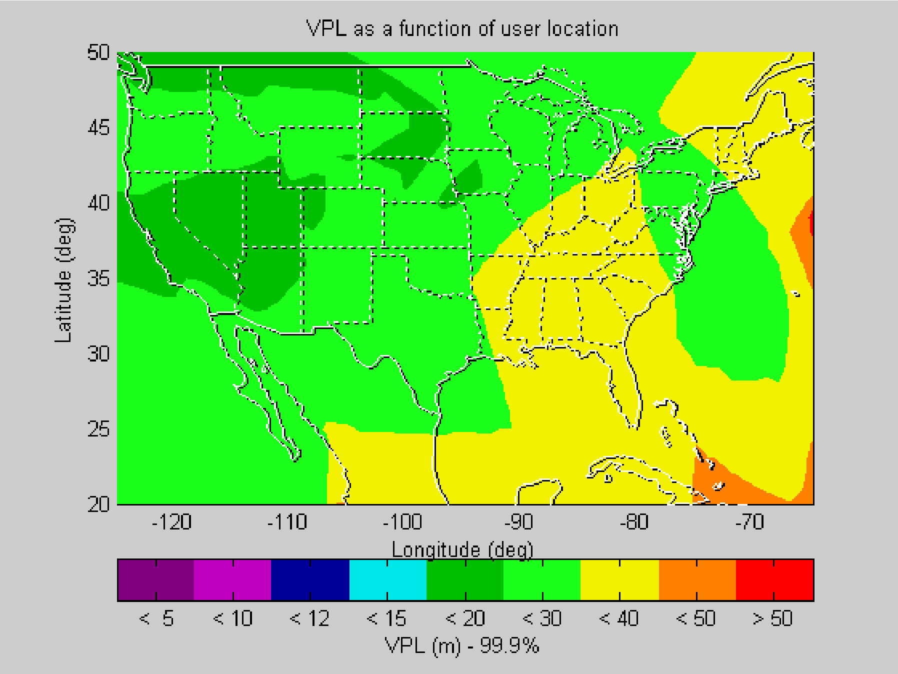

Figure 4.26: The 99.9% VPL contour for an L5 single-frequency user applying the maximum ionospheric delay gradient technique to estimate the ionospheric delay 4.5 minutes after descending into the RFI field.

Figure 4.27 shows the simulation result, which is the 99.9% VPL contour for an L1-L5 dual-frequency user applying the maximum ionospheric delay gradient model technique to bound the ionosphere error 9 minutes after losing the L1-frequency to RFI. Figure 4.27 shows that the VPL values are less than 50m for 99.9% of the time over 100% of CONUS

(Note: LPV VAL = 50m). Based on this simulation result, the L1-L5 dual-frequency aircraft losing the L1-frequency to RFI will be able to use this technique to bound the ionosphere error without using the WAAS grid 9 minutes after entering the RFI field.

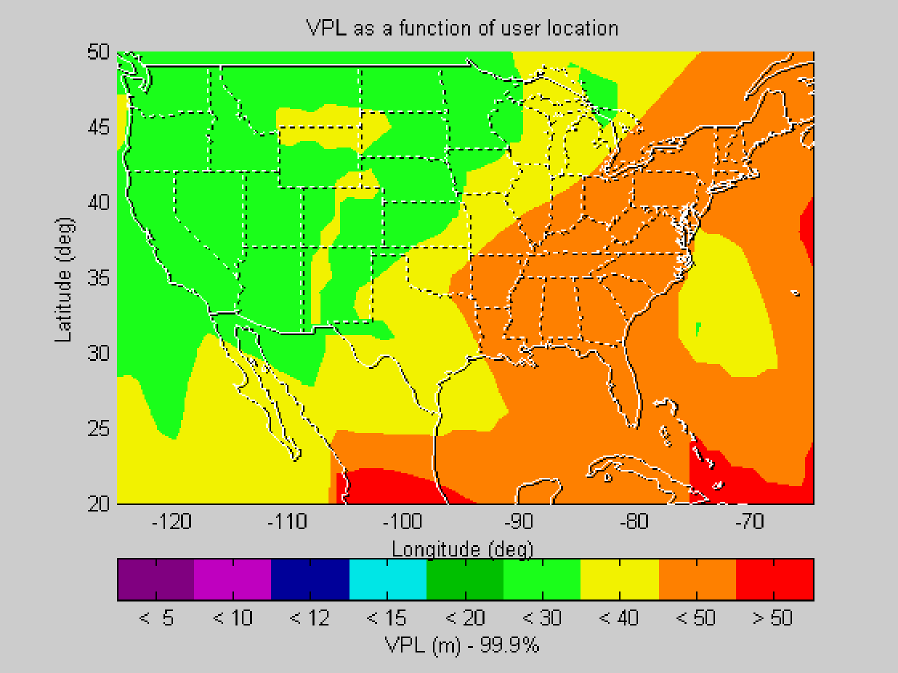

Figure 4.27: The 99.9% VPL contour for an L5 single-frequency user applying the maximum ionospheric delay gradient technique to estimate the ionospheric delay 9 minutes after descending into the RFI field (or at the touchdown point).

To show the benefit for using the maximum ionospheric delay gradient model technique, comparison of two VPL contours is shown in Figure 4.28. The VPL contour on the left is for an L1-L5 dual-frequency user using the maximum ionospheric delay gradient model technique to bound the ionosphere error 9 minutes after losing the L1 frequency to RFI. The VPL values in CONUS on this plot are greater than 20m but less than 50m (LPV VAL). The VPL contour on the right is for an L1-L5 user using the WAAS grid to estimate the ionospheric delay after losing the L1 frequency to RFI. The VPL values in CONUS of this plot are greater than 30m, and some places are greater than 50m (LPV VAL). Therefore, the VPL contour for using the maximum ionospheric delay gradient model technique is better than the VPL contour for using the WAAS grid. Table 4.4 provides a summary table of the MAAST simulation results. As shown in Table 4.4, an

L1-L5 dual-frequency user using the maximum ionospheric delay gradient model technique to estimate the ionospheric delay after losing the L1 frequency to RFI can have a performance similar to the L1-L5 dual-frequency user.

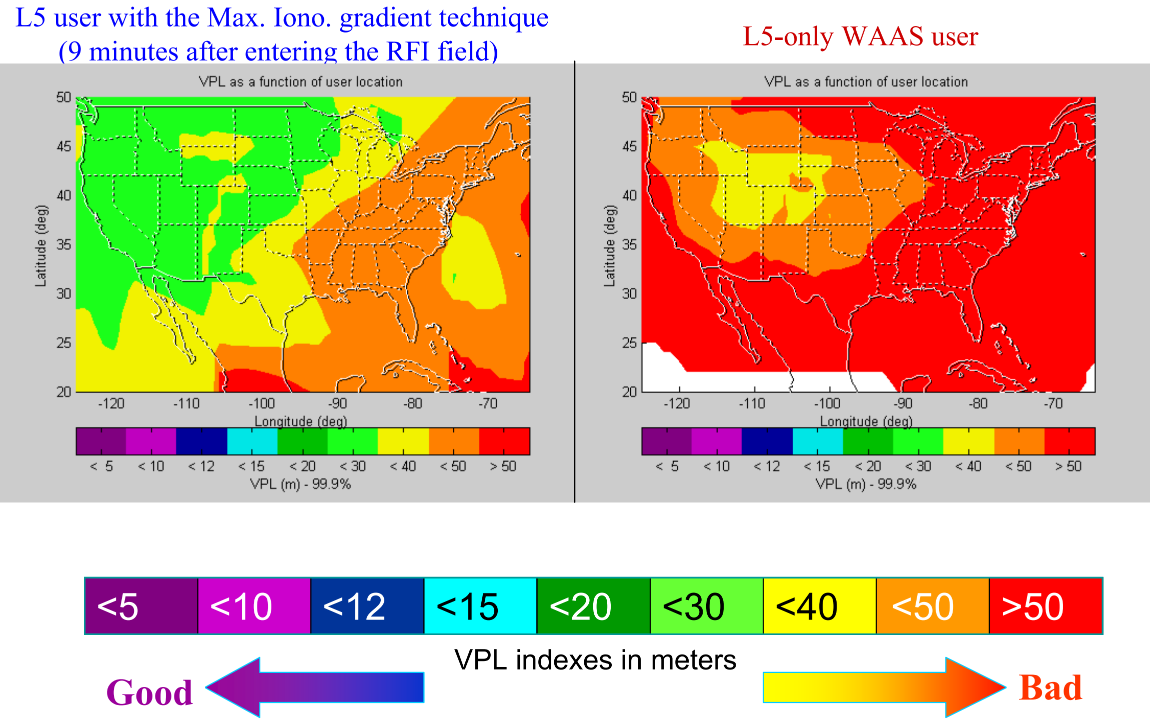

Figure 4.28: The comparison of the VPL contours. The VPL contour on the left is for an L1-L5 dual-frequency user using the maximum ionospheric delay gradient model technique to bound the ionosphere error 9 minutes after losing the L1 frequency to RFI. The VPL contour on the right is for an L1-L5 user using the WAAS grid to estimate the ionospheric delay after losing the L1 frequency to RFI. The color bar shows the VPL indexes in meters. The use of the maximum ionospheric delay gradient model technique provided better ionospheric delay estimation than using the WAAS grid for an L1-L5 dual-frequency airborne user descending into an L1 RFI field.

User Type	CONUS Coverage of LPV precision approach services (Availability ≥ 99.9%)	VPL (in meter)	HPL (in meter)
L1-L5 dual-frequency	100%	12 ≤ VPL < 40	5 ≤ HPL < 20
L1-only single-frequency	97.58%	20 ≤ VPL	15 ≤ HPL
L5-only single-frequency	49.25%	30 ≤ VPL	25 ≤ HPL
L5-only with the code and carrier divergence technique	100%	12 ≤ VPL < 40	5 ≤ HPL < 20
L5-only with the WAAS ionosphere threat model technique (9 minutes after losing L1)	100%	12 ≤ VPL < 40	5 ≤ HPL < 20
L5-only with the maximum ionospheric delay gradient model technique (9 minutes after losing L1)	100%	20 ≤ VPL <50	15 ≤ HPL <30

Table 4.4: The MAAST simulation results.

The above results show that the use of the maximum ionospheric delay gradient model technique outperforms the use of WAAS grid. However, there are many uncertainties about this technique. In the following section, we will discuss two examples to illustrate the uncertainties of this technique. The first example is based on another study which is conducted by the FAA Technical Center, which shows a different maximum ionospheric delay gradient model. This model is based on the ionospheric storm data for April 6-7, 2000. The FAA Technical Center found that the maximum ionospheric delay gradient is 6m/100km in the vertical (which is 6m/19km in [Datta-Barua]). In addition, this study showed that the velocity of the ionospheric wall front is 500m/s (which is 110m/s in [Datta-Barua]). To apply this model, Equation (4.28) is changed as follows:

$$\sigma_{MAX\_IONOgradient} = \left(\frac{6m}{5.33}\right)\cdot\left(\frac{d}{100}\right)\cdot T \qquad (4.33)$$

where,

5.33 is the K_{HMI} value defined in Section 2.3

d is distance from the current position to the place with the last dual-frequency ionospheric delay estimation

T is a multiplier to translate the static receiver model to the dynamic receiver model, which is calculated as follows:

$$T = \frac{V_{Iono\_wall} + V_{IPP} + V_{aircraft}}{V_{Iono\_wall} + V_{IPP}} = \frac{500 + 63 + 46.4}{500 + 63} = 1.0824$$

Therefore, the UIRE calculation for the MAAST simulation is given in Equation (4.34), which is for an L1-L5 dual-frequency user applying this maximum ionospheric delay gradient model technique to bound the ionospheric error 9 minutes after losing the L1-frequency to RFI.

$$\sigma_{UIRE} = \sigma_{UIRE\_L1L5} + \sigma_{MAX\_IONOgradient\_FAA9\min} = \sigma_{UIRE\_L1L5} + 0.3180 \text{ (m)} \qquad (4.34)$$

where,

$$\sigma_{MAX\_IONOgradient\_FAA9\min} = \left(\frac{6}{5.33}\right)\cdot\left(\frac{26.1}{100}\right)\cdot 1.0824 = 0.3180 \text{ (m)}$$

The UIRE value calculated by Equation (4.34) is less than the UIRE value calculated by Equation (4.32). In other words, the performance of the maximum ionospheric delay gradient model developed by the FAA Technical Center is better than the model developed by [Datta-Barua]. The MAAST simulation result for the FAA Technical Center model is shown in Figure 4.29. The VPL values in CONUS on this plot are greater than 20m but less than 50m (LPV VAL).

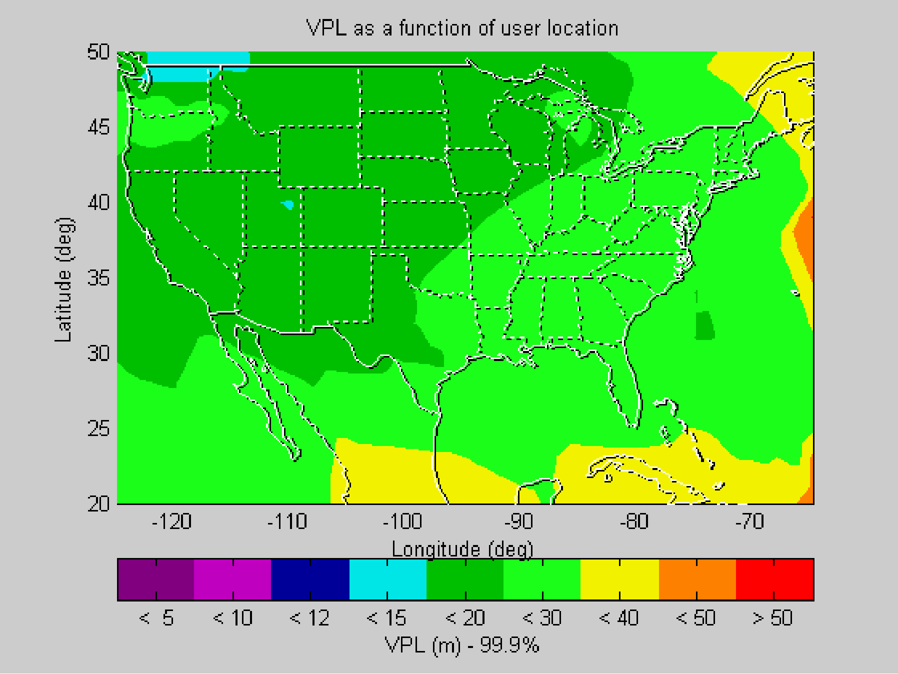

Figure 4.29: The 99.9% VPL contour for an L5 single-frequency user applying the maximum ionospheric delay gradient model developed by the FAA Technical Center to estimate the ionospheric delay 9 minutes after descending into the RFI field (or at the touchdown point).

The second example is to investigate the velocity of IPP. The velocity of IPP (V_{IPP}) used in both the FAA Technical Center's model and Datta-Barua's model is 63m/s, which is nominal velocity for the high elevation IPP. However, as shown in Figure 4.30, the maximum velocity for an IPP at the elevation angle of five degrees can reach 618m/s.

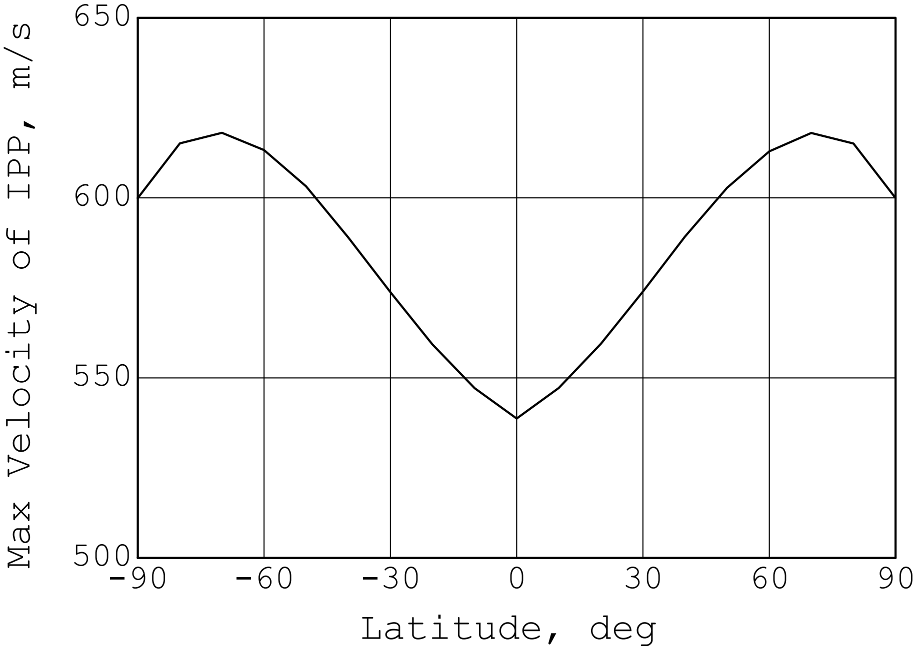

Figure 4.30: The maximum velocity of IPP. The maximum velocity of IPP can reach 618m/s at the latitude of 70^o N. (Courtesy: Takeyasu Sakai)

Take this maximum IPP velocity into account, Equation (4.28) is changed as follows:

$$\sigma_{MAX\_IONOgradient\_V\max IPP} = \left(\frac{6}{5.33}\right) \cdot \left(\frac{d}{19}\right) \cdot T \qquad (4.35)$$

where,

$$T = \frac{V_{Iono\_wall} + V_{IPP} + V_{aircraft}}{V_{Iono\_wall} + V_{IPP}} = \frac{110 + 618 + 46.4}{110 + 63} = 6.7306$$

For an L1-L5 dual-frequency user applying this maximum ionospheric delay gradient model technique to bound the ionospheric error 9 minutes after losing the L1-frequency to RFI, the UIRE is calculated in Equation (4.36)

$$\sigma_{UIRE} = \sigma_{UIRE\_L1L5} + \sigma_{MAX\_IONOgradient\_V\max IPP\_9\min} = \sigma_{UIRE\_L1L5} + 10.4082 \text{ (m)} \qquad (4.36)$$

where,

$$\sigma_{MAX\_IONOgradient\_V\max IPP\_9\min} = \left(\frac{6}{5.33}\right)\cdot\left(\frac{26.1}{19}\right)\cdot 6.7306 = 10.4082 \text{ (m)}$$

The σ_{UIRE} calculated in Equation (4.36) is greater than the nominal σ_{UIRE} for an L5 single-frequency GPS/WAAS user (6m at the coasts and 3.5m at the center). In this case, using the maximum ionospheric delay gradient model to bound the ionospheric error does not provide better performance than using the WAAS grid. However, this example is to illustrate how fast this gradient could grow under some scenarios. Currently, there are many uncertainties of this technique which are still under investigation, therefore, this example is not necessary the worst-case.

In summary, based on the information available to the user, there are three techniques to sustain the dual-frequency ionospheric delay estimation. This analysis uses the typical precision approach example based on SFO to examine the possible solutions, and then uses the MAAST to measure all airports over CONUS. First, one can use the code-carrier divergence technique to continue ionospheric delay estimation; this technique would require that there are no cycle slips. This technique provides good ionospheric delay estimation (better than using the WAAS grid) for the full duration of approach. Second, one can use the WAAS ionosphere threat model technique to bound the error. This technique requires an ionosphere storm detector and additional information be broadcasted to the user. It provides useful ionospheric delay estimation for at least 10 minutes. Third, one can use the maximum ionospheric delay gradient model technique to estimate ionospheric delay during the ionosphere storm period. This technique should only be used when there is no available ionosphere storm detector. The maximum ionospheric delay gradient model technique may provide useful ionospheric delay estimation for at least 10 minutes at mid-latitude. Figure 4.31 shows a summary comparison of the uses of these three techniques at the touchdown point. The VPL contour plots are shown in the order of the VPL performance from top to bottom. The use of the code and carrier divergence technique is the best, the use of the WAAS ionosphere threat model technique is second best, and the use of the maximum ionospheric delay gradient technique places third.

Comparison of the Techniques for Graceful Reversion from Dual to Single Frequency WAAS

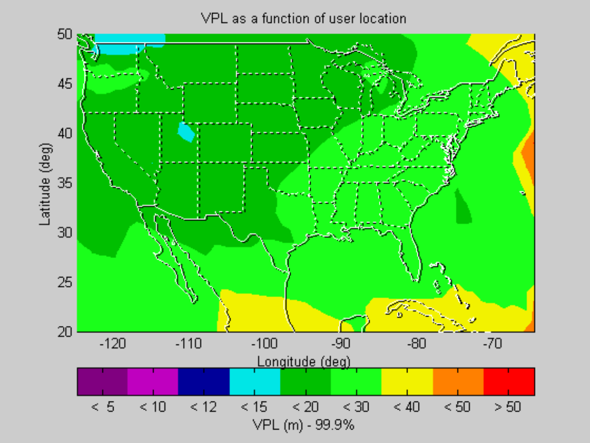

The Code and Carrier Divergence Technique

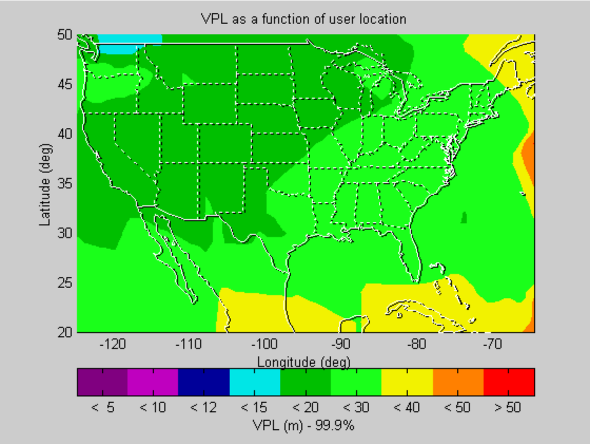

The WAAS Iono. Threat Model Technique

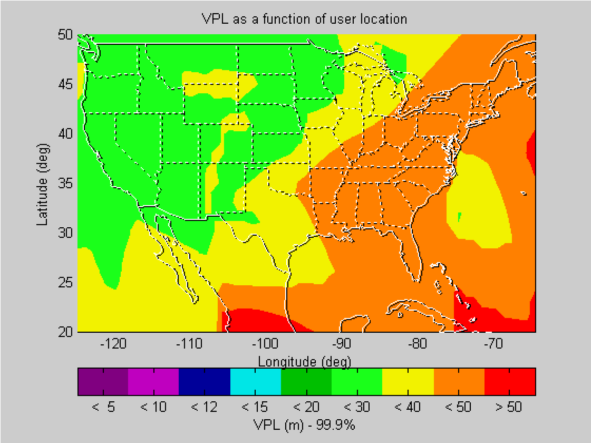

The Max. Iono. Delay Gradient Model Technique

Figure 4.31: A summary comparison of the uses of these three techniques at the touchdown point. The VPL contour plots are shown in the order of the VPL performance from top to bottom.

4.4 CONCLUSIONS

This chapter discussed the situation when an L1-L5 dual-frequency airborne user descended into an RFI field, which introduced the L1-only single frequency case and the L5-only single-frequency case. The effects of parameter changes in the protection level calculation for the L1-only and L5-only single-frequency GPS/WAAS users were discussed in this chapter, and followed by the MAAST simulation results. The MAAST simulation results showed that an L1-only single-frequency user has LPV precision approach services available 99.9% of the time over 97.58% of CONUS and an L5-only single-frequency user has LPV precision approach services available 99.9% of the time over 49.25% of CONUS.

This chapter also provided techniques for users to sustain a performance similar to the dual-frequency users. These techniques are the code and carrier divergence technique, the WAAS ionosphere threat model technique, and the maximum ionospheric delay gradient model technique. This chapter first used the typical precision approach example based on SFO to examine these techniques, and then used the MAAST to measure all airports over CONUS. This thesis assumed that an aircraft loses the L1 frequency to RFI, and there is another condition which is an aircraft losing the L5 frequency to RFI. In this case, the performances of these techniques are as good as the results shown in this chapter.

In order to use the code and carrier divergence technique to estimate the ionospheric delay, this thesis suggested that a more stable cycle slip detector is required for the aviation users. This is because the current cycle slip detector built in the receiver is not adequate for aviation use. In the case of cycle slips, users can use the WAAS ionosphere threat model technique to bound the ionospheric error. Before applying this technique, users need to verify that no ionosphere storm is present. The most efficient way for solving this problem is to include a new WAAS message which will indicate the presence of an ionosphere storm in addition to the GIVE message. Furthermore, if there are cycle slips and there is no available ionosphere storm detector, users might be able to use the maximum ionospheric delay gradient model technique to bound the ionospheric error. However, this technique has many uncertainties that still need to be investigated and resolved. One recommendation made by this thesis is to incorporate all the parameters used in the maximum ionospheric delay gradient model technique into a new WAAS message, that will include the velocity of all IPP, the velocity of ionospheric wall, the applicable range (i.e., 19km or 100km), and the difference of the vertical ionospheric delay over this range (i.e., 6m). This new WAAS message will allow a user to dynamically generate an ionospheric delay gradient model to bound the ionospheric error.

Chapter 5

WAAS Utilization of the New Civil Signal at L2

5.1 INTRODUCTION

GPS modernization not only adds an additional new GPS frequency, L5, in an Aeronautical Radio Navigation Service (ARNS) band but also adds the civil code to L2. Adding the civil code to L2 will improve the use of GPS for civilian applications because it eliminates the need for the fragile semi-codeless tracking technique now used to acquire L2 measurements. As discussed in Section 1.1.1, the ionospheric delay is inversely proportional to the square of signal frequency. Therefore, the ionospheric delay at L2 is 65% larger than at L1, and at L5 it is 80% larger than L1. While L2 outperforms L5 in ionospheric delay, L2 is not in an ARNS band and the FAA does not plan to use its civil signal for aviation applications. In order to maximize the new civil signal benefits to WAAS, this chapter investigates the possible use of L2 for civil aviation applications.

If an L1-L2-L5 three-frequency airborne user experiences moderate RFI and loses one of the GPS frequencies, it will revert to operation using L1-L5, L1-L2, or L2-L5. If the three-frequency user experiences severe RFI and loses two of the GPS frequencies, then it will logically revert to L1-only, L2-only, or L5-only operation. The L1-L5 dual-frequency user was discussed in Chapter 3, and the L1-only and the L5-only single-frequency users were discussed in Chapter 4. This chapter will investigate the L2-only single-frequency user, the L1-L2 dual-frequency user, and the L2-L5 dual-frequency user.

This chapter is organized as follows. Section 5.2 discusses the L2-only single-frequency GPS/WAAS user and the necessary changes in the WAAS protection level calculation for this L2-only user. The MAAST simulation results for an L2-only single-frequency user are included in this section. The L1-L2 and L2-L5 dual-frequency GPS/WAAS users and the changes in the protection level calculation for these two users are discussed in Section 5.3. This section includes the MAAST simulation results for the L1-L2 and L2-L5 dual-frequency users. Section 5.4 presents a summary and concluding remarks.

5.2 L2-ONLY SINGLE-FREQUENCY GPS/WAAS USER

As stated previously, an L1-L2-L5 three-frequency user that loses two of its GPS frequencies will revert to L1-only, L2-only, or L5-only operation. Similar to the L1-only and the L5-only single-frequency users, discussed in Section 4.2, an L2-only single-frequency user relies on WAAS to provide corrections to the GPS satellite clock and ephemeris errors. An L2-only single-frequency airborne user is required to use WAAS for precision approaches. However, the current WAAS corrections are specified for L1-only. Similar to the L5-only single frequency user, the L2-only single frequency users will require some additional modifications before they can apply the WAAS correction to their position-fix.

5.2.1 CHANGES IN THE WAAS PROTECTION LEVEL CALCULATION

When comparing the pseudorange measurement on L2 in Equation (3.2) with the pseudorange measurement on L1 in Equation (3.1), the differences will be the ionospheric delays ($\gamma_{1,2} \cdot I_j^i$), the satellite L1-L2 hardware group delays ($\tau_{gd1,2}$) and user receiver L1-L2 hardware group delays ($IFB_{1,2}$). In Equation (3.2), $\gamma_{1,2}$ equals 1.65. Thus, the ionospheric delay on L2 is 1.65 times larger than the ionospheric delay on L1. That also means the uncertainty of the ionospheric delay estimation on L2 is 1.65 times larger than the uncertainty of the ionospheric delay estimation on L1. Therefore, the WAAS L1 ionospheric delay correction needs to increase 1.65 times for an L2-only user, and the associated variance (confidence) needs to increase $(1.65)^2$ times for an L2-only user. In the WAAS protection level calculation, the new UIRE calculation for an L2-only user is

$$\sigma_{i,UIRE\_L2}^2 = \gamma_{1,2}^2 \cdot \sigma_{i,UIRE\_L1}^2 = (1.65)^2 \cdot \sigma_{i,UIRE\_L1}^2 \tag{5.1}$$

The changes in the UIRE confidence calculation are summarized in Figure 5.1.

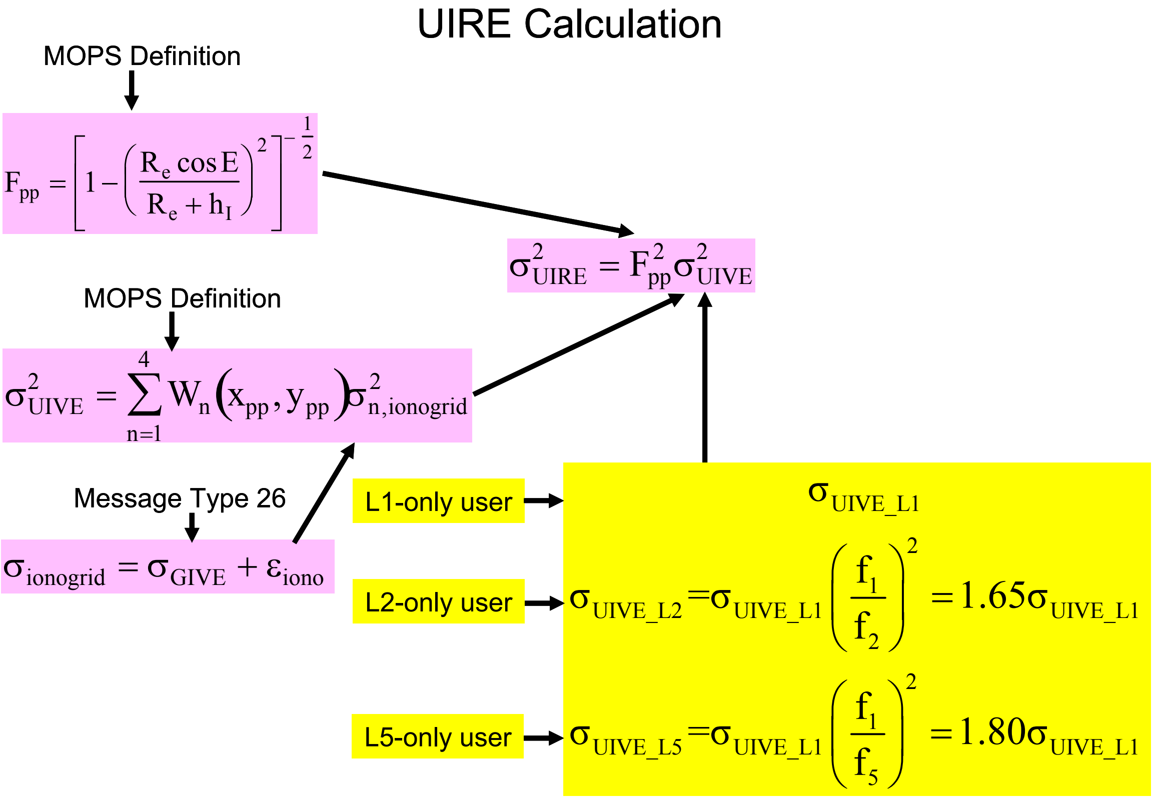

Figure 5.1: Summary of changes in User Ionosphere Range Error (UIRE) confidence calculation.

In addition to the UIRE calculation, the confidence calculation of the satellite L1-L2 group delay ($\tau_{gd1,2}$) is already included in the current UDRE calculation as defined in the WAAS MOPS [RTCA1]. This thesis assumed that all three frequencies were available to ground (WRSs), but not to the airborne user, such that, the $\tau_{gd1,2}$ can be estimated to compute the

UDRE and GIVE. The UDRE model will be unchanged for the L2-only single frequency user.

The protection level calculation for the L1-only, the L2-only, and the L5-only single-frequency GPS/WAAS users is summarized in Figure 5.2, and the yellow highlighted portion represents the changes.

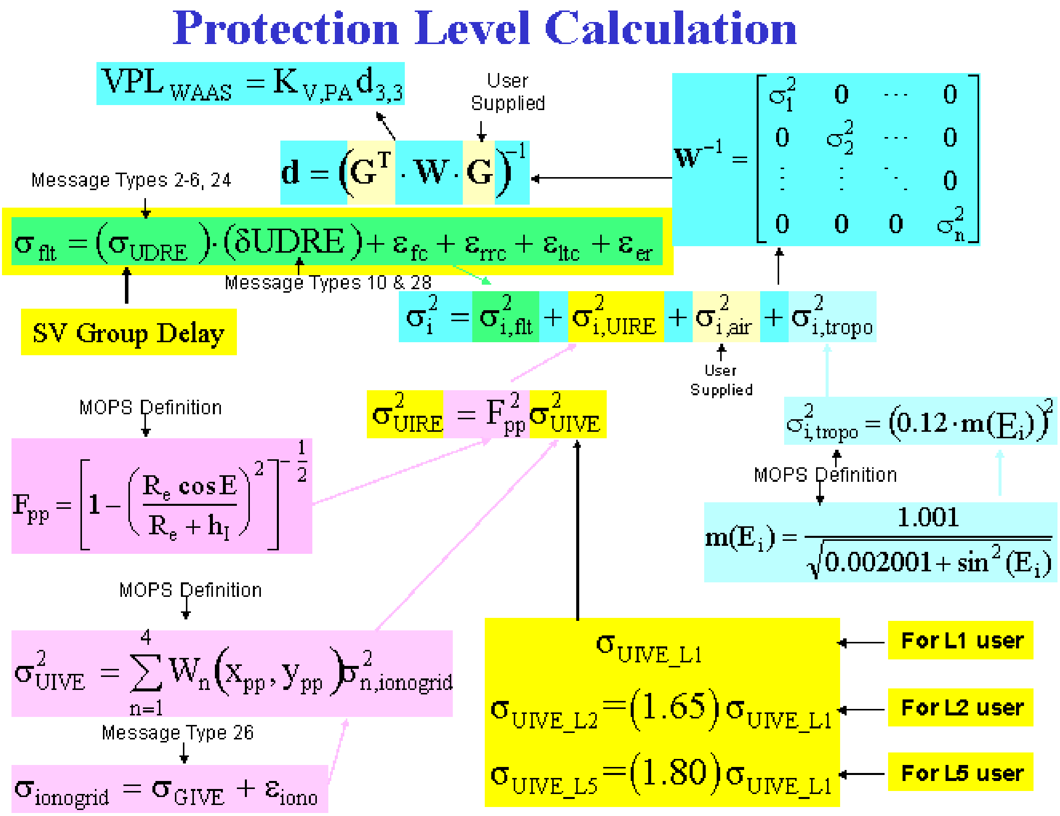

Figure 5.2: Summary of changes in the protection level calculation for the L1-only, the L2-only, and L5-only single-frequency GPS/WAAS users. Only the yellow highlighted portion is changed, the other terms are unchanged as defined in the WAAS MOPS.

5.2.2 MAAST SIMULATION RESULTS

The MAAST was modified to include the protection level calculation shown in Figure 5.2 to simulate the L2-only single-frequency users. To be consistent and for easy of comparison, the simulation configurations of MAAST will be kept the same as in the previous chapters, as shown in Table 3.1.

The simulation results for an L2-only single-frequency GPS/WAAS user are shown in Figures 5.3-5.5. Figure 5.3 shows the LPV coverage simulation results for an L2-only single-frequency user. This user has LPV precision approach services available 99.9% of the time over 58.34% of CONUS. Figure 5.4 shows the VPL contour for an L2-only user in CONUS, and Figure 5.5 represents the HPL contour for an L2-only user in CONUS. The 99.9% shown in Figures 5.3-5.5 represents the fraction of users within those regions that had an availability of 99.9% or greater.

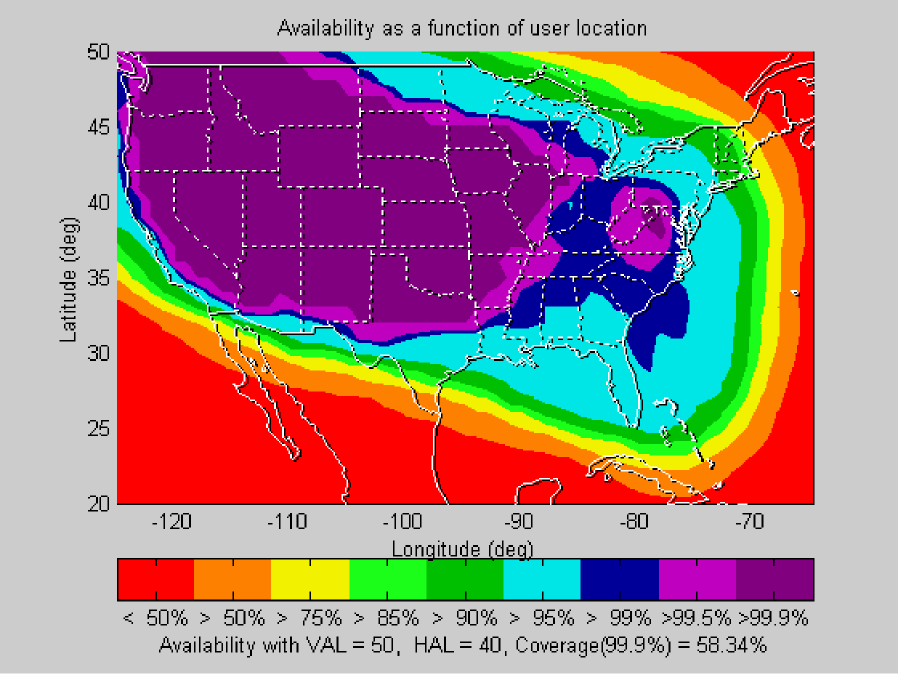

Figure 5.3: Coverage of an L2-only single-frequency GPS/WAAS user in CONUS is 58.34% with VAL = 50m, HAL = 40m.

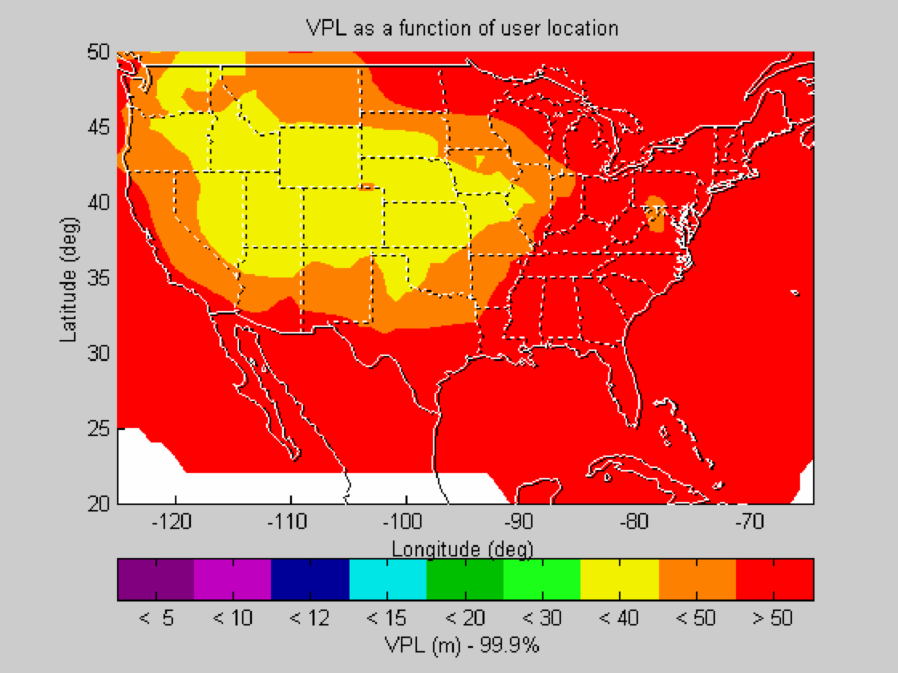

Figure 5.4: Vertical Protection Level (VPL) contour of an L2-only single-frequency GPS/WAAS user in CONUS.

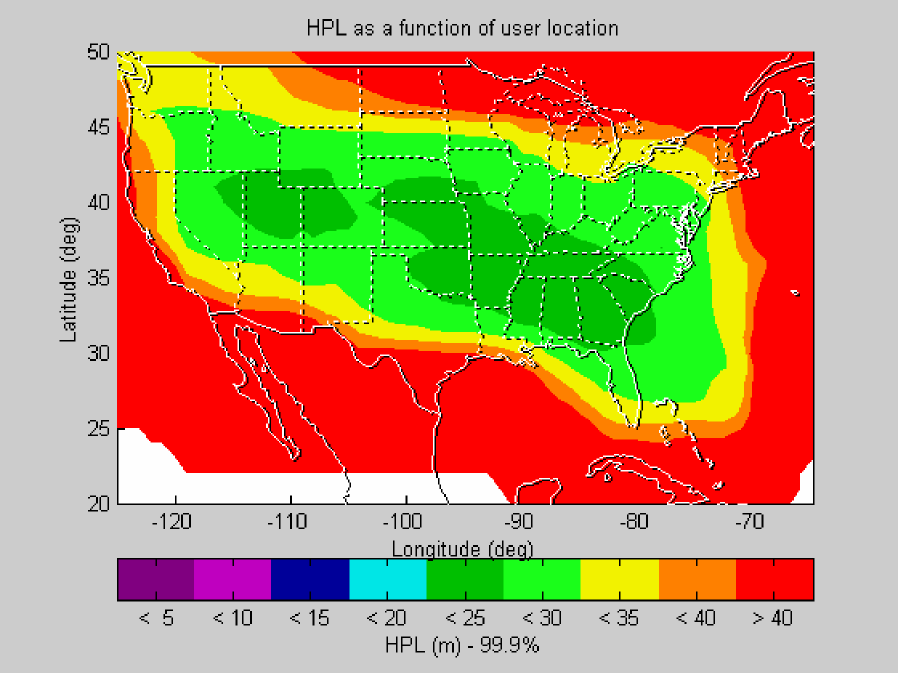

Figure 5.5: Horizontal Protection Level (HPL) contour of an L2-only single-frequency GPS/WAAS user in CONUS.

Examining the MAAST simulation results from Section 4.2.3, the LPV precision approach service coverage of an L1-only single-frequency GPS/WAAS user is 97.58%. This is better than the coverage of an L2-only single-frequency GPS/WAAS user which is 58.34%. It is also better than the coverage of an L5-only single-frequency GPS/WAAS user which is 49.25%. The loss of coverage is due to the lower GPS frequencies having larger ionospheric delay uncertainty. Table 5.1 provides a summary table of our MAAST simulation results.

User Type	CONUS Coverage of LPV precision approach services (Availability ≥ 99.9%)	VPL (in meter)	HPL (in meter)
L1-L5 dual-frequency	100%	$12 \le VPL < 40$	$5 \le HPL < 20$
L1-only single-frequency	97.58%	$20 \le VPL$	$15 \le HPL$
L5-only single-frequency	49.25%	$30 \le VPL$	$25 \le HPL$
L5-only with the code and carrier divergence technique	100%	$12 \le VPL < 40$	$5 \le HPL < 20$
L5-only with the WAAS ionosphere threat model technique (9 minutes after losing L1)	100%	$12 \le VPL < 40$	$5 \le HPL < 20$
L5-only with the maximum ionospheric delay gradient model technique (9 minutes after losing L1)	100%	$20 \le VPL < 50$	$10 \le HPL < 30$
L2-only single-frequency	58.34%	$30 \le VPL$	$20 \le HPL$

Table 5.1: The MAAST simulation results.

5.3 L1-L2 AND L2-L5 DUAL-FREQUENCY USERS

If an L1-L2-L5 three-frequency airborne user experiences moderate RFI and loses one of GPS frequencies, it will revert to operation using L1-L5, L1-L2, or L2-L5. The L1-L5 dual-frequency user case was discussed in Section 3.2. The L1-L2 and the L2-L5 dual-frequency user cases will be investigated in this section.

The ionospheric delay is frequency dependent. Therefore, a dual-frequency user can directly estimate the ionospheric delay in the airplane, and then subtract this estimation from the pseudorange measurement. As stated previously, the τ_{gd} information is required to get the desired dual-frequency performance. This direct use of dual-frequency is more accurate and offers higher availability. This is true for the L1-L5 and the L1-L2 dual-frequency users, but not for an L2-L5 dual-frequency user. The reason will be investigated later in this section. This section discusses the changes in the protection level calculation for the L1-L2 and L2-L5 dual-frequency users in comparison with the current protection level calculation defined in the WAAS MOPS for an L1-only user.

5.3.1 L1-L2 DUAL-FREQUENCY USER

The L1-L2 dual-frequency user is similar to the L1-L5 dual-frequency user described in Section 3.2, and this section discusses specifically the L1-L2 case. The new protection level calculation for an L1-L2 dual-frequency user is summarized in Figure 5.6. Figure 5.6 also shows the section number where the new confidence estimates for the correction are derived. The changes of the protection level calculation for an L1-L2 dual-frequency user are highlighted yellow in Figure 5.6 and summarized as follows:

- The calculation of the fast and long term correction degradation confidence ($\sigma_{i,flt}$) includes the confidence of the satellite L1-L2 group delay (σ_{SV_L1L2}) in the UDRE calculation. The satellite hardware group delays were discussed in Section 3.2.1. The new UDRE calculation will be discussed in Section 5.3.1.1.

- The new calculation of the user ionosphere range error confidence ($\sigma_{i,UIRE\_L1L2}$) will be specified in Section 5.3.1.2.

- There is no separate airborne receiver confidence term ($\sigma_{i,air}$) in the protection level calculation for the L1-L2 dual-frequency GPS user because it was already included in the new $\sigma_{i,UIRE\_L1L2}$ calculation. This will also be discussed in Section 5.3.1.2.

- The calculation of the tropospheric delay confidence ($\sigma_{i,tropo}$) is the same as defined in the WAAS MOPS for an L1-L2 dual-frequency GPS user.

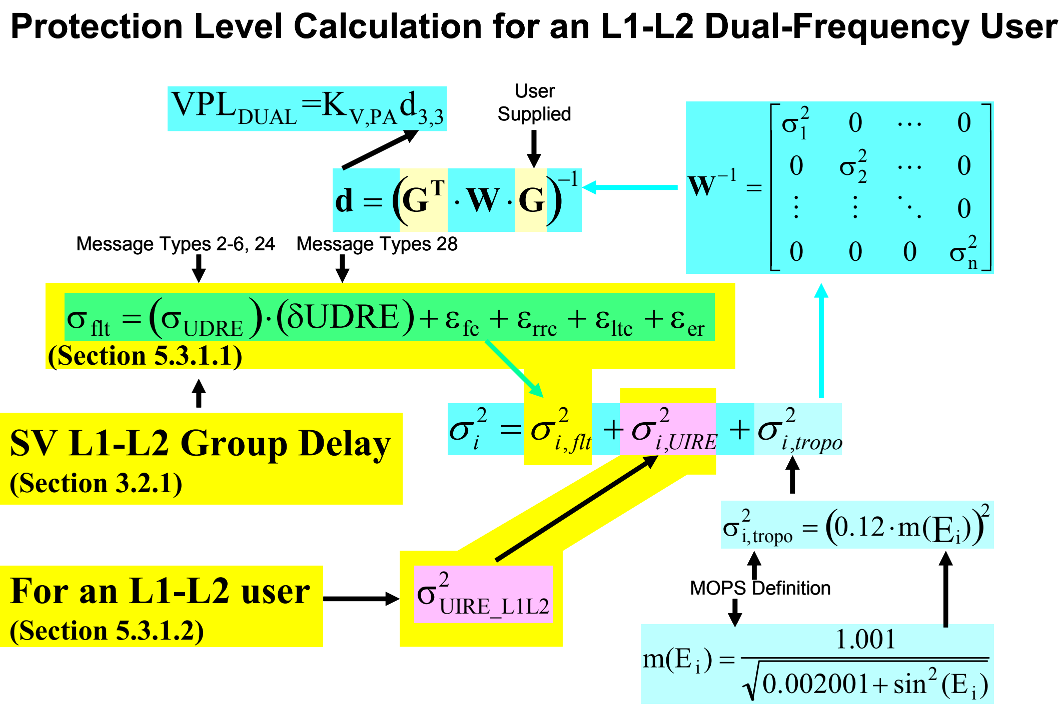

Figure 5.6: Summary of changes in the protection level calculation for an L1-L2 dual-frequency user. Only the highlighted yellow portion is changed, the other terms are unchanged as defined in the WAAS MOPS.

5.3.1.1 UDRE CALCULATION FOR AN L1-L2 DUAL-FREQUENCY USER

For an L1-L2 dual-frequency user, the estimation error of the satellite L1-L2 group delay ($\tau_{gd1,2}$) needs to be taken into account for the UDRE calculation. As a result, the WAAS MOPS will be modified to include either the Satellite hardware group delays ($\tau_{gd1,2}$, $\tau_{gd1,5}$, and $\tau_{gd2,5}$) or the confidence of the estimation error of the satellite hardware group delay (σ_{SV_L1L2}, σ_{SV_L1L5}, and σ_{SV_L2L5}). The confidence of the estimation error of the satellite hardware group delay was discussed in Section 3.2.1. Based on the current observed performance, the confidence of the satellite L1-L2 group delay estimation error (σ_{SV_L1L2}) is 0.192m. As discussed in Section 3.2.1, the new UDRE calculation will include the confidence of the satellite group delay estimation errors, σ_{SV_L1L2}, σ_{SV_L1L5}, and σ_{SV_L2L5}, to protect the L1-L2, L1-L5, and L2-L5 dual-frequency users, respectively.

5.3.1.2 NEW UIRE CALCULATION FOR AN L1-L2 DUAL-FREQUENCY USER

An L1-L2 dual-frequency user can estimate the ionospheric delay directly in the airplane, and then subtract this estimation from the pseudorange measurements. Similar to the L1-L5 dual-frequency user discussed in Section 3.2.2, there are three factors which affect the quality of the L1-L2 dual-frequency ionospheric delay estimation:

- The receiver noise and multipath errors of the L1-L2 dual-frequency receiver.
- The satellite L1-L2 hardware group delay error ($\tau_{gd1,2}$).
- The receiver L1-L2 hardware group delay error ($IFB_{1,2}$).

As discussed in Section 3.2.2, the quality (confidence) of the L1-L2 dual-frequency ionospheric delay estimation can be calculated by Equation (3.19).

$$\sigma^2_{UIRE\_L1L2} = \left[\frac{f_1^2}{f_1^2 - f_2^2}\right]^2 \left[\sigma^2_{air,L1}\right] + \left[\frac{f_2^2}{f_1^2 - f_2^2}\right]^2 \left[\sigma^2_{air,L2}\right] + \left[\sigma^2_{SV\_L1L2}\right] \tag{3.19}$$

As shown in Equation (3.19), the confidence of the residual airborne receiver noise and multipath errors is already included in the calculation of the L1-L2 dual-frequency user ionosphere range error confidence. Thus, there is no additional term needed in the protection level calculation for the airborne receiver confidence for the L1-L2 dual-frequency user.

5.3.1.3 MAAST SIMULATION RESULTS

The MAAST was modified to include all necessary changes in the protection level calculation to simulate the L1-L2 dual-frequency users. The simulation configuration of MAAST will be kept the same as shown in Table 3.1.

The simulation results for an L1-L2 dual-frequency GPS/WAAS user are shown in Figures 5.7-5.9. Figure 5.7 shows the LPV coverage simulation results for an L1-L2 dual-frequency user. This user has LPV precision approach services available 99.9% of the time over 100% of CONUS. Figure 5.8 and Figure 5.9 show the VPL contour and the HPL contour for an L1-L2 dual-frequency user in CONUS, respectively. The 99.9% shown in Figures 5.7-5.9 represents the fraction of users within those regions that had an availability of 99.9% or greater.

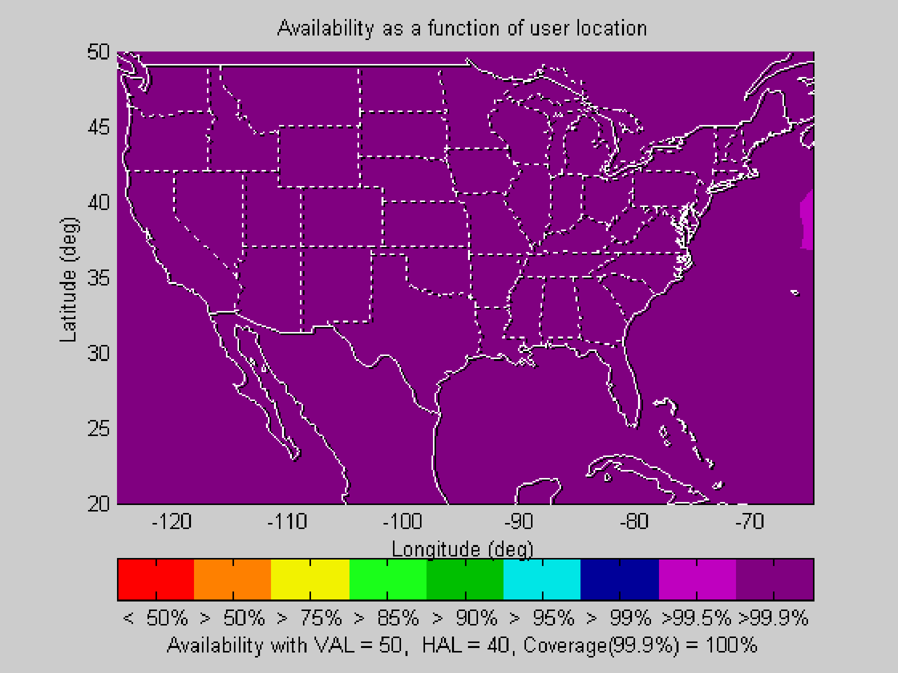

Figure 5.7: Coverage of an L1-L2 dual-frequency GPS/WAAS user in CONUS is 100% with VAL = 50m, HAL = 40m.

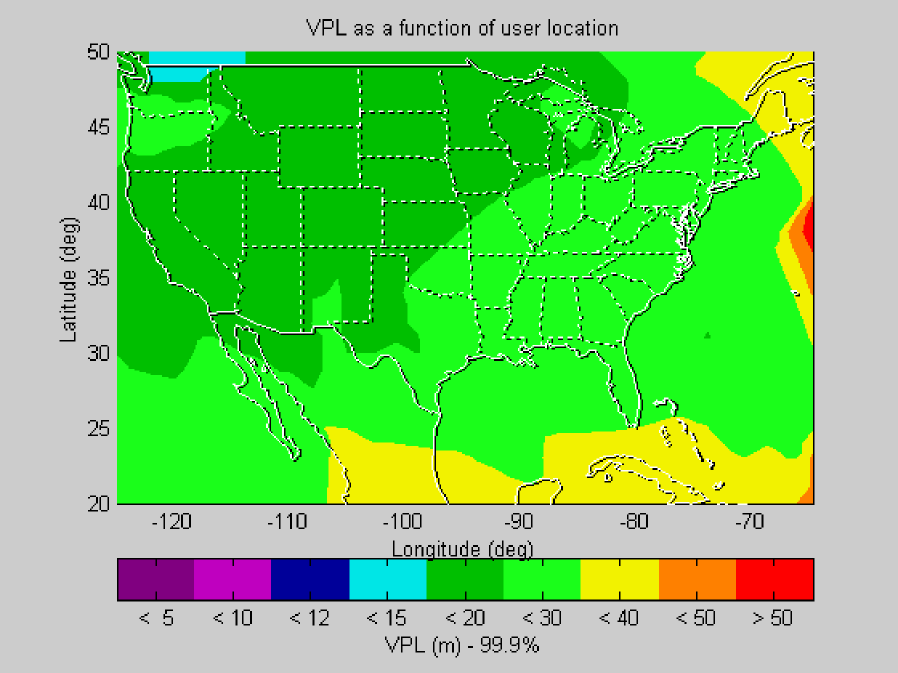

Figure 5.8: Vertical Protection Level (VPL) contour of an L1-L2 dual-frequency user in CONUS.

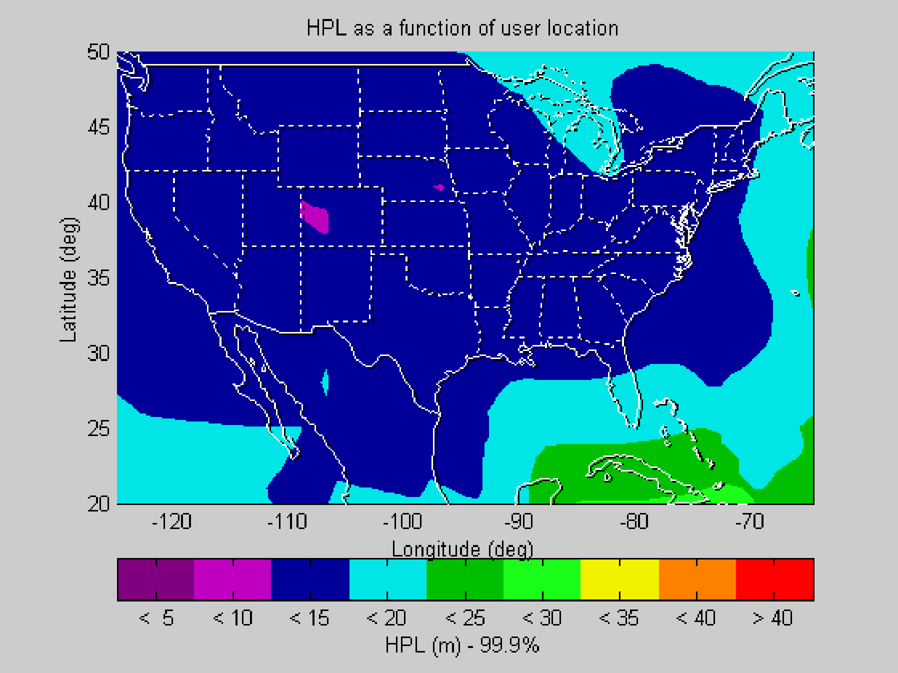

Figure 5.9: Horizontal Protection Level (HPL) contour of an L1-L2 dual-frequency user in CONUS.

Reviewing the MAAST simulation results from Section 3.3, the LPV precision approach service coverage of both the L1-L2 and L1-L5 dual-frequency users are 100%. When comparing the VPL and HPL contours, the L1-L5 dual-frequency user case has a better time availability than the L1-L2 dual-frequency user case. Table 5.2 provides a summary table of the MAAST simulation results.

User Type	CONUS Coverage of LPV precision approach services (Availability ≥ 99.9%)	VPL (in meter)	HPL (in meter)
L1-L5 dual-frequency	100%	12 ≤ VPL < 40	5 ≤ HPL < 20
L1-only single-frequency	97.58%	20 ≤ VPL	15 ≤ HPL
L5-only single-frequency	49.25%	30 ≤ VPL	25 ≤ HPL
L5-only with the code and carrier divergence technique	100%	12 ≤ VPL < 40	5 ≤ HPL < 20
L5-only with the WAAS ionosphere threat model technique (9 minutes after losing L1)	100%	12 ≤ VPL < 40	5 ≤ HPL < 20
L5-only with the maximum ionospheric delay gradient model technique (9 minutes after losing L1)	100%	20 ≤ VPL < 50	10 ≤ HPL < 30
L2-only single-frequency	58.34%	30 ≤ VPL	20 ≤ HPL
L1-L2 dual-frequency	100%	12 ≤ VPL < 40	5 ≤ HPL < 20

Table 5.2: The MAAST simulation results.

5.3.2 L2-L5 DUAL-FREQUENCY USER

A dual-frequency user can directly estimate the ionospheric delay in the airplane, and then subtract this estimation from the pseudorange measurement. In general, this direct use of dual-frequencies should be more accurate and offer higher availability. However, when a three-frequency user loses the L1 frequency to RFI, the most worrisome dual-frequency user case is introduced: L2-L5. This section will show why the direct use of the L2-L5 dual-frequency to estimate the ionospheric delay does not provide higher availability. This section begins with the changes in the protection level calculation for an L2-L5 dual-frequency user.

5.3.2.1 NEW UDRE CALCULATION FOR THE L2-L5 DUAL-FREQUENCY USER

For an L2-L5 dual-frequency user, the estimation error of the satellite L2-L5 group delay needs to be taken into account for the UDRE calculation. The confidence of the estimation error of the satellite hardware group delay was discussed in Section 3.2.1. Based on Equation (3.14), the confidence of the satellite L2-L5 group delay estimation error (σ_{SV_L2L5}) is 0.290m. This confidence will be included in the new UDRE calculation to protect an L2-L5 dual-frequency user.

5.3.2.2 NEW UIRE CALCULATION FOR THE L2-L5 DUAL-FREQUENCY USER

Similar to the L1-L2 and the L1-L5 dual-frequency users, Equation (3.19) measures the confidence of the L2-L5 dual-frequency ionospheric delay estimation.

$$\sigma^2_{UIRE\_L2L5} = \left[\frac{f_2^2}{f_2^2 - f_5^2}\right]^2 \left[\sigma^2_{air,L2}\right] + \left[\frac{f_5^2}{f_2^2 - f_5^2}\right]^2 \left[\sigma^2_{air,L5}\right] + \left[\sigma^2_{SV\_L2L5}\right] \tag{3.19}$$

The two coefficients, $\left[\frac{f_2^2}{f_2^2 - f_5^2}\right]^2$ called *C1* and $\left[\frac{f_5^2}{f_2^2 - f_5^2}\right]^2$ called *C2*, in Equations (3.19), depend on the separation between the L2 and L5 GPS frequencies. As shown in Figure 3.4, the *C1* and *C2* for the L2-L5 dual-frequency user are much larger than the *C1* and *C2* for the L1-L2 and L1-L5 dual-frequency users, because of the much narrower separation between the L2 and L5 frequencies. Therefore, the quality of the L2-L5 dual-frequency ionospheric delay estimation will not be as good as other dual-frequency users.

5.3.2.3 MAAST SIMULATION RESULTS

In comparison with the current protection level calculation defined in the WAAS MOPS, the protection level calculation for an L2-L5 dual-frequency user is summarized as follows:

- The new calculation of the fast and long term correction degradation confidence ($\sigma_{i,flt}$) includes the confidence of the satellite L2-L5 group delay (σ_{SV_L2L5}) in the UDRE calculation.
- The new calculation of the user ionosphere range error confidence ($\sigma_{i,UIRE\_L2L5}$) is specified in this section.
- There is no separate airborne receiver confidence term ($\sigma_{i,air}$) in the protection level calculation for the L2-L5 dual-frequency GPS user because it was already included in the new $\sigma_{i,UIRE\_L2L5}$ calculation.
- The calculation of the tropospheric delay confidence ($\sigma_{i,tropo}$) is the same as defined in the WAAS MOPS for an L2-L5 dual-frequency GPS user.

The MAAST is modified according to the above changes to simulate the L2-L5 dual-frequency user. To be consistent and for easy of comparison, the simulation configurations of MAAST will be kept the same as in the previous chapters, as shown in Table 3.1.

The simulation results for an L2-L5 dual-frequency GPS/WAAS user are shown in Figures 5.10-5.12. Figure 5.10 shows the LPV coverage simulation results for an L2-L5 dual-frequency user. This user has LPV precision approach services available 99.9% of the time over only 10.81% of CONUS. Figure 5.11 and Figure 5.12 show the VPL contour and HPL contour for an L2-L5 dual-frequency user in CONUS, respectively. The 99.9% shown in Figures 5.10-5.12 represents the fraction of users within those regions that had an availability of 99.9% or greater.

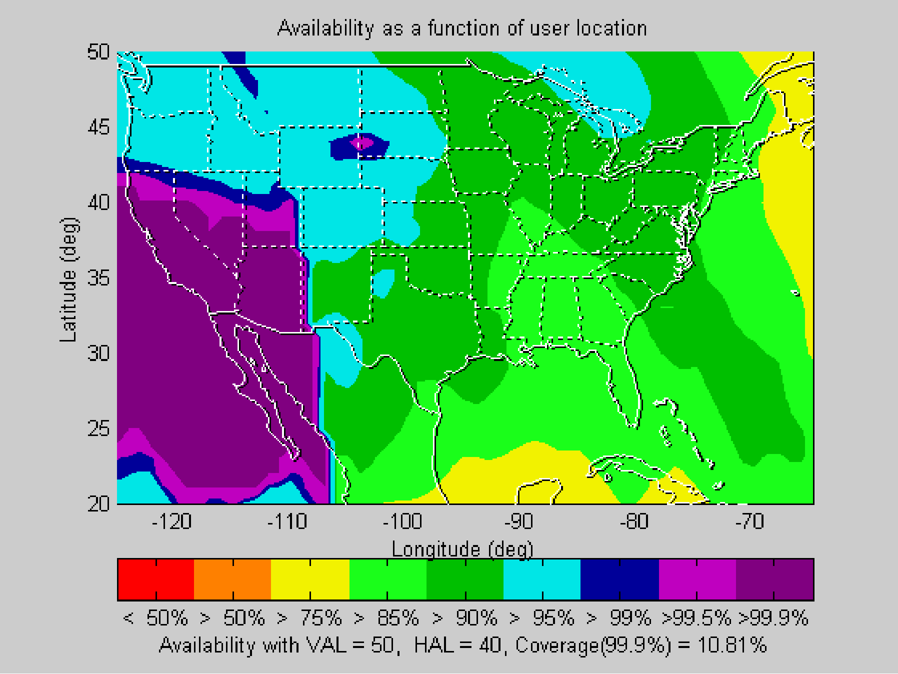

Figure 5.10: Coverage of an L2-L5 dual-frequency GPS/WAAS user in CONUS is only 10.81% with VAL = 50m, HAL = 40m.

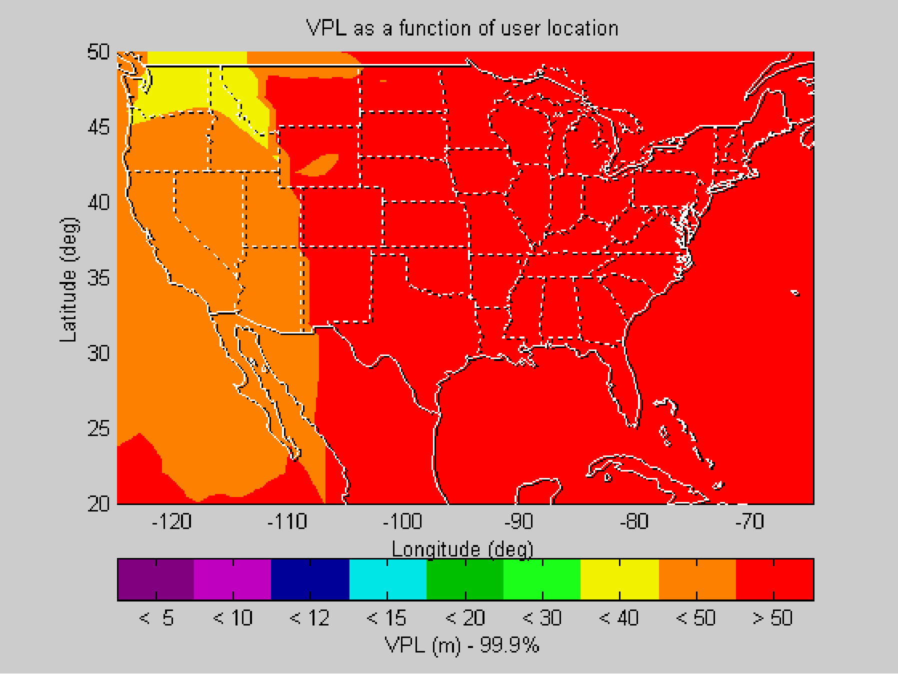

Figure 5.11: Vertical Protection Level (VPL) contour of an L2-L5 dual-frequency user in CONUS.

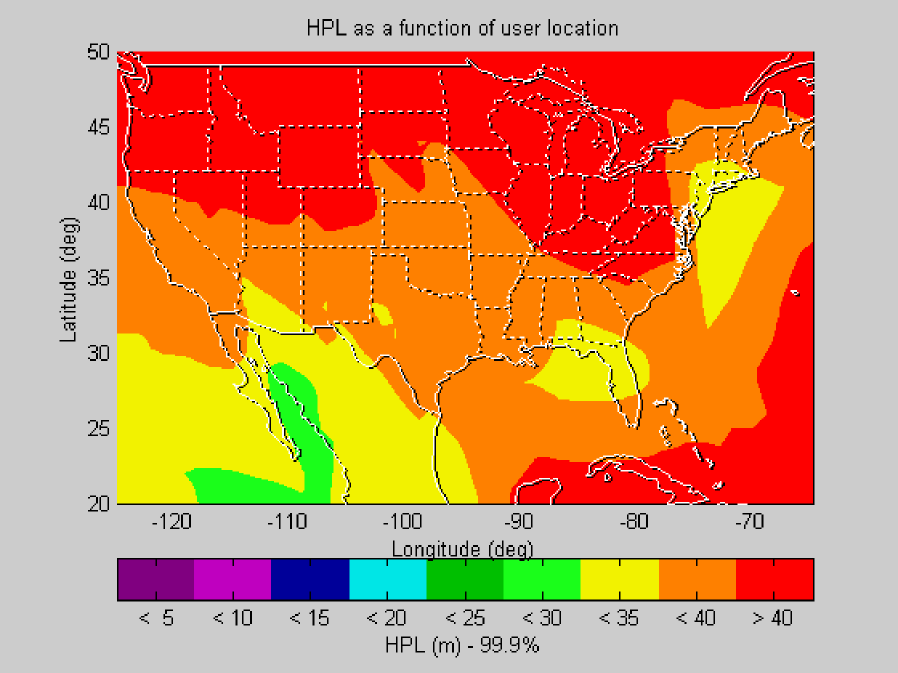

Figure 5.12: Horizontal Protection Level (HPL) contour of an L2-L5 dual-frequency user in CONUS.

There is a sharp border in Figure 5.10 because the GEO (POR) is visible for users on the right side of the border, but the GEO (POR) is not visible for users on the left side of the border. In comparison with the MAAST simulation results for the L1-L5 and the L1-L2 dual-frequency users, the LPV precision approach service coverage of the L2-L5 dual-frequency user is 10.81% which is much less than the coverage of the L1-L5 and the L1-L2 dual-frequency users (100%). Even an L2 single-frequency user has the LPV precision approach service coverage for over 58.34% of CONUS. In the next section the combined use of the WAAS ionospheric correction with the L2-L5 ionospheric delay estimate for the L2-L5 dual-frequency user will be developed.

5.3.2.4 COMBINED USE OF IONOSPHERIC CORRECTION FOR AN L2-L5 DUAL-FREQUENCY USER

The comparison in the MAAST simulation results for both the L2 single-frequency user and the L2-L5 dual-frequency user, Figure 5.13, shows that there will be some improvement in the LPV coverage for the L2-L5 dual-frequency user if the user can combine the WAAS ionospheric correction with the L2-L5 dual-frequency ionospheric delay estimation.

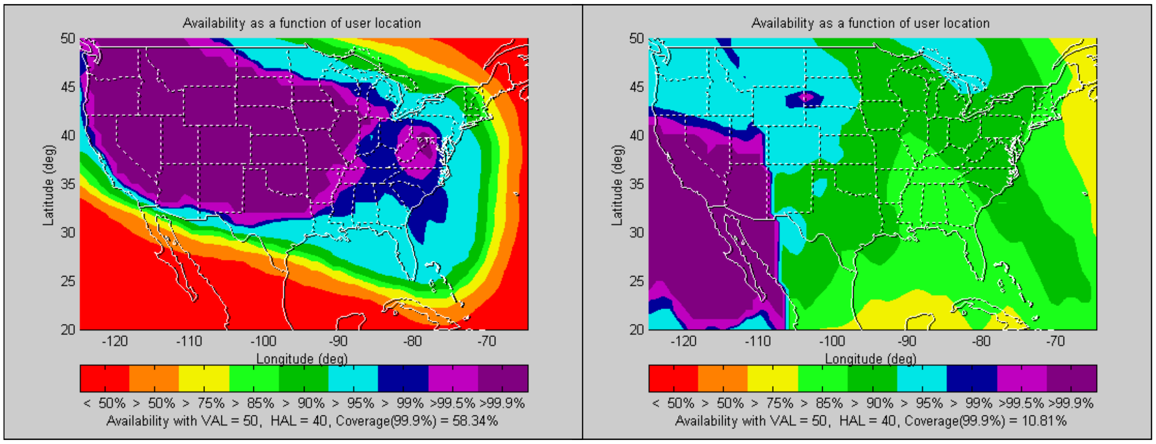

L2 single-frequency user

L2-L5 dual-frequency user

Figure 5.13: The comparison of the MAAST coverage simulation results for both the L2 single-frequency user and the L2-L5 dual-frequency user.

The algorithm of the combined use of ionospheric correction for an L2-L5 dual-frequency user utilizes Equations (5.1) (L2-only) and (3.19) (L2-L5).

$$\sigma^2_{i,UIRE\_L2} = \gamma^2_{1,2} \cdot \sigma^2_{i,UIRE\_L1} = (1.65)^2 \cdot \sigma^2_{i,UIRE\_L1} \tag{5.1}$$

$$\sigma^2_{UIRE\_L2L5} = \left[\frac{f_2^2}{f_2^2 - f_5^2}\right]^2 \left[\sigma^2_{air,L2}\right] + \left[\frac{f_5^2}{f_2^2 - f_5^2}\right]^2 \left[\sigma^2_{air,L5}\right] + \left[\sigma^2_{SV\_L2L5}\right] \tag{3.19}$$

The algorithm will first compare the σ^2_{UIRE} values from Equations (5.1) and (3.19), and then choose the ionospheric corrections method based on which method gives the lower σ^2_{UIRE} value. That is, if $\sigma^2_{i,UIRE\_L2} < \sigma^2_{UIRE\_L2L5}$, the WAAS ionospheric correction method will be used. Conversely, if $\sigma^2_{i,UIRE\_L2} > \sigma^2_{UIRE\_L2L5}$, the L2-L5 dual-frequency ionospheric estimation method will be used. Equation (5.2) represents the logic of this algorithm.

$$\sigma^2_{UIRE\_L2L5\_NEW} = \min\left(\sigma^2_{i,UIRE\_L2}, \sigma^2_{UIRE\_L2L5}\right) \tag{5.2}$$

The protection level calculation for an L2-L5 dual-frequency user is modified to adopt this combined use of ionospheric correction. This modified protection level calculation is summarized in Figure 5.14.

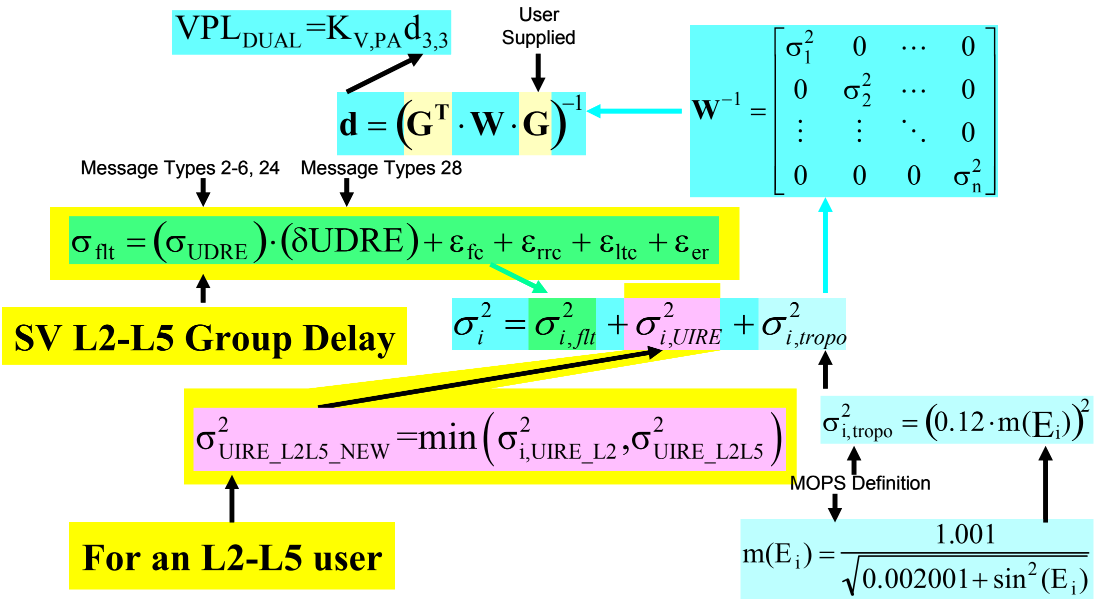

Modified Protection Level Calculation for an L2-L5 Dual-Frequency User

Figure 5.14: The modified protection level calculation for an L2-L5 dual-frequency user, only the yellow highlighted portion is changed, the other terms are unchanged as defined in the WAAS MOPS.

The MAAST was modified to adopt this new combined ionospheric correction algorithm. To be consistent and for easy of comparison, the simulation configurations of MAAST will be kept the same as in Table 3.1.

The new simulation results for an L2-L5 dual-frequency GPS/WAAS user are shown in Figures 5.15-5.17. Figure 5.15 shows the LPV coverage simulation results for an L2-L5 dual-frequency user. An L2-L5 dual-frequency user has LPV precision approach services available 99.9% of the time over 79.97% of CONUS. Figure 5.16 shows the VPL contour for an L2-L5 dual-frequency user in CONUS, and Figure 5.17 represents the HPL contour for an L2-L5 dual-frequency user in CONUS. The 99.9% shown in Figures 5.15-5.17

represents the fraction of users within those regions that had an availability of 99.9% or greater.

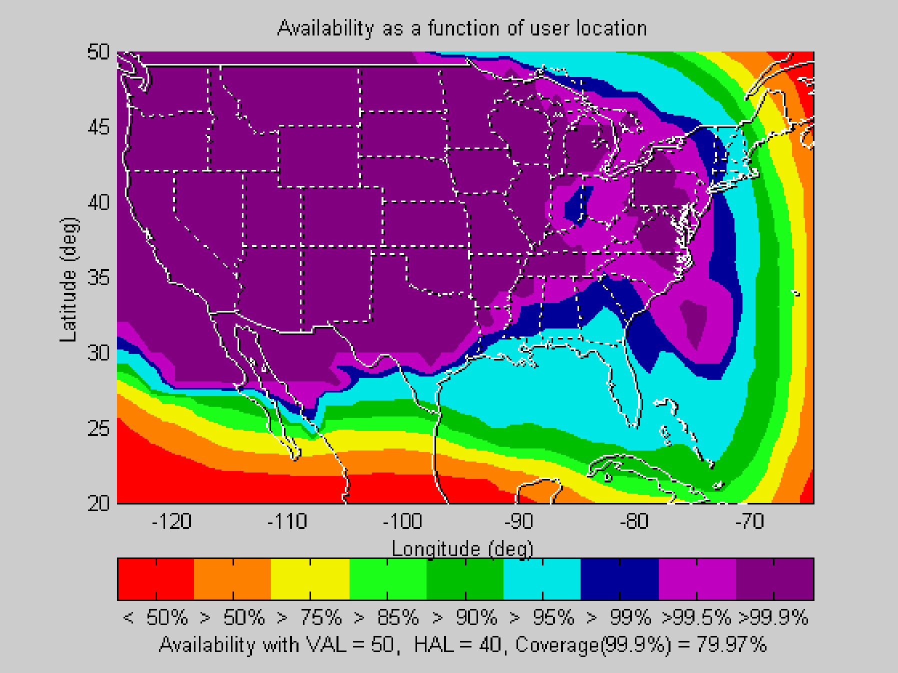

Figure 5.15: Coverage of an L2-L5 dual-frequency GPS/WAAS user in CONUS is 79.97% with VAL = 50m, HAL = 40m.

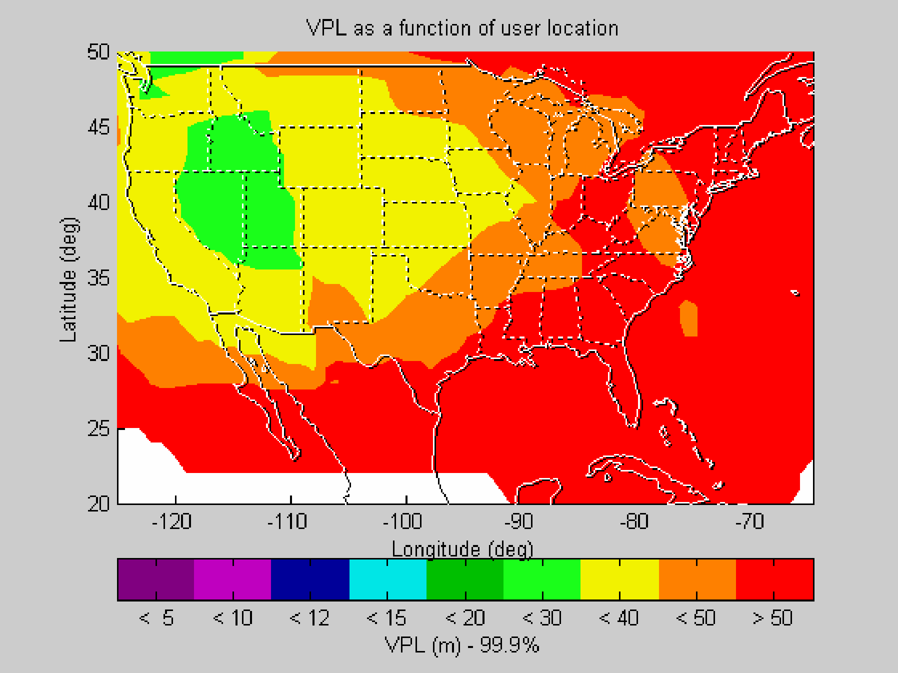

Figure 5.16: Vertical Protection Level (VPL) contour of an L2-L5 dual-frequency user in CONUS.

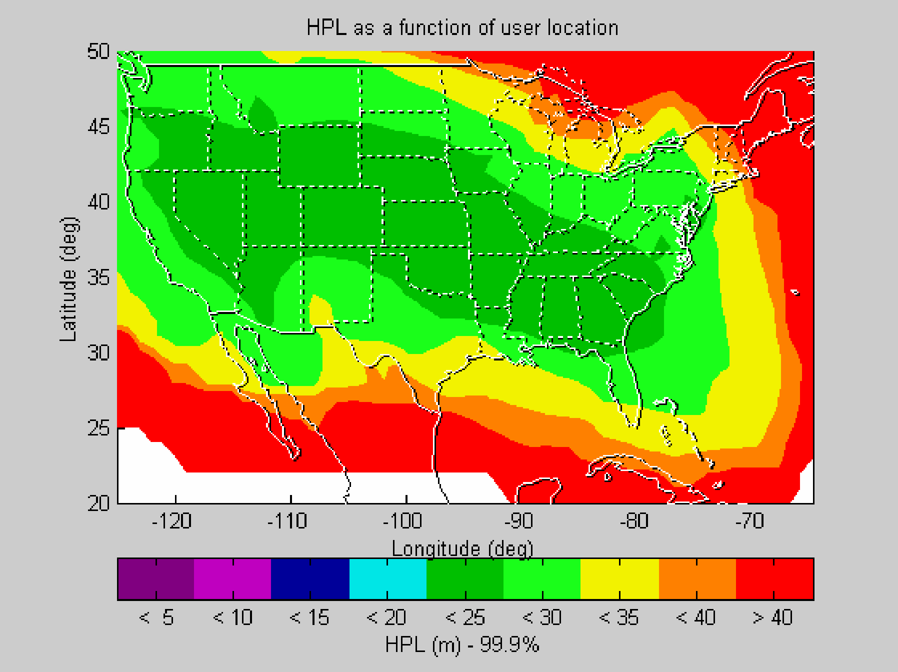

Figure 5.17: Horizontal Protection Level (HPL) contour of an L2-L5 dual-frequency user in CONUS.

The MAAST simulation results for the L2-L5 dual-frequency user in Section 5.3.2.3 showed that the LPV precision approach service coverage of the L2-L5 dual-frequency user with the direct use of the L2-L5 ionospheric delay estimation is 10.81%. In this section, the LPV precision approach service coverage of the L2-L5 dual-frequency user with the combined use of the ionospheric corrections is 79.97%. This represents a 69.16% coverage improvement by applying the combined ionospheric correction algorithm. Figure 5.18 shows the coverage comparison. Table 5.3 provides a summary of our MAAST simulation results.

MAAST Coverage Simulation Results for an L2-L5 Dual-Frequency User

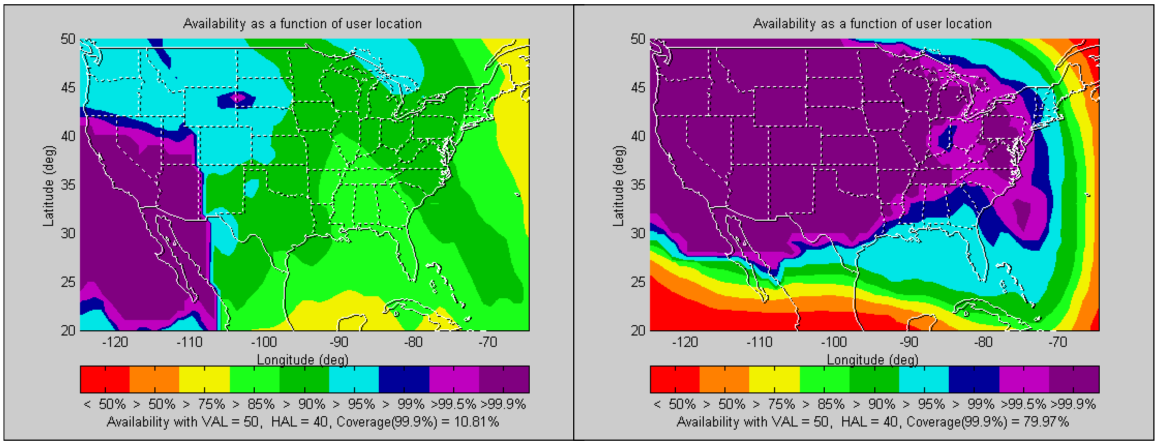

The direct use of L2-L5 dual-frequency ionospheric delay estimation

The combined use of ionospheric correction

Figure 5.18: The MAAST coverage simulation results comparison for an L2-L5 dual-frequency user. The plot on the left side is for an L2-L5 dual-frequency user who directly applied the L2-L5 dual-frequency ionospheric delay estimation. The LPV CONUS coverage is 10.58% for this case. The plot on the right side is for an L2-L5 dual-frequency user who applied the combined ionospheric correction algorithm. The LPV CONUS coverage is 79.97% for this case.

User Type	CONUS Coverage of LPV precision approach services (Availability ≥ 99.9%)	VPL (in meter)	HPL (in meter)
L1-L5 dual-frequency	100%	12 ≤ VPL < 40	5 ≤ HPL < 20
L1-only single-frequency	97.58%	20 ≤ VPL	15 ≤ HPL
L5-only single-frequency	49.25%	30 ≤ VPL	25 ≤ HPL
L5-only with the code and carrier divergence technique	100%	12 ≤ VPL < 40	5 ≤ HPL < 20
L5-only with the WAAS ionosphere threat model technique (9 minutes after losing L1)	100%	12 ≤ VPL < 40	5 ≤ HPL < 20
L5-only with the maximum ionospheric delay gradient model technique (9 minutes after losing L1)	100%	20 ≤ VPL < 50	10 ≤ HPL < 30
L2-only single-frequency	58.34%	30 ≤ VPL	20 ≤ HPL
L1-L2 dual-frequency	100%	12 ≤ VPL < 40	5 ≤ HPL < 20
L2-L5 dual-frequency	79.97%	20 ≤ VPL	20 ≤ HPL

Table 5.3: Summary table of MAAST simulation results.

5.4 CONCLUSIONS

This chapter discussed the L2 frequency usage for civil aviation applications. The presence of L2 introduced three additional user cases: L2-only single-frequency, L1-L2 dual-frequency, and L2-L5 dual-frequency. This chapter first modified the protection level calculation for these three user cases, and then modified the MAAST according to the modified protection level calculation to simulate these three user cases.

An L2-only single-frequency GPS/WAAS user has LPV precision approach service available 99.9% of the time over 58.34% of CONUS. An L1-L2 dual-frequency user has the same service available 99.9% of the time over 100% of CONUS. An L2-L5 dual-frequency user has this service available 99.9% of the time over 79.97% of CONUS if the combined ionospheric correction algorithm is used. The loss of coverage for an L2-L5 dual-frequency user is due to the narrow separation between the L2 and L5 frequencies, which were unable to provide adequate ionospheric delay estimation. The reversionary modes of the previous chapter could also be applied to L2-only.

The evidence suggests that L2 should be used for civil aviation application. However, L2 is not in the ARNS band which prevents its use in safety-of-life applications. It will be very difficult to form an international agreement to assign L2 into the ARNS band. L2 can however be used as a backup navigation aid. For example, L2 can be used to provide ionospheric corrections for aircraft while L1 or L5 is not available due to RFI. While, L2 has better ionospheric delay performance than L5, in no case could L2 be used instead of L5.

Chapter 6

Barometric Altimeter

6.1 INTRODUCTION

In addition to GPS modernization and the WAAS, this thesis also investigates the effect of using a barometric altimeter. As part of this work, a barometric altimeter simulator is developed. The simulator is used to estimate altitude from historical meteorological observation data collected at different locations in the Conterminous United States (CONUS). By comparing the estimated altitude with true altitude, altitude error data is generated. By applying statistical and linear estimation techniques to the altitude error data, a model for barometric altimeter confidence is developed. This barometric altimeter confidence model is evaluated via the historical worst-case meteorological observation data and Stanford flight test data.

This chapter is organized as follows. Section 6.2 discusses the basics of a barometric altimeter. The error sources of a barometric altimeter are discussed in Section 6.3. In Section 6.4, the development of the barometric altimeter confidence model is explained. Section 6.5 describes the verifications of this barometric altimeter confidence model. A short description of the modified MAAST and analysis of results of some simulated cases are given in Section 6.6. Section 6.7 presents a summary and concluding remarks.

6.2 BAROMETRIC ALTIMETER BASICS

There are many kinds of altimeters in general use today. However, they are all constructed on the same basic principle as an aneroid barometer. Barometric altimeters contain a sealed bellows that expands or contracts in response to the change in air pressure associated with a change in altitude. Gears translate the movement of the bellows into the movement of pointers on a dial, which shows the pilot the altitude of the plane in relation to sea level. The dial face of the typical altimeter is graduated with numerals from 0 to 9 inclusive, as shown in Figure 6.1.

Figure 6.1: A barometric altimeter.

The barometric setting is the pressure that must be set in the bottom right window of the altimeter in order for the altimeter to read the true elevation of the station. With altimeter setting dialed into the window, the altimeter will indicate true altitude at one pressure level. Of course, the altimeter setting for any station changes as the atmospheric pressure changes, and altimeter setting varies from one station to another. Therefore, each station must make its own calculations at frequent intervals. For airplanes flying at an altitude greater than

18,000 feet above sea level, the normal procedure is to adjust the barometric altimeter to a standard pressure of 29.92 inches of mercury. For airplanes flying at an altitude less than 18,000 feet above sea level, the normal procedure is to adjust the barometric altimeter to the local barometric pressure provided by air traffic control, as illustrated in Figure 6.2.

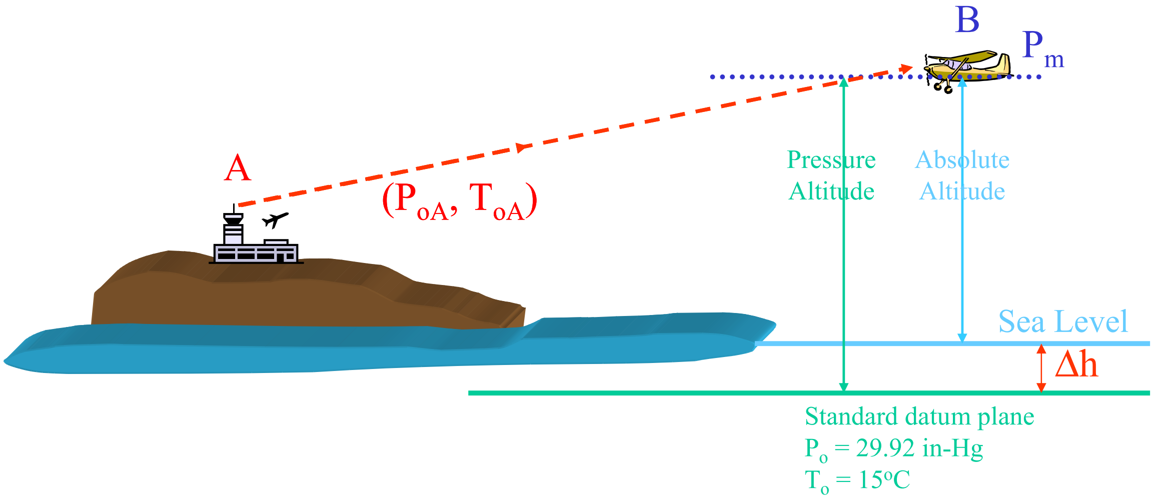

Figure 6.2: A barometric altimeter setting example: An aircraft receives temperature and pressure data from air traffic control.

The conversion of measured air pressure to altitude is based on a theoretical standard atmosphere and a corresponding pressure versus altitude curve as well as the assumption that air is a perfect gas. More precisely, the standard atmosphere [Von Mises] is defined as follows:

The air is a perfect gas with gas constant R=287 $J/(Kg \cdot K)$.

The pressure at sea level is P_0=29.92 *in.-Hg*.

The temperature at sea level is T_0=15^oC.

The temperature gradient (lapse rate) is λ=0.0065$^oC/m$.

The conversion of measured air pressure to altitude is based on the following equation:

$$\hat{h}_c = \frac{T_0}{\lambda}\left[1 - \left(\frac{P_m}{P_0}\right)^{\frac{\lambda R}{g}}\right] \tag{6.1}$$

Where,

$\hat{h}_c$ is estimated altitude

T_0 is temperature at the level of reference

λ is lapse rate

P_0 is pressure at the level of reference

P_m is pressure measured

R is universal gas constant

g is acceleration of gravity

6.3 BAROMETRIC ALTIMETER ERROR SOURCES

The barometric altimeter error sources are summarized as follows:

- Height Difference between MSL (Mean Sea Level) and the Geoid [NIMA]: A barometric altimeter indicates the altitude with respect to MSL. This altitude reading is different than the altitude reading from GPS, which is with respect to WGS-84 (World Geodetic System 1984) [Misra&Enge]. This height difference is corrected by a well known model [NIMA], and this thesis does not try to model this error source.

- System Error: The barometric altimeter system error covers the pressure sensor error, the altitude display error, and the barometric setting error. The barometric altimeter system error is very small when compared to other error sources. This system error either will be provided by the manufacturers or can be calibrated ahead of time. Therefore, this thesis does not model this error.

- Pressure Error: Pressure error includes the pressure variation error and the pressure difference error. The pressure variation error is the difference between the ambient pressure versus altitude relationship and the theoretical standard atmosphere used to calculate altitude as in Equation (6.1). As shown in Figure 6.2, the pressure difference error is the difference between the pressure at the level of reference at location A and the pressure at the level of reference at location B. The pressure error is the major error source of a barometric altimeter. This thesis develops a confidence model of this pressure error based on the historical meteorological observation data. This confidence model is detailed in next section.

6.4 BAROMETRIC ALTIMETER CONFIDENCE MODEL

To estimate the accuracy of the barometric altimeter, we develop a barometric altimeter simulator based on the altitude in Equation (6.1) by using MATLAB®. As shown in Figure 6.3, the analysis assumes that the user at location B receives temperature and pressure data (P_0, T_0) from a reference station (a control tower or weather station) at location A. This user then uses these data along with its own pressure measurement (P_m) and Equation (6.1) to calculate its altitude $\left(\hat{h}_c\right)$. The estimated altitude, $\hat{h}_c$, is compared to the true altitude at the location B $\left(\mathrm{H_B}\right)$ to generate an altitude error.

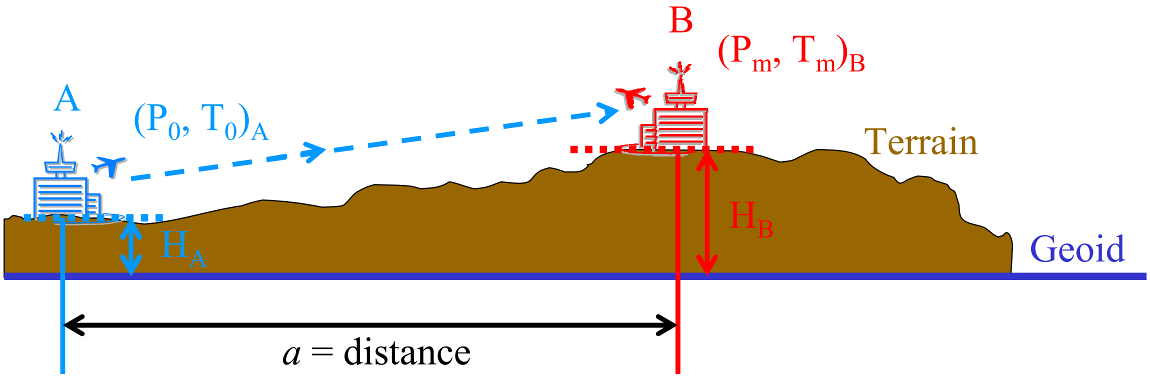

Figure 6.3: The configuration of the simulation: User at place B gets the temperature (T_0) and pressure (P_0) data from air traffic control at place A to estimate his altitude $\left(\hat{h}_c\right)$. The estimated altitude, $\hat{h}_c$, was compared to the true altitude at the location B $\left(H_B\right)$ to generate an altitude error.

The simulation is exercised on historical meteorological data from [NOAA], including hourly meteorological observation data from selected weather stations in the United States. The source data from [NOAA] provides the measured temperatures, measured pressures, time, and positions in LLH (Latitude, Longitude, Height) of locations A and B. The sample data is shown in Figure 6.4. The first row of data shows the station's number (Weather Bureau Army Navy number), station's city, station's state, latitude of the station, longitude of the station, and elevation of the station in meters. Then, the first column is year of observation, the second column is month of observation, etcetera. Hours are measured in local standard time, temperature is in degrees C, and station pressure is in millibars.

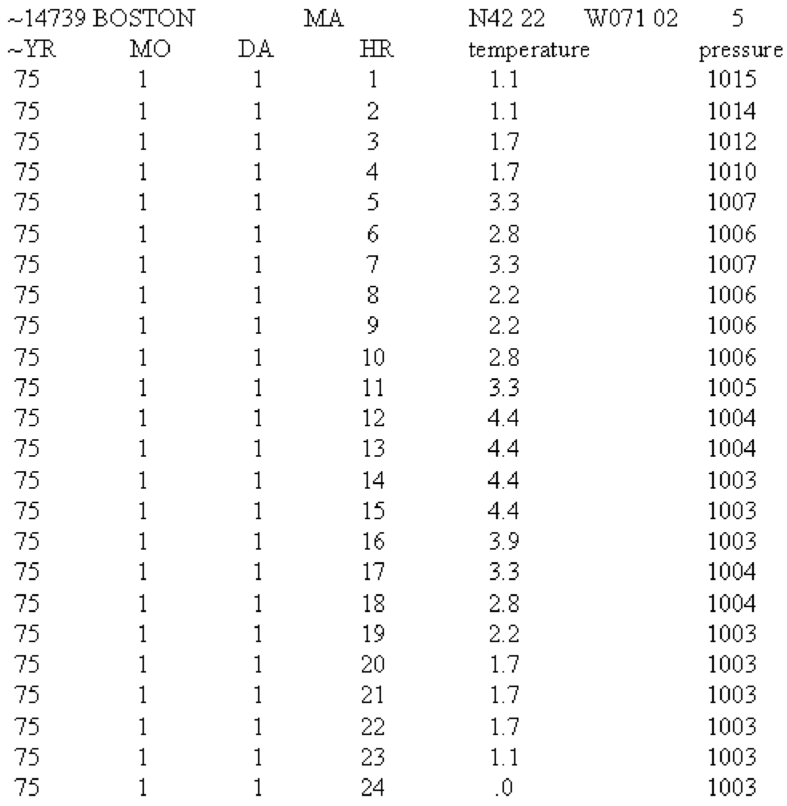

```
~14739 BOSTON          MA            N42 22     W071 02       5
~YR        MO       DA        HR      temperature             pressure
75          1        1         1        1.1                    1015
75          1        1         2        1.1                    1014
75          1        1         3        1.7                    1012
75          1        1         4        1.7                    1010
75          1        1         5        3.3                    1007
75          1        1         6        2.8                    1006
75          1        1         7        3.3                    1007
75          1        1         8        2.2                    1006
75          1        1         9        2.2                    1006
75          1        1        10        2.8                    1006
75          1        1        11        3.3                    1005
75          1        1        12        4.4                    1004
75          1        1        13        4.4                    1004
75          1        1        14        4.4                    1003
75          1        1        15        4.4                    1003
75          1        1        16        3.9                    1003
75          1        1        17        3.3                    1004
75          1        1        18        2.8                    1004
75          1        1        19        2.2                    1003
75          1        1        20        1.7                    1003
75          1        1        21        1.7                    1003
75          1        1        22        1.7                    1003
75          1        1        23        1.1                    1003
75          1        1        24         .0                    1003
```

Figure 6.4: The sample data in [NOAA].

Before we can estimate the altitude error of a barometric altimeter, we must use the measured temperature and pressure (T_0, P_0) at location A to estimate the temperature and pressure at the level of reference (T_m, P_m) via Equations (6.2) and (6.3) based on the perfect gas law [Von Mises],

$$P_0 = P_m \cdot e^{\frac{g\mathrm{H}_\mathrm{A}}{RT_m}} \tag{6.2}$$

$$T_0 = T_m + \lambda \mathrm{H}_\mathrm{A} \tag{6.3}$$

This thesis selected locations in different regions to run our simulation. Two example regions are Atlanta, GA and Toledo, OH. The example regions are shown in Figures 6.5

and 6.6. We then chose one location in each region as the airplane location. In Figure 6.5, it is Atlanta, GA, and in Figure 6.6, it is Toledo, OH.

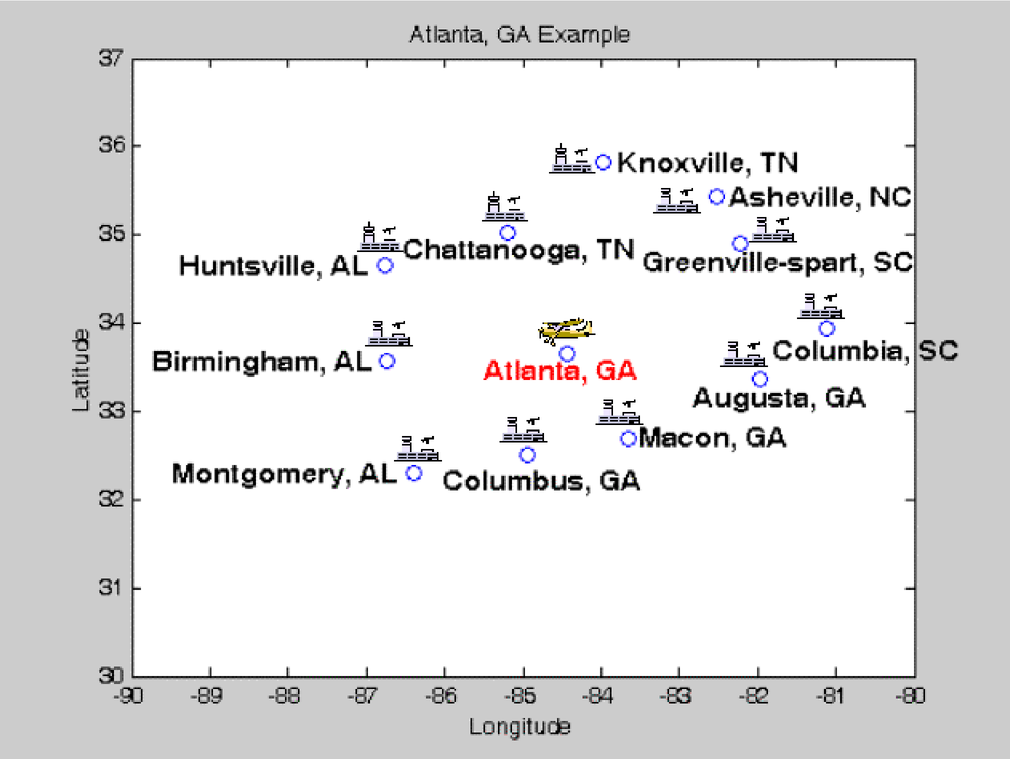

Figure 6.5: A selected region in U.S.. The red lettering indicates that the airplane is at that location, Atlanta, GA in this example.

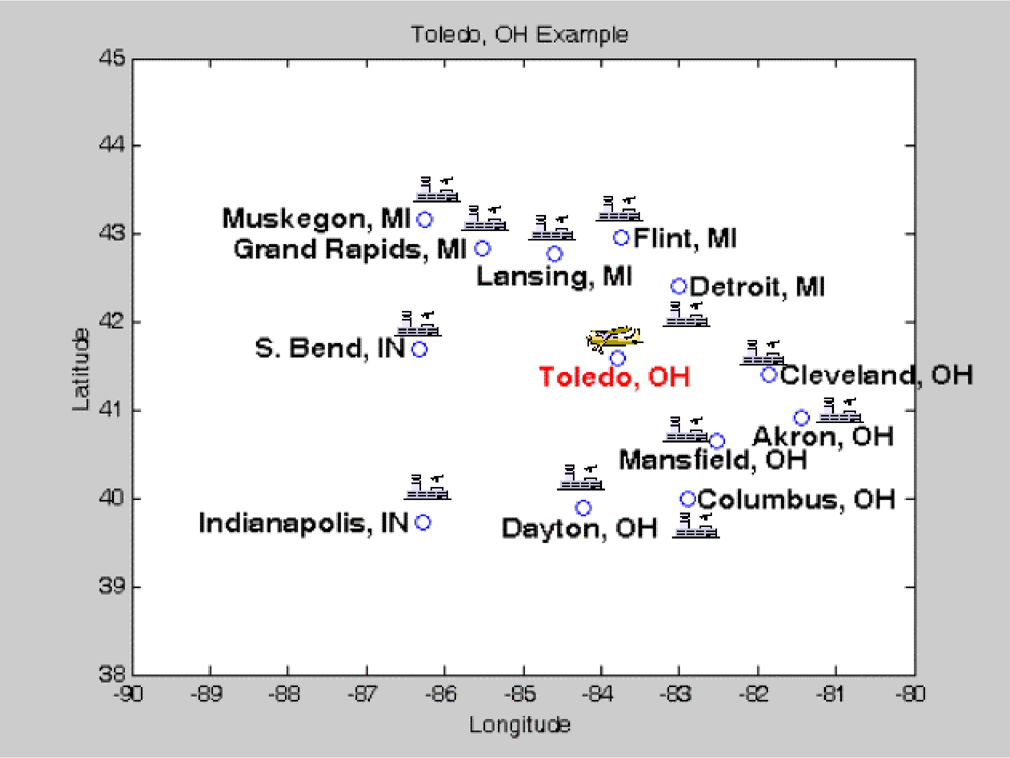

Figure 6.6: A selected region in U.S.. The red lettering indicates that the airplane is at that location, Toledo, OH in this example.

Meteorological observation data was collected at each location for a year. The year of 1987 is selected. All data was then fed into our simulator to estimate the altitude of the airplane. The estimated altitude was then compared with the provided true altitude to generate altitude error data. Figure 6.7 shows an example of altitude error data for an airplane at Toledo, OH. The subplots of Figure 6.7 are in the order of distance between the airplane and the other weather stations. For example, the altitude error using the data from the nearest reference station is shown on the top of Figure 6.7.

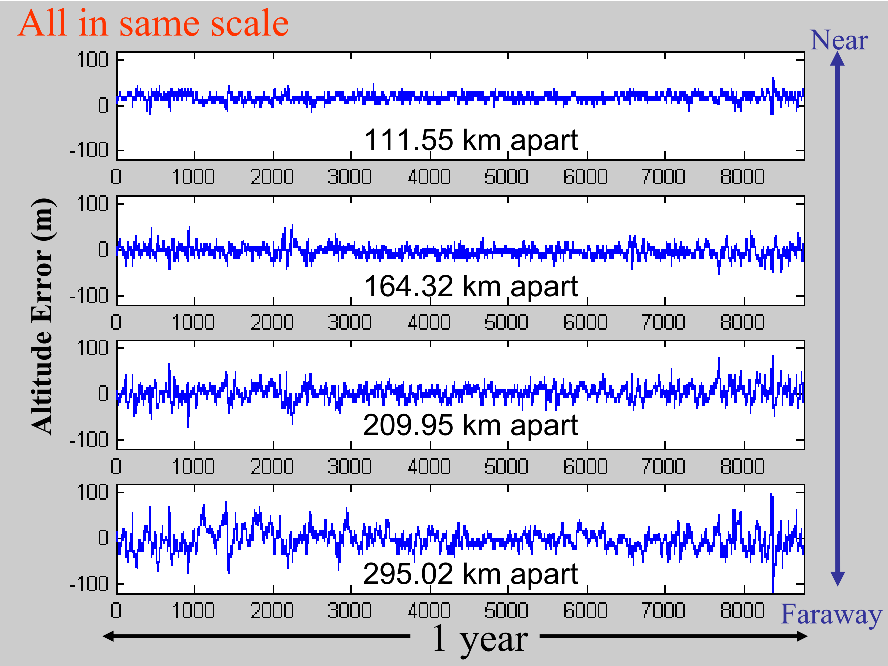

Figure 6.7: This is an example of altitude error data generated from Toledo, OH region.

Figure 6.7 shows that the altitude error data curve using the near weather station's data is smoother than the one using a further away weather station's data. This is because the near weather station has similar weather patterns to the airplane (i.e., smaller temperature and pressure variations between the two sites).

In order to build the barometric altimeter error model, this thesis first calculates the standard deviation (σ) of the altitude error data. We then apply the following linear least-square estimation technique to fit a line to the error data.

$$Y = ax + b \tag{6.4}$$

Where,

Y is the standard deviation of altitude error for one year

a is the distance between Place A and Place B (Km)

x is the slope

b is the constant

Rearrange Equation (6.4) into the Equation (6.5),

$$Y = \begin{bmatrix} a & 1 \end{bmatrix} \begin{bmatrix} x \\ b \end{bmatrix} \tag{6.5}$$

$$A = \begin{bmatrix} a & 1 \end{bmatrix}$$

$$X = \begin{bmatrix} x \\ b \end{bmatrix}$$

Apply the linear least-square estimation technique to the resulting error bounds in different regions,

$$X_{ls} = (A^T A)^{-1} A^T Y \tag{6.6}$$

For Atlanta, GA, the result is

$$Y = 0.0639a + 0.0043 \tag{6.7}$$

For Toledo, OH, the result is

$$Y = 0.0766a + 0.0049 \tag{6.8}$$

The linear estimation results of Equations (6.7) and (6.8) show us the altitude error as a function of the distance between the airplane and the reference weather station. The Atlanta, GA results are shown in Figure 6.8.

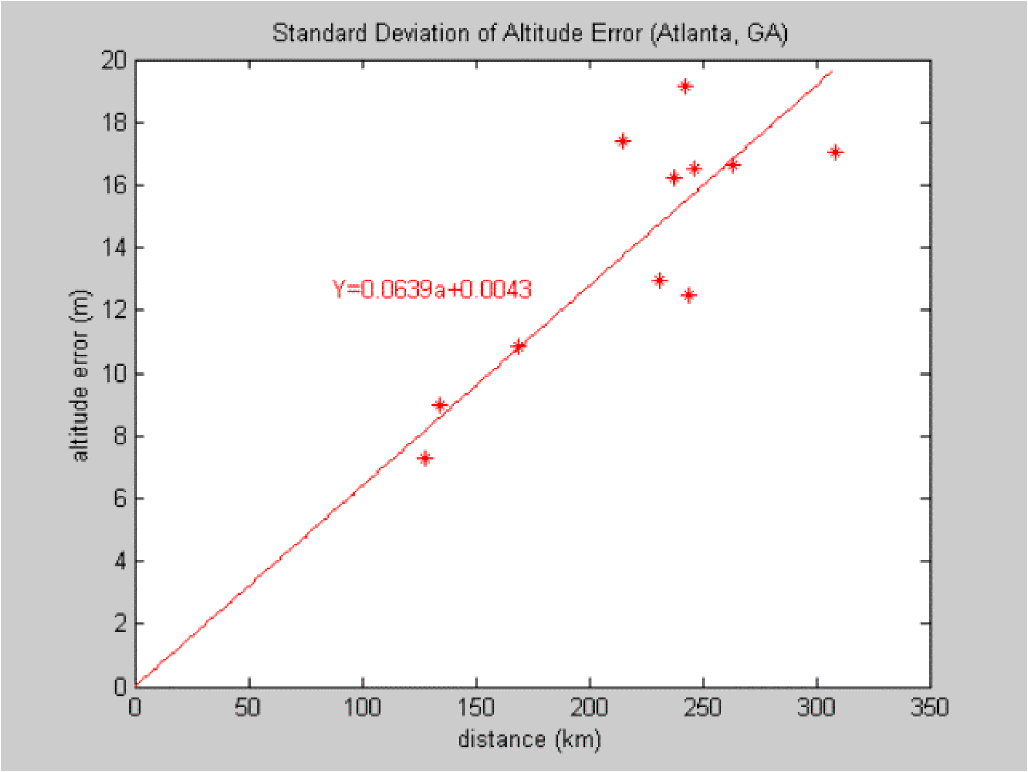

Figure 6.8: The * is the standard deviation of the altitude error, and the red line shows the result of the linear estimation.

The goal is to develop the barometric altimeter confidence model. One standard deviation of altitude error is not conservative enough for safety-of-life applications. Instead, we collected the worst-case error of the data shown in Figure 6.7, and applied the same linear estimation. The results were the following:

For Atlanta, GA,

$$Y = 0.3070a + 18.5478 \tag{6.9}$$

For Toledo, OH,

$$Y = 0.4125a + 20.3868 \tag{6.10}$$

The results are shown in Figure 6.9. From the error point of view, the model of Toledo, OH (Figure 6.6) is worse than the one of Atlanta, GA (Figure 6.5). As a result, the worst-case model of Toledo, OH is chosen as the confidence model for the barometric altimeter. For conservatism, this thesis adds 10% as a safety factor to Equation (6.10). Thus, the barometric altimeter confidence model is

$$Y = 1.1(0.4125a + 20.3868) \tag{6.11}$$

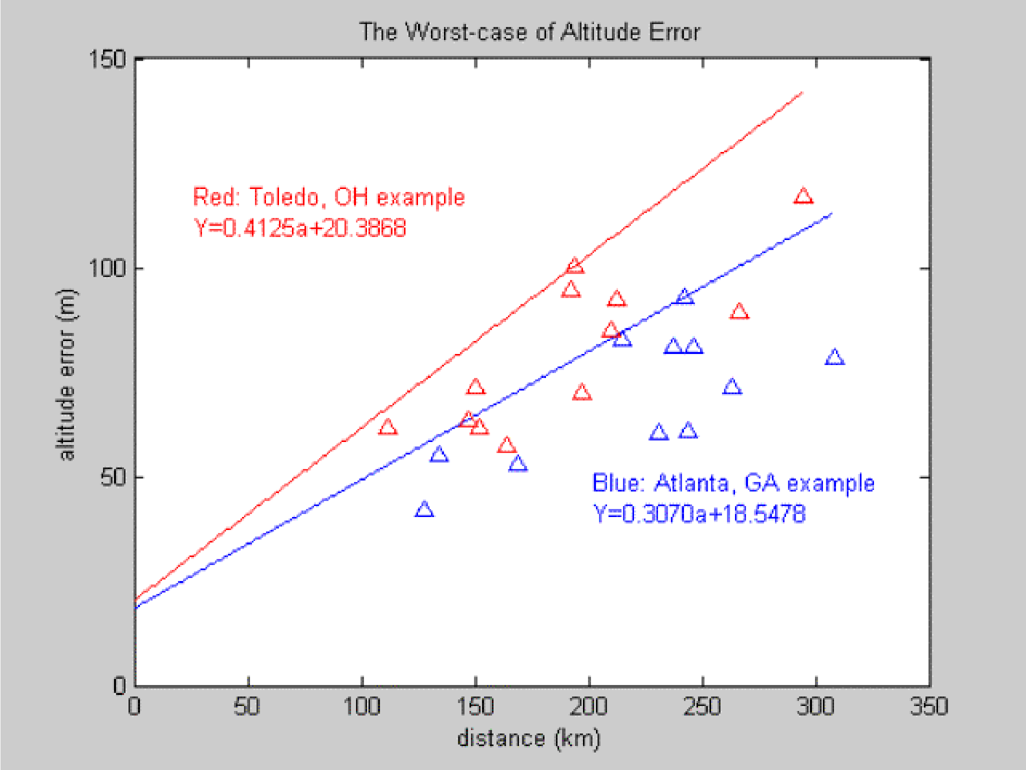

Figure 6.9: The worst-case model for the barometric altimeter, the blue portion is for Atlanta, GA, and the red portion is for Toledo, OH.

6.5 BAROMETRIC ALTIMETER CONFIDENCE MODEL VERIFICATION

Before using this error bound, we must verify it with more data. To this end, 5 years (1983-1987) of meteorological observation data were collected for the same locations as in the Toledo, OH example. We then used the developed MATLAB® simulator to generate the worst-case altitude error data. These worst-case errors were then used to test the confidence model. As shown in Figure 6.10, the confidence model successfully overbounds these worst-case errors. Figure 6.10 also shows that one could successfully bound the worst-case error even without the 10% safety factor.

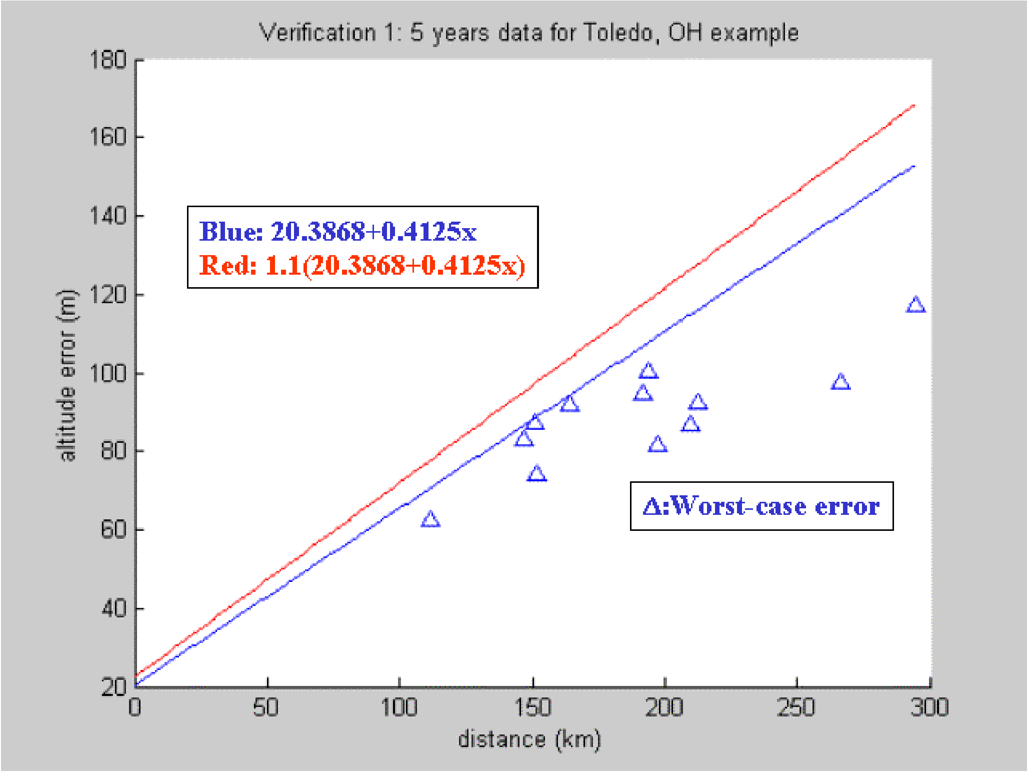

Figure 6.10: Our confidence model successfully bounds these worst-case errors; this figure also shows that the worst-case error is bounded even without the 10% safety factor.

5 years (1985-1989) of meteorological observation data were then collected for Boston, MA and Worcester, MA. It was assumed that the airplane is at Worcester, MA and the

reference weather station is at Boston, MA. These cities 66.9 km apart from each other. Altitude error data is then generated using the same algorithm. The altitude error distribution is shown in Figure 6.11. The statistics for this distribution are as follows:

Total data points = 43824

Maximum error = 47.1136 m

Probability(maximum error) = $\frac{1}{43824}$

The confidence bound (Y) is calculated by substituting the distance $(a = 66.8812 \text{ km})$ into Equation (6.11),

$$\begin{aligned} Y &= 1.1(0.4125a + 20.3868) \\ &= 1.1(0.4125 \cdot 66.8812 + 20.3868) \\ &= 52.7728 \text{ (m)} \end{aligned}$$

The maximum altitude error is well bounded by this barometric altimeter confidence model (47.1136<52.7728). This thesis will use the barometric altimeter confidence bound of the Boston-Worcester example (52.7728m) as the barometric altimeter error bound for all analyses and simulations throughout the rest of this thesis.

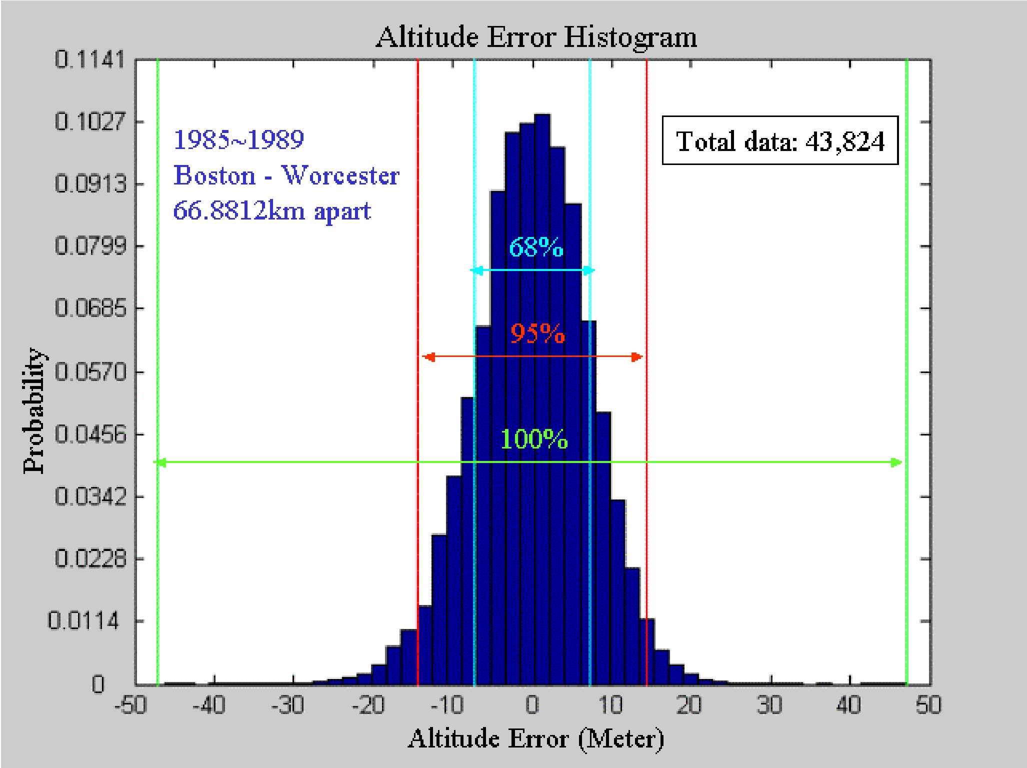

Figure 6.11: The distribution of altitude error. The maximum error is 47.1136 m and is well bounded by our confidence model (52.7728m).

As a final verification of the confidence model, flight test data was collected at Moffett Field, CA, on December 15, 2001. The aircraft used was a Piper Saratoga owned and operated by Sky Research Inc. The flight test procedure assumed the Saratoga was approaching Moffett Field with the barometric setting from the airport control tower, which was 30.11 inches of mercury for this specific approach.

The position of Moffett Field Airport in (latitude, longitude) is (37.4152178, -122.0482944), the height difference between MSL (Mean Sea Level) and the Geoid is about –33.35 (m) at this airport [NIMA]. This flight test recorded the barometric altitude with respect to MSL and the GPS altitude, as shown in the top plot of Figure 6.12. The height difference between Geoid and MSL is reflected in the top plot as well. This flight test also recorded the distance from the airplane to the airport, as shown in the bottom plot of Figure 6.12, which is used in the calculation of the altitude error confidence.

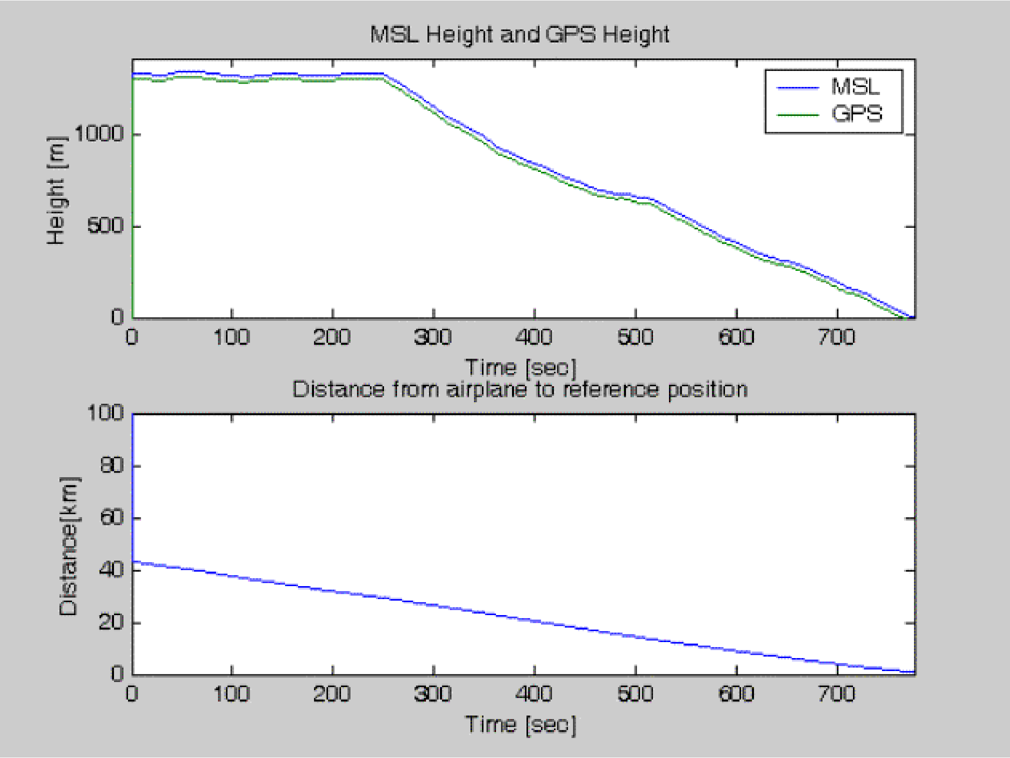

Figure 6.12: The flight test data. The top plot shows the barometric altimeter altitude with respect to mean sea level (blue), and the GPS altitude (green). The bottom plot shows the distance from the aircraft to Moffett Field.

For the barometric altimeter altitude error calculation, this thesis uses GPS altitude as the true altitude. It then calculates the difference between the barometric altimeter altitude and MSL and GPS altitudes. The height difference (-33.35m) between MSL and the Geoid is corrected by a well known model [NIMA], and this thesis does not try to model it. Thus, the barometric altitude error calculation is

$$e = h_{MSL} + \hat{h} - h_{GPS} \tag{6.12}$$

where,

e is barometric altitude error

h_{MSL} is barometric altimeter altitude with respect to the mean sea level

$\hat{h}$ is correction to the height difference between MSL and the Geoid

h_{GPS} is GPS altitude

The result of the calculation is shown in Figure 6.13. Figure 6.13 also shows the barometric altimeter confidence bound, which is based on Equation (6.11). The barometric altimeter altitude error of this flight test is well bounded by the proposed barometric altimeter confidence model. Figure 6.13 also shows an additional barometric altimeter error model derived from the WAAS MOPS [RTCA1].

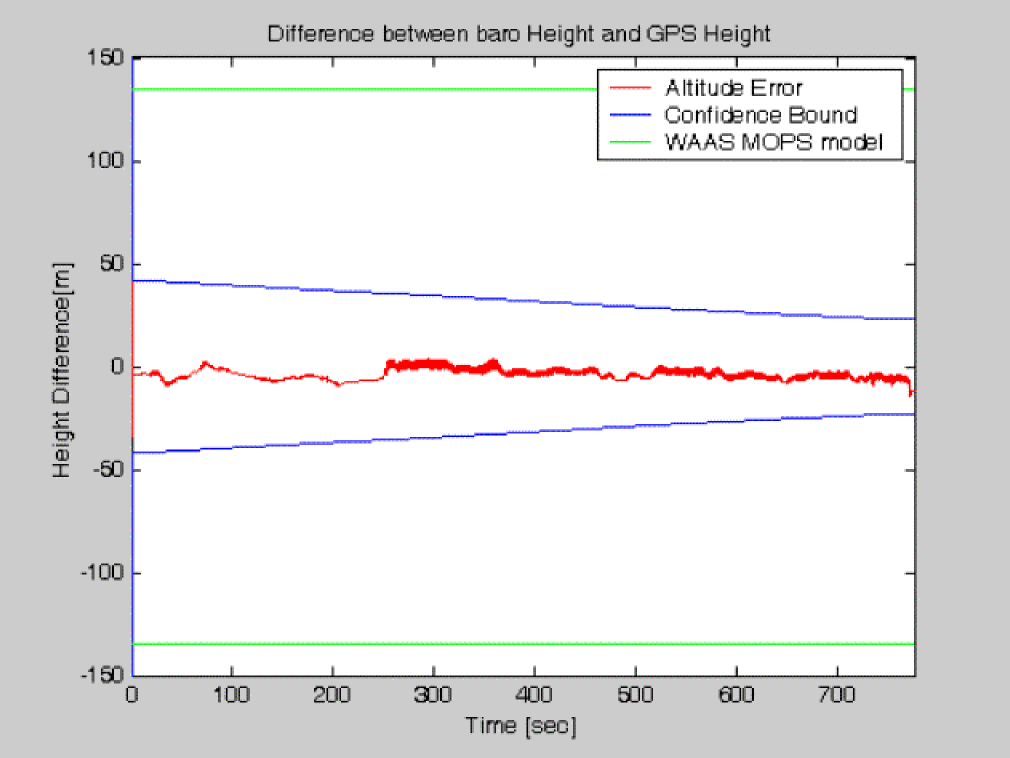

Figure 6.13: The barometric altimeter altitude error of the flight test. The barometric altimeter altitude error is shown in red, and our barometric altimeter confidence bound is shown in blue. The barometric altimeter altitude error is well bounded by our barometric altimeter confidence.

6.6 BAROMETRIC ALTIMETER BENEFITS

The goal of this thesis is to compare the coverage of LPV precision approach services under different scenarios. The simulation tool in this paper is the MATLAB® Algorithm Availability Simulation Tool (MAAST) [Jan01b]. MAAST is available for download from *http://waas.stanford.edu*.

This analysis uses all single-frequency WAAS users and the L2-L5 dual-frequency user as examples. For those users with WAAS and the barometric altimeter cases, the MAAST availability simulation treats the barometric altimeter as a virtual satellite with known clock at the user location. The GPS observation direction cosine matrix, G_{GPS}, in the user's local

East-North-Up frame is modified to $G_{GPS+Baro}$ to include a barometric altimeter in the following manner:

$$G_{GPS+Baro} = \begin{bmatrix} & G_{GPS} & & \\ 0 & 0 & 1 & 0 \end{bmatrix} \tag{6.13}$$

The weighting matrix, W, in the protection level calculation is modified to include the barometric altimeter confidence (σ_{baro}) [RTCA1],

$$W = \begin{bmatrix} \sigma_1^{-1} & 0 & \dots & 0 \\ 0 & \sigma_2^{-1} & \dots & 0 \\ \dots & \dots & \dots & \dots \\ 0 & 0 & \dots & \sigma_{baro}^{-1} \end{bmatrix} \tag{6.14}$$

The confidence of a barometric altimeter is calculated using data from the Boston-Worcester example discussed earlier,

$$\sigma_{baro} = \frac{52.7728}{5.33} = 9.9011(m) \tag{6.15}$$

where, 5.33 is the K_{HMI} value defined in Section 2.3.

To be consistent and for easy of comparison, the simulation configurations of MAAST will be kept the same as in the previous chapters (Table 3.1). The simulation results of an L1-only single-frequency WAAS user in CONUS are shown in Figures 6.14 through 6.16. Figure 6.14 indicates that the coverage for users with availability of at least 99.9% of the time is 97.58% of the CONUS. Figures 6.15 and 6.16 show Horizontal Protection Level (HPL) and Vertical Protection Level (VPL) [RTCA1] contours, respectively. Figures 6.17 through 6.19 show the simulation results of an L1-only single-frequency WAAS user with a barometric altimeter aiding in CONUS. Figure 6.17 indicates that the coverage for users with availability of at least 99.9% of the time is 99.19% of the CONUS. Figures 6.18 and 6.19 show Horizontal Protection Level (HPL) and Vertical Protection Level (VPL) [RTCA1] contours, respectively. Comparing Figure 6.14 and Figure 6.17, one notes that the barometric altimeter aiding provided a 1.61% coverage improvement to 99.9% LPV availability for an L1-only single-frequency WAAS user in CONUS. Table 6.1 provides a comparison table for a single-frequency user with and without barometric altimeter aiding.

User Type	CONUS Coverage of LPV precision approach services (Availability ≥ 99.9%)	VPL (in meter)	HPL (in meter)
L1-only single-frequency w/o baro-aiding	97.58%	20 ≤ VPL	15 ≤ HPL
L1-only single-frequency w/ baro-aiding	99.19%	20 ≤ VPL <50	15 ≤ HPL

Table 6.1: Comparison of a single-frequency user with and without barometric altimeter aiding.

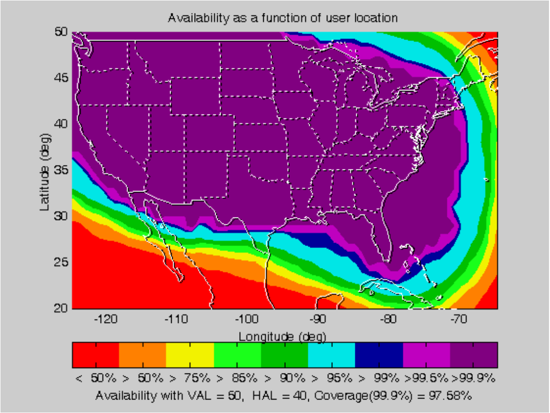

Figure 6.14: Coverage of an L1-only single-frequency WAAS user in CONUS is 97.58% with VAL=50m, HAL=40m.

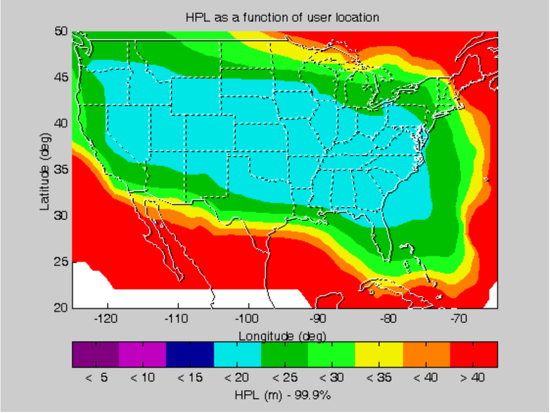

Figure 6.15: Horizontal protection level (HPL) contour of an L1-only single-frequency WAAS user in CONUS.

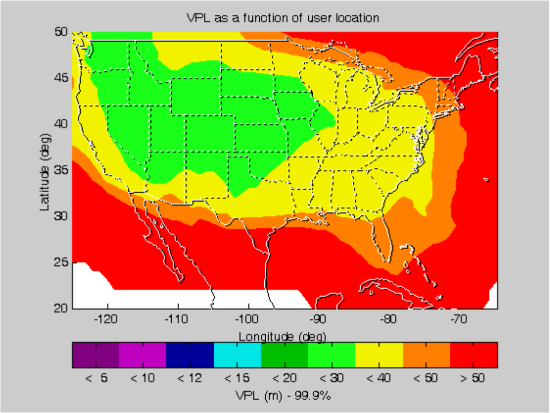

Figure 6.16: Vertical protection level (VPL) contour of an L1-only single-frequency WAAS user in CONUS.

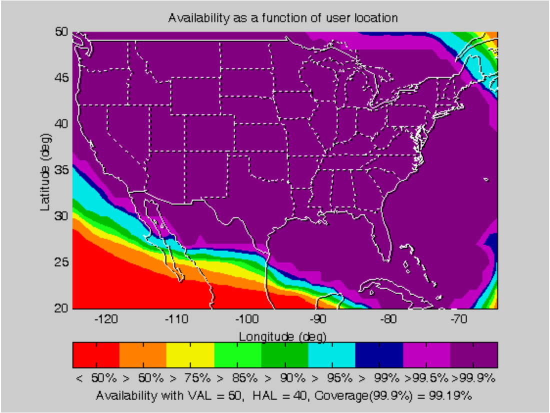

Figure 6.17: Coverage of an L1-only single-frequency WAAS user with baro-aiding in CONUS is 99.19% with VAL=50m, HAL=40m.

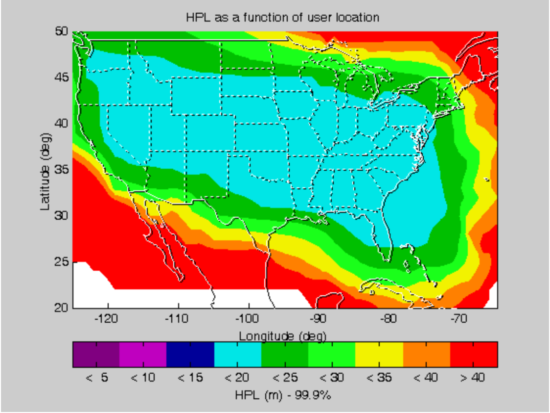

Figure 6.18: Horizontal protection level (HPL) contour of an L1-only single-frequency WAAS user with baro-aiding in CONUS.

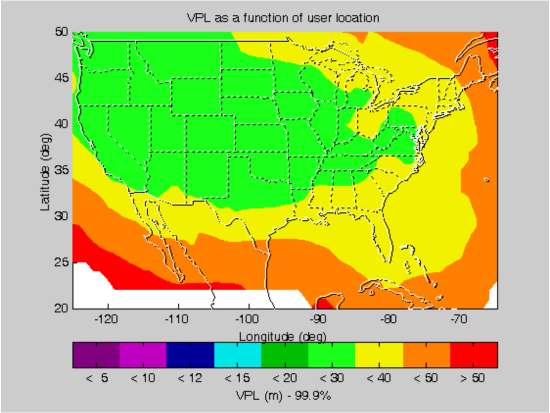

Figure 6.19: Vertical protection level (VPL) contour of an L1-only single-frequency WAAS user with baro-aiding in CONUS.

The simulation results of an L2-only single-frequency WAAS user in CONUS are shown in Figures 6.20 through 6.22. Figure 6.20 indicates that the coverage for users with availability of at least 99.9% of the time is 58.34% of the CONUS. Figures 6.21 and 6.22 show HPL and VPL contours, respectively. Figures 6.23 through 6.25 show the simulation results of an L2-only single-frequency WAAS user with a barometric altimeter aiding in CONUS. Figure 6.23 indicates that the coverage for users with availability of at least 99.9% of the time is 92.63% of the CONUS. Figures 6.24 and 6.25 show HPL and VPL contours, respectively. Comparing Figure 6.20 and Figure 6.23, one notes that the barometric altimeter aiding provided a 34.29% coverage improvement to 99.9% LPV availability for an L2-only single-frequency WAAS user in CONUS. Table 6.2 provides an update comparison table for a single-frequency user with and without barometric altimeter aiding.

User Type	CONUS Coverage of LPV precision approach services (Availability ≥ 99.9%)	VPL (in meter)	HPL (in meter)
L1-only single-frequency w/o baro-aiding	97.58%	20 ≤ VPL	15 ≤ HPL
L1-only single-frequency w/ baro-aiding	99.19%	20 ≤ VPL <50	15 ≤ HPL
L2-only single-frequency w/o baro-aiding	58.34%	30 ≤ VPL	20 ≤ HPL
L2-only single-frequency w/ baro-aiding	92.63%	20 ≤ VPL <50	20 ≤ HPL

Table 6.2: Comparison of a single-frequency user with and without barometric altimeter aiding.

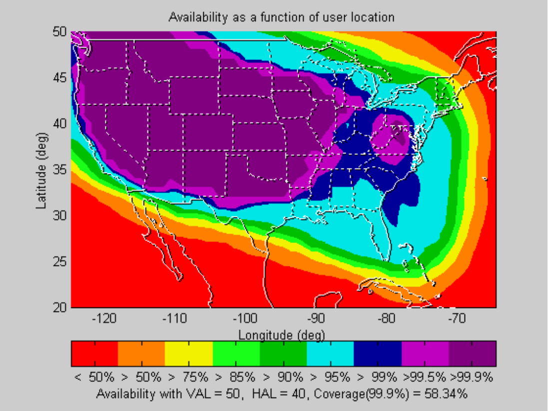

Figure 6.20: Coverage of an L2-only single-frequency WAAS user in CONUS is 58.34% with VAL=50m, HAL=40m.

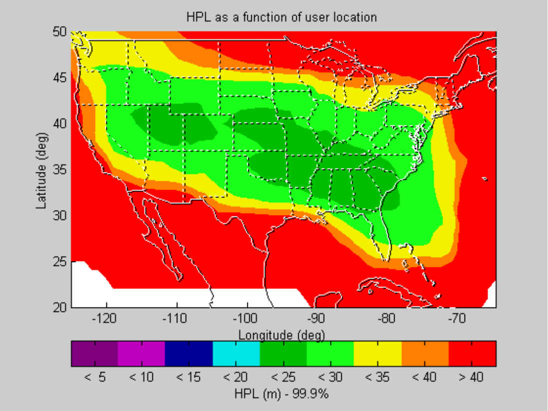

Figure 6.21: Horizontal protection level (HPL) contour of an L2-only single-frequency WAAS user in CONUS.

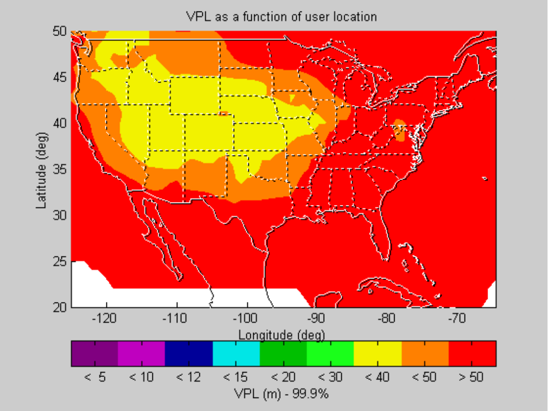

Figure 6.22: Vertical protection level (VPL) contour of an L2-only single-frequency WAAS user in CONUS.

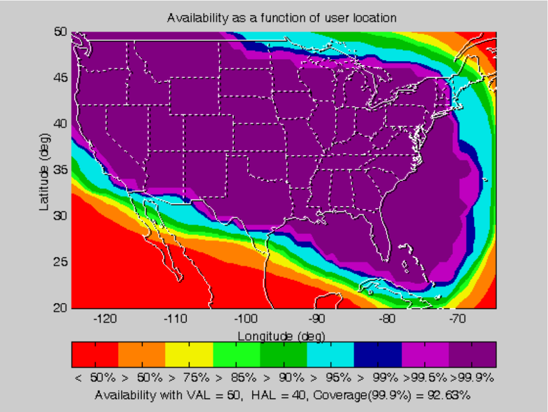

Figure 6.23: Coverage of an L2-only single-frequency WAAS user with baro-aiding in CONUS is 92.63% with VAL=50m, HAL=40m.

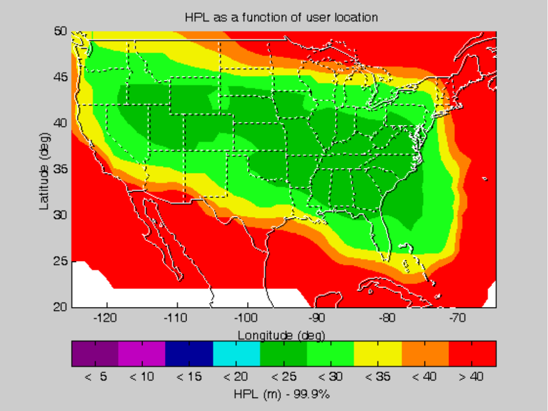

Figure 6.24: Horizontal protection level (HPL) contour of an L2-only single-frequency WAAS user with baro-aiding in CONUS.

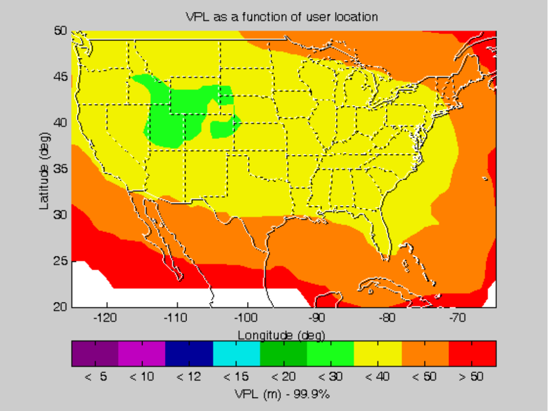

Figure 6.25: Vertical protection level (VPL) contour of an L2-only single-frequency WAAS user with baro-aiding in CONUS.

The simulation results of an L5-only single-frequency WAAS user in CONUS are shown in Figures 6.26 through 6.28. Figure 6.26 indicates that the coverage for users with availability of at least 99.9% of the time is 49.25% of the CONUS. Figures 6.27 and 6.28 show HPL and VPL contours, respectively. Figures 6.29 through 6.31 show the simulation results of an L5-only single-frequency WAAS user with a barometric altimeter aiding in CONUS. Figure 6.29 indicates that the coverage for users with availability of at least 99.9% of the time is 89.29% of the CONUS. Figures 6.30 and 6.31 show HPL and VPL contours, respectively. Comparing Figure 6.26 and Figure 6.29, one notes that the barometric altimeter aiding provided a 40.04% coverage improvement to 99.9% LPV availability for an L5-only single-frequency WAAS user in CONUS. Table 6.3 provides an update comparison table for a single-frequency user with and without barometric altimeter aiding.

User Type	CONUS Coverage of LPV precision approach services (Availability ≥ 99.9%)	VPL (in meter)	HPL (in meter)
L1-only single-frequency w/o baro-aiding	97.58%	20 ≤ VPL	15 ≤ HPL
L1-only single-frequency w/ baro-aiding	99.19%	20 ≤ VPL <50	15 ≤ HPL
L2-only single-frequency w/o baro-aiding	58.34%	30 ≤ VPL	20 ≤ HPL
L2-only single-frequency w/ baro-aiding	92.63%	20 ≤ VPL <50	20 ≤ HPL
L5-only single-frequency w/o baro-aiding	49.25%	30 ≤ VPL	25 ≤ HPL
L5-only single-frequency w/ baro-aiding	89.29%	30 ≤ VPL	20 ≤ HPL

Table 6.3: Comparison of a single-frequency user with and without barometric altimeter aiding.

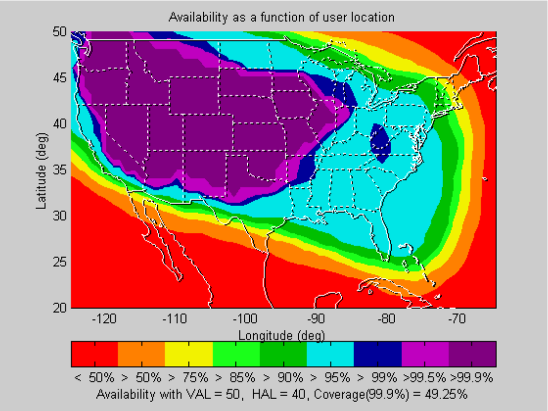

Figure 6.26: Coverage of an L5-only single-frequency WAAS user in CONUS is 49.25% with VAL=50m, HAL=40m.

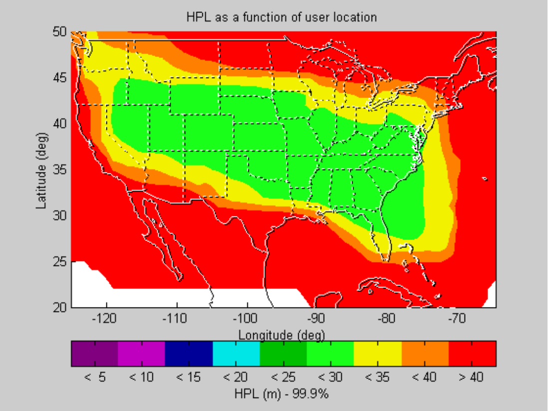

Figure 6.27: Horizontal protection level (HPL) contour of an L5-only single-frequency WAAS user in CONUS.

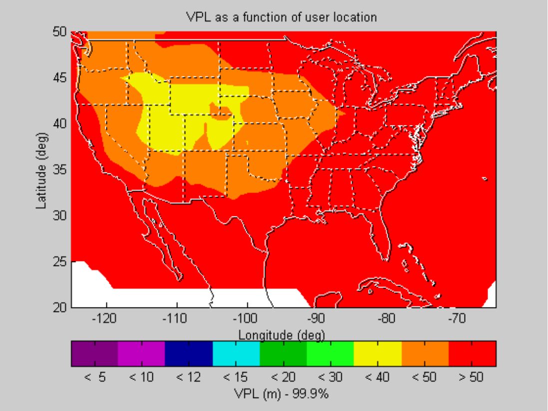

Figure 6.28: Vertical protection level (VPL) contour of an L5-only single-frequency WAAS user in CONUS.

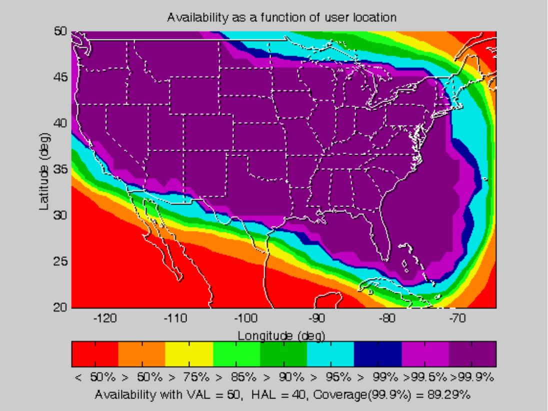

Figure 6.29: Coverage of an L5-only single-frequency WAAS user with baro-aiding in CONUS is 89.29% with VAL=50m, HAL=40m.

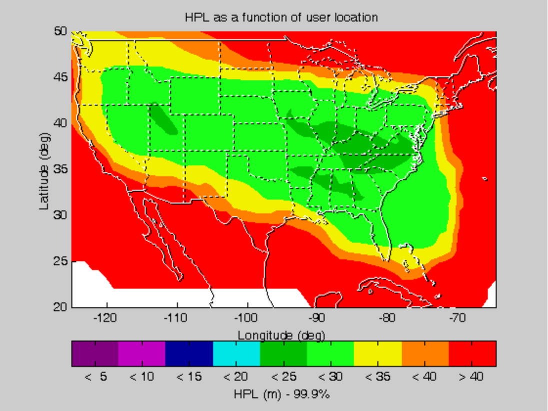

Figure 6.30: Horizontal protection level (HPL) contour of an L5-only single-frequency WAAS user with baro-aiding in CONUS.

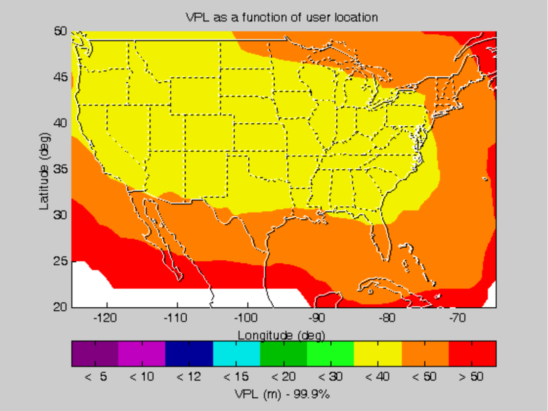

Figure 6.31: Vertical protection level (VPL) contour of an L5-only single-frequency WAAS user with baro-aiding in CONUS.

The simulation results of an L2-L5 dual-frequency user in CONUS are shown in Figures 6.32 through 6.37. Figure 6.32 indicates that the coverage for users with availability of at least 99.9% of the time is 79.97% of the CONUS. Figures 6.33 and 6.34 show HPL and VPL contours, respectively. Figures 6.35 through 6.37 show the simulation results of an L2-L5 dual-frequency user with a barometric altimeter aiding in CONUS. Figure 6.35 indicates that the coverage for users with availability of at least 99.9% of the time is 99.42% of the CONUS. Figures 6.36 and 6.37 show HPL and VPL contours, respectively. Comparing Figure 6.32 and Figure 6.35, one notes that the barometric altimeter aiding provided a 19.45% coverage improvement of 99.9% LPV availability for an L2-L5 dual-frequency GPS/WAAS user in CONUS. Table 6.4 provides a comparison table for an L2-L5 dual-frequency user with and without barometric altimeter aiding.

User Type	CONUS Coverage of LPV precision approach services (Availability ≥ 99.9%)	VPL (in meter)	HPL (in meter)
L2-L5 dual-frequency w/o baro-aiding	79.97%	20 ≤ VPL	20 ≤ HPL
L2-L5 dual-frequency w/ baro-aiding	99.42%	20 ≤ VPL <50	15 ≤ HPL

Table 6.4: Comparison of an L2-L5 dual-frequency user with and without a barometric altimeter aiding.

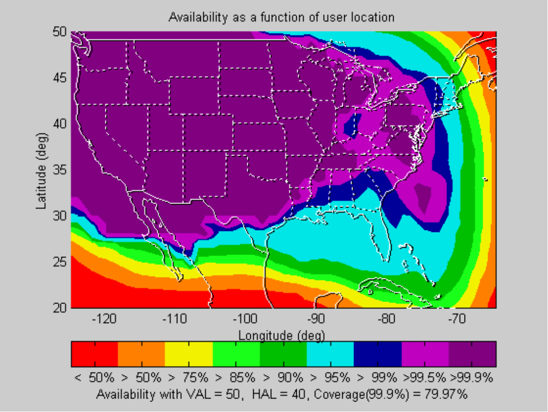

Figure 6.32: Coverage of an L2-L5 dual-frequency WAAS user in CONUS is 79.97% with VAL=50m, HAL=40m.

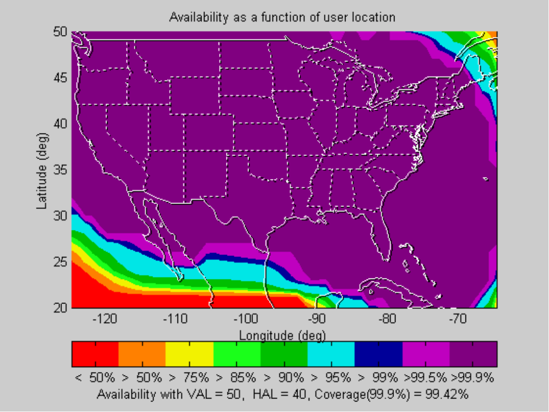

Figure 6.35: Coverage of an L2-L5 dual-frequency WAAS user with baro-aiding in CONUS is 99.42% with VAL=50m, HAL=40m.

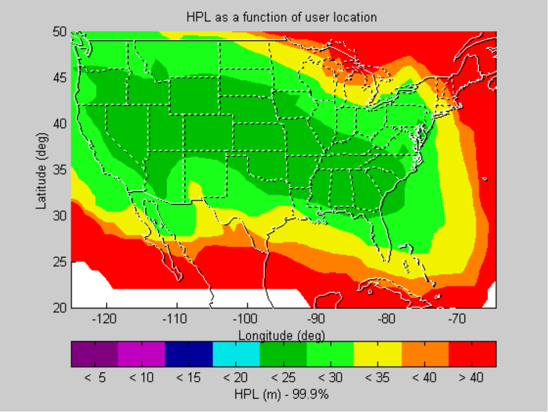

Figure 6.33: Horizontal protection level (HPL) contour of an L2-L5 dual-frequency WAAS user in CONUS.

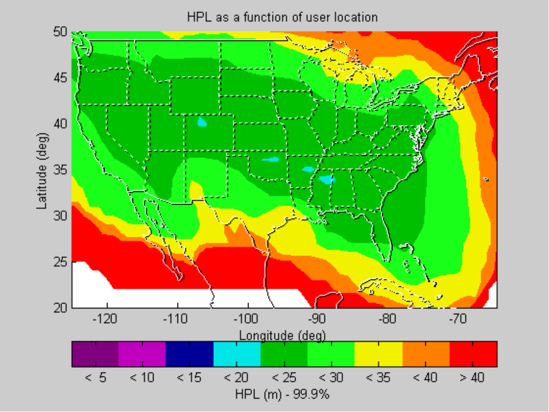

Figure 6.36: Horizontal protection level (HPL) contour of an L2-L5 dual-frequency WAAS user with baro-aiding in CONUS.

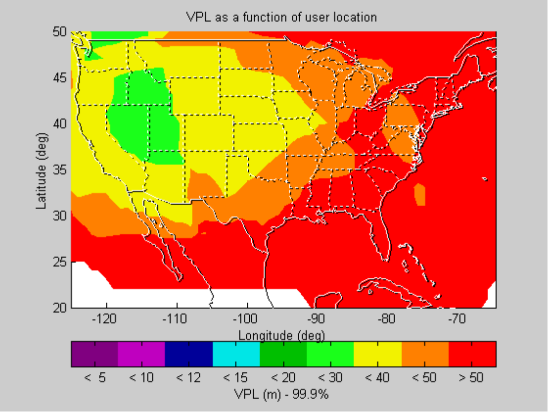

Figure 6.34: Vertical protection level (VPL) contour of an L2-L5 dual-frequency WAAS user in CONUS.

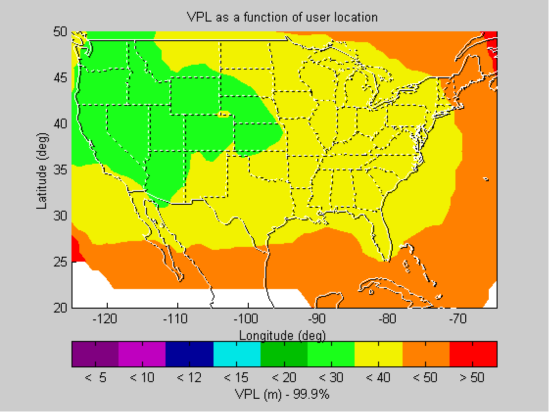

Figure 6.37: Vertical protection level (VPL) contour of an L2-L5 dual-frequency WAAS user with baro-aiding in CONUS.

6.7 CONCLUSIONS

This chapter used MAAST to analyze the LPV CONUS coverage of the single-frequency WAAS users and the L2-L5 dual-frequency user both with and without a barometric altimeter aiding. Because the barometric altimeter acts as a virtual satellite above the user location, barometric altimeter information is extremely beneficial, primarily in the vertical. It is particularly useful when the other satellites have bad geometry.

The MAAST simulation results of the barometric altimeter aiding show greater coverage improvements in L2-only and L5-only single-frequency users than in L1-only single-frequency users. That is because most of the VPL values of L2-only and L5-only single-frequency users above the LPV VAL (i.e., 50m) are not much over 50m. Therefore, with the barometric altimeter aiding, these VPL values can be improved to be less than 50m. This is why the MAAST simulation results show greater coverage improvement in L2-only and L5-only. However, the LPV CONUS coverage of L1-only with barometric altimeter aiding (99.19%) is better than the coverage of the L2-only with barometric altimeter aiding (92.63%) and L5-only with barometric altimeter aiding (89.29%).

Chapter 7

Conclusions

7.1 SUMMARY OF THESIS CONTRIBUTIONS

The research has shown many advantages of GPS modernization. The new civil signals on L2 and L5 significantly enhance the availability of the augmented GPS system for aviation. The nominal performance with all 3 signals increases to 100% availability for the LPV approaches in CONUS. Furthermore, with one signal interfered with, the availability is 99.9% for 100% of CONUS. Even the worst case with 2 signals blocked by interference yields a 50% or better CONUS coverage of LPV approaches for 99.9% availability. Details of the results are in the following sections.

7.1.1 DEVELOPED NEW PROTECTION LEVEL (PL) CALCULATIONS

The current WAAS Master Station (WMS) algorithms use the coded L1 signal and codeless L2 signal to generate the WAAS corrections and error bounds. In modernized GPS, both L1 and L5 will be used for civil aviation safety-of-life services. Thus, the WMS algorithms will change to use the L1 and L5 signals to generate the WAAS corrections and error bounds. This thesis derived new WAAS WMS UDRE and GIVE algorithms to accomplish the change from the codeless L2 to the coded L5.

The current WAAS PL calculation defined in the WAAS MOPS was designed for an L1-only single-frequency user. This thesis derived the new WAAS PL calculations for the L2-only and the L5-only single-frequency users. The changes are mainly in the UIRE (User Ionosphere Range Error) calculations. The summary of the changes in the WMS algorithm and the new WAAS PL calculations for the single-frequency users are highlighted yellow in Figure 7.1.

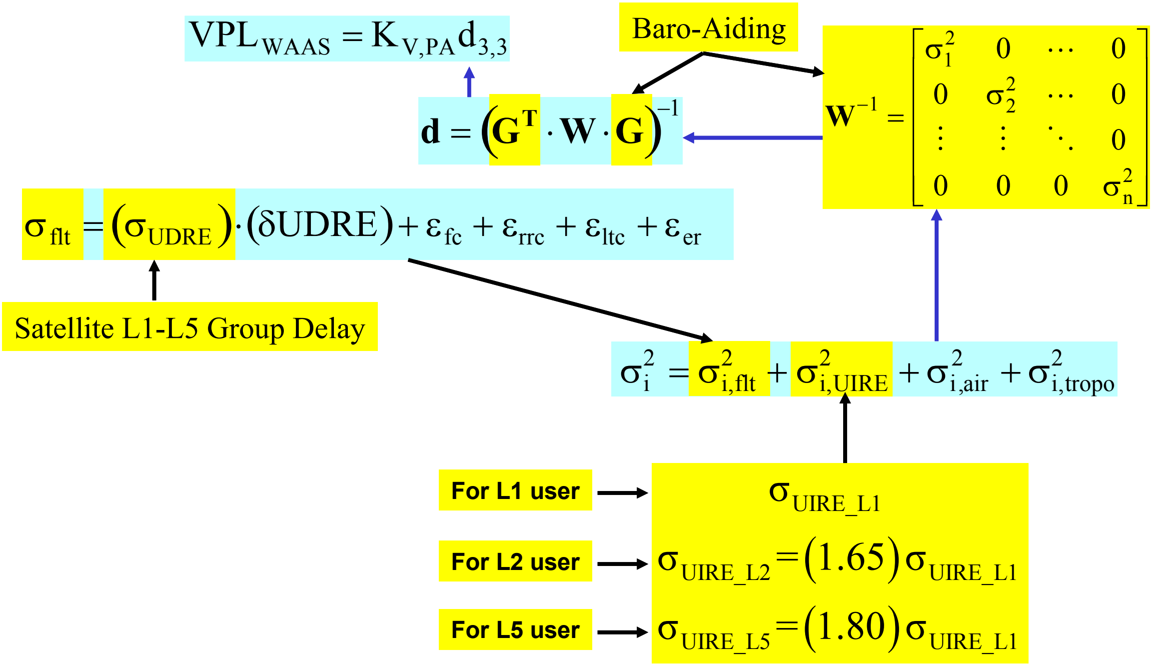

Figure 7.1: Summary of the new WAAS protection level calculations for the single frequency users. The yellow highlighted portion shows the differences in comparison with the current WAAS protection level calculation.

This thesis also derived the new PL calculations for dual-frequency users. The new UDRE (User Differential Range Error) calculation included all the confidences of the different satellite hardware group delay estimations (σ_{SV_L1L2}, σ_{SV_L1L5}, and σ_{SV_L2L5}) to protect the

L1-L2, L1-L5, and L2-L5 dual-frequency users, respectively. The new UIRE calculation for the dual-frequency users included the confidence of the residual airborne receiver noise and multipath errors. Thus, there is no additional $\sigma_{i,air}$ term needed in the PL calculation for the dual-frequency users. Additionally, for an L2-L5 dual-frequency user, the optimal use of ionospheric corrections either from the WAAS or directly from the L2-L5 dual-frequency receiver is required. A summary of the new protection level calculation for dual-frequency users is shown in Figure 7.2.

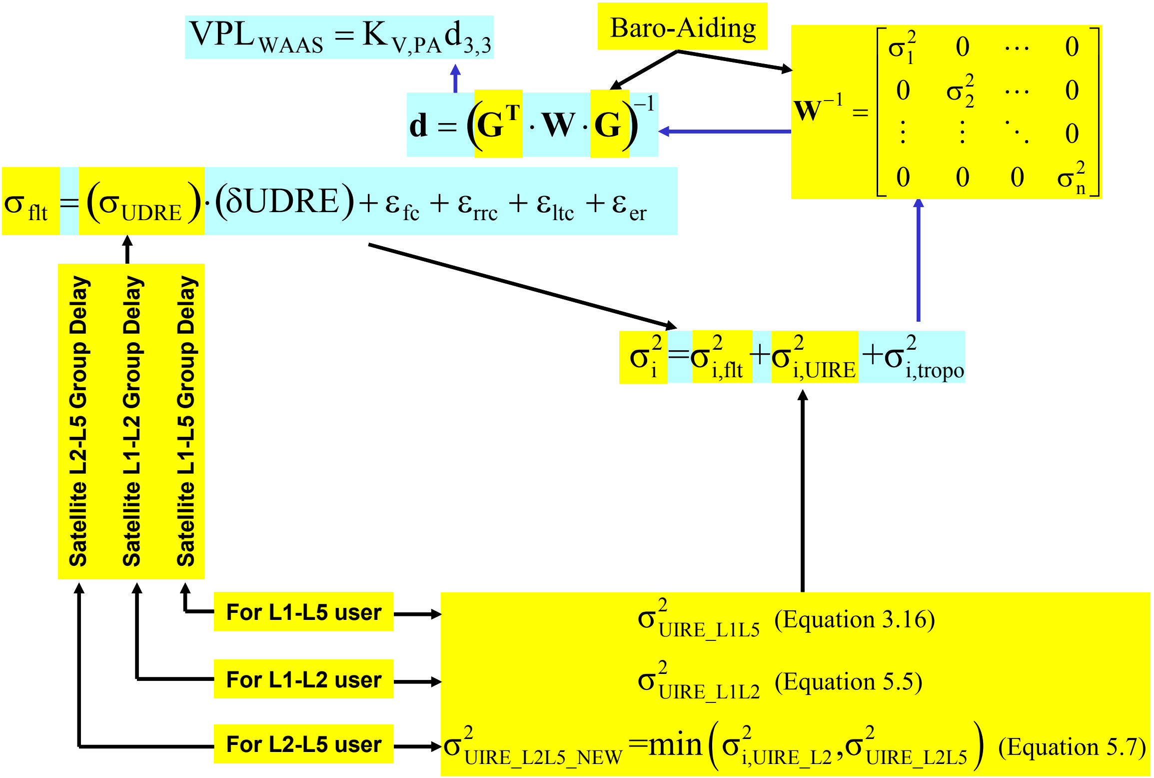

Figure 7.2: Summary of the new WAAS protection level calculations for the dual-frequency users. The yellow highlighted portion shows the differences in comparison with the current WAAS protection level calculation.

7.1.2 SUSTAINED MULTI-FREQUENCY PERFORMANCE FOR AN AIRCRAFT DESCENDING INTO AN RFI FIELD

This thesis developed three techniques based on current and future information available to aircraft for graceful reversion from dual to single frequency WAAS. First, one can use the code-carrier divergence technique to continue ionospheric delay estimation. This technique requires a reliable cycle slip detector. Second, one can use the WAAS ionospheric threat model technique to bound the ionosphere error. This technique requires an ionosphere storm detector. This ionosphere storm detector is designed to listen to the new WAAS message indicating the presence of ionosphere storm. Third, one can use the maximum ionospheric delay gradient model technique to estimate ionospheric delay during the ionosphere storm period. This technique should only be used when there is no available ionosphere storm detector. All of these techniques have the ability to provide good ionospheric delay estimation (better than using the WAAS grid) after the onset of RFI.

Figure 7.3 shows the summary comparison of the VPL contours. These VPL contours from the top to the bottom are in the order of VPL performance 9 minutes after losing a signal to RFI. According to Figure 7.3, the best VPL performance is the use of the code and carrier divergence technique. The next best VPL performance is the use of the WAAS ionosphere threat model technique. The third best is the use of the maximum ionospheric delay gradient model technique. The base line shown is the use of the WAAS grids. Therefore, all three techniques outperformed the use of the WAAS grid.

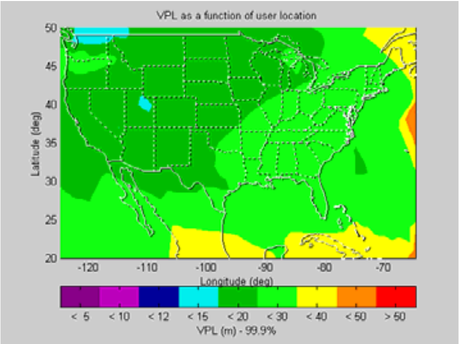

Code and Carrier Divergence Technique

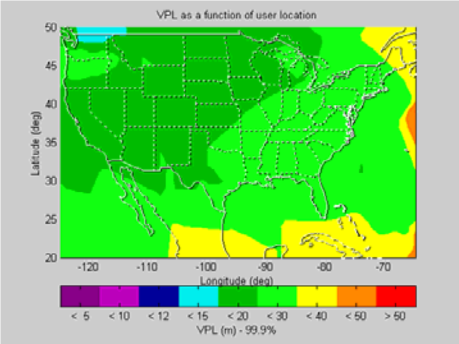

WAAS Iono. Threat Model Technique

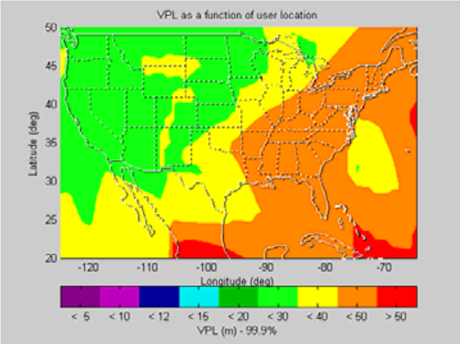

Max. Iono. Delay Gradient Model Technique

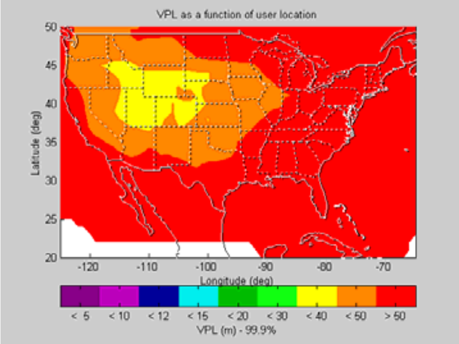

WAAS grid

Figure 7.3: A summary comparison of the uses of all techniques 9 minutes after entering an RFI field. These VPL contour plots are shown in the order of VPL performance from top to bottom. All of the first three techniques outperform the WAAS grids.

The 9-minute final approach duration used in this thesis was derived from the final approach velocity of a general aviation (GA) aircraft, but these techniques are not limited to GA aircraft. The final approach velocities of the commercial airliner are faster than the GA aircraft, so the final approach duration is shorter in time. Therefore, these three techniques will perform better on the commercial airliners than on GA aircraft.

7.1.3 PREDICTED THE FIRST THREE-FREQUENCY GPS/WAAS LPV COVERAGE IN CONUS

This thesis first co-developed the MAAST, which implemented the real WMS algorithm. MAAST was intended as an efficient and effective tool for algorithm development and optimization. It does not guarantee that we will see exactly the indicated level of availability at each location. In creating MAAST a number of assumptions were made. MAAST algorithms are for confidence bounding only; they do not model corrections. Furthermore, MAAST is strictly deterministic, and does not model asset failures in a probabilistic manner. Despite these limitations, MAAST allows users to rapidly model availability and coverage and is valuable for WAAS algorithm research. MAAST was modified to analyze all changes in the PL calculations considered in this thesis.

A three-frequency GPS/WAAS user can take advantage of both the dual-frequency ionospheric delay estimation and frequency diversity in the presence of RFI. Figure 7.4 shows a summary of our MASST results. As shown: a three-frequency user, an L1-L5 and an L1-L2 dual-frequency user all have LPV precision approach services available 99.9% of the time over 100% of CONUS. An L2-L5 user has 79.97% coverage, an L1-only user has 97.58% coverage, an L2-only user has 58.34% coverage, and an L5-only user has 49.25% coverage. For an L2-L5 dual-frequency user, the loss of coverage (in comparison with the other dual-frequency user cases) is due to the narrow frequency separation between the GPS L2 and L5 signals. For the L2-only and the L5-only single-frequency users, the loss of coverage (in comparison with the L1-only single-frequency user) is due to the lower GPS frequency having larger ionospheric delay uncertainty.

7.1.4 DEVELOPED BAROMETRIC ALTIMETER CONFIDENCE MODEL

This thesis quantified (analytically and experimentally) error bounds for a barometric altimeter. In addition to the multi-frequency GPS and WAAS, this thesis also investigated the effect of using a barometric altimeter. The analysis estimated the altitude from historical meteorological observation data collected at different locations in the CONUS. By comparing the estimated altitude with true altitude, altitude error data was generated. By applying statistical and linear estimation techniques to the altitude error data, a model for barometric altimeter confidence was developed. This barometric altimeter confidence model was evaluated via the historical worst-case meteorological observation data and the Stanford flight test data.

This thesis developed barometric altimeter aiding to complement GPS navigation. MAAST was modified to include the barometric altimeter aiding, which was treated as a virtual satellite with known clock at the user location during the availability simulation. The MAAST simulation results showed that when combining the modernized GPS, the WAAS, and the barometric altimeter aiding, a three-frequency user, an L1-L5 and an L1-L2 dual-frequency user all had LPV precision approach services available 99.9% of the time over 100% of CONUS. An L2-L5 user has 99.42% coverage, L1-only user has 99.19% coverage, an L2-only user has 92.63% coverage, and an L5-only user has 89.29% coverage. Figure 7.4 shows the MAAST simulation results for a GPS/WAAS user with barometric altimeter aiding.

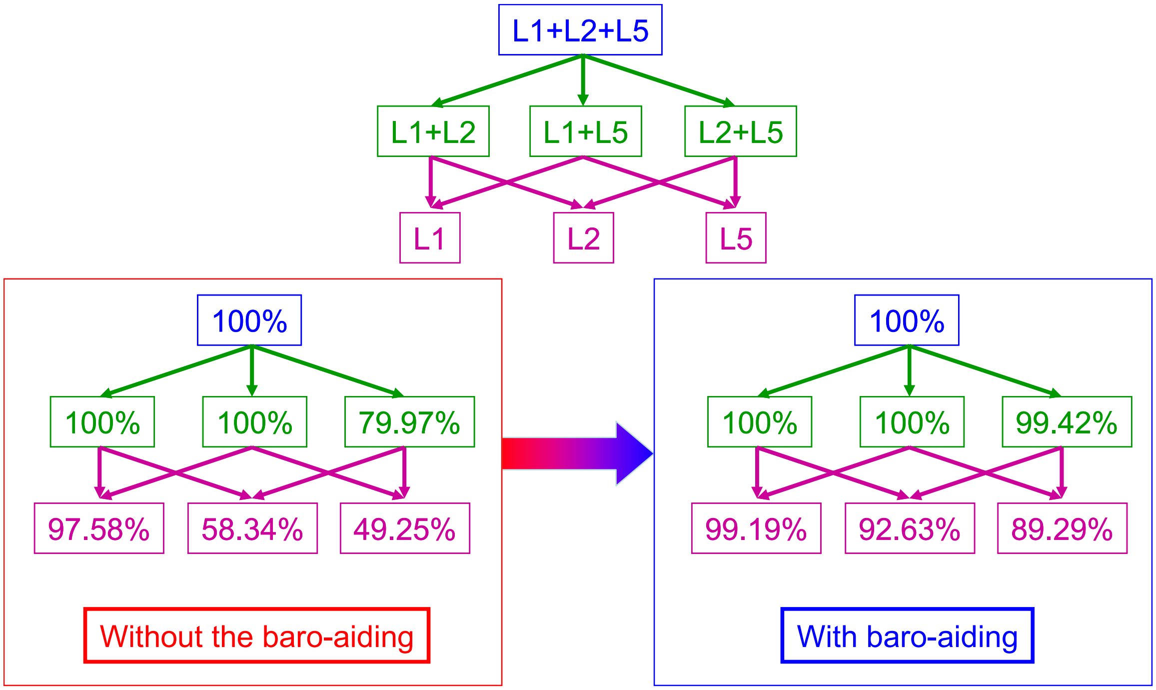

Figure 7.4: The summary of MAAST simulation results.

To show the actual coverage of a dual-frequency user, the MAAST is modified to include all countries in North and South America. Because of the memory limitation of the computer, the simulation configuration is also modified to use a 5-degree user grid and a 300-second time step in comparison with the previous simulation configuration listed in Table 3.1. The MAAST's wider coverage results are shown in Figures 7.5 and 7.6. Figure 7.5 shows the wider coverage map for an L1-L2 dual-frequency user, and Figure 7.6 shows the wider coverage map for an L1-L5 dual-frequency user. An L1-L2 dual-frequency user has LPV precision approach services available 99.9% of the time over 34.27% of North and South America, and an L1-L5 dual-frequency user has LPV precision approach services available 99.9% of the time over 34.94% of North and South America.

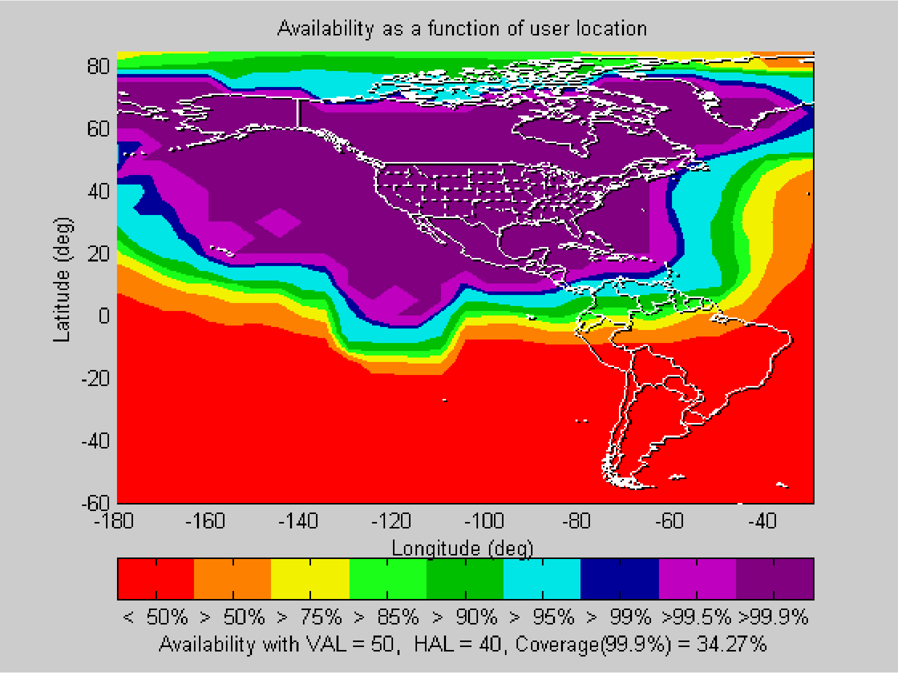

Figure 7.5: Coverage of an L1-L2 dual-frequency GPS/WAAS user in North and South America is 34.27% with VAL = 50m, HAL = 40m.

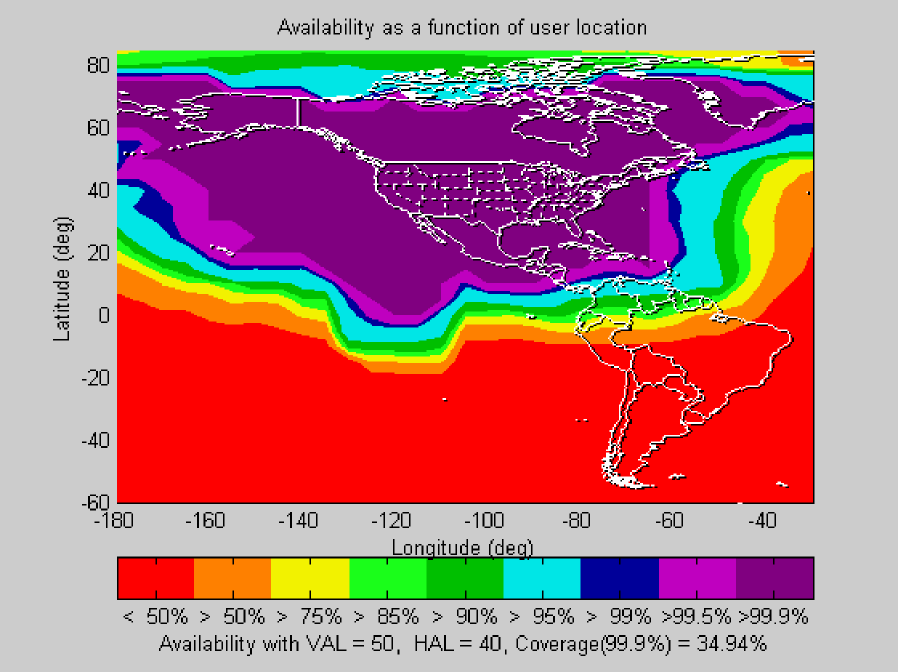

Figure 7.6: Coverage of an L1-L5 dual-frequency GPS/WAAS user in North and South America is 34.94% with VAL = 50m, HAL = 40m.

7.2 RECOMMENDATIONS FOR FUTURE WORK

This thesis showed the benefits of modernized GPS and WAAS. Future research will be to build it and fly it. The development of a three-frequency GPS receiver will investigate both the hardware and software aspects in advance of the availability of the second and third civil frequency signals. There will be two prototype three-frequency platforms [Akos]. The first option is to construct a transmitter, channel model, and receiver for laboratory-based experimentation. The second option is to locate an existing satellite broadcasting on three frequencies using a common clock.

7.3 CLOSING REMARKS

The Global Navigation Satellite System (GNSS) will be the primary-means aircraft navigation system. GPS modernization and WAAS will further enhance the accuracy, integrity and availability of this system. This research developed new algorithms for using a modernized three-frequency (L1, L2, and L5) GPS/WAAS receiver and a barometric altimeter, that is robust to bad weather, disturbed ionosphere, and radio frequency interference. The research allows users to operate longer and with significantly greater availability in the presence of these threats versus single-frequency GPS/WAAS.

Appendix A

Using GPS to Synthesize a Large Antenna Aperture Comprised of Mobile Antenna Elements

A.1 INTRODUCTION

This chapter presents a design for a transmitting antenna array comprised of mobile antenna elements [HansenR] [Gerlach], where GPS is used to estimate the current location and velocity of those elements. GPS is also used to synchronize the clocks carried by the elements. With this information, a central algorithm can control the phase of the radio signal radiated from each element so that the multiple signals add constructively at the desired receiving site. The algorithm can also control the elemental phases to cause destructive interference at any undesired receiving site. In this way, GPS is used to synthesize an antenna aperture larger than any single robot or human could carry. This enhanced system is able to communicate over longer distances and has the capability to avoid communication to undesired listeners.

To evaluate the results, the GPS-based array is compared to a more conventional adaptive antenna array [Compton] [Nicolau] [Tsunami] [Widrow67]. The latter array uses signal strength measurement feedback from the desired receiving direction and the undesired receiving direction. This conventional approach will be our baseline to evaluate the efficacy of GPS. When some of the mobile antenna elements are not reporting GPS, the two algorithms will be combined.

A.2 ASSUMPTIONS AND CONFIGURATION

This analysis assumes that the distributed antenna array includes a finite number of mobile antenna elements, as shown in Figure A.1. Each of these will include a radiating element operating at a single common frequency, a GPS receiver, a means to communicate GPS information back to a central processor, and a means to control the phase of the radiated signal. The network is also aware of the bearings to a desired receiving site and an undesired receiving site.

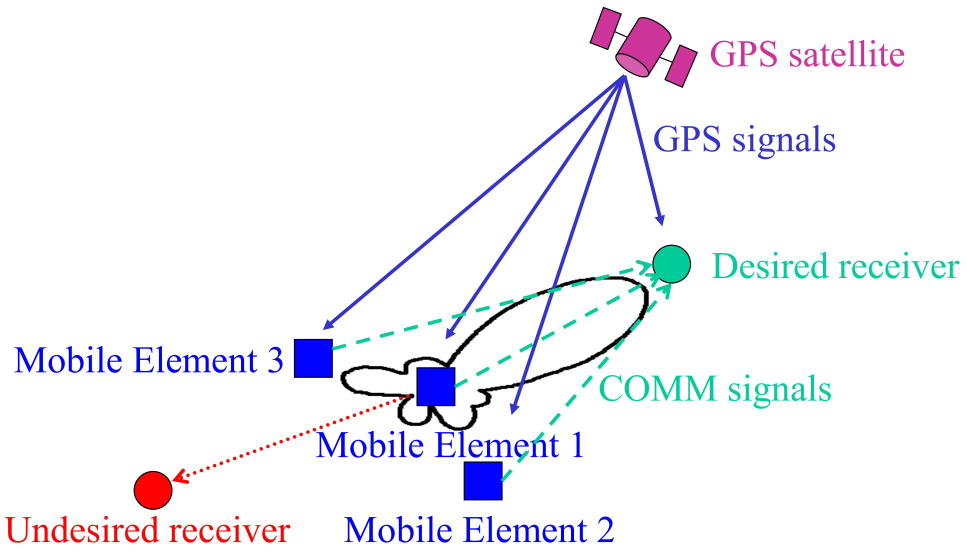

Figure A.1: Configuration.

The central processor processes the received GPS measurements and estimates the relative position of the mobile antenna elements. The central processor also controls the phase of the signal radiated from each element. The control commands enable the signals from the individual mobiles to combine so that the desired pattern is achieved.

Several control algorithms are illustrated in this analysis. They are divided into three categories.

Signal Strength Feedback Only: A closed loop control algorithm based solely on signal strength measurement feedback without using GPS positioning. This technique most closely resembles the conventional use of an adaptive antenna array [Compton] [Nicolau] [Tsunami] [Widrow67]. The conventional array will be our baseline to evaluate the efficacy of our GPS-based array, as shown in Figure A.2.

GPS Positioning Only: An open loop control algorithm using GPS positioning without applying signal strength measurement feedback. This technique was designed to control the phases of the signal from the mobile antenna elements, as shown in Figure A.3.

GPS Positioning and Signal Strength Feedback: A closed loop control algorithm combining GPS positioning and signal strength measurement feedback. This is a new technique to control the mobile antenna elements, as shown in Figure A.4.

This combination is used to mitigate GPS position errors and timing errors, or the absence of GPS measurements from some of the mobile antenna elements.

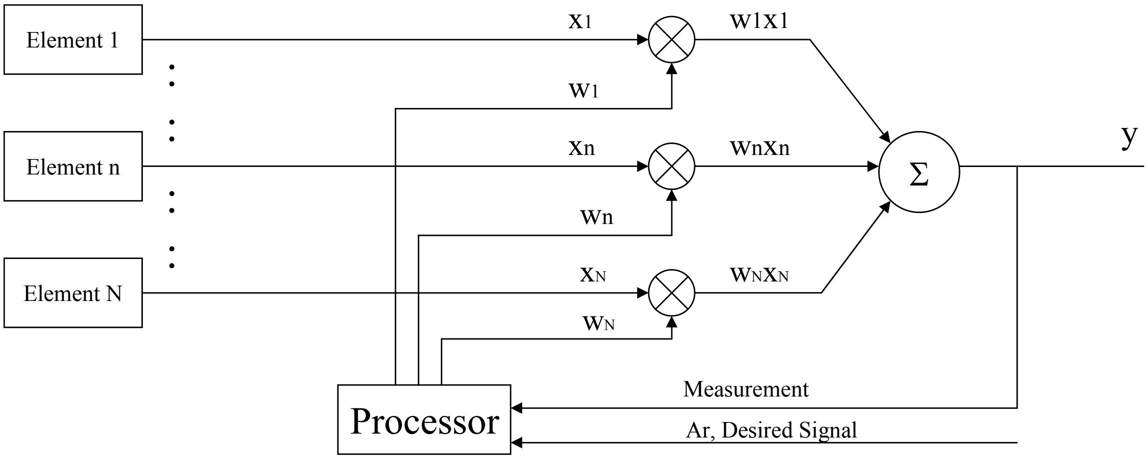

Figure A.2: Two cases: Feedback from the desired direction only and feedback from the desired and undesired directions.

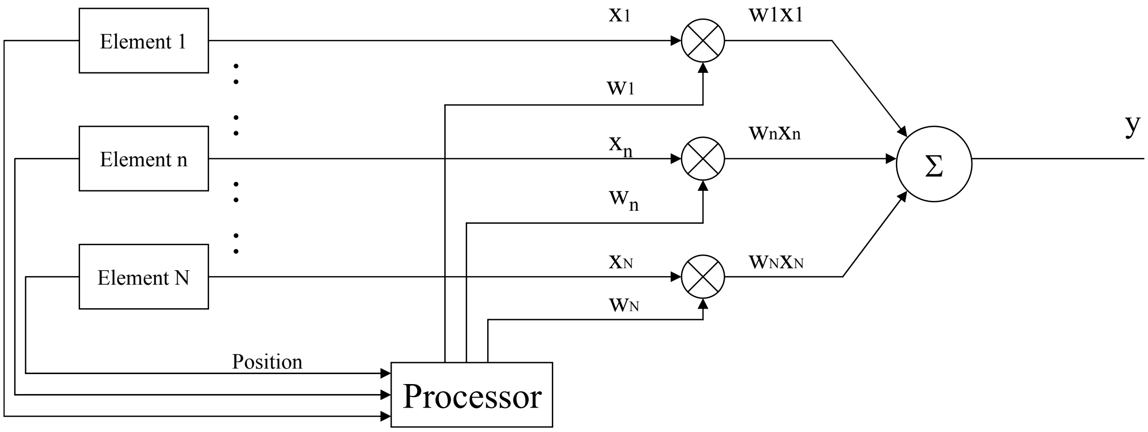

Figure A.3: Using GPS positioning only (open loop), no feedback from the desired or undesired directions.

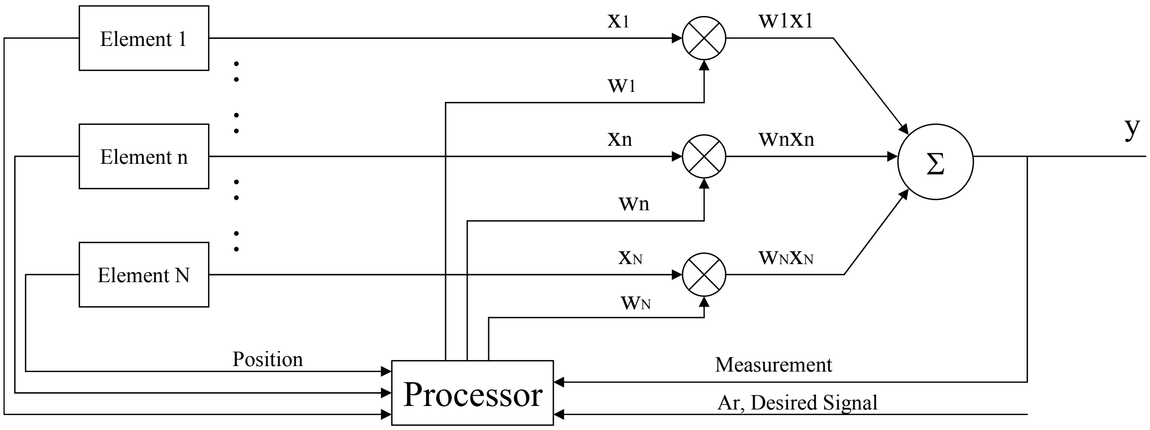

Figure A.4: GPS and feedback from the desired direction, GPS and feedback from the desired and undesired directions, partial GPS and feedback from the desired direction.

The evaluation of the different control algorithms is based on the following three performance goals:

- Maximizing the directivity of the combined signal toward the desired receiver.
- Maximizing the *SIR*, $\left(\frac{S}{I}\right)$, where S is the field strength at the desired receiving location, and I is the field strength at the undesired receiving location.

- Finding the positions of the mobile antenna elements.

The evaluations will be based on computer simulation of an example with eight mobile antenna elements.

A.3 BASICS OF ANTENNA ARRAYS

This analysis presents a potentially simpler scheme using GPS for obtaining antenna gain with an array of mobile antenna elements. Therefore, this analysis makes the following assumptions.

- After a radio wavefront has left the transmitting antenna, its power density is independent of azimuth, and so we neglect any complexity in the radio propagation environment. Despite the diffraction, refraction and multiple reflections, the propagation environment can be represented as a linear system.

- All mobile antenna elements are identical and each is a point source of radiation.

- Far field observation gives us a simple geometric interpretation, "parallel ray approximation" [Kraus]. It is a good approximation for radiation calculations, and each mobile antenna element is considered as a point source based on this assumption.

The signal vector X of the mobile antenna elements is

$$X = \begin{bmatrix} A_1 e^{(j\phi_1)} \\ A_2 e^{(j\phi_2)} \\ . \\ . \\ . \\ A_n e^{(j\phi_n)} \end{bmatrix} = \begin{bmatrix} x_1 \\ x_2 \\ . \\ . \\ . \\ x_n \end{bmatrix} \tag{A.1}$$

where,

A_i is radiation amplitude of each mobile element. This is a function of the distance and elevation of the mobile antenna element. This analysis lets A_i = 1, which implies that isotropic antennae are considered.

ϕ_i is radiation phase of each mobile element

i is *1,2,3,……n*, number of mobile elements

The weight vector W of the phase commands can be represented as

$$W = \begin{bmatrix} e^{(j\theta_1)} \\ e^{(j\theta_2)} \\ . \\ . \\ . \\ e^{(j\theta_n)} \end{bmatrix} = \begin{bmatrix} w_1 \\ w_2 \\ . \\ . \\ . \\ w_n \end{bmatrix} \tag{A.2}$$

where,

θ_i is designed phase for each mobile element

i is *1,2,3,……n*, number of mobile elements

The combined radiation signal field Y is

$$Y = W^T X \tag{A.3}$$

The difference between the measurements and the desired signal field forms the error signal ε:

$$\varepsilon = A_r - Y \tag{A.4}$$

where,

A_r is desired signal pattern

As shown in Figure A.5, the weight update equation of the least mean square (LMS) adaptive algorithm is [Widrow85]

$$W(j+1) = W(j) + 2\mu\varepsilon\left(X^*\right) \tag{A.5}$$

where,

μ is adaptive coefficient

W(j) is weight vector before adaptation

W(j+1) is weight vector after adaptation

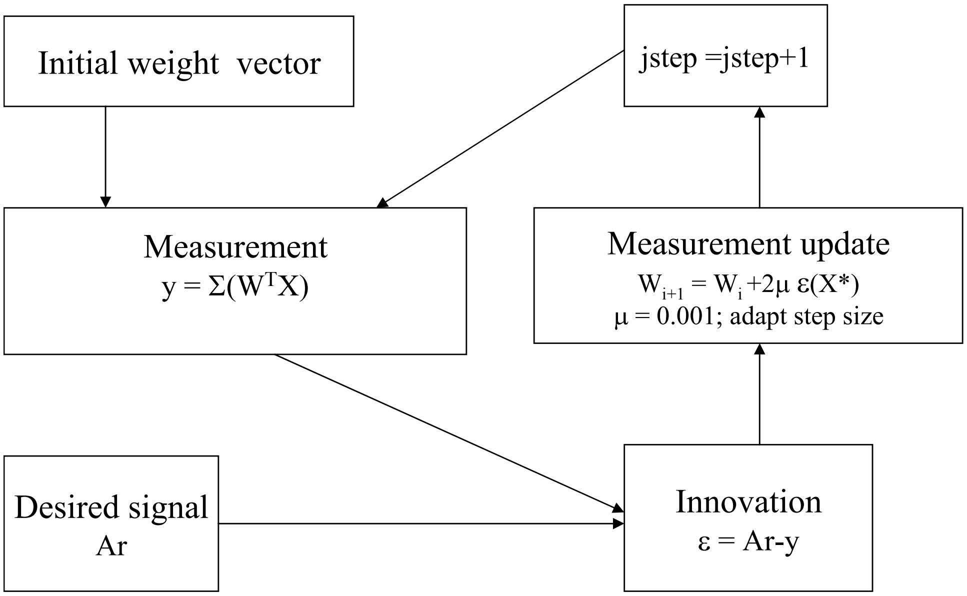

Figure A.5: Block diagram for the least mean square (LMS) adaptive algorithm [Widrow85].

A.4 SIGNAL STRENGTH MEASUREMENT FEEDBACK ONLY - NO GPS

This section does not use GPS. The control concept of this section is the closest to the conventional adaptive antenna and assumes signal strength feedback from the desired direction [Compton] [Nicolau] [Tsunami] [Widrow67]. This analysis considers two systems: one with signal strength feedback from the desired direction only and the other with signal strength feedback from the desired and undesired directions. As shown in Figure A.6, an example antenna array used in this section includes eight mobile antenna elements, a desired receiving site, and an undesired receiving site.

For the first system, the only signal strength measurement feedback was from the desired receiving direction. The central processor based on the least mean square (LMS) adaptive algorithm compares this measured field strength to the desired field strength. The resulting commands cause the signals from the individual mobiles to combine so that an approximation of the desired field strength is achieved. This fulfills the first performance goal, as shown in Figure A.7. However, this system will not be guaranteed to reduce the field strength in the undesired receiving direction because it does not have a measurement from that direction. Consequently, it fails the second performance goal. The third performance goal of positioning cannot be met because the central processor uses the phase control command to calculate the positions of the mobile antenna elements, but fails to do so because of the wavelength ambiguity. As shown in Figure A.8, the resulting position solutions are one wavelength apart, and thus we cannot distinguish which one of them is the true position solution.

The second system installs another signal strength sensor on one of the mobile elements to measure the field strength in the direction of the undesired receiving site. With this measurement feedback and the one from the desired receiving direction, the central processor using the least mean square (LMS) adaptive algorithm will be able to maximize the *SIR*. This additional sensor helps us achieve the second performance goal, as shown in Figure A.9, but it does not enable accurate positioning of the mobile antenna elements.

The systems in this section are the performance baseline and are summarized in Table A.1. In the following section, this analysis will show that GPS improves the performance of the network of the mobile antenna elements relative to this baseline.

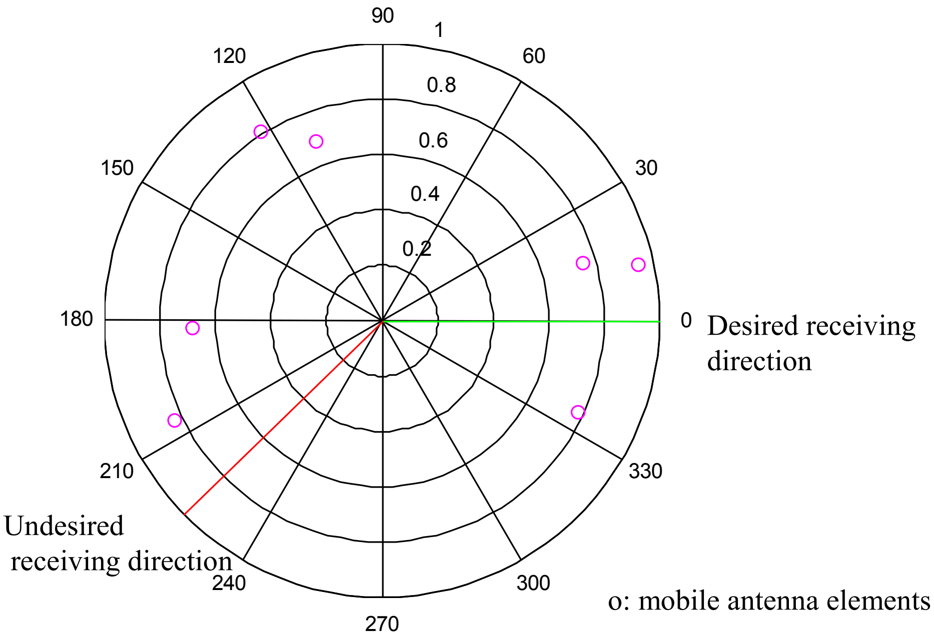

Figure A.6: An example of mobile antenna elements used for evaluation and comparison.

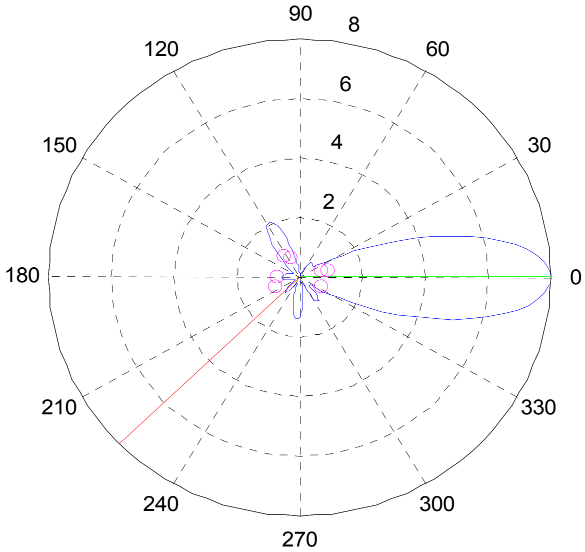

Figure A.7: Result for the signal strength measurement feedback from the desired receiving direction only.

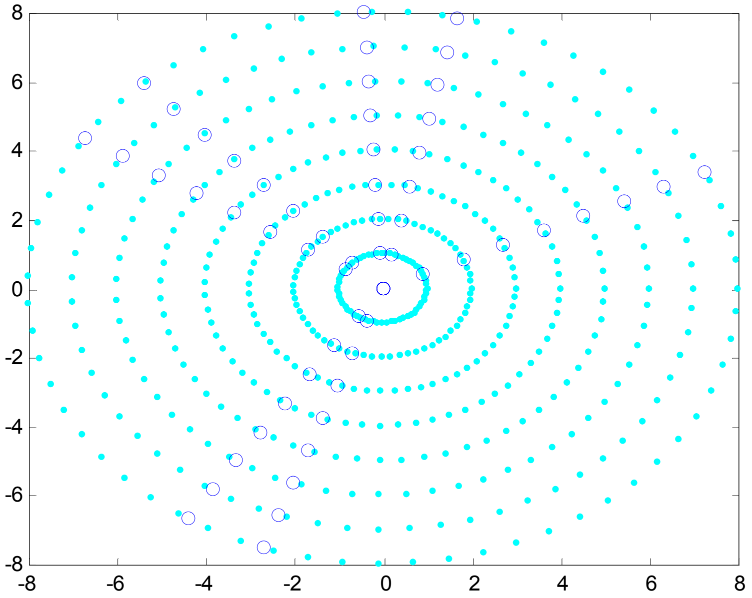

Figure A.8: Position solution for using signal strength feedback only without using GPS positioning.

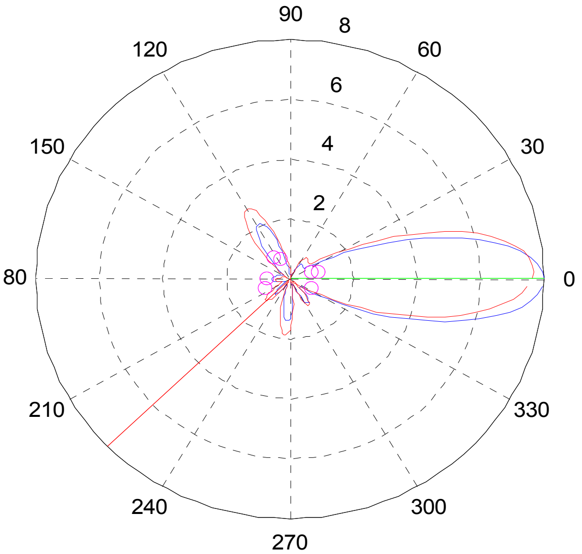

Figure A.9: Result for the feedback from the desired and undesired receiving directions.

	Maximizing the directivity toward desired receiving site	Maximizing the *SIR*	Positioning of the mobile antenna elements
Feedback from desired receiving site only	Achieved	Failed	Failed
Feedback from desired and undesired receiving direction	Achieved	Achieved	Failed

Table A.1: Summary for using signal strength feedback only

A.5 GPS POSITIONING WITHOUT SIGNAL STRENGTH MEASUREMENT FEEDBACK

In this section, signal strength measurement feedback is assumed to be unavailable, and as a result, GPS positioning is the only data available to achieve the performance goals.

The first goal is to maximize the signal strength at the desired receiving site only. GPS is used to estimate the current locations of the mobile antenna elements. With this information, the central processor controls the phase of the radio signal radiated from each mobile so that the multiple signals add constructively at the desired receiving location. Control is based on the differences of the distances from the mobile antenna elements to the desired receiving site.

Let one of the mobile antenna elements be the master element, and the others be slave elements. The distance difference d_i is defined as:

$$d_i = d_{slave} - d_{master} \tag{A.6}$$

where,

d_i is distance difference

d_{slave} is distance from the slave elements to the receivers

d_{master} is distance from the master elements to the receivers

i is $1,2,3,\ldots\ldots,n$, number of mobile antenna elements

The relation between the phase control commands and the distance differences is

$$\theta_i = \frac{2\pi d_i}{\lambda} \tag{A.7}$$

where,

θ_i is phase command for mobile antenna element

λ is operation wavelength

i is $1,2,3,\ldots\ldots,n$, number of mobile antenna elements

Now, the weight vector of the phase commands can be written as:

$$W = \begin{bmatrix} e^{(j\theta_1)} \\ e^{(j\theta_2)} \\ . \\ . \\ . \\ e^{(j\theta_n)} \end{bmatrix} \tag{A.8}$$

The combined signal, Y, radiated in the field is

$$Y = W^T X \tag{A.9}$$

The directivity will be maximized in the desired receiving direction by using this control algorithm. The first performance goal is achieved, and an example is shown in Figure A.10. However, we cannot achieve the second goal with this control algorithm.

A similar goal may be to maximize the signal strength toward an undesired receiving direction and to use this signal to spoof the receiver – to send a false signal. The central processor can generate another weight vector based on the same control algorithm in order to generate the spoofing signal toward the undesired receiving direction, as shown in Figure A.11. Since GPS provides the locations of the mobile antenna elements, the third performance goal is also achieved.

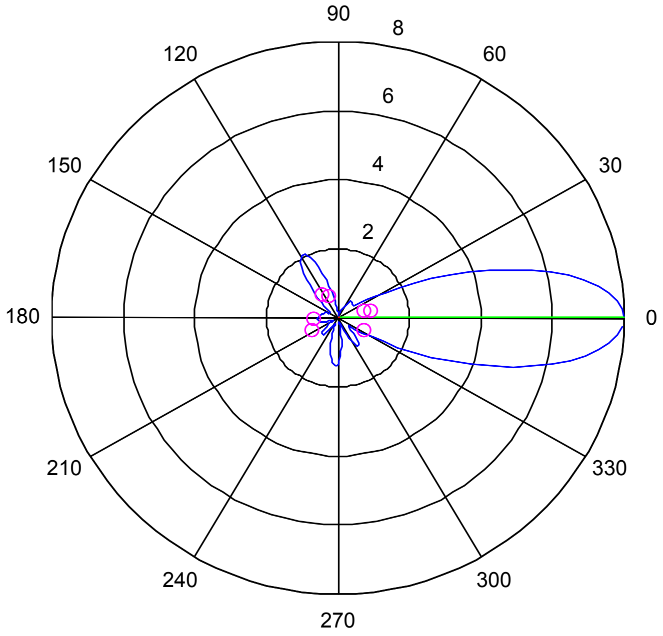

Figure A.10: Result for using GPS positioning only, no signal strength feedback from the desired or undesired direction.

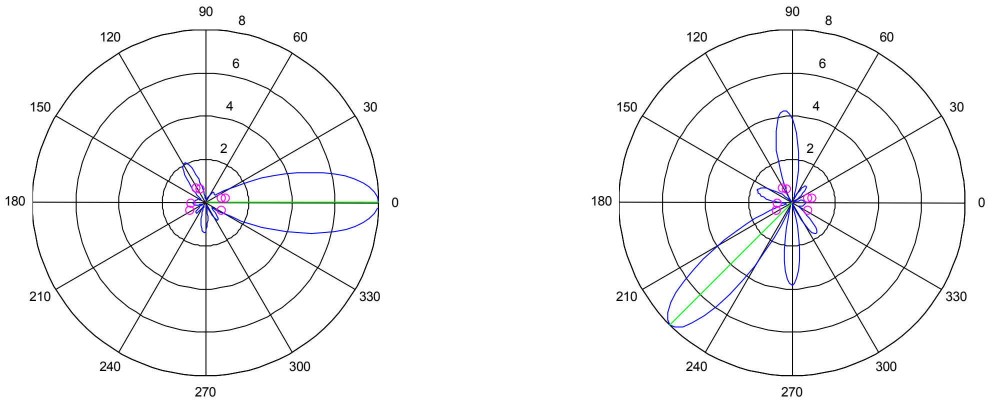

Figure A.11: Result for using GPS positioning only, sending the spoofing signal in an arbitrary direction.

The second goal is to maximize *SIR* and to aim the maximum directivity toward the desired receiving direction. These two objectives might conflict with each other. The cost function we define is

$$Max\left(F_1\left(SIR\right)+F_2\left(Directivity\right)\right) \qquad \text{(A.10)}$$

The compromise of these two objectives gives the optimal solution of the cost function. As shown in Figure A.12, the maximum directivity is not exactly toward the desired receiving location, because the objective is to maximize *SIR*. This is the result of the computer numerical optimal solution of the cost function. The second and third performance goals are achieved by using GPS positioning with the cost function we defined.

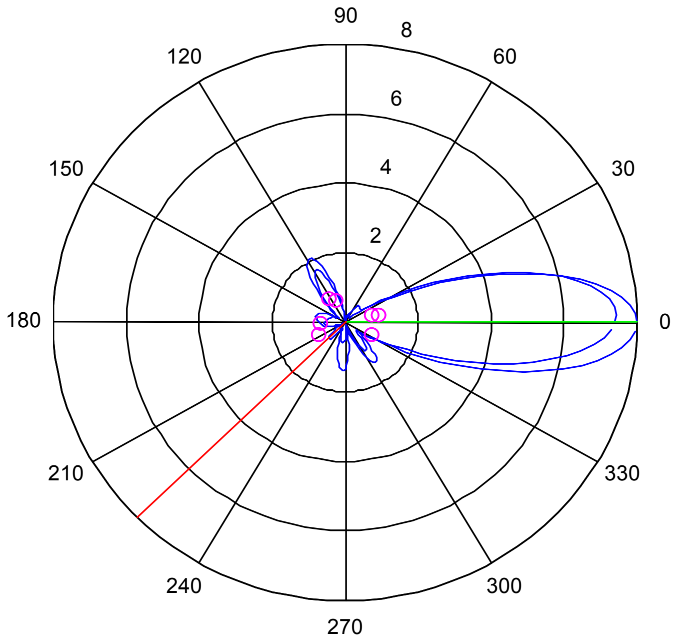

Figure A.12: Result for using GPS positioning and the cost function (A.10).

	Maximizing the directivity toward desired receiving site	Maximizing the *SIR*	Positioning of the mobile antenna elements
GPS only	Achieved	Failed	Achieved
GPS and the cost function (A.10)	Achieved	Achieved	Achieved

Table A.2: Summary for using GPS positioning only

A.6 COMBINED GPS POSITIONING AND SIGNAL STRENGTH MEASUREMENT FEEDBACK

While all three goals can be achieved with GPS positioning alone. This section shows how performance can be improved by combining GPS positioning and signal strength measurement feedback. It also anticipates the next section, which discusses the use of signal strength measurement feedback to recover from partial GPS outages.

The example network used in this section includes eight mobile antenna elements, a desired receiving site, and an undesired receiving site: an example is shown in Figure A.6. The different examples use different sources of field strength measurements. This section also discusses the position and timing errors of GPS.

Recall that the first goal is to maximize the directivity toward the desired receiving direction. Based on the combined algorithms, this goal is achieved, as shown in Figure A.13. This result is the same as the result for using GPS positioning alone or using signal strength measurement feedback alone.

With respect to the second goal, this section is different from the section using signal strength measurement feedback alone. The section with signal strength measurement feedback alone uses random equal weight values as an initial condition to begin the adaptive process. With the combined GPS positioning and signal strength measurement feedback, the adaptive process used weight values that achieve the first performance goal by using GPS positioning only as the initial condition. This condition helped speed up convergence and avoided the divergence of the adaptation. The algorithm combining GPS positioning and signal strength measurement feedback gives the better result: *SIR* = 15.3dB, as shown in Figure A.14. The resulting *SIR* for using GPS positioning alone is 14.7dB, and the resulting *SIR* for using signal strength measurement feedback alone is 9.2dB. This is the advantage of combining GPS positioning and signal strength measurement feedback.

The third goal is to locate the positions of the mobile antenna elements. GPS provides the information that lets the central processor determine those mobile antenna elements' locations.

When GPS position error and timing error are present, the phase commands of the central processor are not the same as those of the mobile antenna elements required to form a desired signal pattern. As a result, larger GPS errors cause worse performance of the mobile antenna elements, as shown in Figures A.15, A.16, and A.17. Based on the sensitivity analysis between GPS errors and system performance, the analysis can decide what kind of GPS is needed to fulfill the specific performance, as shown in Figures A.18, A.19, A.20, and A.21. For example, if the operation frequency is 30 MHz and there is 3dB loss in the directivity (Figure A.15), it means that the directivity is reduced from 8 to 4, and the corresponding position error is 16% of wavelength which is 1.6 meters under this operating frequency. According to Figure A.18, the system is then required to use Local Area Code GPS to satisfy the performance requirement.

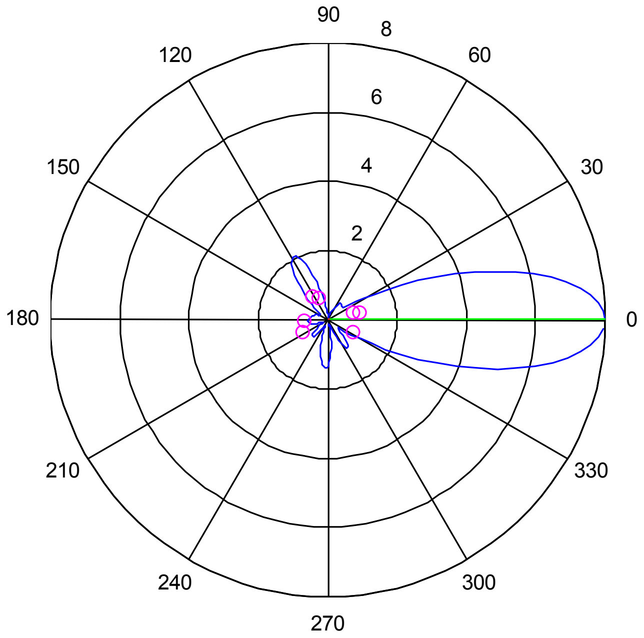

Figure A.13: Result for using GPS positioning and signal strength feedback from the desired receiving direction only.

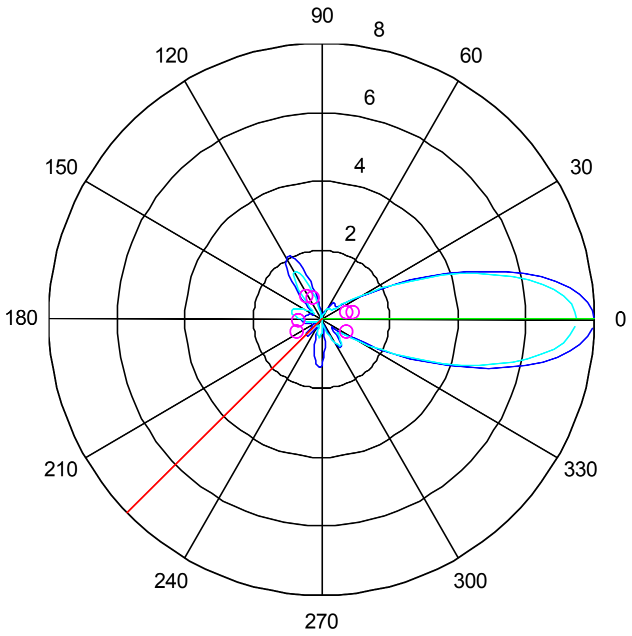

Figure A.14: Result for using GPS positioning and signal strength feedback from the desired and undesired directions.

	Maximizing the directivity toward desired receiving site	Maximizing the *SIR*	Positioning of the mobile antenna elements
Combined GPS and adaptation, measurement feedback from the desired receiving site	Achieved	Failed	Achieved
Combined GPS and adaptation, measurement feedback from the desired and undesired receiving directions	Achieved	Achieved	Achieved

Table A.3: Summary for using GPS positioning and signal strength feedback

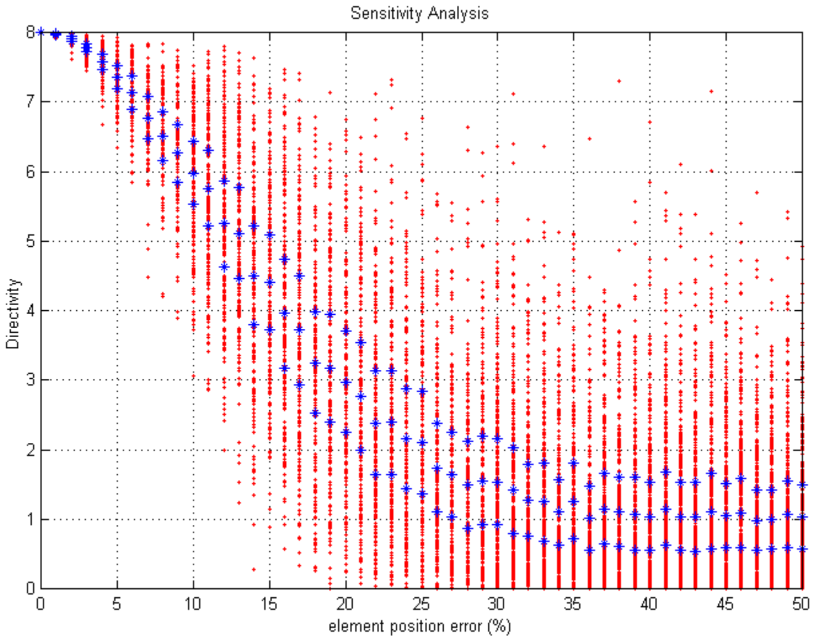

Figure A.15: Sensitivity analysis, directivity, using GPS positioning only; the desired receiving site is the only destination.

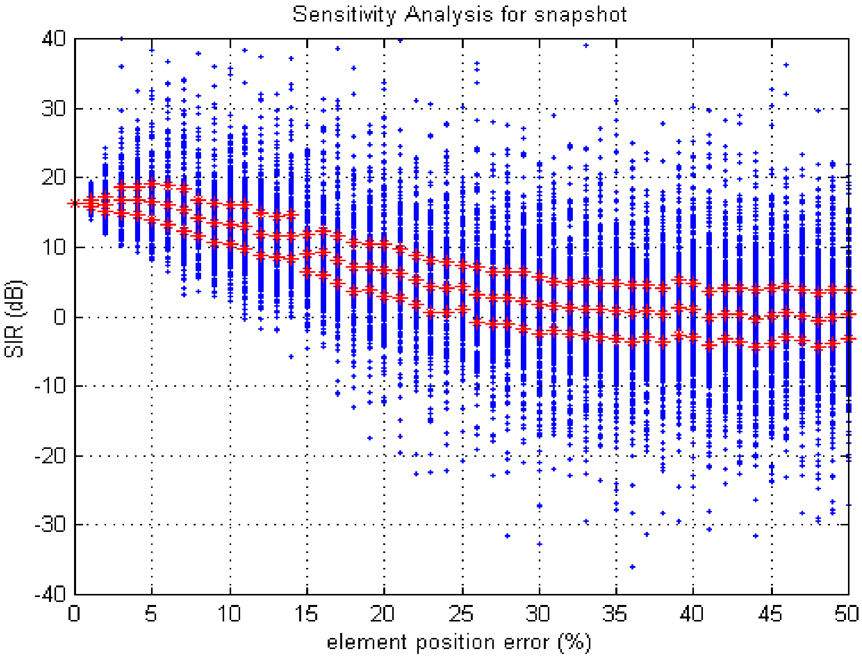

Figure A.16: Sensitivity analysis, *SIR*, using GPS positioning only.

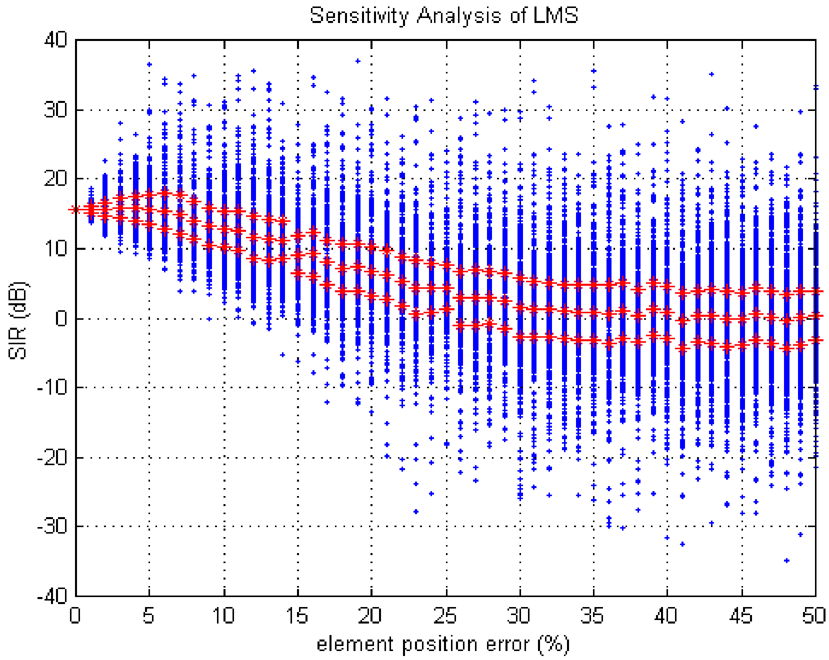

Figure A.17: Sensitivity analysis, ***SIR***, combined GPS positioning and signal strength feedback.

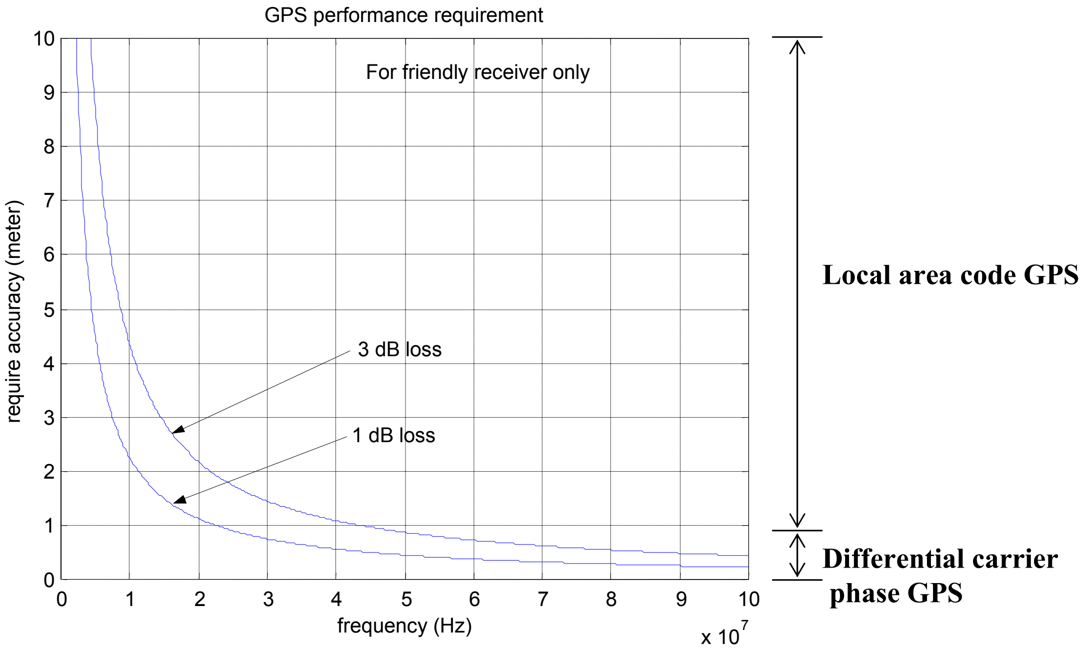

Figure A.18: System requirement for using GPS positioning only; the desired receiving site is the only destination.

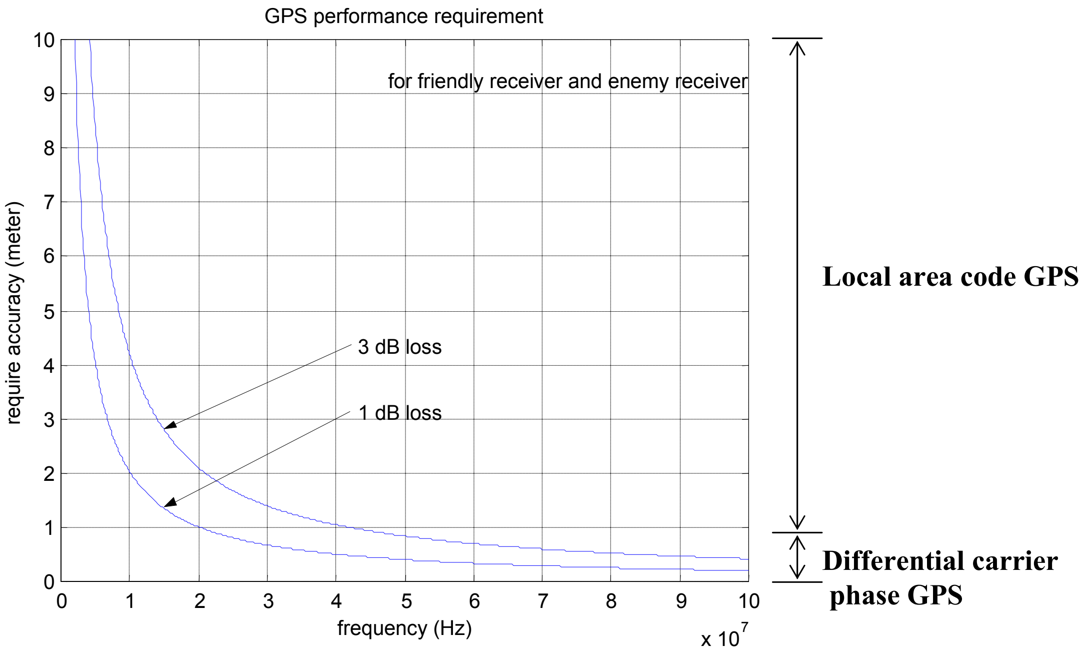

Figure A.19: System requirement for using GPS positioning only.

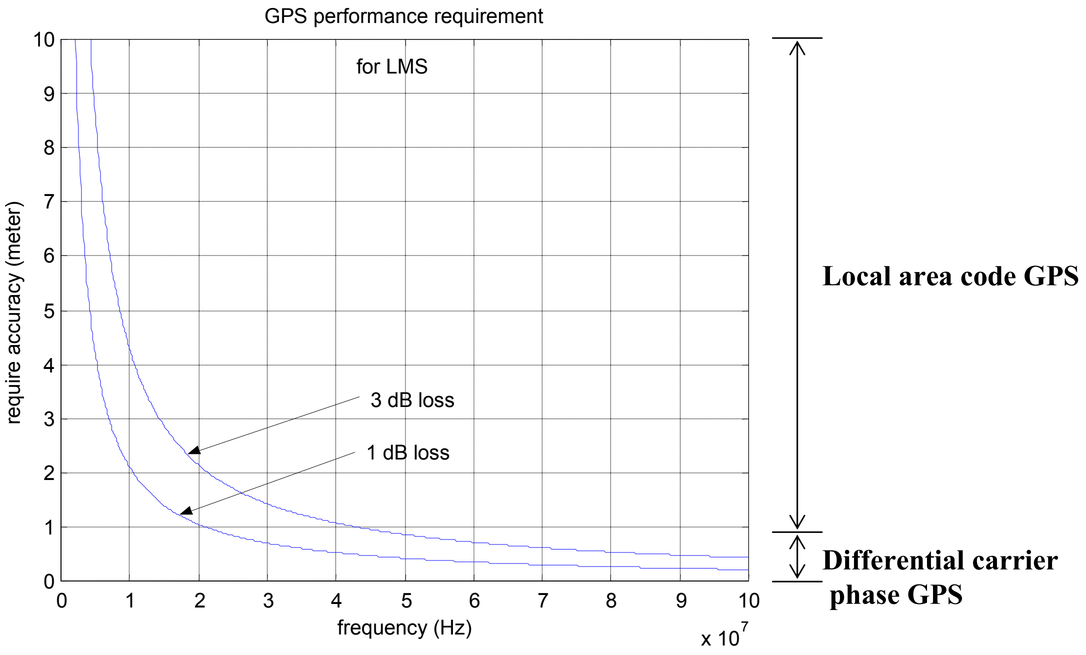

Figure A.20: System requirement for using GPS positioning and signal strength feedback.

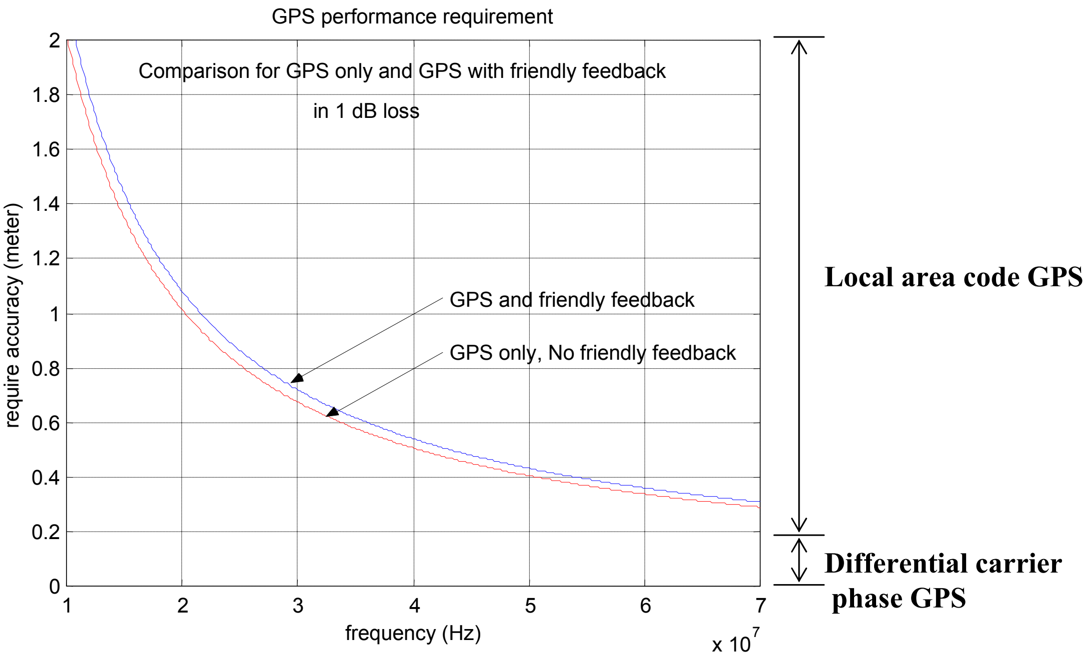

Figure A.21: Comparison of system requirements: using GPS positioning only and using GPS positioning and signal strength feedback.

A.7 PARTIAL GPS

The system has redundant sensor information: some are based on GPS positioning and the rest are based on signal strength measurement feedback. Each of these sensors can be the backup system for the other. For example, when the signal strength measurement link is lost, the system using GPS positioning can sustain the overall function. Or when GPS outages occur, the system using signal strength measurement feedback can maintain the mission.

The systems discussed in this analysis can be found when multiple mobiles are deployed in a remote and possibly hostile area. Even if one of the mobiles were lost, the control concept would enable the survivors to sustain most of the mission objectives. This section will discuss the situation where some of the mobile antenna elements are not reporting GPS.

When some of the mobile antenna elements are not reporting GPS, the signal strength measurement feedback will sustain the function controlling the phase of the remaining mobile antenna elements such that the multiple signals add constructively at the desired receiving location and destructively at the undesired receiving location. The first and second performance goals are thereby achieved, as shown in Figures A.22a and A.23a. However, the mobile antenna elements that are not reporting GPS will not be able to determine their position, because of the wavelength ambiguity, as shown in Figures A.22b and A.23b. As a result, the system cannot fully meet the third performance goal.

As shown in Figure A.24, this analysis assumes that the system cannot control the mobile antenna elements which are not reporting GPS. This is the worst performance of this network system. The resulting *SIR* of mobile antenna elements, in the case where one of them is not reporting GPS, is 14.6 dB. The resulting *SIR* of the previous section that combined GPS positioning and signal strength measurement feedback is 15.3 dB. The resulting *SIR* of the mobile antenna elements for two of them not reporting GPS is 11.0 dB. The resulting *SIR* of mobile antenna elements using signal strength measurement feedback is only 9.2 dB. As a result, the system combining GPS positioning and signal strength measurement feedback is better than the system using signal strength measurement feedback only, even if the system combining GPS positioning and signal strength measurement feedback has fewer mobile antenna elements than the one using signal strength measurement feedback only. This is another advantage of using GPS positioning in the networks of mobile antenna elements.

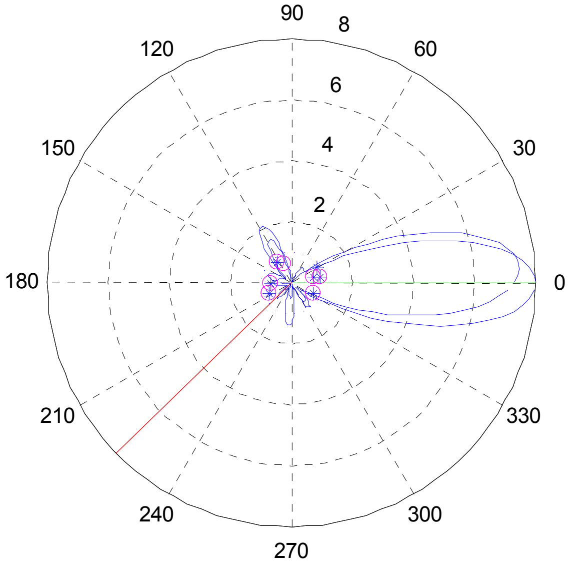

SIR decrease from 15.3 dB to 14.6 dB

Figure A.22a: Beam solution when one of the mobile antenna elements is not reporting GPS.

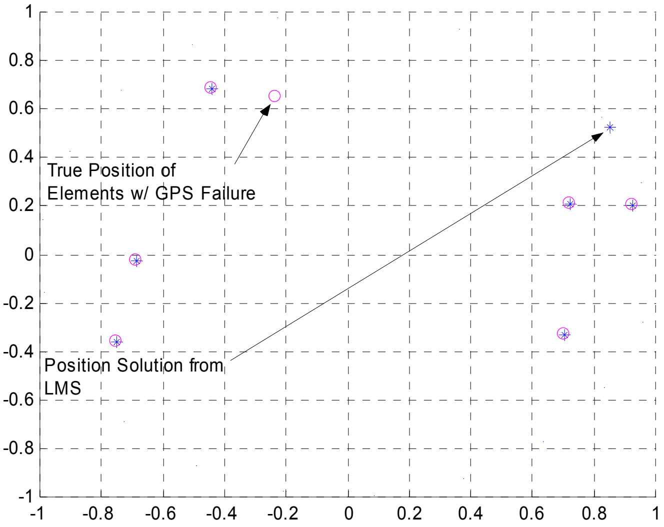

o: elements with GPS failure
***: position solution from LMS (with ambiguity)**

Figure A.22b: Position solution when one of the mobile antenna elements is not reporting GPS.

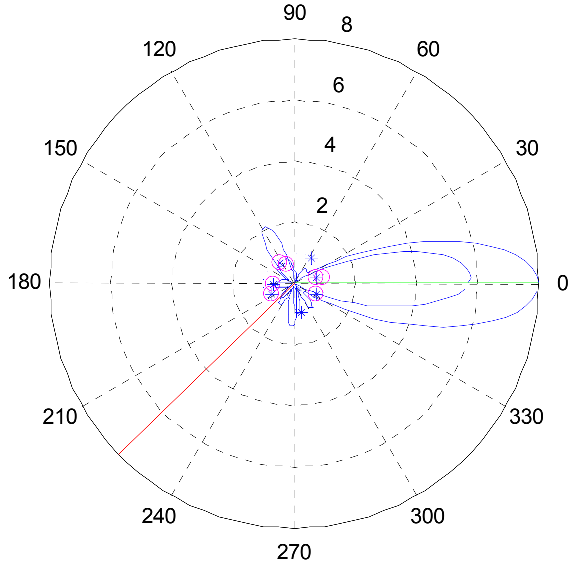

SIR decrease from 15.3 dB to 11.0 dB

Figure A.23a: Beam solution when two of the mobile antenna elements are not reporting GPS.

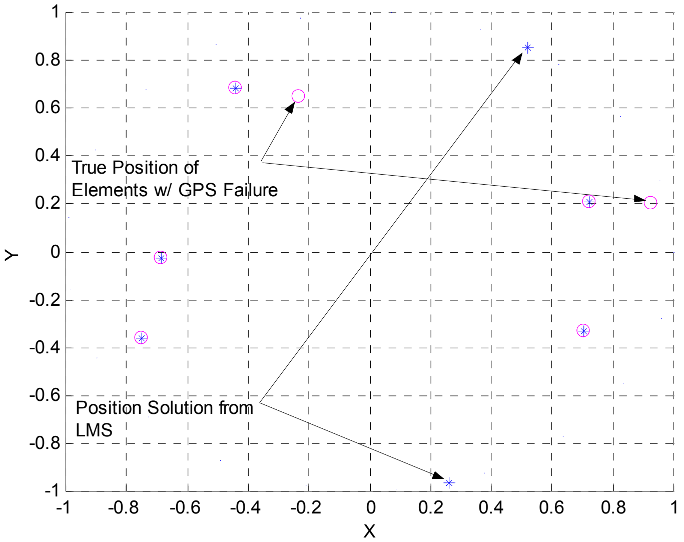

o: elements with GPS failure
***: position solution from LMS (with ambiguity)**

Figure A.23b: Position solution when two of the mobile antenna elements are not reporting GPS.

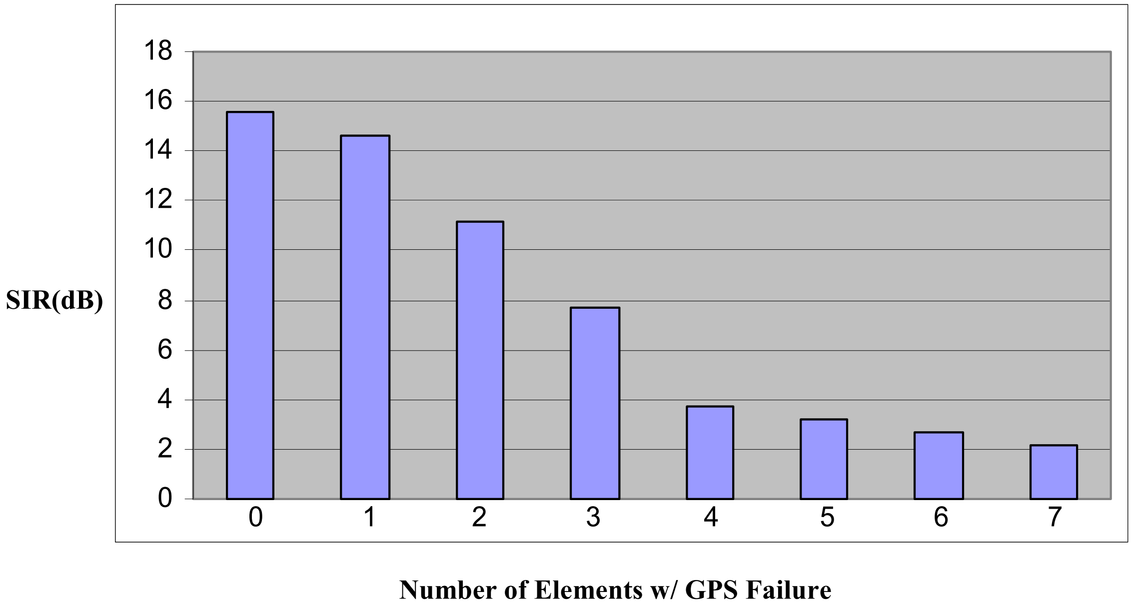

Figure A.24: Performance result for when some of the mobile antenna elements are not reporting GPS.

A.8 CONCLUSIONS

There are two advantages for using GPS. One advantage is that GPS provides better initial conditions for the adaptive process, which helps speed up convergence and avoids the divergence of the adaptation. The other advantage is that the system combining GPS positioning and signal strength measurement feedback provides better performance than the system with signal strength measurement feedback alone [Jan00].

When GPS position and timing errors are present, several GPS systems such as Local Area Code GPS or Differential Carrier Phase GPS can allow us to remove the effect of these measurement errors to satisfy the required performance.

As shown in Table A.4, the control algorithms presented in this paper can be applied to processing the output of the individual mobile antenna elements in the network. The techniques with GPS positioning successfully achieved all the performance goals.

	Maximizing the directivity toward desired receiving site	Maximizing the *SIR*	Positioning of the mobile antenna elements
Feedback from desired receiving site only	Achieved	Failed	Failed
Feedback from desired and undesired receiving direction	Achieved	Achieved	Failed
GPS only	Achieved	Failed	Achieved
GPS and the cost function (A.10)	Achieved	Achieved	Achieved
Combined GPS and adaptation, measurement feedback from the desired receiving site	Achieved	Failed	Achieved
Combined GPS and adaptation, measurement feedback from the desired and undesired receiving directions	Achieved	Achieved	Achieved

Table A.4: Summary

Future work will seek control strategies that can be applied to networks of mobile elements. Each mobile element will have two functions: sensing and communication. These two functions might conflict with each other. As a result, the control strategies should be energy-efficient, able to adapt to changes in the environment or mission, and robust to the failure of one or more of the mobile elements. In order to accomplish these goals, the controllers may use position and time information from GPS. Eventually new control strategies that are fault-tolerant, energy-efficient and adaptive will be built to control networks of mobile sensors.

Appendix B

Finding Electromagnetic Interference (EMI) Sources to GPS Using a Network of Sensors

B.1 INTRODUCTION

This chapter studies the use of a terrestrial and/or airborne sensor network to estimate the location of electromagnetic interference (EMI) sources. Radio systems play an increasing role in our military and civilian infrastructure, and many of these systems are vulnerable to accidental and malevolent EMI attack. Malevolent EMI attack on civil aircraft would not be new, and will probably increase in our society where computer hacking has become a pastime for malcontents. A rapid interference finding capability is needed to protect these systems and mitigate the threat.

This research assumes an EMI attack on GPS aircraft operations. However, the results presented in this research have broader applicability. GPS is a space-to-earth signal and the received signal power is -160 dBW. This low power level makes GPS highly susceptible to interference. It presently serves around 10 million users in sea, air, terrestrial, and space applications. Many of these applications are safety-of-life operations. For example, GPS is used to guide ships while approaching harbor and navigating within narrow waterways.

GPS also provides guidance in terrestrial emergency applications, such as ambulances and police cars, while they conduct their critical missions. In addition, GPS serves many aviation applications including the most demanding phase of flight – aircraft approach and landing. Most aircraft approach operations allow no more than one missed approach per 100,000 landings. Today, radio frequency interference is the single greatest threat to this continuity of service. The conclusion of the *GPS Risk Assessment Study* by the Applied Physics Laboratory at the Johns Hopkins University reads: "the only GPS risks that proved significant are interference and ionosphere propagation effects" [APL].

This work is organized as follows. Section B.2 discusses the prior work in this area. The basics of EMI source position estimation are summarized in Section B.3. Section B.4 will explain the configurations and assumptions of this work, which uses a network of sensors. Two kinds of sensors are considered. Examples and results are also given in Section B.4. Section B.5 presents a summary and concluding remarks.

B.2 PRIOR ART

This section discusses a GPS Interference Source Location and Avoidance System which was developed by the U.S. DOT Volpe National Transportation Systems Center [Winer]. This system is called the Aircraft RFI Localization and Avoidance System (ARLAS), and uses a GPS antenna mounted on the top of an aircraft to detect the location of interference. As shown in Figure B.1, their work for determining the direction of a GPS interference source from an aircraft (ARLAS) exploits the vertical gain pattern of the aircraft's top-mounted GPS antenna. The signal-to-noise ratio (SNR) received at the top-mounted GPS antenna can be calculated by the GPS receiver and the different values of roll, pitch, and heading which are measured by the aircraft gyroscopes. When the aircraft is banked, the antenna illuminates some area on the ground and obscures others. When the aircraft flies a tight circle, it can scan the ground and obtain data to estimate the direction to an interference source.

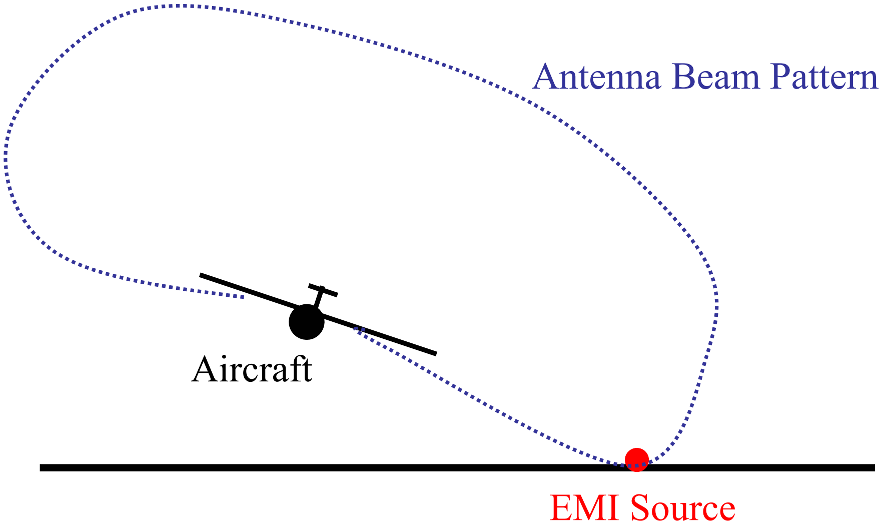

Figure B.1: The work of the Volpe National Transportation Systems Center. When the aircraft is banked, the antenna illuminates some areas on the ground and obscures others [Winer].

The DOT Volpe center flight tested the ARLAS concept in March 1999. This system could not determine the interference's bearing with sufficient reliability to validate the approach. Performance was limited because the ARLAS could not collect sufficient bearing measurement samples simultaneously. Moreover, pilots dislike the observation maneuvers required for this bearings-only tracking system because the ARLAS requires multiple turns for normal operation.

Based on the results of the DOT Volpe center flight test, this research proposes the use of sensor networks to estimate the location of electromagnetic interference (EMI) sources. The network of distributed sensors has several advantages. First, this analysis can place the sensors to give good performance for any interferers near the airport. Secondly, an optimal observer maneuver is not required because the requisite geometric diversity of measurements can be achieved by proper location of the network of distributed sensors. In this research, a terrestrial network is preferable, but the analysis is also applicable to airborne sensors which could be used to augment the ground network.

B.3 BASCIS OF POSITION ESTIMATION

The concept of locating a stationary EMI source from passive measurements can be found in a wide variety of radar and sonar publications [Becker] [Brown] [Winer] [Wohlfiel]. The location of an EMI source can be estimated either by a network of distributed sensors or by a single sensor. There are at least two methods to estimate the emitter location. The conventional method is based on different bearing measurements at different points along the sensor trajectory. The other method is to measure the Doppler shift of the EMI source frequency caused by the relative motion between the sensor and the EMI source.

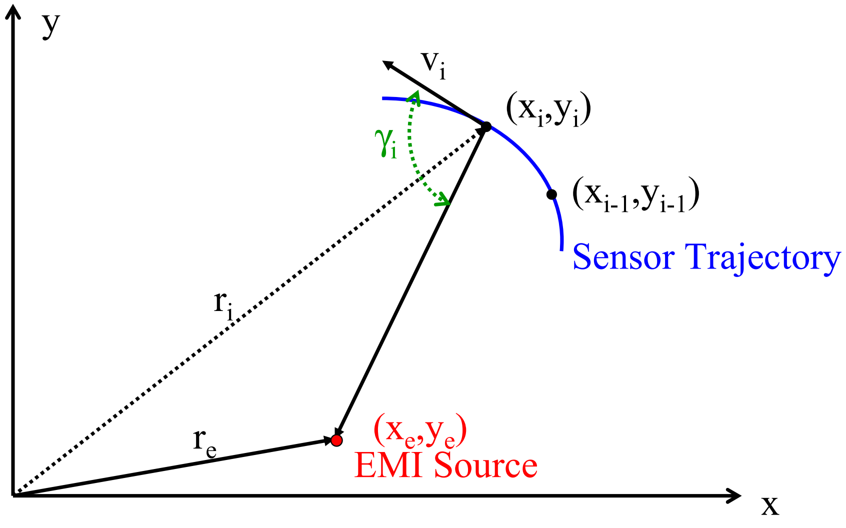

Figure B.2: An example two-dimensional geometry of the sensor and the EMI source.

As shown in Figure B.2, (x_e, y_e) is the unknown two-dimensional position of the stationary EMI source, (x_i, y_i) is the known sensor position at the i^{th} epoch. The velocity of the sensor is $v_i = (\dot{x}_i, \dot{y}_i)$, and γ_i is the noise-free bearing measurement to the EMI source relative to the velocity vector of the sensor. This analysis assumes that f_i is the Doppler shifted but noise-free signal frequency at the i^{th} measurement point along the sensor trajectory, c is the speed of light, and f_0 is the transmitted signal frequency. The relations between these parameters are

$$\gamma_i = \cos^{-1}\left[\frac{v_i \cdot (r_e - r_i)}{|v_i| \cdot |r_e - r_i|}\right] = \cos^{-1}\left[\frac{\dot{x}_i \cdot (x_e - x_i) + \dot{y}_i \cdot (y_e - y_i)}{\sqrt{\dot{x}_i^2 + \dot{y}_i^2} \cdot \sqrt{(x_e - x_i)^2 + (y_e - y_i)^2}}\right] \tag{B.1}$$

and

$$f_i = f_0 + \frac{f_0}{c} \cdot \frac{v_i \cdot (r_e - r_i)}{|r_e - r_i|} = f_0 + \frac{f_0}{c} \cdot \frac{\dot{x}_i \cdot (x_e - x_i) + \dot{y}_i \cdot (y_e - y_i)}{\sqrt{(x_e - x_i)^2 + (y_e - y_i)^2}} \tag{B.2}$$

With additive noise, either observation equation can be written as

$$\varphi^m = \varphi(a) + n \tag{B.3}$$

where,

φ^m is the measured bearing or frequency

$\varphi(a)$ is the true (noise free) bearing or frequency

$a_B = \begin{bmatrix} x_e \\ y_e \end{bmatrix}$ for bearing measurements

$a_F = \begin{bmatrix} f_0 \\ x_e \\ y_e \end{bmatrix}$ for frequency measurements

n are measurement errors

If the EMI transmitted frequency is unknown, f_0 will need to be estimated as well. This is why a_F includes f_0. The measurement noise, n, is assumed to be zero mean $(E[n_B] = E[n_F] = 0)$ with a normal probability distribution, and the measurements are independent of each other. Therefore, the variances are independent of the measurement points and the covariance matrices for this two dimensional example are

$$N_B = E[(n_B - E[n_B])(n_B - E[n_B])^T]$$

$$\because E[n_B] = 0, \left(N_B\right)_{ij} = 0, \left(N_B\right)_{ii} = \sigma_B^2$$

$$\Rightarrow N_B = E[(n_B)(n_B)^T] = \begin{bmatrix} \sigma_B^2 & 0 \\ 0 & \sigma_B^2 \end{bmatrix}$$

$$N_F = E[(n_F - E[n_F])(n_F - E[n_F])^T]$$

$$\because E[n_F] = 0, \left(N_F\right)_{ij} = 0, \left(N_F\right)_{ii} = \sigma_F^2$$

$$\Rightarrow N_F = E[(n_F)(n_F)^T] = \begin{bmatrix} \sigma_F^2 & 0 \\ 0 & \sigma_F^2 \end{bmatrix}$$

where, the subscript *B* is for bearing measurements, and the subscript *F* is for frequency measurements. This analysis assumes that the measurement noise follows a Gaussian distribution. As a result, we can write the conditional probability distribution of the measurements as follows

$$p\left\langle \varphi^m \middle| a \right\rangle = \frac{1}{\left(2\pi\right)^{M/2}\sqrt{\det N}} \exp\left(-\frac{1}{2}\sum_{i=1}^{M} \frac{\left(\varphi_i^m - \varphi_i\left(a\right)\right)^2}{N_{ii}} \right) \tag{B.4}$$

The Cramer-Rao inequality provides a lower bound on the estimation accuracy [Van Trees]. We define the estimation error as

$$\overset{\wedge}{\Delta a} = \hat{a}\left(\varphi^m\right) - a \tag{B.5}$$

where,

$\overset{\wedge}{\Delta a}$ is estimation error

$\hat{a}\left(\varphi^m\right)$ is the unbiased estimate of a

The covariance matrix of the estimation error, C, is bounded by the inverse of the Fisher Information Matrix, J. Specifically, $C \geq J^{-1}$, where

$$J_{kl} = -E\left[\frac{\partial^2 \ln p\left\langle \varphi^m \middle| a \right\rangle}{\partial a_k \partial a_l}\right]$$

The covariance matrix can be represented geometrically in the space as an ellipse that bounds the estimation errors. That is,

$$\overset{\wedge}{\Delta a}^{T} C^{-1} \overset{\wedge}{\Delta a} = \kappa \tag{B.6}$$

where, κ is a constant which determines the size of the ellipse.

From $C \geq J^{-1}$, we can rewrite (B.6) as

$$\overset{\wedge}{\Delta a}^{T} J \overset{\wedge}{\Delta a} = \kappa \tag{B.7}$$

$$\overset{\wedge}{\Delta a}^{T} J \overset{\wedge}{\Delta a} = \sum_{i=1}^{n} \lambda_i \xi_i^2 = \kappa \tag{B.8}$$

where,

λ_i are the eigenvalues of J

ξ_i are the corresponding eigenvectors

The size and orientation of the error ellipse can be described in terms of the eigenvalues $\left(\lambda_i\right)$ and the eigenvectors $\left(\xi_i\right)$ of the Fisher Information Matrix. If λ_i is zero, then the length of the semiaxes of the ellipse is infinite. That means it is an unobserved state. If λ_i is not zero, then the length of the semiaxes of the ellipse are $\sqrt{\kappa/\lambda_i}$.

To derive the elements of the Fisher Information Matrix, we take the logarithm and differentiate

$$J_{kl} = -E\left[\frac{\partial^2 \ln p\left\langle \varphi^m \middle| a\right\rangle}{\partial a_k \partial a_l}\right] = \sum_{i=1}^{M} \frac{1}{N_{ii}} \cdot \frac{\partial \varphi_i}{\partial a_k} \cdot \frac{\partial \varphi_i}{\partial a_l} \tag{B.9}$$

Rewriting in matrix form

$$J = \sum_{i=1}^{M} \frac{1}{N_{ii}} \nabla_a \varphi_i \left(\nabla_a \varphi_i\right)^T \tag{B.10}$$

where,

∇_a is the gradient with respect to a

$\nabla_{a_B} = \left(\frac{\partial}{\partial x_e}, \frac{\partial}{\partial y_e}\right)^T$ for bearing measurements

$\nabla_{a_F} = \left(\frac{\partial}{\partial f_0}, \frac{\partial}{\partial x_e}, \frac{\partial}{\partial y_e}\right)^T$ for frequency measurements

For bearing measurements, we get

$$\nabla_{a_B} \gamma_i = \left(\frac{\partial \gamma_i}{\partial x_e}, \frac{\partial \gamma_i}{\partial y_e}\right)^T = \frac{1}{\left|r_e - r_i\right|^2} \cdot \begin{pmatrix} y_i - y_e \\ x_e - x_i \end{pmatrix} \tag{B.11}$$

For frequency measurements, we get

$$\nabla_{a_F} f_i = \left(\frac{\partial f_i}{\partial f_0}, \frac{\partial f_i}{\partial x_e}, \frac{\partial f_i}{\partial y_e} \right)^T = \begin{pmatrix} 1 + \dfrac{1}{c \cdot |r_e - r_i|} \cdot \left(\dot{x}_i \cdot (x_e - x_i) + \dot{y}_i \cdot (y_e - y_i) \right) \\ \dfrac{c}{f_0} \cdot \dfrac{y_e - y_i}{|r_e - r_i|^3} \cdot \left(\dot{x}_i \cdot (y_e - y_i) + \dot{y}_i \cdot (x_e - x_i) \right) \\ \dfrac{c}{f_0} \cdot \dfrac{x_e - x_i}{|r_e - r_i|^3} \cdot \left(\dot{y}_i \cdot (x_e - x_i) + \dot{x}_i \cdot (y_e - y_i) \right) \end{pmatrix} \tag{B.12}$$

This analysis gives two examples to illustrate the single measurement case. Figure B.3 shows the initial sensor position and the EMI source position.

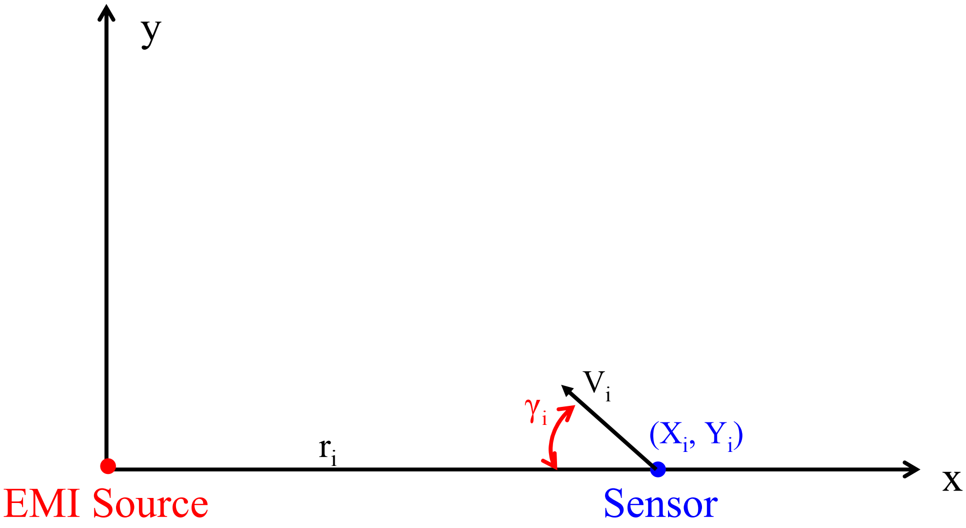

Figure B.3: A two-dimensional geometry example of the sensor and the EMI source.

B.3.1 SINGLE BEARING MEASUREMENT EXAMPLE

From Equation (B.10), we can derive the Fisher Information Matrix as

$$J = \frac{1}{\sigma_B^2} \cdot \nabla_{a_B} \gamma \left(\nabla_{a_B} \gamma \right)^T \tag{B.13}$$

From Figure B.3, we can compute (B.11) to get

$$\nabla_{a_B}\gamma = \frac{1}{r}\begin{pmatrix} 0 \\ -1 \end{pmatrix} \tag{B.14}$$

Substituting (B.13) into (B.14) yields

$$J = \frac{1}{\sigma_B^2 r^2}\cdot\begin{pmatrix} 0 & 0 \\ 0 & 1 \end{pmatrix} \tag{B.15}$$

The eigenvalues and the corresponding eigenvectors of J are

$$\begin{aligned} \lambda_1 &= 0 \\ \lambda_2 &= \frac{1}{\sigma_B^2 r^2} \\ \xi_1 &= \begin{pmatrix} 1 \\ 0 \end{pmatrix} \\ \xi_2 &= \begin{pmatrix} 0 \\ 1 \end{pmatrix} \end{aligned} \tag{B.16}$$

Then calculate the length of the semiaxes

$$\begin{aligned} d_1 &= \infty \\ d_2 &= \sqrt{\frac{\kappa}{\lambda_2}} \end{aligned} \tag{B.17}$$

The result of this example is shown in Figure B.4. It is a strip in the line of sight direction with $2d_2$ width. The multiple measurements case can be interpreted as the result of the intersection of several such individual strips.

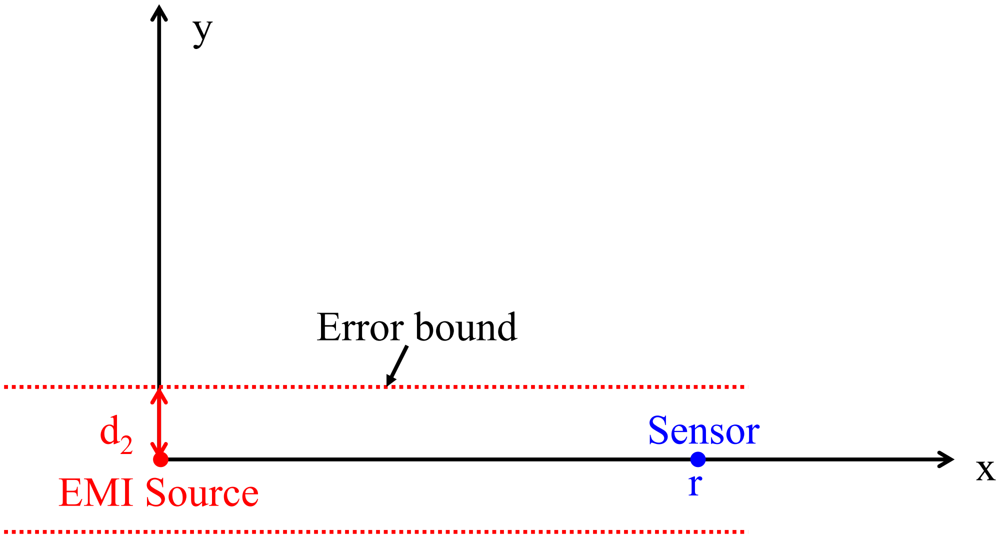

Figure B.4: The result of the single bearing measurement example.

B.3.2 SINGLE FREQUENCY MEASUREMENT EXAMPLE

If the sensor in Figure B.2 uses frequency measurements instead of bearing measurements, this analysis then derives the Fisher Information Matrix from Equation (B.10) as follows

$$J = \frac{1}{\sigma_F^2} \cdot \nabla_{a_F} f (\nabla_{a_F} f)^T \tag{B.18}$$

Based on Figure B.2, one can calculate (B.11) and get

$$\nabla_{a_F} f = \begin{bmatrix} 1 + \frac{1}{c \cdot |r_e - r_i|^3} \cdot \left(\dot{x}_i \cdot (x_e - x_i) + \dot{y}_i \cdot (y_e - y_i)\right) \\ \frac{c}{f_0} \cdot \frac{y_e - y_i}{|r_e - r_i|^3} \cdot \left(\dot{x}_i \cdot (y_e - y_i) + \dot{y}_i \cdot (x_e - x_i)\right) \\ \frac{c}{f_0} \cdot \frac{x_e - x_i}{|r_e - r_i|^3} \cdot \left(\dot{y}_i \cdot (x_e - x_i) + \dot{x}_i \cdot (y_e - y_i)\right) \end{bmatrix}$$

$$= \begin{bmatrix} 1+\frac{1}{cr}\cdot\left((-v_i\cos\gamma_i)\cdot(-r)\right) \\ 0 \\ \frac{f_0}{c}\cdot\frac{-r}{r^3}\cdot\left((v_i\sin\gamma_i)\cdot(-r)\right) \end{bmatrix} = \begin{bmatrix} 1+\frac{1}{c}\cdot(v_i\cos\gamma_i) \\ 0 \\ \frac{f_0}{cr}\cdot(v_i\sin\gamma_i) \end{bmatrix} \tag{B.19}$$

Then substitute (B.18) into (B.19), to obtain the Fisher Information Matrix

$$J = \frac{f_0^2}{\sigma_F^2}\cdot P \tag{B.20}$$

where,

$$P = \begin{bmatrix} u^2 & 0 & uw \\ 0 & 0 & 0 \\ uw & 0 & w^2 \end{bmatrix}$$

$$u = \frac{1}{f_0}\cdot\left(1+\frac{v_i}{c}\cdot\cos\gamma_i\right)$$

$$w = \frac{v_i}{cr}\cdot\sin\gamma_i$$

The eigenvalues and the corresponding eigenvectors of J are

$$\begin{aligned} &\lambda_1 = u_2 + w_2\,, \lambda_2 = \lambda_3 = 0 \\ &\xi_1 = \frac{1}{\sqrt{u^2+w^2}}\cdot\begin{bmatrix} u \\ 0 \\ w \end{bmatrix} \\ &\xi_2 = \begin{bmatrix} 0 \\ 1 \\ 0 \end{bmatrix} \\ &\xi_3 = \frac{1}{\sqrt{u^2+w^2}}\cdot\begin{bmatrix} -w \\ 0 \\ u \end{bmatrix} \end{aligned} \tag{B.21}$$

Then compute the length of the semiaxes

$$
\begin{aligned}
d_1 &= \frac{\sigma_F \cdot \sqrt{\kappa}}{f_0 \cdot \sqrt{u^2 + w^2}} \\
d_2 &= \infty \\
d_3 &= \infty \\
\cos\theta &= \xi_1 \cdot e_y = \frac{w}{\sqrt{u^2 + w^2}} \\
\theta &= \cos^{-1}\left(\frac{w}{\sqrt{u^2 + w^2}}\right)
\end{aligned}
\tag{B.22}
$$

The result is shown in Figure B.5. It is a disk in the position and frequency space. Figure B.5 plots the projection on the $\hat{f} - y$ plane. The angle θ between the eigenvector ξ_1 and the line of sight can be computed from Equation (B.22).

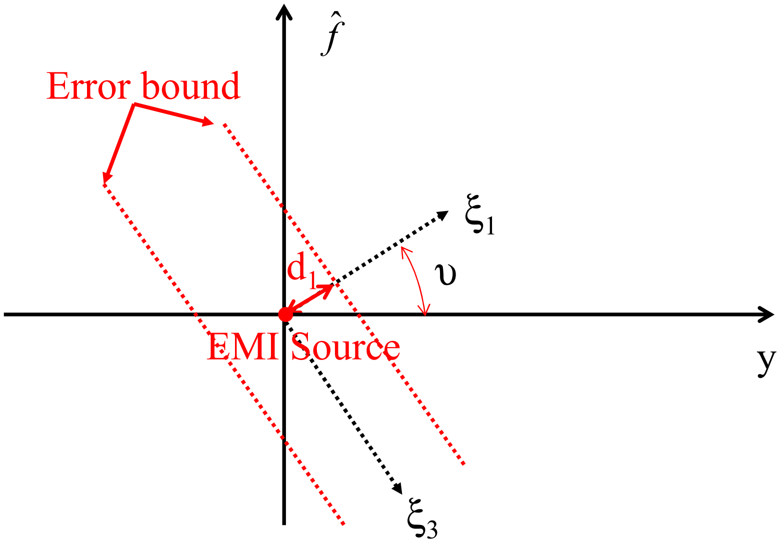

Figure B.5: The result of the single frequency measurement example.

The results of the previous two examples can be used to predict positioning accuracy for a system that uses multiple sensors or one moving sensor, as shown in Figure B.6. The smaller area of intersection of the strips gives the better bearing tracking performance. Figure B.7 shows that the optimal observer maneuver is required for the better tracking performance.

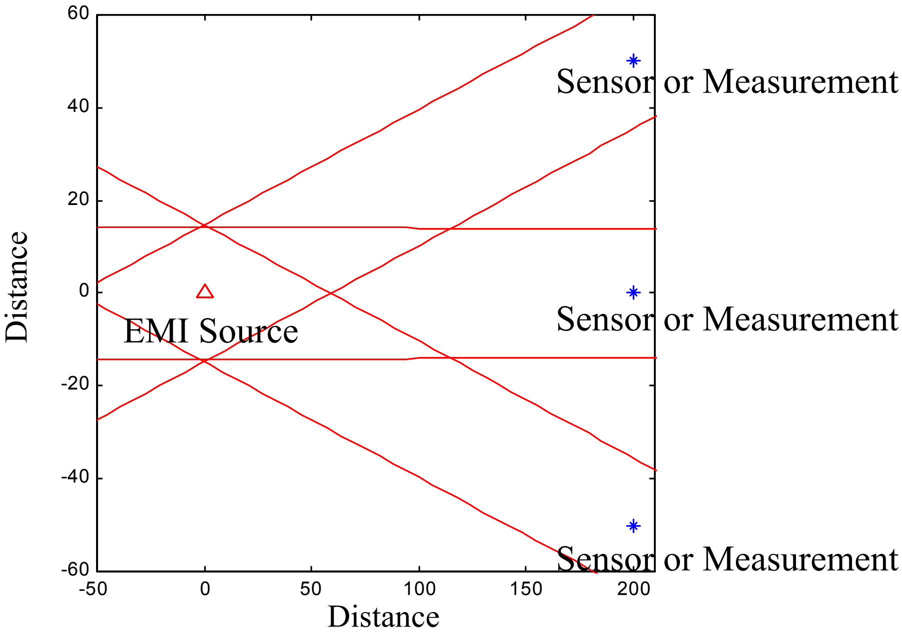

Figure B.6: Three sufficient measurements are required to locate the EMI source.

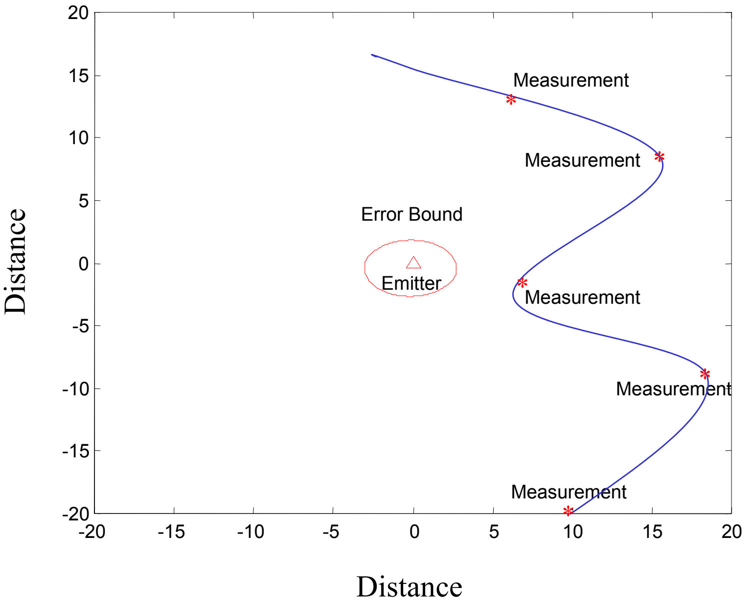

Figure B.7: The optimal observer maneuver is required for better tracking performance.

B.4 NETWORK OF SENSORS

This section characterizes the performance of a network of distributed sensors with respect to the following parameters: number of sensors, distance between sensors and interference source, separation of the sensors, and geometry of the sensors. An example network of sensors is shown in Figure B.8.

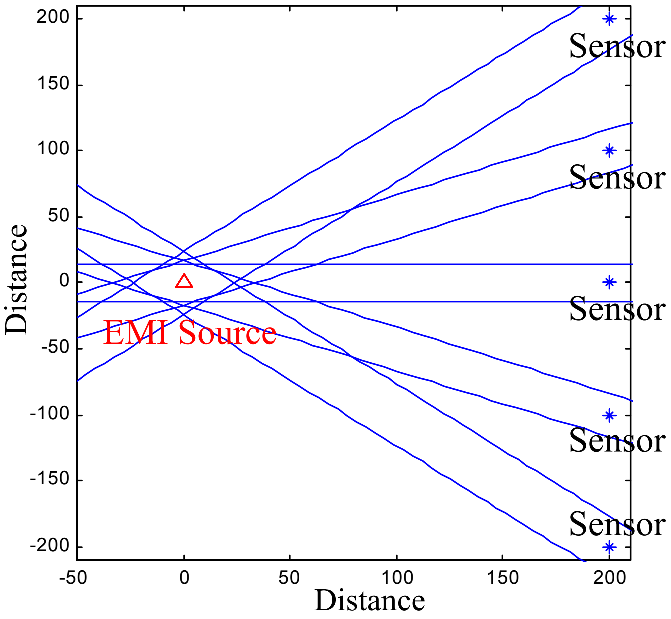

Figure B.8: An example of a network of sensors.

B.4.1 MULTIPLICITY OF SENSORS AND SENSOR SPAN

The first example investigates the relation between bearing tracking performance and the number of sensors. This example considers two networks, one with three sensors, and the other with seven sensors. The separations of the sensors are the same in both systems, and the seven sensor system spans triple the distance. These networks are shown in Figure B.9. The bearing tracking performance (accuracy) of the network system with seven sensors is better than that of the network system with three sensors because the span of the network system with seven sensors is triple that of the smaller network.

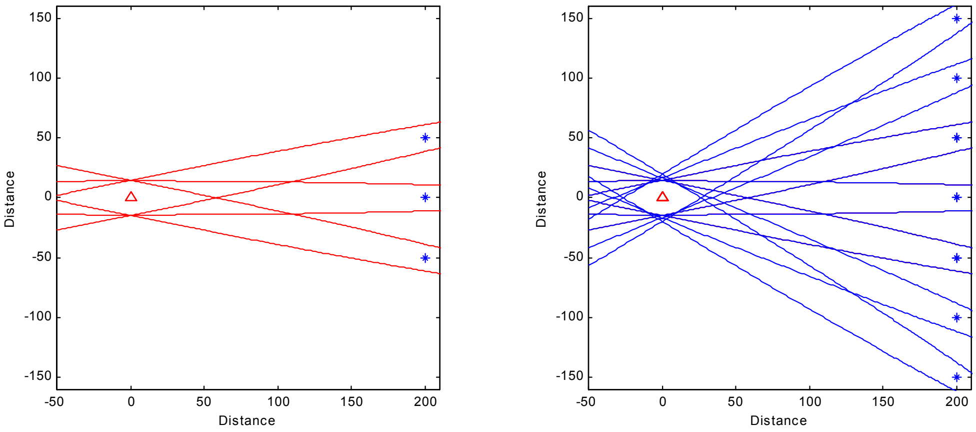

Figure B.9: Comparison of system with different numbers of sensors. The bearing tracking performance of the network system with seven sensors (right) is better than that of the network system with three sensors (left).

B.4.2 DISTANCE FROM SENSORS TO EMI SOURCE

The second example investigates how the distances between the EMI source and the sensors can affect the bearing tracking performance. This example also has two systems, and both systems are five sensor networks. The distance from the EMI source to the first network of sensors is $1/4$ of the distance from the same EMI source to the second network of sensors. The separations of the sensors are equal. The bearing tracking performance of the nearby network system is better than the performance of the distant network system. The larger geometric diversity of the nearby network gives the better bearing tracking performance. The result is shown in Figure B.10.

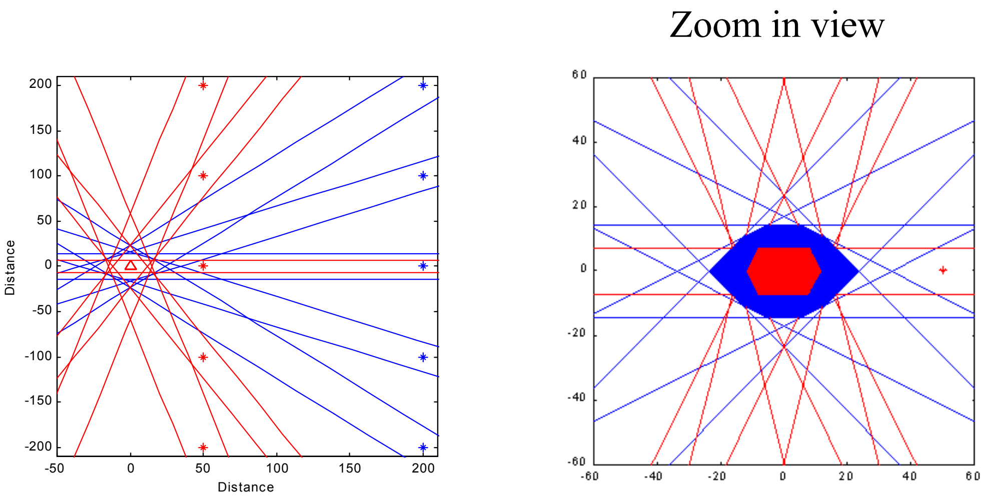

Figure B.10: Comparison of systems varying distances from an EMI source. The system which is near the EMI source gives the better bearing tracking performance because of the larger geometric diversity.

B.4.3 SENSOR SEPARATION

The third example tests the separations of the sensor. The results are shown in Figure B.11. As expected, the network with the larger span gives the better bearing tracking performance. This is also the reason why the conventional bearing-only tracking systems require maneuvers. These systems require bearing measurements over a long span of distance. The approach of this research only needs to make sure that the separations of sensors are large enough to fulfill certain performance requirements. This is an advantage to this type of approach because no optimal maneuver is needed.

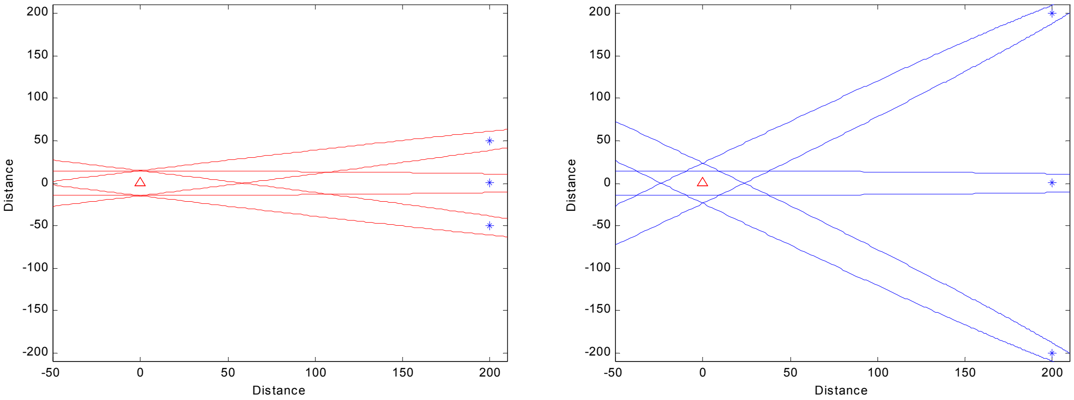

Figure B.11: Comparison of different separations of the sensors. The larger the geometric diversity of the network of sensors the better bearing tracking performance.

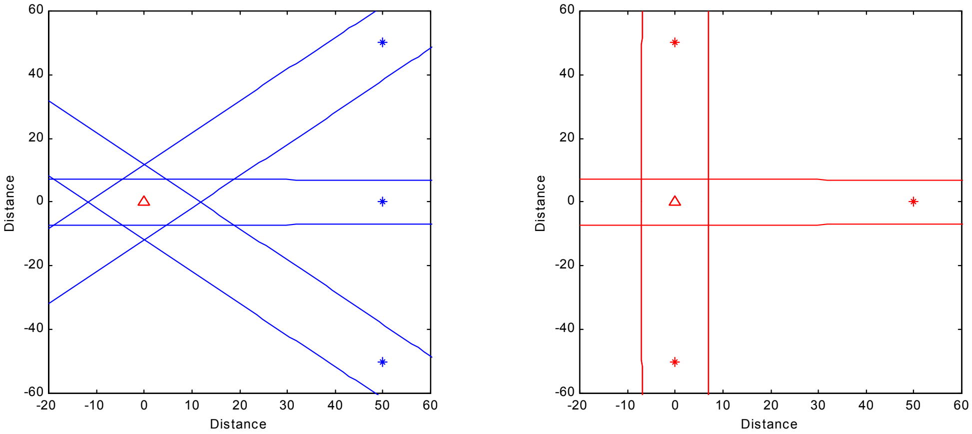

Figure B.12: Comparison of different geometries of the sensors. The smaller area of the intersection of the ellipses gives the better bearing tracking performance.

B.4.4 SENSOR FAILURE

The fourth example illustrates how the geometry of the distributed sensors can improve the bearing tracking performance. It also shows the design of networks that is robust to sensor failures. As shown in Figure B.12, the left-hand network of sensors is distributed in a straight line, and the right-hand network of sensors is distributed in a triangular shape. The right-hand network system has greater geometric diversity than the left-hand network system. Therefore, the right-hand network of sensors gives the better bearing tracking performance. The result of this example suggested that one might be able to maintain the bearing tracking performance when some of the sensors failed by moving existing sensors to form the better geometry. For instance, one can remove a sensor on the top of the EMI source from the right-hand network system in Figure B.12, and get the same bearing tracking performance as before. That is, when one of the sensors in the left-hand network has failed, one can move the two existing sensors to be in the geometry of the right-hand network system to maintain bearing tracking performance. Actually, this performance is better than the original system, as shown in Figure B.13. As shown, the network is robust to sensor failures.

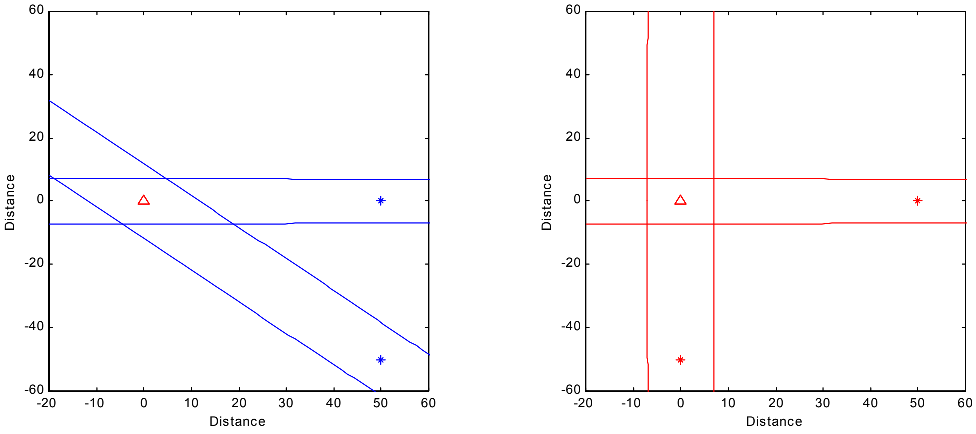

Figure B.13: An example of the network system in the presence of sensor failures. We can maintain the bearing tracking performance when some of the sensors fail by moving existing sensors to form the better geometry.

B.5 CONCLUDING COMPARISON

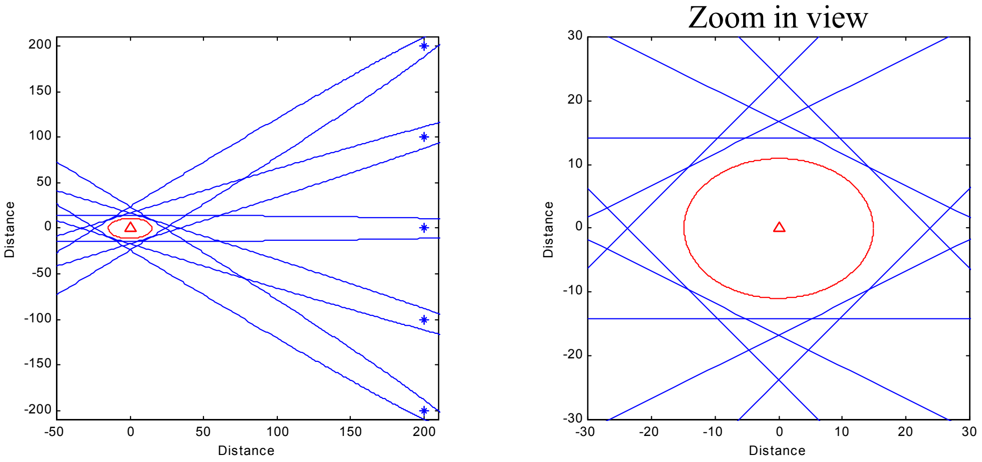

Figure B.14: Comparison of the prior art and our approach.

As shown in Figure B.14, the red error ellipse is the result of five sequential bearing measurements by using single sensor, and the blue strips are the results of the five individual bearing measurements from five different sensors. The area of the intersection of the blue strips is almost the same as that of the red error ellipse. However, it is very difficult to achieve this bearing tracking performance (the red error ellipse) by using a single sensor, because the EMI source may turn off before the maneuver is completed.

The approach to locate the EMI source by using a network of sensors has two major advantages. First, no sensor motion is needed and EMI source location is estimated instantaneously. One can simply change the separations of the sensors or the geometry of the sensors to fulfill the bearing tracking performance requirements. Second, it is robust to sensor failures. That is, even when some of the sensors have failed, one can maintain the bearing tracking performance by moving existing sensors to form better sensor geometry. Therefore, it is recommended that the sensor network approach presented in this appendix should be used to estimate the EMI source location.

Bibliography

[Akos] Akos, D. M., Gromov, K., Walter, T., Enge, P., "A Prototype 3-Frequency SBAS Receiver & Tset Results," *Proceedings of ION Annual Meeting 2001*, Albuquerque, NM, June 11-13, 2001.

[APL] *GPS Risk Assessment Study*, Final Report, Applied Physics Laboratory, John Hopkins University, January 1999.

[Balanis] Balanis, C. A., *Antenna Theory Analysis and Design*, John Wiely & Sons, Inc., Second edition, 1997.

[Becker] Becker, K., "An Efficient Method of Passive Emitter Location," *IEEE Transactions on Aerospace and Electronic Systems, Vol. 28, NO. 4*, October 1992.

[Bishop] Bishop, J., "Study and Performance of a New Technique for Mitigation of Pseudorange Multipath Effects in GPS Ground Stations," *Proceedings of ION NTM 1994*, San Diego, CA, January 24-26, 1994.

[Black] Black, H. D., "An Easily Implemented Algorithm for the Tropospheric Range Correction," *Journal of Geophysical Research*, 83(84): 1825-1828, April 1978.

[Brown] Brown, A., Reynolds, D., Robert, D., "Jammer and Interference Location System-Design and Initial test Results," *Proceedings of ION GPS 1999*, Nashville, TN, September 14-17, 1999.

[Cabler] Cabler, H., DeCleene, B., "LPV: New, Improved WAAS Instrument Approach," *Proceedings of ION GPS 2002*, Portland, OR, September 24-27, 2002.

[Chao] Chao, Y. C., *Real Time Implementation of the Wide Area Augmentation System for the Global Positioning System with Emphasis on Ionospheric Modeling*, PhD Thesis, Department of Aeronautics and Astronautics, Stanford University, March, 1997.

[Cosentino] Cosentino, R. J., Diggle, D. W., "Differential GPS," Elloit D. Kaplan, Editor, Artech House, Boston 1996, pp. 321-384.

[Dai] Dai, D. H., Walter, T., Enge, P., Powell, J. D., "Optimal Use of Ionospheric Corrections for Wide Area Augmentation System (WAAS) Users," *IEEE Position Location and Navigation Symposium*, Rancho Mirage, CA, April 20-23, 1998.

[Compton] Compton, R. T. J. , *Adaptive Antennas Concepts and Performance*, Prentice Hall, Inc., 1988.

[Datta-Barua] Datta-Barua, S., Walter, T., Pullen, S., Luo, M., Blanch, J., Enge, P., "Using WAAS Ionospheric Data to Estimate LAAS Short Baseline Gradients," *Proceedings of ION NTM 2001*, San Diego, CA, January 28-30, 2001.

[Dobyne] Dobyne, J., "The Accuracy of Barometric Altimeters with Respect to Geometric Altitude," *Proceedings of ION Satellite Division's International Technical Meeting 1988*, Springs, CO, September 19-23, 1988.

[Diesel] Diesel, J. W., "GPS/INS Integration for Civil Aviation," *Proceedings of 1991 National Telesystems Conference*, Atlanta, GA, March 26-27, 1991.

[Enge96] Enge, P., Walter, T., Pullen, S., Kee, C., Chao, Y. C., Tsai, Y. J., "Wide Area Augmentation of the Global Positioning System," *Proceedings of the IEEE, Volume: 84 Issue: 8*, August, 1996.

[FAA2002] *Navigation and Landing Transition Strategy*, Federal Aviation Administration (FAA), Washington, D.C., August 2002.

[Fontana1] Fontana, R., Latterman, D., "GPS Modernization and the Future," *Proceedings of ION Annual Meeting 2000*, San Diego, CA, June 26-28, 2000.

[Fontana2] Fontana, R., Cheung, W., Novak, P. M., Stansell, T. A., "The New L2 Civil Signal," *Proceedings of ION GPS 2001*, Salt Lake City, UT, September 11-14, 2001.

[Gebre] Gebre-Egziabher, D., *Design and Performance Analysis of a Low-cost Aided Dead Reckoning Navigator*, PhD Thesis, Department of Aeronautics and Astronautics, Stanford University, 2001.

[Gerlach] Gerlach, D., *Adaptive Transmitting Antenna Arrays at The Base Station in Mobile Radio Networks*, PhD Thesis, Department of Electrical Engineering, Stanford University, 1995

[Gromov] Gromov, K., Akos, D., Pullen, S., Enge, P., Parkinson, B., Pervan, B., "Interference Direction Finding for Aviation Applications of GPS," *Proceedings of ION GPS 1999*, Nashville, TN, September 14-17, 1999.

[HansenR] Hansen, R. C., *Phase Array Antenna*, John Wiley & Sons, Inc., 1998.

[Hansen] Hansen, A. J., *Tomographic Estimation of the Ionosphere Using Terrestrial GPS Sensors*, PhD Thesis, Department of Electrical Engineering, Stanford University, 2002.

[Hegarty] Hegarty, C. J., "Analytical Derivation of Maximum Tolerable In-Band Interference Levels for Aviation Applications of GNSS," *Navigation: Journal of the Institute of Navigation, Vol. 44, No. 1*, Spring 1997.

[Holmes] Holmes, J. K., *Coherent Spread Spectrum Communications*, Krieger Publishing Company, Malabar, FL, 1990.

[Howe] Howe, B., Runciman, K., Secan, J. A., "Tomography of the Ionosphere: Four-Dimensional Simulations," *Radio Science 33 (1),* January-February, 1998.

[ICAO] ICAO, GNSS SARPS, ICAO, 1999.

[ICD-GPS-200C] ICD-GPS-200C, *NAVSTAR GPS Space Segment / Navigation User Interface*, Arinc Research Corporation, El Segundo, CA, October 10, 1993, and subsequent IRNs 1 through 4, April 12, 2000.

[ICD-GPS-705] ICD-GPS-705, *NAVSTAR GPS Space Segment / User Segment L5 Interfaces*, Arinc Research Corporation, El Segundo, CA, Initial Release, March 29, 2002.

[IWG] Service Volume Model Standard Document, IWG, 1999.

[Jablon] Jablon, M. K., *Adaptive Beamforming with Imperfect Arrays*, PhD Thesis, Department of Electrical Engineering, Stanford University, 1985.

[Jan00] Jan, S. S., Enge, P., "Using GPS to Synthesize A Large Antenna Aperture When the Elements are Mobile," *Proceedings of ION NTM 2000*, Anaheim, CA, January 26-28, 2000.

[Jan01a] Jan, S. S., Enge, P., "Finding Source of Electromagnetic Interference (EMI) to GPS Using a Network Sensors," *Proceedings of ION NTM 2001*, Long Beach, CA, January 22-24, 2001.

[Jan01b] Jan, S. S., Chan, W., Walter, T., Enge, P., "MATLAB Simulation Toolset for SBAS Availability Analysis," *Proceedings of ION GPS 2001*, Salt Lake City, UT, September 11-14, 2001.

[Jan02a] Jan, S. S., Gebre-Egziabher, D., Walter, T. Enge, P., "Worst-Case Analysis of a 3-Frequency Receiver to Land a General Aviation Airplane," *Proceedings of ION NTM 2002*, San Diego, CA, January 28-30, 2002.

[Jan02b] Jan, S. S., Walter, T., Enge, P., "Analysis of a Three-Frequency GPS/WAAS Receiver to Land an Airplane," *Proceedings of ION GPS 2002*, Portland, OR, September 24-27, 2002.

[Jung] Jung, J., *High Integrity Carrier Phase Navigation Using Multiple Civil GPS Signals*, PhD Thesis, Department of Aeronautics and Astronautics, Stanford University, August, 2000.

[Kelly] Kelly, R. J., Davis, J. M., "Required Navigation Performance (RNP) for Precision Approach and Landing GNSS Application," *Navigation, Journal of the Institute of Navigation, Vol. 41, No. 1*, Spring 1994.

[Klobuchar] Klobuchar, J., "Design and Characteristics of the GPS Ionospheric Time Delay Algorithm for Single Frequency Users," *Rec. IEEE 1986 Position Location and Navigation Symp.*, Las Vegas, NV, November, 1986.

[Kollsman] Kollsman Inc., http://www.kollsman.com.

[Kovach] Kovach, K., "New User Equivalent Range Error (UERE) Budget for the Modernized Navstar Global Positioning System (GPS)," *Proceedings of ION NTM 2000*, Anaheim, CA, January 26-28, 2000.

[Kraus] Kraus, J. D., *Antennas*, John Wiley & Sons, Inc., Second edition, 1988.

[Lawrence] Lawrence, D. G., *Aircraft Landing Using GPS*, PhD Thesis, Department of Aeronautics and Astronautics, Stanford University, 1996.

[Lee] Lee, Y. C., "Receiver Autonomous Integrity Monitoring Availability for GPS Augmented with Barometric Altimeter Aiding and Clock Coasting," *Global Positioning System: Theory and Application*, AIAA Publication, 1996.

[Lo] Lo, S., *Broadcasting GPS Integrity Information Using Loran-C*, PhD Thesis, Department of Aeronautics and Astronautics, Stanford University, 2002.

[Malla98] Malla, R., Wu, J. T., "The Service Volume Model Its Philosophy and Implementation," *Proceedings of ION GPS 1998*, Nashville, TN, September 15-18, 1998.

[Maslin] Maslin, N., *HF Communications, A Systems Approach*, A Division of Plenum Publishing Corporation, 1987.

[MATLAB] MATLAB, The MathWorks Inc., MATLAB is a software tool for doing mathematical computations.

[McDonald] McDonald, K. D., Hegarty, C., "Post-Modernization GPS Performance Capabilities," *Proceedings of ION Annual Meeting 2000*, San Diego, CA, June 26-28, 2000.

[McGraw] McGraw, G. A., Murphy, T., Brenner, M., Pullen, S., Van Dierendonck, A. J., "Development of the LAAS Accuracy Models," *Proceedings of ION GPS 2000*, Salt Lake City, UT, September 19-22, 2000.

[Misra&Enge] Misra, P., Enge, P., *Global Positioning System Signal, Measurements, and Performance*, Ganga-Jamuna Press, Lincoln, MA, 2001.

[Nicolau] Nicolau, E., Zaharia, D., *Adaptive Arrays*, Elsevier Science Publishing Company, Inc., 1983.

[NIMA] National Imagery and Mapping Agency, http://164.214.2.59/.

[NOAA] *Solar and Meteorological Surface Observation Network 1961-1990*, V. 1.0, NOAA, U. S. Department of Commerce, September, 1993.

[Parkinson96] Parkinson, B. W., Spilker, J. J., *Global Positioning System: Theory and Application*, AIAA Publication, 1996.

[Peck] Peck, S., Tekawy, J., "User Differential Range Error Algorithms for the Wide Area Augmentation System," *Proceedings of the 53rd Annual Meeting*, Albuquerque, NM, June 30 – July 2, 1997.

[Pervan] Pervan, B. S., *Navigation Integrity for Aircraft Precision Landing Using the Global Positioning System*, PhD Thesis, Department of Aeronautics and Astronautics, Stanford University, 1996.

[Poor] Poor, W., Chawla, J., Greanias, S., Hashemi, D., Yen, P., "A Wide Area Augmentation System (WAAS) Availability Model and Its Use in Evaluating WAAS Architecture Design Sensitivities," *Global Positioning System Vol. VI*, The Institute of Navigation, Alexandria, VA, 1999.

[Pullen98] Pullen, S., Opshaug, G., Hansen, A., Walter, T., Enge, P., Parkinson, B., "A Preliminary Study of the Effect of Ionospheric Scintillation on WAAS User Availability in Equatorial Regions," *Proceedings of ION GPS 1998*, Nashville, TN, September 15-18, 1998.

[PPIRN-200C-007] PPIRN-200C-007, *Pre-Proposed Interface Revision Notice to ICD-GPS-200C for L2 Civil Signal,* Arinc Research Corporation, El Segundo, CA, May 31, 2001.

[RTCA1] RTCA SC-159, *Minimum Operational Performance Standard for Global Positioning System/Wide Area Augmentation System Airborne Equipment*, RTCA/DO-229B, October 6, 1999.

[RTCA2] RTCA SC-159, *Minimum Aviation System Performance Standard for Local Area Augmentation Systems*, RTCA/DO-245, September 28, 1998.

[RTCA3] RTCA SC-159, *Assessment of Radio Frequency Interference for L1/L5 Relevant to the GNSS*, RTCA Paper No. 157-02/SC159-896, 2002.

[Spilker] Spilker Jr., J. J., "GPS Navigation Data," *Global Positioning System: Theory and Applications, Volume I*, AIAA, Washington D.C., 1996.

[Schempp] Schempp, T., Peck, S., Fries, R., "WAAS Algorithm Contribution to Hazardously Misleading Information (HMI)," *Proceedings of ION GPS 2001*, Salt Lake City, UT, September 11-14, 2001.

[Shallberg] Shallberg, K., Shloss, P., Altshuler, E., Tahmazyan, L., "WAAS Measurement Processing, Reducing the Effects of Multipath," *Proceedings of ION GPS 2001*, Salt Lake City, UT, September 11-14, 2001.

[Sparks] Sparks, L., Mannucci, A. J., Altshuler, E., Fries, R., Walter, T., Hansen, A., Blanch, J., Enge, P., "The WAAS Ionospheric Threat Model," *Beacon Satellite Symposium*, Boston, MA, 2001.

[Stutzman] Stutzman, W. L., Thiele, G. A., *Antenna Theory and Design*, John Wiley & Sons, Inc., first edition., 1981.

[Swider] Swider, R., Miller, D., Shakarian, A., Flannigan, S., Fernow, J., "Development of Local Area Augmentation System Requirements," *Proceedings of ION GPS 1996*, Kansas City, MI, September 17-20, 1996.

[Tsai] Tsai, Y. J., *Wide Area Differential Operation of the Global Positioning System: Ephemeris and Clock Algorithms*, PhD Thesis, Department of Mechanical Engineering, Stanford University, 1999.

[Tsunami] Tsunami Partners, "Report on mobile Adaptive Array Processing Algorithms," ERA report 95-0907, ERA project 82-01-1054, ERA Technology Ltd., 1995.

[Van Dierendonck] Van Dierendonck, A. J., “Signal Specification for the Future GPS Civil Signal at L5,” *Proceedings of ION Annual Meeting 2000*, San Diego, CA, June 26-28, 2000.

[Van Trees] Van Trees, H. L., *Detection, Estimation, and Modulation, Part I*, John Wiley & Sons, Inc., 2001.

[Volpe] *Vulnerability Assessment of the Transportation Infrastructure Relying on the Global Positioning System*, Final report, John A. Volpe National Transportation Center, August 29, 2001.

[Von Mises] Von Mises, R., *Theory of Flight*, Dover, 1959.

[Walter95] Walter, T., Enge, P., “Weighted RAIM for Precision Approach,” *Proceedings of ION GPS 1995*, Palm Springs, CA, September 12-15, 1995.

[Walter97] Walter, T., Enge, P., Hansen, A., “A Proposed Integrity Equation for WAAS MOPS,” *Proceedings of ION GPS 1997*, Kansas City, MI, September 16-19, 1997.

[Walter00] Walter, T., Hansen, A., Blanch, J., Enge, P., Mannucci, T., Pi, X., Sparks, L., Iijima, B., El-Arini, B., Lejeune, R., Hagen, M., Altshuler, E., Fries, R., Chu, A., “Robust Detection of Ionospheric Irregularities,” *Proceedings of ION GPS 2000*, Salt Lake City, UT, September 19-22, 2000.

[Walter01] Walter, T., “Message Type 28,” *Proceedings of ION NTM 2001*, Long Beach, CA, January 22-24, 2001.

[Widrow67] Widrow, B., Mantey, P. E., Griffiths, L. J., Goode, B. B., Adaptive Antenna Systems,” *Proceedings of The IEEE, VOL. 55, NO. 12*, December 1967.

[Widrow85] Widrow, B., Stearns, S. D., *Adaptive Signal Processing*, Prentice Hall, Inc., 1985.

[Winer] Winer, B. M., Manning P., Geyer, E. M., Ruggiero, J., McCarty, P., “GPS Interference Source Location and Avoidance Systems,” *Proceedings of ION Annual Meeting 1997*, June 30 – July 2,1997.

[WIPP1] "Algorithm Description Document for the User Differential Range Error (UDRE) Monitor of the Wide Area Augmentation System (UDRE ADD)," CDRL Sequence No. A014-009, WAAS Integrity Performance Panel (WIPP), December 22, 2000.

[WIPP2] "Algorithm Description Document for the Grid Ionospheric Vertical Error (GIVE) Monitor of the Wide Area Augmentation System (GIVE ADD)," CDRL Sequence No. A014-006, WAAS Integrity Performance Panel (WIPP), January 22, 2001.

[Wohlfiel] Wohlfiel, J. E., Tanju, B., "Location of GPS Interference," *Proceedings of ION GPS 1999*, Nashville, TN, September 14-17, 1999.

[Wu] Wu, J. T., Peck, S., "An Analysis of Satellite Integrity Monitoring Improvement for WAAS," *Proceedings of ION GPS 2002*, Portland, OR, September 24-27, 2002.